Experimental and numerical modeling of flow and sediment transport in shallow reservoirs

CIFRE convention EDF R&D, ANRT N° 2019/1262

Thesis prepared at Saint-Venant Laboratory for Hydraulics (LHSV), EDF R&D LNHE (France), and Hydraulics in Environmental and Civil Engineering (HECE) research group at Liege University (Belgium)

Defense expected on December 15th, 2023, by:

El Mehdi CHAGDALI

Jury composition :

Prof. Virginia, STOVIN	**Reviewer**	University of Sheffield
Prof. Rita, FERNANDES DE CARVALHO	**Reviewer**	University of Coimbra
Prof. Pierre, DEWALLEF	**Examinator**	University of Liège
Prof. Nils, RUTHER	**Examinator**	Technical University of Munich
Dr. Eddy, LANGENDOEN	**Examinator**	National Sedimentation Laboratory, USDA
Dr. Kamal, EL KADI ABDERREZZAK	**Thesis Director**	EDF R&D & LHSV
Prof. Benjamin, DEWALS	**Thesis Co-director**	University of Liège
Dr. Sébastien, ERPICUM	**Thesis Supervisor**	University of Liège
Dr. Cedric, GOEURY	**Guest**	EDF R&D & LHSV
Eng. Matthieu, SECHER	**Guest**	EDF CIH

Modélisation expérimentale et numérique des écoulements et du transport sédimentaire dans les réservoirs peu profonds

Convention CIFRE EDF R&D, ANRT N° 2019/1262

Thèse préparée au sein du Laboratoire Hydraulique Saint-Venant (LHSV), EDF R&D LNHE (France), et Hydraulics in Environmental and Civil Engineering (HECE) de l'Université de Liège (Belgique)

Défense prévue pour le 15 décembre 2023 par:

El Mehdi CHAGDALI

Composition du jury :

Prof. Virginia, STOVIN	**Rapporteur**	University of Sheffield
Prof. Rita, FERNANDES DE CARVALHO	**Rapporteur**	University of Coimbra
Prof. Pierre, DEWALLEF	**Examinateur**	University of Sheffield
Prof. Nils, RUTHER	**Examinateur**	Technical University of Munich
Dr. Eddy, LANGENDOEN	**Examinateur**	National Sedimentation Laboratory, USDA
Dr. Kamal, EL KADI ABDERREZZAK	**Directeur de thèse**	EDF R&D & LHSV
Prof. Benjamin, DEWALS	**Co-directeur de thèse**	University of Liège
Dr. Sébastien, ERPICUM	**Encadrant**	University of Liège
Dr. Cedric, GOEURY	**Invité**	EDF R&D & LHSV
Eng. Matthieu, SECHER	**Invité**	EDF CIH

Résumé : Les retenues (i.e., réservoirs) peu profondes sont largement utilisées en ingénierie hydraulique (e.g., stockage temporaire de l'eau, bassins de décantation), et bien qu'elles soient en général de géométrie relativement simple (e.g., rectangulaire), les écoulements y sont souvent complexes (e.g., recirculations, jets rattachés ou oscillants,) voire instables. Ceci impacte le transport solide et la sédimentation (e.g., taux de déposition, localisation), et en conséquence l'efficacité opérationnelle des retenues. L'objet de ces travaux de thèse est d'améliorer nos connaissances sur les processus physiques hydro-sédimentaires dans les réservoirs peu profonds, en combinant l'expérimentation en laboratoire et la modélisation numérique. La conception des configurations expérimentales s'est inspirée de retenues réelles et a été réalisée à partir d'analyse dimensionnelle et de pré-simulations numériques avec le code numérique bi-dimensionnel (2D) et tri-dimensionnel (3D) à surface libre TELEMAC-2D et TELEMAC-3D. Au total quarante-deux (42) expériences avec de l'eau claire et quinze (15) expériences avec une injection sédimentaire en amont ont été effectuées. Le champ des vitesses a été mesuré avec la technique LSPIV (Large Scale Particle Image Velocimetry) ainsi que des sondes intrusives de types ADV (Acoustic Doppler Velocimeter) et ADVP (Acoustic Doppler Velocimeter Profiler). Cette dernière technique a permis d'évaluer de manière précise et avancée les vitesses moyennes ainsi que les caractéristiques turbulentes de l'écoulement. La sédimentation a été cartographiée à l'aide d'échosondeur, alors que l'évolution spatio-temporelle des dépôts a été analysée par traitement d'images. Les expériences ont permis de clarifier l'effet des conditions aux limites (canal à surface libre *vs* conduite sous pression), des conditions géométriques (réservoir court *vs* réservoir long), hydrauliques ou encore sédimentaires. Les travaux numériques ont été menés en utilisant code_saturne afin d'évaluer la capacité des modèles de turbulence bas et haut Reynolds de premier et second ordre à reproduire les typologies d'écoulement observés dans une sélection d'expériences. Finalement, un exemple d'application sur un cas réel a été simulé à l'aide de TELEMAC-2D couplé avec son module de transport solide GAIA.

Abstract: Shallow reservoirs are widely used in hydraulic engineering, whether for temporary water storage, or as settling basins. Many of these reservoirs have a relatively simple geometric configuration (i.e., rectangular), but exhibit complex flow phenomena (i.e., eddies, recirculation zones, attached or oscillating jets) and even instable flow patterns. This impacts the sediment transport and sedimentation (e.g., deposition rate, location), and thus the operational efficiency of reservoirs. The objective of this thesis is to enhance our understanding of the physical hydro-sedimentary processes in shallow reservoirs through experimentation and numerical modeling. Design of the laboratory setup was inspired by real basins and was carried out based on dimensional analysis and preliminary numerical simulations using the open source two-depth averaged model TELEMAC-2D (2D) and three-dimensional (3D) model TELEMAC-3D. A series of forty-two (42) experiments with clear water and fifteen (15) experiments with inlet sediment injection were conducted. Velocity fields were measured using the LSPIV (Large Scale Particle Image Velocimetry) technique as well as intrusive probes such as the ADV (Acoustic Doppler Velocimeter) and ADVP (Acoustic Doppler Velocimeter Profiler). This later technique allowed precise and advanced evaluation of average velocities and flow turbulent characteristics. Sedimentation within the reservoir was mapped using an echosounder, while the time-evolution of deposit pattern was analyzed through image processing. These experiments helped to clarify the impact of inlet boundary conditions (open channel *vs* pressurized jet), geometric (short *vs* long reservoirs), hydraulic and sediment conditions. Using the experimental data, the software code_saturne was used to assess the capability of turbulence models, both low and high Reynolds numbers, to observed replicate stable and unstable flow patterns. Finally, a real-world case was stimulated using TELEMAC-2D coupled with its sediment transport module GAIA.

Table of Contents

List of Tables

List of Figures

Chapter 1. Introduction and research objectives

Shallow reservoirs are used in a wide range of applications such as temporary water storage (e.g., compensation basins used as part of Hydropower Plants (HPP)) and sediment settling tanks. Therefore, reservoir sedimentation must be minimized or maximized. Sedimentation depends on the flow typology, which in turn depends on the reservoir geometry and boundary conditions. Over the last decade, major improvements have been brought to these topics, based on laboratory experiments and numerical modeling. in this chapter, we provide a comprehensive review of the French electricity company (Electricité de France) EDF global context, followed by a literature review on laboratory experiments, measurement techniques, numerical modeling, and field surveys. Drawing from the conclusions of these investigations and considering EDF's engineering needs, the research objectives are delineated.

1.1. General context

Shallow reservoirs, also named tanks, basins or ponds, are used in wide range of applications such as temporary water storage (e.g., compensation basins used as part of Hydropower Plants (HPP), Figure 1) or tanks for sediment settling. Their main objectives are to ensure storage of water (e.g., flood control by reducing peak flow discharge, temporary storage in hydropower stations), or to trap sediments. They are often utilized as part of Pumped Storage Hydropower Stations (PSHS) (e.g., Switzerland, France, Morocco, Dubai, Spain, Uzbekistan, Tunisia) (Görtz et al., 2022). Existing reals shallow reservoirs are characterized by various shapes, hydraulic conditions, boundary conditions and sediment characteristics. Previous works on the subject showed that even for simple reservoir shapes (e.g., rectangular), particularly complex flow patterns could be developed (large recirculation, attached or oscillating jets...), depending on the geometry and hydraulic conditions.

Numerical and experimental research on the hydro-sedimentary functioning of shallow reservoirs highlighted that operational performance (e.g., dynamics and location of sediment deposits), are controlled by hydrodynamics. Therefore, for practical engineering design for such reservoirs, it is for utmost importance that the flow field is predicted in a reliable way, in order to avoid ill-designs leading to an accelerated decrease in the water storage capacity and hydropower production, an increase on the maintenance costs and frequency of sediment

flushing operations, with a significant environmental impact due to a sudden increase in turbidity and total solid concentration in the receiving water bodies.

Figure 1: La Coche reservoir (France) (EDF credits)

Sediment management in shallow reservoirs is a significant concern for EDF because the accumulation of sediments reduces the water storage capacity, leading to a direct impact, for instance, on electricity production in the case of hydroelectric dams. Therefore, it is important to accurately model these flow dynamics to potentially assist in reservoir design or address sedimentation-related issues. The storage capacity of shallow reservoirs is compromised by excessive deposition of fine sediments (Figure 2). This significantly affects hydroelectric production and necessitates more frequent sediment flushing operations, which have a notable environmental impact. The hydro-informatic free-surface system TELEMAC-MASCARET is widely used in engineering to predict the hydro-sedimentary behavior in these reservoirs, enabling idealized management and maintenance. It is suitable for use in large domains (on the order of several km^2), features a solid transport module with bed evolution capabilities, and provides relatively fast computations in an engineering context. However, previous studies highlighted the need for numerical modelling validation against accurate measurement data.

Schleiss et al. (2016) discussed the effect of the deposition of sediments in reservoirs, physical processes, management strategies and economic considerations. In the present review, we focus on shallow reservoirs, covering advances in understanding the physics of flow and sediment transport through laboratory experiments, numerical modeling, and field studies.

Figure 2: Longefan Reservoir (France). Aerial view (left), and reservoir after (right) sediment flushing (EDF credits)

1.2. Literature review

Experimentation through physical models with simple geometry configurations is an adequate way for deepening our understanding of physical phenomena, but also for recording data for model calibration/validation. Validated numerical models enable optimizing design of basins and improving the management and overall performance. Real basins studies allow an effective validation of models, the hydro-sedimentary behavior of those structures and a better understanding of the physical processes at field scale. The aim of this section is to summarize the current state of art on hydrodynamics and sedimentation in shallow reservoir.

1.2.1. Laboratory experiments

Flow entering shallow reservoirs can be regarded as a flow passing through a narrow inlet channel entering a suddenly expanded channel. A summary of existing laboratory studies is given in Table 1, in which mainly water was used as fluid and rectangular shape as reservoir and boundary conditions' geometry. Note that non-rectangular basins, such as circular (Quarini et al., 1996), lozenge and hexagon (Kantoush, 2008) were rarely tested in the laboratory.

The first experimental studies on shallow water reservoirs focused on the effect of the sudden expansion occurring when an inlet free surface channel is connected to a rectangular reservoir. Abbott and Kline (1962) were the first to study experimentally the turbulent free surface flow passing through a narrow inlet channel into a symmetric (i.e., double-lateral) sudden expansion that was assimilated to a reservoir with infinite length. They observed three regions in the

expansion area: a first region at the immediate inlet of the reservoir with a 3-D stationary recirculation, flowed by a 2-D stationary region with a point of attachment, and a third unsteady tail region, periodically changing in size. Abbot and Kline (1962) observed that there was no appreciable variation in the lengths of the three zones provided the flow was fully turbulent at the expansion entrance. Using air as fluid, Durst et al. (1974) and Cherdron et al. (1978) observed symmetrical pattern at low Reynolds numbers. For higher Reynolds numbers, an asymmetry was found and explained by the small perturbations involved in the shear layer between the main flow and the recirculation in the reservoir corner. In line with the previous works, Restivo and Whitelaw (1978) showed that flow asymmetry is a characteristic of turbulent flow regime. Fearn et al. (1990) showed that asymmetry occurs beyond a point of bifurcation (pitchfork bifurcation); the geometrical imperfections lead to small perturbations, thereby generating a flow asymmetry and even unsteady state. Aloui and Souhar (2000) and Escudier et al. (2002) confirmed previous results in duct expansion. Battaglia et al. (2006) studied air flow passing a symmetric sudden expansion under low Reynolds numbers and found that the ratio of the expanding geometry implies effects of the sidewall which increased the three-dimensionality character of the expanding flow. As a continuation on the work on sudden expansion through an inlet free surface channel, Mizushima and Shiotani (2001) evaluated the effect of a downstream contraction combined with an upstream expansion at the basin entrance. The inlet and outlet channels were of the same width. Authors found that the downstream contraction restabilized the symmetric state of flow.

Kantoush et al. (2008a, b) studied the flow pattern in different shallow rectangular reservoirs with free surface channels at the inlet and outlet. Starting with a reference reservoir, the length was gradually reduced while keeping a fixed width. Conversely, while keeping a fixed length, the width was modified. Different ranges of Reynolds number and Froude number were studied. Dissymmetric flows were observed for some configurations despite of the symmetry of the reservoir geometry and boundary conditions. Dufresne et al. (2010a) clarified the transition between symmetric and asymmetric flows in rectangular reservoirs using the shape factor defined as $SF = L_1/(\Delta B^{0.6}\, b^{0.4})$, with L_1 the reservoir length, b the inlet channel width, and $\Delta B = (B - b)/2$ the width of the sudden expansion with B as the reservoir width. It appears that symmetric flows occur for $SF < 6.2$ and asymmetric flows take place for $SF > 6.8$. Camnasio et al. (2011) enriched the existing database by performing laboratory experiments in a rectangular reservoir with a symmetrical inlet and outlet open channels, under a large range of combinations of reservoir width and length. Five different types of flow patterns were identified depending on

the values of the length-to-width ratio and expansion ratio of the reservoir: channel-like flow, two symmetric flow patterns characterized by two or four large eddies, and two asymmetrical flow patterns. Camnasio et al. (2013) confirmed experimentally the impact of varying the position of the inlet and outlet channels on the velocity field. Camnasio et al. (2014) studied rectangular basins with symmetrical inflow and outflow and proposed a relationship between the specific mean kinetic energy and the reservoir shape factor defined by Dufresne et al. (2010a). Choufi et al. (2014) examined the effect of bottom roughness in a rectangular basin with variable geometry and symmetrical inlet and outlet channels. They stated that asymmetric flows could develop depending on certain edge conditions (e.g., small perturbations in initial and boundary conditions). On a rough bottom the symmetrical flow remained perfectly, while on a smooth bottom, the flow pattern was an asymmetrical unstable jet.

Some authors were interested on inlet boundary conditions with turbulent circular jet. Stovin and Saul (1996) performed a series of experiments on a rectangular reservoir whose inlet and outlet were circular pipes. Adamsson et al. (2005) performed an experimental study on a large basin with a circular jet inlet and an outlet weir. They observed two large symmetrical patterns. Dufresne et al. (2009) conducted fifty-five (55) experiments in a rectangular reservoir with a circular pipe at the inlet, and another pipe combined with a weir at the outlet. They observed asymmetrical and stationary flow patterns for low water depths in the reservoir (i.e., no overflow) and symmetrical and stationary patterns for high water depth (i.e., overflow over the weir).

Using a free surface inlet condition, Peltier et al. (2014) investigated oscillatory flows of "meandering jet" type in about fifty (50) experiments performed in rectangular reservoirs with rectangular surface channel at the inlet. The frequency, wavelength and lateral expansion of the flow were extracted from Large Scale Particle Image Velocimetry (LSPIV) measurements using a Proper Orthogonal Decomposition (POD). Threshold values on the shape factor and on the inlet Froude number were identified to predict the occurrence of a meandering jet type flow. Relationships were obtained between the characteristics of the meandering jet and friction number S, which was defined by Peltier et al. (2014) as $S = \lambda \Delta B/(8H)$ with H the water depth and λ the friction coefficient. Meandering jet was also studied for inlet jet boundary. Using inlet jet, Maurel et al. (1996) studied rectangular cavities and observed for low Reynolds numbers three different types of flow, namely a stable regime, a cavity oscillation, and a free jet type oscillation, characterized by a relationship between the Reynolds number and the ratio of reservoir length to inlet pipe diameter. Miozzi et al. (2020) studied a confined jet (i.e., similar to wall jet) and observed jet oscillations.

For flow and sediment transport in shallow reservoirs, a limited number of laboratory experiments have been published. Saul and Ellis (1992) showed the direct link between sediment transport processes and flow pattern in the reservoir, also confirmed by Kantoush et al. (2010) and Camnasio et al. (2013). Using crushed olives as sediment particles, Stovin and Saul (1994) showed the important impact of velocity field distribution and bottom shear stress on sedimentation. Luyckx et al. (1999) conducted experiments on rectangular basins with a pressurized jet at the inlet and a lateral weir at the outlet. Twenty geometries were studied to evaluate the sediment trapping capacity. Kantoush and Schleiss (2009) performed experiments with sediment-laden water, and studied the efficiency of sediment flushing in various reservoir conditions. On a configuration tested by Camnasio et al. (2013), the flow pattern changed with a deposit height of no more than 10% of the water depth. Kantoush and Schleiss (2014) developed an empirical formula to describe the influence of geometry shape factor on trapping efficiency defined as the proportion of incoming and outcoming sediment and flushing efficiencies for different geometrical shapes.

The previous studies show some limitations in terms of representativeness of real basins, boundary conditions and sedimentary characteristics (grain size, cohesion). On the other hand, the existing results remain difficult to exploit or generalize for the case of real basins with complex geometric shapes and different types and positions of boundary conditions other than those tested in the laboratory.

Table 1: Summary of laboratory experimental studies. Rect. = Rectangle, RC = Rectangular Channel, Circ. J = Circular jet, W =Weir

Authors	Working fluid	Type of basin	Inlet boundary	Outlet boundary	Hydraulics Measurements	Sediment measurements
Abbott and Kline (1962)	Water	Rect.	RC	Infinite length	Yes	No
Drust et al.et al. (1974)	Air	Rect.	RC	Infinite length	Yes	No
Cherdron et al. (1978)	Air	Rect.	RC	Infinite length	Yes	No
Restivo et Whitelaw (1978)	Air	Rect.	RC	Infinite length	Yes	No
Fearn et al. (1989)	Water glycerol mixtures-Distilled Water	Rect.	RC	Infinite length	Yes	No
Stovin and Saul (1994)	Water	Rect.	CJ	Gate	Yes	Yes
Maurel et al. (1996)	Water	Rect.	Convergent nozzle consisting of two quarter-circle	RC	Yes	No
Quarini et al. (1996)	Water	Circular tank	CJ	W	Yes	Yes
Luyckx et al. (1999)	Water	Rect.	RC	W	No	Yes
Aloui and Souhar (2000)	Water	Rect.	RC	RC	No	No

Escudier et al. (2002)	Water	Rect.	RC	Tank	Yes	No
Battaglia et al. (2006)	Air	Rect.	RC	Tank	Yes	No
Kantoush et al. (2008a)	Water	Rect.	RC	RC	Yes	No
Kantoush et al. (2008b)	Water	Rect.	RC	RC	Yes	Yes
Kantoush and Schleiss (2009)	Water	Rect. + geometries with expansion angles	RC	RC	Yes	Yes
Kantoush et al. (2010)	Water	Rect.	RC	RC	Yes	Yes
Kantoush et al. (2014)	Water	Rect. + geometries with expansion angles	RC	RC	Yes	Yes
Dufresne et al. (2008)	Water	Rect.	CJ	CJ and W	Yes	Yes
Dufresne et al. (2010a)	Water	Rect.	RC	RC	Yes	No
Dufresne et al. (2010b)	Water	Rect.	RC	RC	Yes	Yes
Camnasio et al. (2011)	Water	Rect.	RC	RC	Yes	No
Camnasio et al. (2013)	Water	Rect.	RC	RC	Yes	No

Camnasio et al. (2014)	Water	Rect.	RC	RC	Yes	No
Peltier et al. (2014)	Water	Rect.	RC	RC	Yes	No
Choufi et al. (2014)	Water	Rect.	RC	RC	Yes	No
Guzman et al. (2018)	Water	Rect.	RC	RC	Yes	No
Miozzi et al. (2020)	Water	Rect.	CJ	W	Yes	No

1.2.2. Measurement techniques in laboratory experiments

Table 2 summarizes the main characteristics of measurement techniques applied in shallow reservoir studies at laboratory scale. For the hydraulic part, laboratory studies were mainly interested in the spatial-temporal evolution of velocity field, using mainly two measurement techniques: intrusive techniques which consist of introducing a probe in the flow for measuring the velocity locally, and non-intrusive technique which are used for analyzing the time – motion of natural or artificial tracer added to the flow. Among the available intrusive techniques for measuring the velocity at laboratory scale, seven ones are widely used in literature (see review by Nezu and Nakagawa (1993)): total head tube, propellor current meter, ultrasonic current meter, electromagnetic current meter, hot film anemometer, Laser-Doppler Anemometer (LDA), and Acoustic Doppler Velocity (ADV) technique.

For shallow reservoir, the Ultrasonic Velocity Profiling (UVP) (Metflow, 2002, UVP-DUO) techniques were used by Kantoush et al. (2008a,b), Camnasio et al. (2013, 2014) and Choufi et al. (2014). This instrument allows quantitative measurements of the three-velocity component by Doppler effect techniques. The emitted signal is reflected by the flowing particles. The comparison of the emitted and received signals by measuring the time delay of the echoes to reach the instrument and the Doppler frequency shift allow determining the velocity of the particle and so the velocity of the liquid flow. Hot film anemometer is common instrument for measuring velocity and fluid directions. The operating principle is based on the relation between sensor heat transfer on the fluid velocity, temperature, and composition (see details by Bradshaw (1971) and Hinze (1975)). Nezu and Nakagawa (1993) described various hot-film probes and main issues (e.g., impurities, air bubbles) that could yield inaccuracies in the measurement. Quantitative measurements of mean velocity and turbulence intensity using this technique were carried out by Abbot and Kline (1962) and Aloui and Souhar (2000). Stovin and Saul (1994) measured the mean components of the velocity distribution in the reservoir using another technique, called a miniature propeller meter.

Concerning flow visualization, different techniques have been developed. The use of dye or smoked injection, hydrogen bubbles and buoyant tracers allow displaying the flow patterns and turbulence structures in steady and unsteady flows. The processing of image series allows describing qualitatively and quantitively the flow field using techniques such as Particle image velocimetry (PIV). On the other hand, Laser Doppler Velocimeters (LDV), commonly referred to as Laser Doppler Anemometers (LDA) is a technique that could be used to measure the velocity field combined with some conditional averaging methods. In this context, Abbot and Kline (1962) used a needle trace method, with a line of dye being placed at the wall. Cherdron et al. (1978) used particles in the form of oil droplets, identifying therefore regions of

instantaneous recirculation, evolution of flow field and formation of vortices. Fearn et al. (1989) used light reflecting Mearlmaid particles mixed with the flow and illuminated by luminous rays. Using potassium permanganate dissolved in water, Quarini et al. (1996) recorded experiments at reference points and extracted longitudinal velocities from video treatment. Dufresne et al. (2010a) used dye injection to identify symmetric and asymmetric flow patterns. By injecting 100 drops of dye every two seconds, they were able to determine accurately the reattachment point position in their experiments. Aloui and Souhar (2000) injected small amounts of gas bubbles (i.e., tracers) to determine the direction of flow. Guzman et al. (2018) measured the residence time distribution of different basin design using a rhodamine solution dye injected into the inlet channel. The concentration of the tracer was measured at the outlet with a fluorometer. Battaglia et al. (2006) used the Particle Image Velocimetry (PIV) technique with injection of smoke for measuring instantaneous velocity in the reservoir. Large Scale Particle Image Velocimetry (LSPIV) was utilized for measuring the surface velocity field: Kantoush et al. (2008a, b), Choufi et al. (2014) used polypropylene plastics of diameter equal to 3.4 mm, and Peltier et al. (2014) used seeds of diameter equal to 2 mm. The horizontal structures of the studied flows were correctly characterized. Laser Doppler Velocimeters (LDV) were used by Cherdron et al. (1978), Restivo and Whitelaw (1978), and Fearn et al. (1989). Miozzi et al. (2020) used floating particles of the OMEGA-SPHERES type with a diameter equal to 150 μm and extracted amplitude and frequency of oscillation of the global meandering motion. Peltier et al. (2014) performed a Proper Orthogonal Method (POD) analysis to extract the characteristics of the meandering flow (frequency, wavelength and mean lateral expansion of the meandering jet) from velocity field measured by LSPIV technique.

Flow visualization has the advantage to be less expensive and to allow obtaining a global description of the flow in the entire domain. It requires nevertheless an adequate choice of seeding material or tracers, a carefully set of reflection of the light as well as important post-processing to extract quantitative information of the flow. On the other hand, intrusive techniques allow more accurate measurements of turbulent flow components, but they have the disadvantage of recording local measurements or along specific profile (e.g., UVP). The intrusiveness of the instrument can also influence the flow pattern for high Reynolds numbers. Subsequent post-processing may be necessary to recover a good signal quality. For example, despiking filters by Goring and Nikora (2002) or denoising filters (Hurther and Lemmin, 2001) are often used especially for instruments that use the Acoustic Doppler technique. Non-intrusive and intrusive techniques can be complementary and allow a global and accurate description of the flow pattern, turbulent structures of velocity components in shallow reservoir.

Concerning the sediment transport, measurements mainly concerned the deposit as well as the sediment concentration. Sediment deposition has been evaluated visually for most of the

experiments (e.g., Stovin and Saul, 1994; Luyckx et al., 1999; Dufresne et al, 2009). Kantoush et al. (2008b) used a Mini-echo-sounder UWS for measurements of sediment thickness and the total volume of sediment deposited in the reservoir. The UWS emits an ultrasound impulse which is reflected by the bottom. The reflected signal (echo) is received by the ultrasound sensor. The run time for the signal from the sensor to the bottom and from the bottom to the sensor must be determined. When the run-time is well known, the target distance could be calculated. Camnasio et al. (2013) used a Laser technique to measure the deposits in the reservoir. For experiments with suspended load, Kantoush et al. (2008b) and Camnasio et al. (2013) monitored sediment concentrations with turbidity-meters (Solitax).

The choice of suitable sediments is crucial for the laboratory-scale study. Previous studies have used mainly non-cohesive sediments. Indeed, the study of shallow reservoirs at the laboratory scale with cohesive sediments is a real challenge. Several types of materials to model non-cohesive sediment with different D_{50} and sediment density were used, as set forth herein (Table 3). Stovin and Saul (1994) used crushed olive pits, Quarini et al. (1996), used glass balls and aluminium flakes, Luyckx et al. (1999), Bakelite and Nylon, Kantoush (2008), used Crushed nuts, Dufresne et al. (2009), used Polystyrol sediment, Dufresne et al. (2010b) used granular plastic (Styrolux 656 C), Camnasio et al. (2013) used crushed walnut shells.

Several techniques of flow and sediment transport measurements could be used to perform the laboratory experiments. We distinguish more particularly the intrusive measurement techniques and the visualization techniques. Each technique has its particularities and requires a mastery of the calibration and post-processing process. These techniques have allowed a quantitative and qualitative understanding of the flow typologies in these reservoirs. Each instrument types have its specificity in terms of calibration, post processing, sensitivity, maneuverability, effect of environments on results. The choice of a specific technique depends on the purpose of the study, expectations, and environmental constraints. Previous studies have not pushed more analysis on 3D phenomena (presence of secondary currents) and quantification of turbulence (e.g., Reynolds tensor, bursting...). Given the turbulent character of flows shallow reservoirs, it seems necessary to push further this analysis to ensure a better understanding of the turbulence and a better validation of the numerical models. On the other side, more accurate measurements of sediment transport patterns would provide a better understanding of sediment dynamics.

Table 2: Summary of laboratory measurement techniques applied to shallow reservoirs. u: longitudinal velocity, v: transversal velocity, w: vertical velocity.

	Flow measurements					Sediment measurements		
Authors	Techniques	Intrusive /Non-intrusive	Velocity components	Type of sediment	Median diameter d_{50} (µm)	Technique	Intrusive or visualization	Deposition/ Suspension
Abbott and Kline (1962)	Hot film anometer+ dye injections	Intrusive + Non-intrusive	*u, v, u', v'*	-	-	-	-	-
Drust et al. (1974)	LDA+ dye injections	Non-intrusive	*u, u'*	-	-	-	-	-
Cherdron et al. (1977)	LDA+ dye injections	Non-intrusive	*u, u'*	-	-	-	-	-
Restivo et Whitelaw (1978)	LDA	Non-intrusive	*u, u'*	-	-	-	-	-
Fearn et al. (1989)	LDV + dye injections	Non-intrusive	*u, w*	-	-	-	-	-
Stovin and Saul (1994)	Propeller meter	Intrusive	*u, w*	Crushed olive pits	47	Visualization	Visualization	Deposition
Maurel et al. (1996)	Laser induced fluorescence LIF	Non-intrusive	Oscillation regime	-	-	-	-	-
Quarini et al. (1996)	Dye injection	Non-intrusive	*u*	Glass balls and Aluminium flakes	500	Visualization	Visualization	Suspension

Luyckx et al. (1999)	-	-	-	Bakelite and Nylon	400-2000	Visualization	Visualization	Deposition
Aloui and Souhar (2000)	Hot film probe + injections	Intrusive + Non-intrusive	*u*	-	-	-	-	-
Escudier et al. (2002)	LDA	Intrusive	*u, u', v, v'*	-	-	-	-	-
Battaglia et al. (2006)	LDA + Dye injections	Intrusive + Non-intrusive	*u*	-	-	-	-	-
Kantoush et al. (2008a)	LSPIV+UVP	Intrusive + Non Intrusive	*u, v, w*	-	-	-	-	-
Kantoush et al. (2008b)	LSPIV+UVP	Intrusive + Non-intrusive	*u, v, w*	Crushed nuts	5	Turbidity meter +Mini Echo Sounder	Intrusive	Deposition-Suspension
Kantoush and Schleiss (2009)	LSPIV+UVP	Intrusive + Non-intrusive	*u, v, w*	Crushed nuts	50	Mini Echo Sounder UWS	Intrusive	Deposition
Kantoush et al. (2010)	LSPIV	Non-intrusive	*u, v*	Crushed nuts	51	Mini Echo Sounder UWS	Intrusive	Deposition
Kantoush et al. (2014)	-	-	-	Crushed nuts	51	Mini Echo Sounder UWS	Intrusive	Deposition
Dufresne et al. (2009)	ADV	Intrusive	*u, v, w*	Polystyrol sediment	350 - 1400	Visualization	Visualization	Depositon

Dufresne et al. (2010a)	Dye injections	Non-intrusive	-	-	-	-	-	-
Dufresne et al. (2010b)	Dye injections	Non-intrusive	-	Granular plastic	2400	Visualization	Visualization	Deposition
Camnasio et al. (2011)	UVP transducers	Intrusive	*u, v*	-	-	-	-	-
Camnasio et al. (2013)	UVP transducers	Intrusive	*u, v*	Crushed walnut shells	89	Laser technique	Visualization	Deposition
Camnasio et al. (2014)	UVP transducers	Intrusive	*u, v*	-	-	-	-	-
Peltier et al. (2014)	LSPIV	Non-intrusive	*u, v*	-	-	-	-	-
Choufi et al. (2014)	UVP + LSPIV	Intrusive + Non-intrusive	*u, v*	-	-	-	-	-
Guzman et al. (2018)	Dye injection	Non-intrusive	-	-	-	-	-	-
Miozzi et al. (2020)	Tracer	Non-intrusive	*u, v*	-	-	-	-	-

1.2.3. Numerical modeling

Existing research mainly focused on evaluating the ability of numerical codes to reproduce experimental laboratory measurements. Dewals et al. (2008), Dufresne et al. (2011), Camnasio et al. (2013) and Camnasio et al. (2014) showed that 2D modeling based on the Shallow water equations correctly simulate the flow pattern in a shallow rectangular basin with symmetric inlet and outlet and flat bottom. Camnasio et al. (2013) validated the same model for rectangular reservoirs with asymmetric inlet and outlet positions, flat bottom, and bottom with deposits. By comparing experimental measurements of turbulent kinetic energy and numerical predictions, Camnasio et al. (2014) showed that the k–ε turbulence model was more appropriate than an algebraic model as it provides satisfactory reproduction of the turbulent kinetic energy in the main jet, but it leads to overestimations in the recirculation zones. Using the 2D code TLEMAC-2D, Secher et al. (2013) found good qualitative and quantitative model-data agreement in reproducing velocity field of symmetric and asymmetric configurations.

Peltier et al. (2014) studied meandering jets numerically. Based on proper orthogonal decomposition, the numerical results were analyzed through six parameters: mean fluctuating kinetic energy per mode, sum of the mean fluctuating kinetic energy in the first ten modes, frequency, and mean amplitude of the first four temporal coefficients, and the longitudinal and lateral variation of first four spatial modes. Peltier et al. (2014) reproduced the global behavior of the unsteady flows but could not find accurate shapes of the structures developing inside shallow reservoirs.

Given the turbulent flow, a correct turbulence modeling is a key element for accurate flow reproduction. In all previous 2D numerical modeling applications, The Reynolds Averaged Navier-Stoke (RANS) equations were solved. A k–ε closure turbulence model was used by Dewals et al. (2008), Dufresne et al. (2011), Peltier et al. (2014), Camnasio et al. (2013), Camnasio et al. (2015), and Ferrara et al. (2018). Other turbulent closures were also applied: Persson (2000) used the Smagorinsky model, Kantoush et al. (2008b) used the Integrated Parabolic Model (DIPM) and depth-Integrated Mixing Length Model (DIMLM) eddy viscosity models. Peng et al. (2011) used two-dimensional lattice Boltzmann method to approximate numerical solutions to the shallow water equations. The results showed a good reproduction of flow patterns and a similar accuracy as in previous studies.

Codes solving Navier-Stokes equations have been used and validated against laboratory configurations. Quarini et al. (2016) showed that predictions of 3D models were in good agreement with the main flow structures observed for a circular reservoir. Adamson et al. (2005) found good agreement between measurements and simulations concerning both flow pattern and residence time distribution curves for high flow rates in a rectangular reservoir.

Dufresne et al. (2009) found good data agreement for simulations with high water depth with overflow for rectangular reservoir with inlet pipe and outlet weir. Esmaeili et al. (2015) managed to reproduce the 3D velocity field in rectangular shallow reservoirs with various geometries on fixed and deformed bed as well. To assess the reliability of numerical models, some authors used existing experimental data. Tarpagkou et al. (2013) used depth-average velocity magnitude observed by Armaly et al. (1983) and Dufresne et al. (2009), a satisfactory model-data agreement is found. Lakzian et al. (2020) validated a 3D code from the experimental data of Camnasio et al. (2013). They found that the lateral velocity modelled at certain sections was in good agreement with measurements, and they revealed the existence of secondary currents. For turbulence modeling, RANS models with standard k–ε model were used by Dufresne et al. (2009), Esmaeili et al. (2015), and Lakzian et al. (2020). Other Reynolds-Averaged Navier-Stokes (RANS) models were also applied: Tarpagkou et al. (2013) used the RNG version of k–ε model, which is used to accounts for the effects of smaller scales of motion through changes in the dissipation term (ε) and Isenmann et al. (2016) used k-w SST (Shear-Stress Transport) model. More sophisticated way to consider turbulence were applied using the Large Eddy Simulations (LES), in which the turbulence scales smaller than the mesh size are filtered and modeled while the large scales containing most of the flow energy are completely simulated. Because of its important calculation cost, few of LES simulations were used this for these studies. An application of LES with Smagorinsky-Lilly subgrid-scale (SGS) model on rectangular reservoirs was presented by Zahabi et al. (2018). Finite volume and finite element are also used. In case of unknow water-level, a two-phase modeling is possible. In this case, the Navier Stokes equations are not solved for the water phase alone, but for a combination of water and air phases. In this context, Tarpagkou et al. (2013), Isenmann et al. (2016), and Zahabi et al. (2018) used the Volume of Fluid (VOF) method.

For solid transport modeling, three approaches may be distinguished: Solving Exner equation and advection/diffusion equation considering erosion and deposition as source terms derived from empirical formulas, Eulero-Eulerian approach, and Eulero-Lagrangian approach. In the latter one, fluid is described in a Eulerian way, while the sediment particles are treated in a discrete way by simulating the trajectory of large number of particles and their interactions with bottom and other particles. The number of tracked particles shall be large enough for the results to be statistically representative. Stovin and Saul (1996) discussed the definition of bed boundary conditions for this approach. The ‘trap condition’ was used and lead to an overestimation of the reservoir trapping because particles can be resuspended after contacting the bed. Adamsson et al. (2003) implemented an improved boundary condition based on bed shear stress. The obtained results were more accurate in terms of efficiency and pattern of sediment deposits. Dufresne et al. (2009) used a boundary condition based on the bed shear

stress for relatively low water depths and based on the bed turbulent kinetic energy for higher water depths. A good agreement was obtained for mass percentages and location of sediment deposits. Isennman et al. (2016) numerically studied the experiments of Stovin and Saul (1994) and Dufresne et al., (2009) using further improved boundary condition. The comparison of numerical and experimental results shows a good reproduction of the deposition rates and quantities. Following Eulerian description for the flow and the sediments, Zahabi et al. (2018) used Eulerian suspended load equation and Meyer-Peter and Müller (1948) formula for bed-load transport. Computed and observed profiles of deposition in the reservoir compared well with differences not exceeding 5%. Lakzian et al. (2020) used a Drift-flux model, in which individual phase is considered as continuous and described by conservation. The model was applied to the tests of Dufresne et al. (2009). Results showed that numerical results agree with the experimental zone of deposition. Shoarinezhad et al. (2023) utilized an automated calibration tool that employs the gradient-based Gauss–Marquardt–Levenberg optimization algorithm to calibrate 3D morphodynamic numerical models for a reservoir with hexagonal and lozenge-shaped configurations, previously studied by Kantoush (2008). The results demonstrate good agreement between the model and data when calibrating two critical parameters, namely, roughness height and sediment active layer thickness.

Some studies focused on the improvement of reservoir performance using numerical models. Persson (2000) evaluated the hydraulic efficiency of thirteen shallow basins with 2D numerical modeling and found that the presence of an obstacle in front of the basin entrance increases the trapping efficiency. Using a 2D numerical model, Ferrara et al. (2018) evaluated the effect of varying the inlet and outlet position on flow field for rectangular shallow basins. Using 2D hydro-sedimentary numerical model and Brent's optimization method, an inverse calculation model was applied to a rectangular reservoir by Liu et al. (2013). A best baffle horizontal position could be found using this approach. Based on a 3D model, Tamayol et al. (2010) tested three baffle positions and found that the most suitable position is related to the importance on buoyancy forces. A reflection baffle may improve the tank performance for low buoyancy forces, while a baffle place at the bottom of the tank would improve the performance for strong buoyancy forces. Using a 3D numerical model, Zahabi et al. (2018) evaluated the effects of geometry, position of boundary conditions and flow characteristics on trapping efficiency. Lakzian et al. (2020) tested inlet angle effect on the trapping efficiency.

Various approaches of numerical simulations were studied. So far, different methods to consider the free surface, to solve the equations of motion, to model turbulence, or to simulate the transport and deposition of sediment are found. The 2D approaches solving Shallow water equation (with hydrostatic assumption of the pressure) have shown satisfactory results for the reproduction of flows in various configurations with free surface boundary conditions. The 3D

approaches allow a better representation of the boundary conditions (e.g., pressurized jet) but also allow a complete resolution of the Navier-stokes equations. They are nevertheless more expensive in terms of computation time than the 2D approach but provide an understanding of the flow typology on the vertical. We distinguish two main uses of the numerical model in this subject, on the one hand the validation of the code from experimental measurements and on the other hand the use of the code as a tool for prediction and optimization of the performance of these tanks. Future work should include hydrodynamic model validation with boundary conditions (types and positions) and geometries more similar cases to those of real basins. A finer validation of the numerical models is also needed, through a comparison with turbulence measurements as well as the use of more developed turbulence methods, such as the LES, for a better representation of turbulent structures. For sediment transport, model validation in the presence of cohesive and mixed sediments is still to be achieved, as well as the evaluation of others physical phenomena such as the effects of wind, stratification, flocculation.

Table 3: Summary of existing numerical studies on shallow reservoirs

			Hydraulics				Sediment transport		
Authors	Examination	Numerical model	Equation	2D/ 3D	Turbulence modeling / models	Methods of resolutions	Suspension-Bedload	Euler/Lagrangian	Equations/ Formulas
Fearn et al. (1989)	Validation	In house model	Shallow water	2D	-	Finite element	-	-	-
Persson (2000)	Optimization	MIKE21	Shallow water	2D	RANS - Smagorinsky	Finite volume	-	-	-
Kantoush et al. (2008a)	Validation	CCHE2D	Shallow water	2D	Eddy viscosity	Finite element	-		-
Kantoush et al. (2008b)	Validation	CCHE2D	Shallow water	2D	Eddy viscosity	Finite element	Suspension+ Bedload	Eulerian	Advection-Diffusion + bedload formula
Dewals et al. (2008)	Validation	WOLF-2D	Shallow water	2D	RANS -k-ε	Finite volume	-	-	-
Dufresne et al. (2011)	Validation	WOLF-2D	Shallow water	2D	RANS -k-ε	Finite volume	-	-	-
Peng et al. (2011)	Validation	Nine-speed square lattice (D2Q9) model	Lattice Boltzmann equation for shallow water	2D	Lattice Boltzmann equation for shallow water	-	-	-	-

Camnasio et al. (2013)	Validation	WOLF-2D	Shallow water	2D	RANS -k-ε	Finite volume	-	-	-
Secher et al. (2013)	Validation	TELEMAC-2D	Shallow water	2D	RANS -k-ε	Finite element			
Xiodan et al. (2013)	Optimization	In house model	Shallow water	2D	URANS k-ε	Finite element	Suspension	Eulerian	Advection-Diffusion
Peltier et al. (2014)	Validation	WOLF-2D	Shallow water	2D	RANS -k-ε	Finite volume	-	-	-
Camnasio et al. (2015)	Validation	WOLF-2D	Shallow water	2D	RANS -k-ε and Algebraic model	Finite volume	-	-	-
Ferrara et al. (2018)	Optimization	WOLF-2D	Shallow water	2D	RANS -k-ε	Finite volume	-	-	-
Hoechenli et al. (2021)	Validation and optimization	OPENFOAM	Shallow water	2D	-	-	Suspension	Eulerian	Advection-Diffusion
Stovin and Saul (1996)	Validation	FLUENT	Navier-stokes	3D	RANS -k-ε	Finite volume	Suspension	Lagrangian	Particle tracking
Quarini et al. (1996)	Validation	FLOW 3D	Navier-stokes	3D	RANS -k-ε	-	-	-	-
Adamsson et al. (2005)	Validation	FLUENT	Navier-stokes	3D	RANS -k-ε	Finite volume	-	-	-
Dufresne et al. (2009)	Validation	FLUENT	Navier-stokes	3D	RANS - k-ε	Finite volume	Suspension	Lagrangian	Particle tracking

Tamayol et al. (2010)	Validation and optimization	-	Navier-stokes	3D	RANS -k-ε	Finite volume	Suspension	Eulerian	Advection-Diffusion
Tarpagkou et al. (2013)	Validation	FLUENT	Navier-Stokes	3D	RANS k–ε (RNG)	Volume Of Fluid	Suspension	Lagrangian	Particle tracking
Esmaeili et al. (2015)	Validation	SSIIM	Navier-Stokes	3D	RANS -k-ε	Finite volume	-	-	-
Isenmann et al. (2016)	Validation	OPENFOAM	Navier-Stokes	3D	RANS -k-ω SST	Volume Of Fluid	Suspension	Lagrangian	Particle tracking
Zahabi et al. (2018)	Validation and optimization	FLOW 3D	Navier-Stokes	3D	LES - Smagorinsky subgrid-scale (SGS)	Volume Of Fluid		Eulerian	Advection-Diffusion + bedload formula
Lakzian et al. (2020)	Validation and optimization	OPENFOAM	Navier-Stokes	3D	RANS -k-ε	Finite volume	Suspension	Eulerian drift flux	Advection-Diffusion
Shoarinezh ad et al. (2023)	Validation		Navier-Stokes	3D	RANS -k-ε	Finite volume	Bedload	Eulerian	Advection-Diffusion + bedload formula

1.2.4. Real basin applications

In this section, real basins cases studies are presented. Some studies were conducted to validate the numerical model and others to enhance the performance of real reservoirs. Mouris et al. (2018) carried out using 3D numerical simulations to validate the computation of flow and suspended sediment transport in a real reservoir. Stationary Acoustic Doppler Current Profiler (ADCP) measurements were used to validate the model. Claude et al. (2019) performed a 2D and 3D hydro-sedimentary numerical study on a real shallow reservoir using TELEMAC-3D. The code captured accurately the overall behavior of the hydrodynamic and transport of cohesive sediment after the establishment of a sedimentation velocity that varies with sediment concentration. A field campaign using ADCP measurements and sediment concentration gauging allowed measuring 3D flow structures and spatio-temporal evolution of sediment concentration, which were used to calibrate the numerical model. Izdori et al. (2019) simulated sludge accumulation patterns in a real basin and conducted field surveys. The influence of wind, which has a significant effect on sludge accumulation, and was considered in the numerical model. Results showed good data-agreement.

Using 2D hydrodynamic and water quality transport models, Koskiaho (2003) proposed upgrades for two retention reservoirs. Baffles were introduced to guide the primary flow and maximize the utilization of the wetland area, significantly enhancing the hydraulic efficiency. Stamou (2002) studied and compared four arrangements of guiding walls in a reservoir. Stamou (2008) studied the increase in hydraulic efficiency through modifying the geometry of nine basins. Tsavidaris et al. (2015) used a 3D model to study the effect of vegetation on flow patterns in a real reservoir. Thereafter, several shapes of reservoirs have been tested to promote uniform flow profiles. Elliptical-shaped reservoir with central berm showed the best performance compared to elliptical and triangular shapes.

This overview of applications on real basins shows their complexity compared to simple (idealised) experimental configurations. In addition to the reservoir characteristics discussed above (geometry, boundary conditions, hydro-sedimentary conditions), the consideration of wind, temperature, and vegetation increase the complexity of the numerical modeling.

1.2.5. Conclusions and perspectives

This chapter reviewed the studies carried out so far for the analysis of flow, sediment transport and morphodynamics in shallow reservoirs. Several authors were interested experimentally in the effect of varying the reservoir geometry and the influence of boundary conditions on the flow field.

Sediment transport has been the subject of several studies, with interest in sediment transport and deposition zones. The experimental measurement techniques used in the laboratory experiments provide qualitative and quantitative information on the characteristics of the flow and sediment deposition. Available numerical studies considered different set of equations, methods of resolution, turbulence closures. This review showed that the three approaches, experimental, numerical and in-situ, are complementary.

Despite advances made, previous studies show some limitations in terms of representativeness of real basins, boundary conditions and sediment characteristics (e.g., cohesive sediment). On the other hand, the results found remain difficult to exploit or generalize for the case of basins with complex geometrical shapes and different boundary conditions often located at positions different than those tested in experimental set-ups.

The representativeness of real basins by their geometric shapes, boundary conditions and hydro-sedimentary characteristics, as discussed by Kantoush et al. (2010) and Camnasio et al. (2013), is a necessary element for the design of new experimental set-ups. Measurements in transient regime, 3D flows and more precise measurements on turbulence would also allow a better validation of numerical tools. More elaborated turbulences models (LES) would certainly ensure an enhance representation of the flow fields and hence of transport processes.

1.3. Research objectives

To comprehensively address these research inquiries, a combined approach intertwining experimentation and numerical modeling has been embraced. The main objectives of this project are to improve the understanding of the processes involved in shallow reservoirs by means of experimental modeling. New laboratory experiments have been conducted, with the focus on the effect of inlet condition. Adequate monitoring of flow and sediment deposition within the reservoir were used. Using the laboratory data, the applicability of code_saturne to replicate the measurements is assessed.

The remaining manuscript is organised as follows:

- Chapter 2 encompasses an overview of the numerical tools harnessed throughout this thesis, namely TELEMAC-2D, TELEMAC-3D, GAIA, and code_saturne.
- Chapter 3 entails the validation of TELEMAC-2D through the utilization of prior experiments. For clear-water experments, in-depth analysis of the impact of mesh quality, numerical schemes, and turbulence models was performed on symmetric and

asymmetric experiments involving open-channel inlet and outlet flows. The model is then used for designing a novel complementary set of experiments.

- Chapter 4 presents the experiments we conducted with clear water in shallow reservoirs, employing inlet boundary condition in the form of open-channel or pressurized jet. Various hydraulic and geometric conditions were tested, leading to the creation of a substantial database that enable the assessment of the effects of different parameters on flow patterns and turbulent features.
- Chapter 5 presents the sediment-related aspects observed in our laboratory experiments, emphasizing the role of inlet jet condition.
- Chapter 6 involves the comparison of experimental data from Chapter 4 with simulated results. The primary objective of this chapter is to evaluate the effects of various turbulence models on the simulation outcomes.
- Chapter 7 focuses on a practical application case involving the addition of a deflector.

By intricately weaving together experimentation and numerical modeling, this thesis advances the understanding of hydraulic sediment transport dynamics in shallow reservoir.

Chapter 2. Numerical tools

This chapter provides an overview of the numerical models employed in this thesis: the free surface environmental hydraulic system TELEMAC-MASCARET and the computational fluid dynamics code_saturne software. Within the TELEMAC-MASCARET system, three distinct modules were employed: TELEMAC-2D, which tackles the shallow water equations using finite-element and finite-volume methods; TELEMAC-3D which employs the same horizontally unstructured mesh as TELEMAC-2D but solves the Navier-Stokes equations, whether in a hydrostatic or non-hydrostatic regime; and GAIA, a state-of-the-art module for simulating sediment transport, encompassing cohesive and non-cohesive materials and bed evolution. On the other hand, code_saturne employs a co-located finite-volume approach compatible with meshes of various cell types and can be used in conjunction with various Unsteady Reynolds-Averaged Navier-Stokes (URANS) turbulence models and Large Eddy Simulation (LES).

2.1. Free surface hydroinformatic TELEMAC-MASCARET

2.1.1. Two-dimensional hydrodynamic TELEMAC-2D solver

TELEMAC-2D solves the shallow water equations which are derived by depth-integrating the Navier–Stokes equations. The given equations are expressed in Cartesian coordinates here below. The first equation represents the mass conservation (continuity equation), while equation two and three correspond to the momentum equations in the *x* and *y* dimensions, respectively.

$$\frac{\partial H}{\partial t} + \mathbf{u}\,.\nabla H + H\,\nabla.(\mathbf{u}) = S_h \tag{1}$$

$$\frac{\partial u}{\partial \mathrm{t}} + \mathbf{u}.\nabla u = -g\,\frac{\partial z_b}{\partial \mathrm{z}} + S_x + \frac{1}{H}\nabla.(H\,\nu_t\,\nabla\,u\,) \tag{2}$$

$$\frac{\partial v}{\partial t} + \mathbf{u}.\nabla v = -g\,\frac{\partial z_b}{\partial z} + S_y + \frac{1}{H}\nabla.(H\;\nu_t\,\nabla v) \tag{3}$$

with *t* is time; *H* is the flow depth; *u* and *v* are depth-averaged velocities in *x* and *y* directions, respectively; **u** is the depth-averaged velocity vector (*u*, *v*); z_b is bed elevation, *g* is gravity acceleration; ν_t is momentum diffusion coefficient; ∇ is the gradient operator (*∂*/*∂*x, *∂*/*∂*y), and ∇. is the divergence operator. S_h is fluid sources or sinks, and S_x and S_y are momentum source terms in the *x* and *y* directions, respectively, encompassing factors such as wind, Coriolis force, bottom

and lateral friction, wind stress, atmospheric pressure gradients, wave forces. Considering only the bottom friction, S_x and S_y are written as follows:

$$S_x = \frac{1}{2} C_f \frac{u\|\mathbf{u}\|}{H} \tag{4}$$

$$S_x = \frac{1}{2} C_f \frac{v\|\mathbf{u}\|}{H} \tag{5}$$

with C_f a dimensionless friction coefficient that can be calculated according to Strickler equation.

TELEMAC-2D is designed to solve the shallow water equations on an unstructured triangular mesh grid. These equations can be solved using either the Finite Elements method or the Finite Volumes method. The classical approach involves first calculating the water depth *h* and the velocity components *u* and *v* across the entire domain. Various schemes are available for addressing the advection step. In the subsequent step, propagation, diffusion, and source terms within the momentum equations are taken into consideration. The final velocity field is determined by utilizing the previously calculated advected velocities. The discretized equations together form a linear system, which is solved using an iterative solver such as the conjugate gradient method for instance (Hervouet, 2007).

TELEMAC-2D provides six options for modeling turbulence, which are: (i) constant viscosity, (ii) Elder model, (iii) k-ε model, and (iv) Smagorinski model, (v) Mixing length model, and (vi) Spallart-Allmaras model. Several numerical schemes for solving the advection step for velocity and turbulence for finite element are available: method of characteristics, centered semi-implicit scheme with SUPG (Streamline Upwind Petrov Galerkin) method, N distributive scheme, Positive Streamwise Invariant (PSI), PSI scheme with Locally semi-Implicit Predictor-corrector Scheme (LIPS), edge-by-edge implementations of schemes N and PSI designed to work on tidal flats and element by element Residual distributive Iterative Advection scheme (ERIA) (Hervouet, 2017).

2.1.2. Three-dimensional hydrodynamic TELEMAC-3D solver

TELEMAC-3D, a module of the open TELEMAC-MASCARET system, is employed for solving three-dimensional Navier-Stokes equations, which account for a time-varying free surface. The conservation of mass equation assumes a negligible water density variation, indicating an incompressible fluid. The Boussinesq approximation is employed, considering only buoyant forces for variations in momentum density. These assumptions lead to the solution of the following three-dimensional equations:

$$\nabla . \mathbf{u} = 0 \tag{6}$$

$$\frac{\partial \mathbf{u}}{\partial t} + \mathbf{u} . \nabla \mathbf{u} = -\frac{1}{\rho} \nabla P + \nabla . \nu_t \nabla \mathbf{u} + \mathbf{F} \tag{7}$$

Where, **u** is the 3D velocity vector (*u*, *v, w*), ρ is water density, *P* is the pressure term**,** and **F** represents external forces plus buoyancy terms. The basic algorithm for resolving these governing equations is divided into three steps: (i) calculation of the convective velocity components by solving only the convection terms of the momentum equations, (ii) from the convective velocity, computation of the new velocity components considering the diffusion terms and the source terms of the momentum equations, and (iii) calculation of flow depth from the vertical integration of the continuity equation and momentum equations containing only the pressure-continuity terms. Given that the free surface evolves over time, it becomes necessary to discretize the spatial domain to be flexible and adaptable. TELEMAC-3D uses a sigma transformation on the vertical (non-conforming transformation) which facilitates the construction of a 3D mesh. This transformation allows having a structured mesh on the vertical, built as an extrusion of a 2D mesh along the vertical, then divided into layers. To ensure the immobility of the spatial domain, a variable change is employed for the vertical coordinate *z* using the sigma transformation.

2.1.3. Sediment transport module GAIA

TELEMAC-2D/3D can be coupled to GAIA the 2D sediment transport module, which computes the evolution of bed geometry from the sediment continuity equation (also called Exner equation). For bedload transport, the equation reads as:

$$\left(1 - \lambda_p\right) \frac{\partial z_b}{\partial t} + \nabla . \boldsymbol{Q_b} = 0 \tag{8}$$

with the vector of volumetric transport rate per unit width without pores $\boldsymbol{Q_b}$, expressed in (m²/s), with components Q_{bx} , Q_{by} in the *x* and *y* direction respectively, and λ_p the bed porosity.

$$\boldsymbol{Q_b} = \left(Q_{bx}, Q_{by}\right) = \left(Q_b \cos\alpha, Q_b \sin\alpha \right)$$

Q_b is the bedload transport rate per unit width, computed by a sediment transport capacity formula; and *α* is the angle between the sediment transport vector and the downstream direction (x−axis).

For suspended load, the 2D advection-diffusion equation is solved:

$$\frac{\partial hC}{\partial t} + \frac{\partial huC}{\partial x} + \frac{\partial hvC}{\partial y} = \frac{\partial}{\partial x}\left(h\varepsilon_x \frac{\partial C}{\partial x}\right) + \frac{\partial}{\partial y}\left(h\varepsilon_y \frac{\partial C}{\partial y}\right) + (E - D) \tag{9}$$

with C the depth-averaged concentration expressed in % volume, (u, v) the depth-averaged components of the velocity in the x and y directions, ε is the turbulent diffusivity of the sediment often related to the eddy viscosity $\varepsilon = \nu_t/S_c$ with S_c the Schmidt number $[0.5 - 1.0]$ and *E* and *D* are respectively erosion and deposition fluxes. The bed evolution is computed as:

$$\left(1 - \lambda_p\right)\frac{\partial z_b}{\partial t} = D - E \tag{10}$$

For non-cohesive sediment, the net sediment flux $E - D$ is determined based on the concept of equilibrium concentration:

$$(E - D) = w_s\left(C_{eq} - C_{zref}\right) \tag{11}$$

With w_s is the settling velocity of sediment, C_{zref} is the near-bed concentration, and C_{eq} is equilibrium near-bed concentration that can be computed by empirical formula.

For cohesive sediment, the erosion flux is computed with the Partheniades formula (1965):

$$E = \begin{cases} M\left[\left(\frac{\tau_b}{\tau_{ce}}\right) - 1\right] & \text{if } \tau_b > \tau_{ce} \\ 0 & \text{otherwise} \end{cases} \tag{12}$$

with M the Partheniades erosion law constant $[\mathrm{kg/m^2/s}]$, τ_b the bed shear stress, and τ_{ce} the critical bed shear stress for initiation of motion.

The deposition flux for cohesive sediment is computed as (Krone, 1962):

$$D = w_s C\left[1 - \left(\frac{\sqrt{\frac{\tau_b}{\rho}}}{u_{*mud}^{cr}}\right)^2\right] \tag{13}$$

Where u_{*mud}^{cr} is the critical shear velocity for deposition of cohesive material.

2.2. code_saturne

code_saturne is a numerical simulation software developed by EDF for solving fluid mechanics and (Navier-Stokes equations) heat transfer problems using the finite volume method. This numerical approach discretizes the governing equations of fluid and heat exchange. code_saturne stands out for its ability to be massively parallelized to leverage modern computing architectures, including supercomputers and clusters. For laminar flow, the resolved system is:

$$\frac{\partial \rho}{\partial t} + \underline{\nabla}.\left(\rho \underline{u}\right) = \Gamma \underline{u}^{in} \tag{14}$$

$$\frac{\partial}{\partial t}\left(\rho \underline{u}\right) + \underline{\nabla}.\left(\underline{u} \otimes \rho \underline{u}\right) = -\underline{\nabla} P + \underline{\nabla}.\left(\mu\left[\ \underline{\underline{\nabla}}\,\underline{u} + \underline{\underline{\nabla u}}^T - \frac{2}{3} tr\left(\underline{\underline{\nabla u}}\right)\underline{\underline{Id}}\ \right]\right) + \rho \underline{g} + \underline{ST}_{\underline{u}} - \rho \underline{\underline{K}}\,\underline{u}' + \Gamma \underline{u}^{in} \tag{15}$$

where $\underline{\underline{S}}$ the strain rate tensor:

$$\underline{\underline{S}} = \frac{1}{2}\left(\underline{\underline{\nabla u}} + \underline{\underline{\nabla u}}^{T}\right) \tag{16}$$

where $\underline{ST_u}$ and $\rho\underline{\underline{K}}\underline{u}'$ represent additional momentum source terms, such as head loss, which are typically treated as implicit by default. These source terms can be prescribed by the user, such as the contribution $\Gamma\underline{u}^{in}$ associated with a user-defined mass source term. It's important to highlight that *K* is a symmetric positive tensor as per its definition, resulting in a negative contribution to the kinetic energy balance (For additional details, please refer to Appendix M).

Chapter 3. Design of experimental tests for validation of numerical models

The objective of this chapter is to design a set of new laboratory configurations representative of real reservoirs, by means of numerical simulations. A first step is to assess the performance of TELEMAC-2D and -3D models to simulate flow patterns in simple shallow reservoir geometries. Existing laboratory data measured in rectangular reservoirs with different locations of inlet and outlet channels and bottom topography (i.e., flat bottom, sediment deposits) were considered. The case of the Cheylas reservoir was then studied, but idealization of the reservoir geometry and scaling down its dimensions for physical modelling in the laboratory was not possible.

An alternative was to propose new configurations of shallow reservoir adapted to physical modeling constraints while mimicking the specificities of real reservoirs managed by EDF. Various configurations were studied: free surface channel or pressurized jet at the inlet, free surface channel or weir at the outlet, angular or curved reservoir corners, and aligned or angled inlet-outlet boundary conditions. A wide range of flow conditions representative of real reservoirs were investigated to identify by means of numerical modeling the geometric parameters with most significant impact on the flow pattern. Two configurations stand out showing the most interest in being experimentally tested: configuration with inlet jet and configuration with side wall inlet.

3.1. Introduction

The flow in rectangular shallow reservoirs is governed by eight parameters (Peltier et al., 2014) (Figure 3), namely reservoir length L_1, reservoir width B, inlet channel width (or jet diameter) b, flow depth H, mean depth-averaged velocity in the inlet channel U_{in}, roughness height k_s, kinematic viscosity ν, and gravitational acceleration g. The velocity is calculated as $U_{in} = Q/(bH)$, with Q the inlet flow rate. According to Vaschy Buckingham theorem, seven dimensionless parameters can be defined: lateral expansion ratio B/b, length-to-width ratio L/B, flow depth-to-width ratio (i.e., shallowness parameter) H/B, Froude number $F = U_{in} / (gH)^{1/2}$, Reynolds number $R = 4\, U_{in}\, H / \nu$, relative elevation of the inlet section centroid Z_{jet} / H, and relative roughness height k_s / H. Following Peltier et al. (2014), k_s / H and R can be merged into the friction number $S = \lambda\, B / H$, in which the friction coefficient λ is evaluated with Colebrook-White formula. Peltier et al. (2014) defined the friction number S considering the expansion width ΔB instead of the

reservoir width *B* as a characteristic length. Their approach does not allow to consider non symmetric reservoirs.

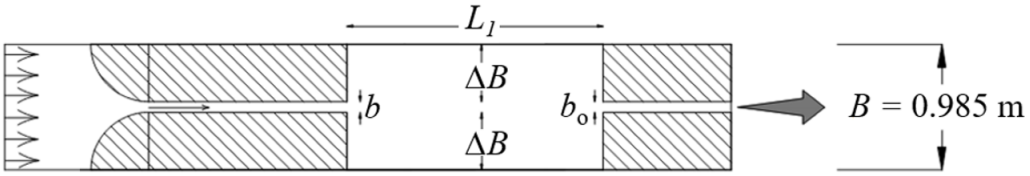

Figure 3: Parameters governing flow in a shallow reservoir

Existing experimental works depicted in Chapter 1 show certain limitations in terms of engineering needs, as they mainly focus on simple rectangular reservoirs with inlet and outlet rectangular free surface boundary channels, generally situated on opposite sides. On the other hand, real reservoirs feature a variety of boundary condition characteristics, encompassing distinct types and positions within the reservoir (Claude et al., 2019) (Figure 4 and Table 4).

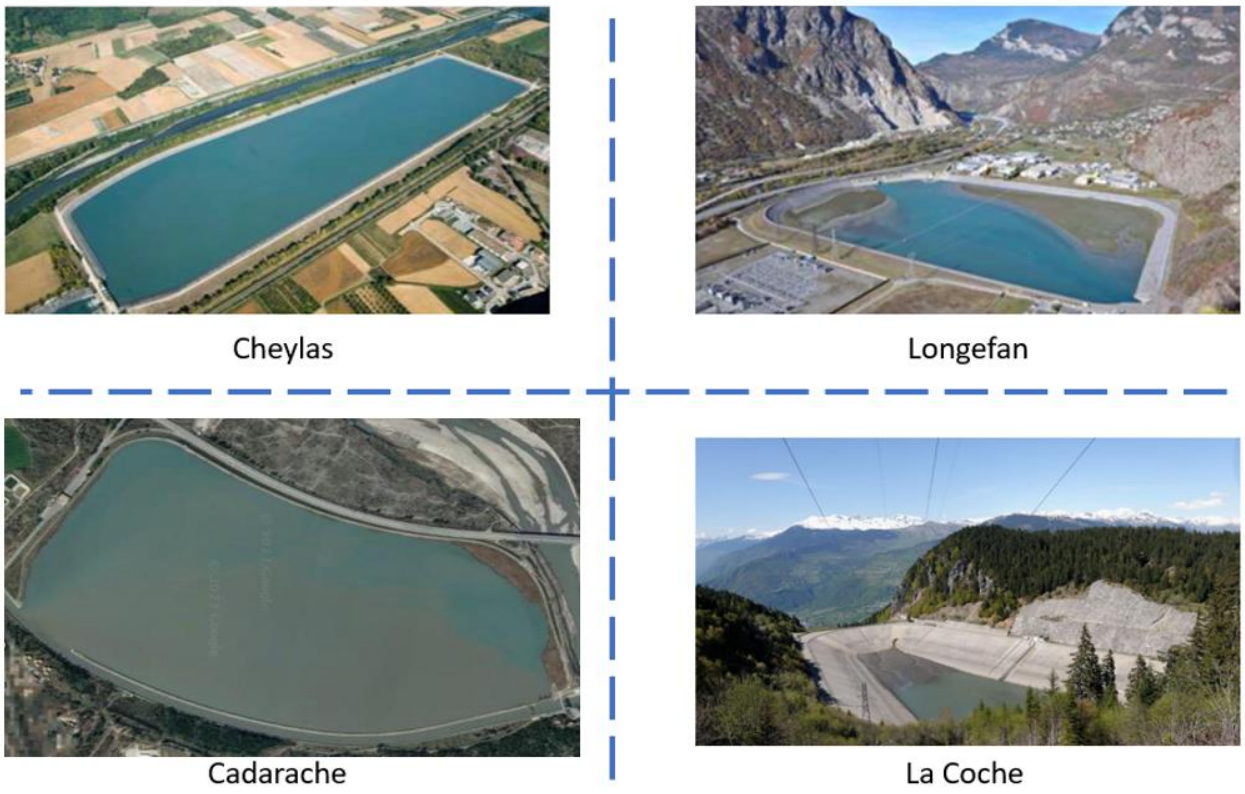

Figure 4: Aerial view of real shallow reservoirs operated by EDF

Table 4: Boundary conditions of shallow reservoirs operated by EDF

Reservoirs	Inlet boundary			Outlet boundary		
	Type	Number	Position	Type	Number	Position
Cheylas	Pressurized jet (plant outtake gallery)	1	Inside	Flap gate Pressurized water intake (plant intake gallery)	3 1	Lateral wall Inside
Longefan	Free surface channel	1	Corner	Weir	1	Corner
Cadarache	Radial gates	2	Lateral wall	Weir	1	Lateral wall
La Coche	Pressurized jet (plant outtake gallery + water supply gallery)	2	Lateral wall	Pressurized water intake (plant intake gallery)	1	Inside

The objective of this chapter is to design a set of new laboratory configurations representative of a wide range of real cases, complementary to existing studies. The ongoing investigation is limited to clear water and does not consider sediment transport. The chapter is structured as follows: Section 3.2 consists in the validation of two numerical models applied to Camnasio et al.'s (2013) laboratory experiments. In Section 3.3, numerical modeling is used to examine the possibility to simplify and scale the geometry of Cheylas reservoir for laboratory setup. Section 3.4 enables to define specific configurations of shallow reservoir adapted to physical modeling constraint while mimicking specificities of real reservoirs. Section 3.5 consists in the numerical modeling of these configurations to select the most interesting ones. Finally, Section 6 presents conclusions.

3.2. Validation of TELEMAC-2D and TELEMAC-3D

3.2.1. Data for comparison

Before delving into the details of designing new laboratory configurations, the capacity of TELEMAC-2D and TELEMAC-3D is assessed to replicate the flow patterns at a laboratory scale. Laboratory experiments conducted by Camnasio et al. (2013) are considered for the validation of the two numerical models used in the research. The experimental setup consisted of a rectangular horizontal basin, L_1 = 4.5 m long and B = 4 m wide, and two rectangular free surface channels, l = 1 m long and b = 0.25 m wide each (Figure 5). Bottom and side walls are made of PVC. Four configurations of inlet/outlet channels positioning are considered (Figure 5), referred to C-C (symmetric case), L-L, L-R and C-R (asymmetric cases), respectively.

A constant clear water discharge of Q = 0.007 m^3/s is imposed at the inlet open channel, while a flap gate located at the outlet channel end regulated the flow depth in the reservoir at H = 0.2 m. The Froude and Reynolds numbers in the inlet channel are F= 0.1 and R = 112 000, respectively. The same experiments were repeated while feeding the inlet channel continuously with crushed walnut shells (density ρ_s = 1500 kg/m^3, median diameter d_{50} = 89 µm) at a mean inflow concentration of C_{in} = 2 g/l.

The horizontal velocity field was measured using Ultrasonic Velocity Profiler (UVP) transducers placed at 8 cm (= 0.4H) from the bottom for two scenarios: one with clear water flow and the other with suspended sediments. The thickness of sediment deposits in the reservoir was measured by a laser technique after 2 h and 4 h of sediment feeding. Distinct flow patterns were identified for the various configurations. Similar flow patterns were observed for the two scenarios, except for

the L-R configuration. In the C-C setup, two large symmetrical patterns were observed. The L-L configuration exhibited the primary jet being deflected towards the adjacent side wall until reaching the outlet channel. In the L-R configuration, a single reattachment point was observed on the left side in the scenario with clear water. A change in flow patterns occurred after 30 minutes of sediment supply, leading to a configuration without reattachment points. In the C-R configuration, two eddies of differing sizes formed on both sides of the primary jet.

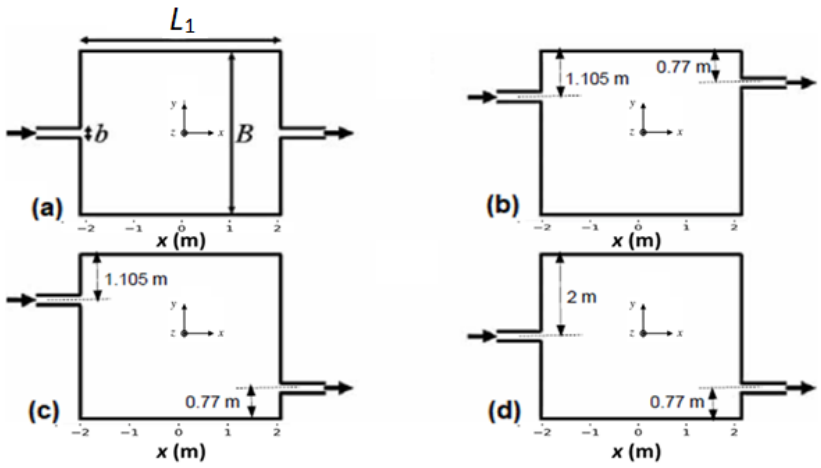

Figure 5 : Plane view of laboratory configurations: (a) C-C, (b) L-L, (c) L-R, and (d) C-R

3.2.2. Modeling with TELEMAC-2D

The simulations are performed with the finite element version of the depth-averaged TELEMAC-2D hydrodynamic model (V8P2) (El kadi Abderrezzak et al., 2016). For all the configurations, a Strickler formula with a coefficient equal to 80 $m^{1/3} s^{-1}$ (corresponding to PVC) is used. The effect of sidewall friction was tested and no influence on the numerical results was noted. A CFL number lower than 0.8 is used, and a grid size of 0.025 m is retained according to a mesh convergence study. The numerical model is first used to simulate the “clear water” cases (i.e., reservoir flat bottom). Then, it is used to simulate the flow field in the reservoir with the measured bathymetry after 4 h of sediment supply. For the sake of brevity, only selected results are shown below.

For clear water tests, several numerical schemes for solving the advection step for velocity and turbulence are compared: method of characteristics, N distributive scheme, Positive Streamwise Invariant (PSI), PSI scheme with Locally semi-Implicit Predictor-corrector Scheme (LIPS), and Element by element Residual distributive Iterative Advection scheme (ERIA). The effect of numerical scheme, illustrated in Figure 6 is weak for C-C configuration, and this finding remains valid for all configurations and turbulence models. Consequently, the LIPS is chosen for the rest of the study, as the scheme is less diffusive.

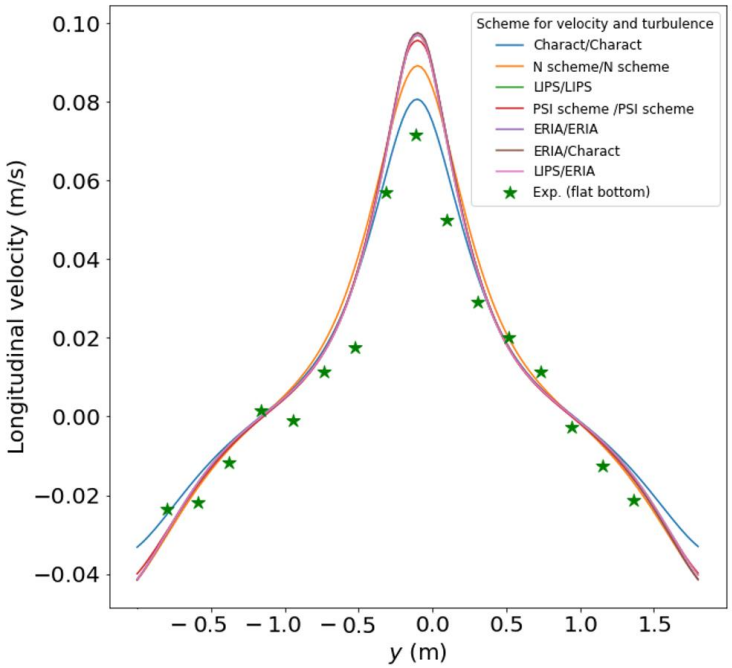

Figure 6: C-C configuration: Measured and computed cross-sectional profiles of longitudinal velocity at x = 1.73 m with different numerical schemes for advection of velocity and turbulence. Flat bottom, k–ε turbulence model and mesh size of 0.025 m

Figure 7 shows a comparison between experimental and computed velocity fields for C-C, C-R, L-L and L-R configurations (clear water, i.e., flat bottom) using Spalart-Allmaras (Bourgoin et al., 2021), k–ε, Elder turbulence models and constant viscosity (10^{-3} m² s^{-1}). The Spalart-Allmaras turbulence model provides satisfactory results of flow pattern for the four configurations. The k–ε, Elder and constant viscosity (10^{-3} m² s^{-1}) turbulence models yield satisfactory results for C-C, L-L and C-R configurations, but do not allow replicating the reattachment point on the left side for the L-R configuration. Figure 8 shows the longitudinal velocity profiles for different turbulence models. The k–ε and Elder models reproduce the shape of measurements accurately but overestimate the velocity peak. The Spalart-Allmaras and constant viscosity (10^{-3} m² s^{-1}) turbulence models reproduce less well the shape of measurement and underestimate the velocity peak. Finally, it can be concluded that Spalart-Allmaras (SA) model stands out from other turbulence models because it could correctly replicate the velocity fields without changing the initial conditions.

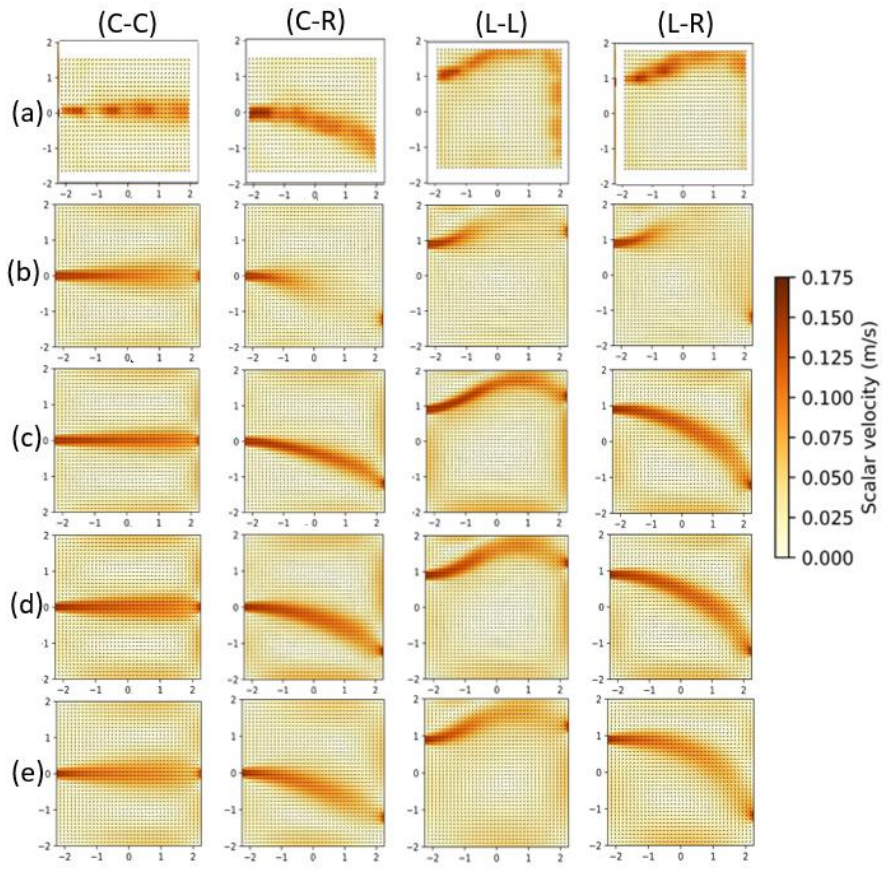

Figure 7: (a) Experimental, and computed velocities using (b) Spalart-Allmaras model, (c) k–ε model, (d) Elder model, and (e) constant viscosity (10^{-3} m^2 s^{-1}) model. Flat bottom, LIPS and mesh size of 0.025 m

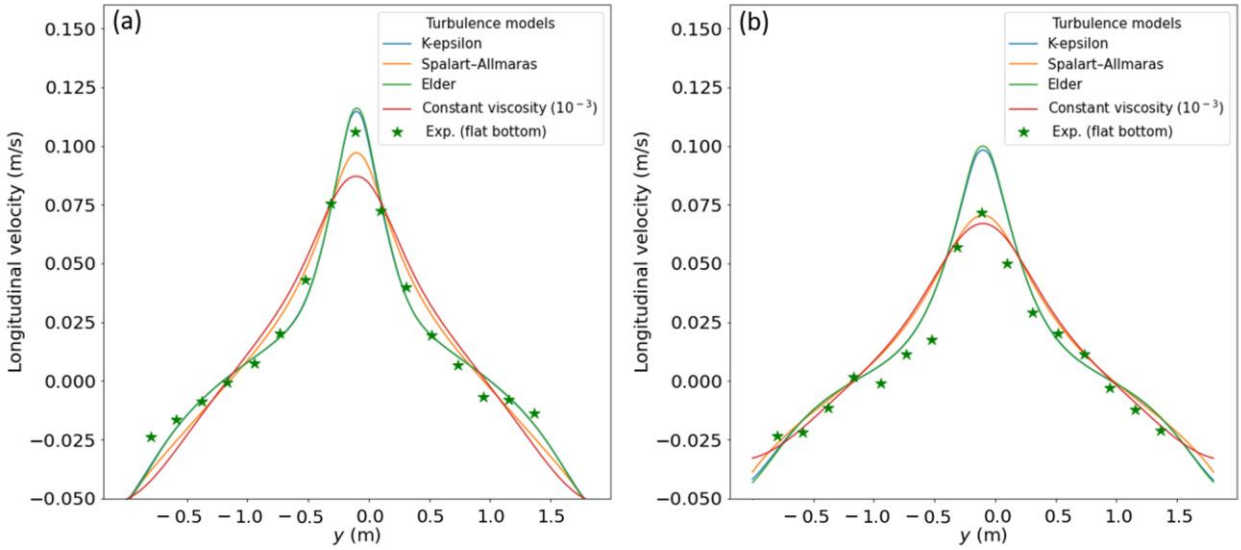

Figure 8: C-C configuration: measured and computed cross-sectional profiles of longitudinal velocity at (a) x = 0.71 m, and (b) x= 1.73 m. Flat bottom, LIPS and mesh size of 0.025 m

The Mixing Length turbulence model correctly reproduces the velocity vector maps for C-R and L-L configurations. However, the model does not replicate the steady state for the C-C configuration and the reattachment point observed for the L-R configuration (Figure 9).

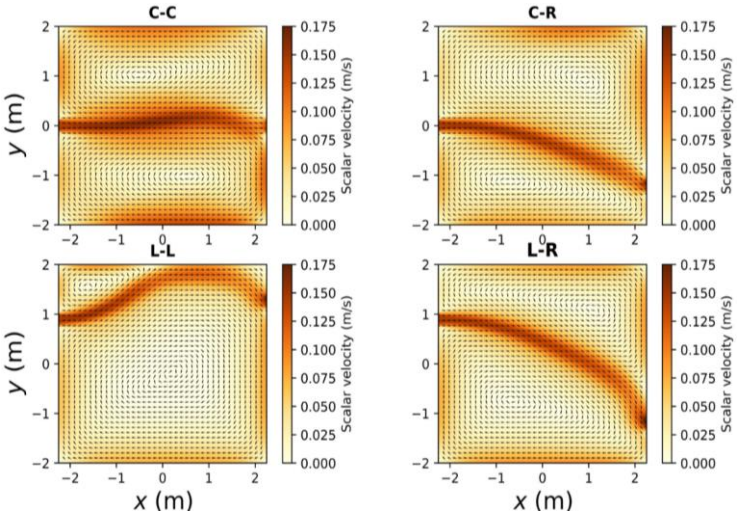

Figure 9: Computed velocity fields using Mixing length turbulence model for C-C, C-R, L-L and L-R configurations. Flat bottom, LIPS and mesh size of 0.0025 m

The Smagorinsky scale model calculates the viscosity as $\nu_t = C_s\Delta^2(S_{ij}S_{ij})^{1/2}$, with C_s a dimensionless coefficient to be calibrated, Δ the mesh size derived from the surface, and S_{ij} the stress tensor. This model ignores the effect of dispersion due to heterogeneity of velocities on the vertical direction. The numerical results are not satisfactory. Using C_s= 0.12, 0.15, 0.18, 0.25, 0.3, or 0.4 instead of the defaults value of 0.2 yields also inaccurate results. The steady state is not reached; an oscillatory state is found which can be due to numerical diffusion (Figure 10).

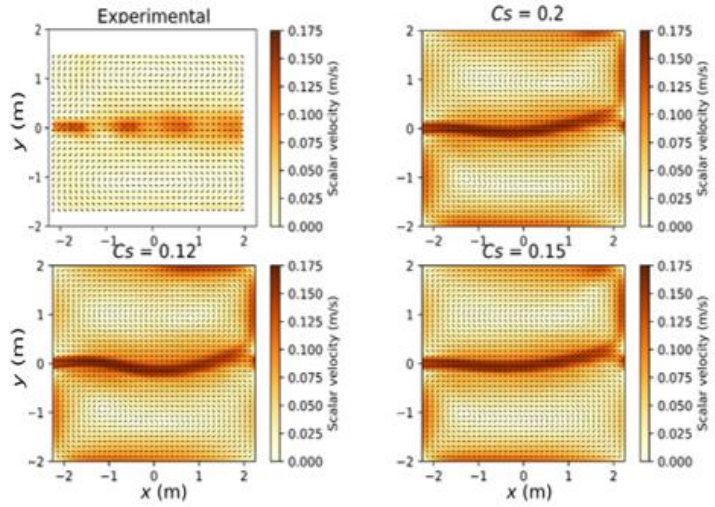

Figure 10: C-C configuration - Oscillatory state found using Smagorinsky turbulence model with C_s=0.12 (LIPS and mesh size of 0.0025 m)

The Elder model considers the role of dispersion and includes two coefficients for calculating the longitudinal ($K_l = a_l u^* h$) and transversal ($K_t = a_t u^* h$) diffusion terms (u^* as the shear velocity stress, and a_l and a_t are dimensionless coefficients of dispersion, set in TELEMAC-2D by default to 6 and 0.6, respectively). Similarly, to the standard k–ε and constant viscosity models, Elder's model fails in replicating the flow patterns for the L-R configuration (Figure 11) The effect of K_l and K_t has been evaluated by changing values of (al, at): (1, 0.1), (2, 0.2), (3. 0.3), (4, 0.4), (5, 0.5), (7, 0.7), (10, 1). Model-data comparison does not show any noticeable improvement of the results, as illustrated for L-R configuration in Figure 11.

The k–ε model reproduces fairly well the velocity magnitude and vector, except for the L-R case, where a flow field with one reattachment point was observed experimentally, but not numerically (Figure 12). Using a k–ε turbulence model, (Camnasio et al. 2013) showed that employing a steady flow pattern with lateral reattachment as initial conditions allowed for more satisfactory model-data agreement. Similar results are obtained with the TELEMAC-2D model (Figure 12).

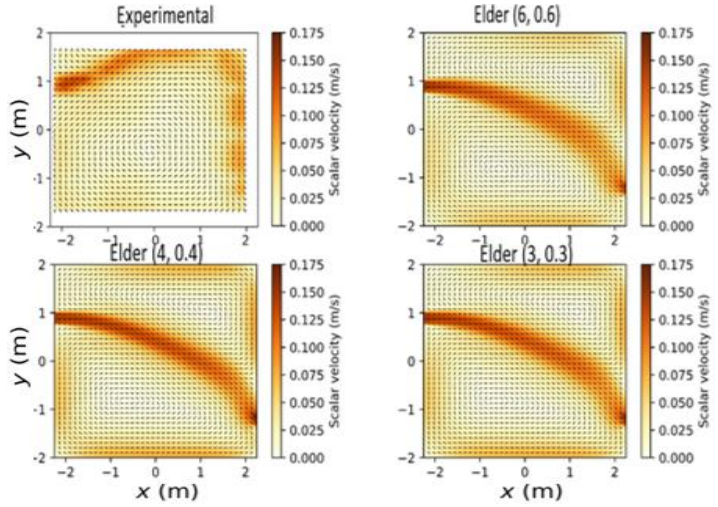

Figure 11: L-R configuration – measured and computed velocity fields using Elder's turbulence model with different dimensionless coefficients a_l and a_t. Flat bottom, LIPS and mesh size of 0.0025 m

The influence of bottom topography on flow pattern is analyzed while adding a bathymetry equivalent to the sediment deposits thickness after 4h for C-C configuration (Figure 13). Figure 14 plots measurements and computed longitudinal velocity profiles using k–ε, Spalart-Allmaras (SA), constant viscosity (10^{-3} m² s^{-1}) and Elder turbulence models. Similar conclusions to the configuration presented previously with a flat bottom are found, except with the k–ε turbulence model which presents an unsteady regime for the case with sediment deposit. This regime can be observed on Figure 14 by a slight deviation of the position of the velocity peak.

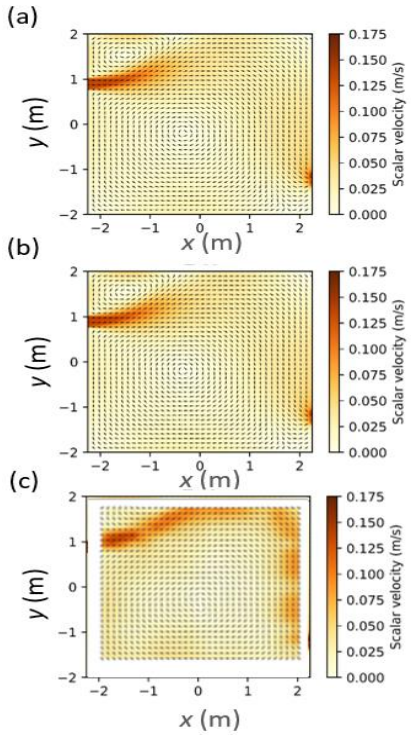

Figure 12: L-R configuration - (a) Initial condition with reattached jet, (b) k–ε model results at steady state, and (c) measurements. Flat bottom, LIPS and mesh size of 0.025 m

The influence of bottom topography on flow pattern is analyzed while adding a bathymetry equivalent to the sediment deposits thickness after 4h for C-C configuration (Figure 13). Figure 14 plots measurements and computed longitudinal velocity profiles using k–ε, Spalart-Allmaras (SA), constant viscosity (10^{-3} m² s^{-1}) and Elder turbulence models. Similar conclusions to the configuration presented previously with a flat bottom are found, except with the k–ε turbulence model which presents an unsteady regime for the case with sediment deposit. This regime can be observed on Figure 14 by a slight deviation of the position of the velocity peak.

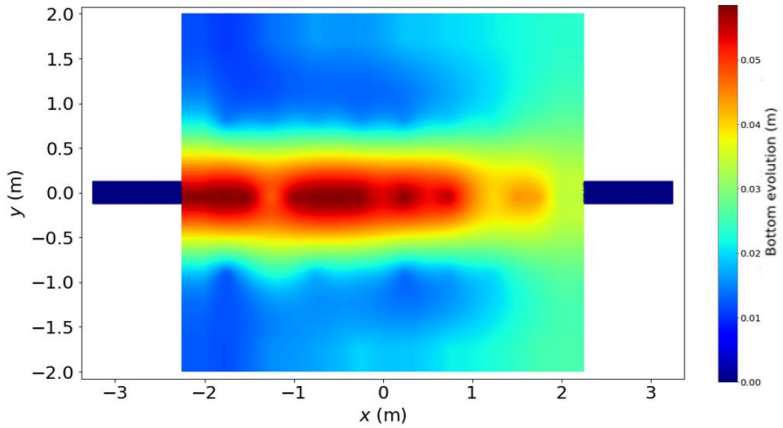

Figure 13: C-C configuration -measured bottom elevation after 4 h of sediment supply

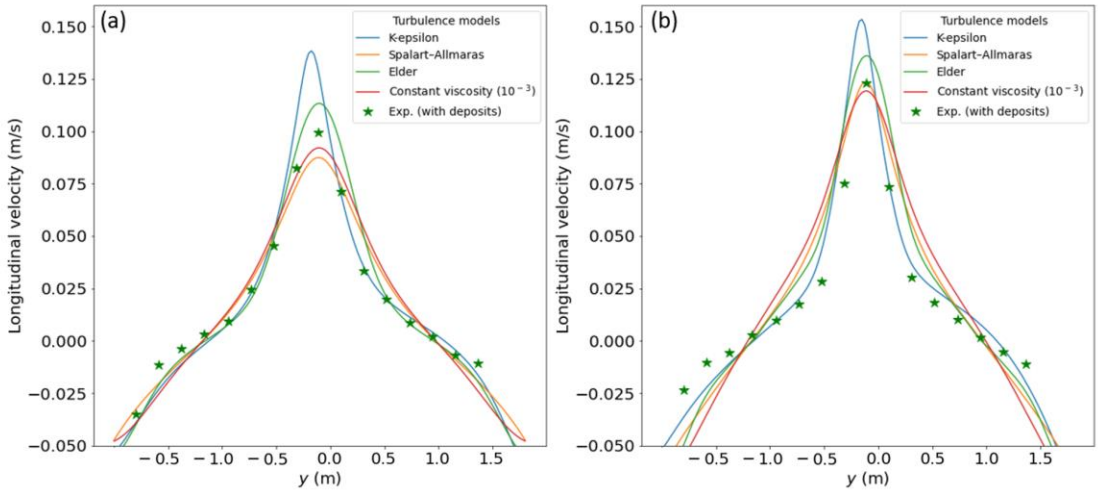

Figure 14: C-C configuration: measured and computed cross-sectional profiles of longitudinal velocity at (a) x = 0.71 m, (b) x = 1.73 m. Reservoir with deposits, LIPS and mesh size of 0.025 m

3.2.3. Modeling with TELEMAC-3D

TELEMAC-3D was applied with non-hydrostatic pressure distribution for C-C, L-L, L-R and C-R configurations using k–ε model in both horizontal and vertical directions, and LIPS scheme for advection of velocity and turbulence. The 3D model is composed of five layers uniformly distributed on the vertical, based on 2D unstructured mesh (0.025 m space step). For TELEMAC-3D, the standard k–ε model correctly reproduces the measured velocity vector field for C-C and C-R cases but does not reproduce the reattachment point for L-L and L-R configurations. Figure 15 shows the 3D streamlines and velocity vectors for C-C and L-R configurations.

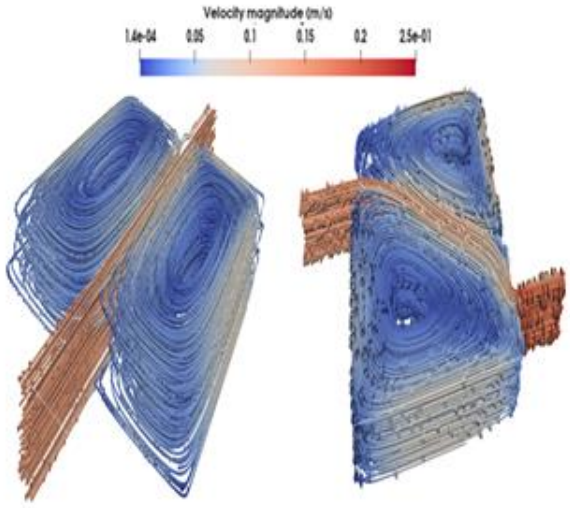

Figure 15: TELEMAC-3D simulations - Streamlines and velocity vectors for configurations C-C (left) and L-R (right) with standard k–ε turbulence model

3.2.4. Conclusions

Applying TELEMAC-2D for laboratory experiments performed with clear water (flat bottom), satisfactory model-data agreements were obtained using the Spalart-Allmaras turbulence model. The k–ε, Elder and constant viscosity (10^{-3} m^2 s^{-1}) turbulence models yielded satisfactory model-data agreement and a good reproduction of velocity magnitudes for C-C, L-L and C-R cases, but did not allow replicating the point of attachment for case L-R. Numerical simulations showed also that TELEMAC-2D allows a good representation of bathymetric effect on the flow pattern. Using TELEMAC-3D, the standard k-ε model accurately replicated the observed velocity vector field for C-C and C-R configurations but failed to replicate the point of reattachment for L-L and L-R configurations. Overall, the results presented showed that both numerical models can reproduce the main features of flow in rectangular shallow reservoirs. They can thus be used to investigate new configurations of interest to reproduce the specific characteristics of real reservoirs.

3.3. Modeling Cheylas reservoir

The most straightforward way to get experimental data depicting flow conditions in a real reservoir is to consider a (scale) physical model of this reservoir. The possibility to do so is investigated considering the Cheylas reservoir, which is the lower basin of the Cheylas-Flumet Pumped Storage Energy Transfer Station. The basin horizontal layout results from site constraints and is therefore not rectangular. The inlet is a gallery between the basin and the Cheylas hydropower plant, while the outlet is composed of gates controlling the downstream restitution channel.

Building and operating a physical model for every real reservoir of interest is not an economical nor efficient way to proceed. Therefore, it is relevant to find an idealized geometry prone to represent several real basins on the same experimental model. The Cheylas basin can be simplified as a rectangular basin while keeping the specific location of inlet and outlet. After doing so, the problem of the size of real reservoirs must be solved. This requires scaling the length to accommodate space available in the experimental facility and scaling the flow accordingly considering the Froude number similitude (free surface flow). In the case of Cheylas reservoir and considering the 0.985 wide flume available in the laboratory, this required horizontal scale factor of 1:426. Resulting water depths in the laboratory are less than 1 mm and thus unpracticable. Distortion can be a solution to increase the experimental water depth. Two distortion ratios are considered. This results in five configurations (Table 5), which have been modeled numerically

using TELEMAC-2D to examine their relevance, and to verify that the idealized geometries maintain the flow pattern of the real basin (Figure 16).

Table 5: Geometric and hydraulic characteristics of real basin, idealized basin and three scale models. Distortion factor is defined by the ratio of horizontal to vertical scales

Parameters	Real reservoir	Idealized reservoir	Non-distorted (1 :426)	Distorted (factor 2)	Distorted (factor 4)
Length (m)	1390	1194	2.802	2.802	2.802
Width (m)	450	420	0.985	0.985	0.985
Width at the inlet (m)	38	38	0.089	0.089	0.089
Water level (m)	14	14	0.032	0.064	0.128
Flowrate at the inlet (m^3/s)	98	98	2.62×10^{-5}	7.40×10^{-5}	2.09×10^{-4}
Manning coefficient	0.02	0.02	0.007	0.011	0.018

Results for the real and idealized basins are relatively consistent with measurements presented by Claude et al. (2019) (Figure 16). Numerical and experimental results show a recirculation to the north, generated by the outgoing flow from the inlet jet in a direction perpendicular to the length axis of the basin. The main inlet jet splits in two on the right bank of the basin. Most of the flow heads south, remaining close to the bank before joining the outlet of the basin. This generates a large recirculation on most of the left bank of the basin. The undistorted model does not reproduce the recirculation to the north of the channel. The distorted models (factors of 2 and 4) correctly reproduce the flow pattern. The velocity intensities differ between the distorted and non-distorted idealized models. Overall, the numerical results show that main flow typology of this real reservoir can be reproduced considering scale physical models with idealized geometry.

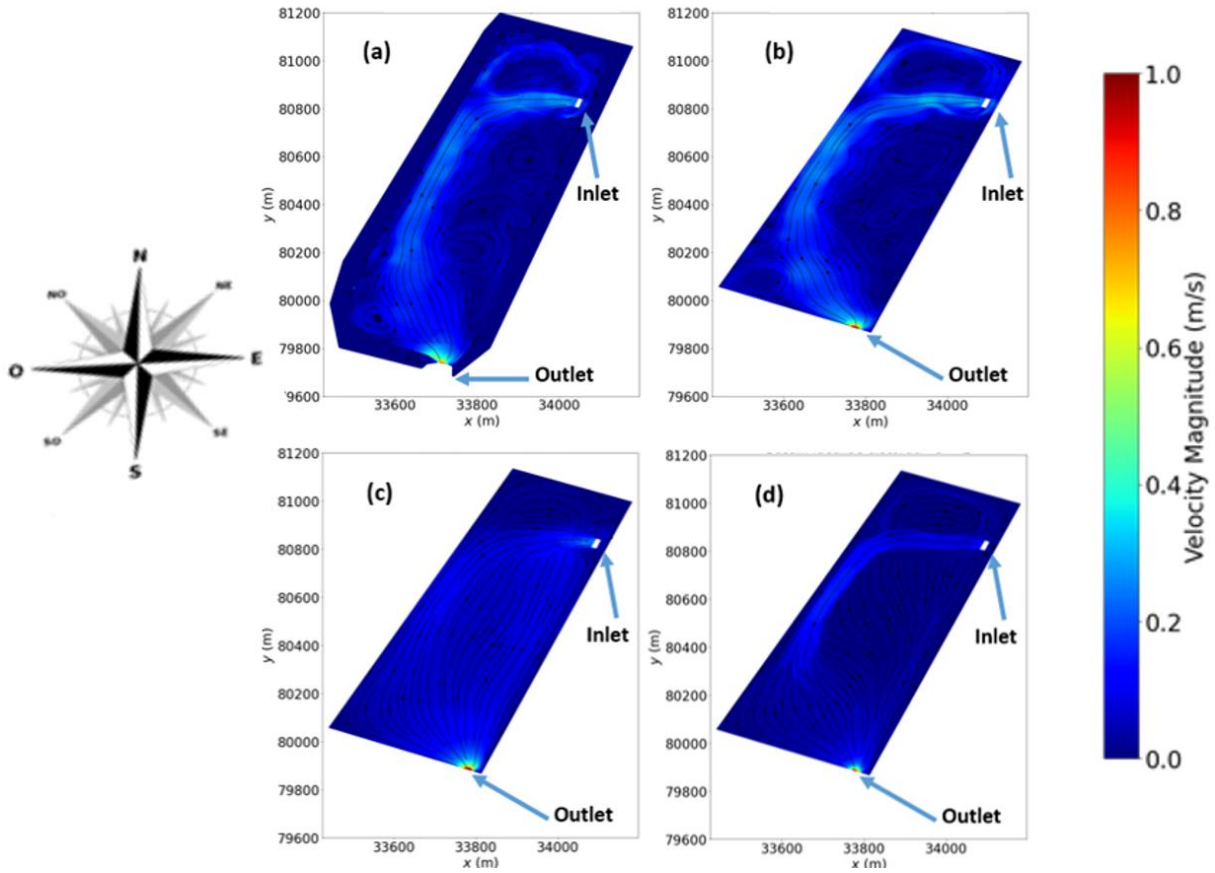

Figure 16: Velocity magnitude and streamlines modeled with TELEMAC-2D - (a) Real basin, (b) Idealized basin, (c) Undistorted scaled idealized basin, and (d) Distorted scaled (factor of 2) idealized basin. LIPS/LIPS (Locally semi-Implicit Predictor-corrector) schemes and k - ε turbulence model

3.4. New experimental configurations

3.4.1. Experimental facility:

The physical experiments had to be conducted in the laboratory of the Hydraulics in Environmental and Civil Engineering (HECE) research group at Liege University (Belgium), considering the facility used by Dufresne et al. (2010a) and Peltier et al. (2014) (Figure 17). The reservoir geometries had to fit in an existing horizontal flume L = 10.4 m long, B = 0.985 m wide and 0.50 m deep. Considering a safety margin of 5 cm, the maximum water depth is about 0.45 m. The flume bottom and walls are fixed and made of glass. The maximum reservoir width is equal to the flume width and the downstream and upstream extremities are created by solid blocks placed in the flume. The position of these blocks can be modified to change the reservoir length L_1. Regarding the pump characteristics, the flow rate can vary in the range 0.0002 to 0.006 m^3/s.

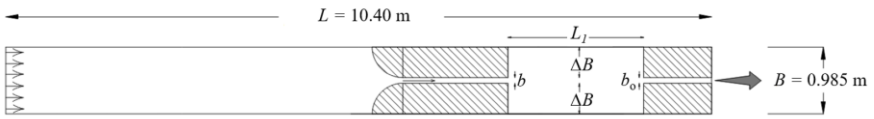

Figure 17: Sketch illustrating existing experimental flume at HECE laboratory, University of Liège (not to scale)

3.4.2. Reservoir and boundary conditions geometry:

The geometric features of a shallow reservoir influencing the flow conditions can be segmented into three parts (Figure 18):

- The first one is the inlet. While mostly free-surface channels have been previously considered in the context of rectangular shallow water reservoirs, the Cheylas and La Coche cases present a pressurized inlet. In addition, in Cadarache and La Coche reservoirs, inlet and outlet are located on adjacent sides, while all the studies to date considered inlet and outlet on opposite sides,
- The second part is the reservoir geometry. All the studies so far considered rectangular reservoirs, while real ones exhibit much less regular horizontal geometries. Notably, the presence of curved sides is a common feature (e.g., Cadarache, Longefan),
- The third part is the outlet. Again, mostly free surface channel has been considered so far while in the case of Longefan and Cadarache reservoirs, a weir is used.

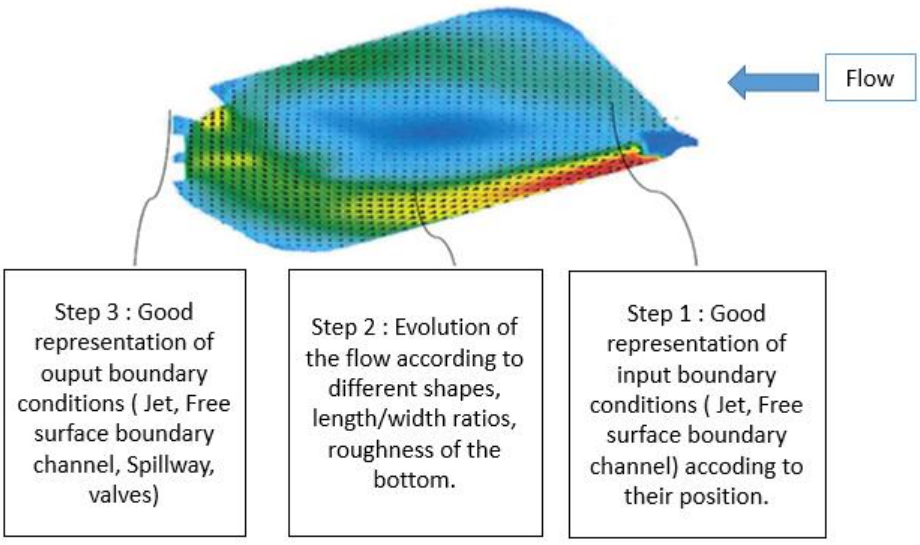

Figure 18: Analysis of important steps to validate numerical model, with a numerical simulation of Longefan real reservoir

In the following, the three parts have been covered considering four reservoir geometries (Figure 19b-e). A reference case (Figure 19a) is also considered for sake of comparison. It consists of a rectangular reservoir with an inlet and an outlet channel positioned opposite to each other, such as considered in most of the experimental studies to date. While maintaining the same outlet and reservoir conditions as in the reference case, configuration (b) considers a pressurized jet at the inlet, while configuration (d) depicts a free surface channel inlet positioned on the side adjacent to the outlet one. Configuration (c) assess how reservoir side curvatures impact the flow condition while keeping the same inlet and outlet conditions as in the reference case. Finally, the impact of the outlet condition (e) is investigated considering a weir at the outlet while keeping the same inlet conditions and reservoir geometry as in the reference case.

The blocks employed in the experiments by Peltier et al. (2014) will be reused for practical reasons. This choice results in an inlet and outlet channel width of $b = b_0$ =0.08 m. The inlet jet diameter is defined by the desired condition of H/b = 2.5 and by the minimum water depth required for perform measurements using ADVP profiler. This device requires a minimum water depth of 0.07 m (3 cm of probe immersion and 4 cm for measurement window). Considering 3 cm of safety margins, b = 0.04 m has been chosen for the jet case, with a minimum water depth H = 0.10 m.

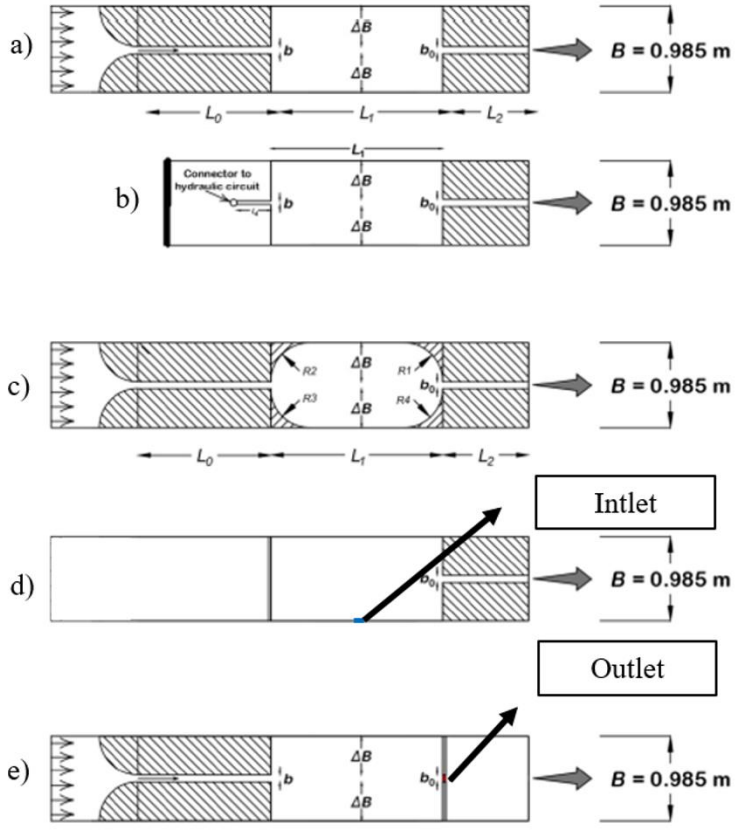

Figure 19 :Sketch illustrating of proposed geometries (not to scale)

Table 6 summarizes the geometrical parameters for reference and jet inlet configurations. Both short and long reservoirs were examined in each case. The differentiation was made based on the shape factor, with short reservoirs defined as those with SF < 6.2 and long reservoirs as those with SF > 6.2. To allow a comparison between configurations with open-channel inlet and jet inlet, the shape factor is calculated with respect to the outlet channel width rather than the inlet channel width, such a SF = $L_1/(\Delta B^{0.6}\ b_0^{0.4})$ with $\Delta B = (B - b_0)/2$. For curved corner configurations, four geometries are considered, depending on which corner is curved. These configurations include R1R2, R2R3, R1R3, and R1R2R3R4 (Figure 19c). These configurations enable to investigate symmetric cases along the x-axis, y-axis, and diagonal. Regarding the lateral boundary cases, three different positions are selected, specifically at $L_1/4$, $L_1/2$, and $L_1/4$. The position of the outlet condition is fixed, with its center set at $B/2$. The weir case is identical to the reference case with a weir 0.05 m height all along the reservoir side opposite to the inlet side.

Table 6: Geometric and hydraulic characteristics of real basin, idealized basin and three scale models. Distortion factor is defined by ratio of horizontal to vertical scales

L_1 (m)	ΔB (m)	b (m)	b_0 (m)	Shape factor (SF)	Inlet boundary conditions	Jet position
2.00	0.4525	0.08	0.08	8.84 (Long reservoir)	Rectangular channel	-
1.05				4.64 (Short reservoir)		-
2.00		0.04	0.08	8.84 (Long reservoir)	Jet	Center
1.05				4.64 (Short reservoir)		
2.00		0.04	0.08	8.84 (Long reservoir)	Jet	Right side
1.05				4.64 (Short reservoir)		
2.00		0.04	0.08	8.84 (Long reservoir)	Jet	Left side
1.05				4.64 (Short reservoir)		
2.00		0.04	0.08	8.84 (Long reservoir)	Jet	Downstream from center
1.05				4.64 (Short reservoir)		
2.00		0.04	0.08	8.84 (Long reservoir)	Jet	Upstream from center
1.05				4.64 (Short reservoir)	Jet	

3.4.3. Hydraulic conditions

Figure 20 represent the Froude and friction numbers for real reservoirs and experiments from the literature. The issue is to determine experimental values of Q and H that allow reaching minimal and maximal values of Friction and Froude numbers in the scatter plot while considering

experimental constraints. For the sake of future comparisons, identical values of F and S are configured for all cases, and thus in particular for both free surface channel and jet at the inlet.

The theoretical flow rate Q of the facility lies within the interval of 2×10^{-4} to 5×10^{-3} m^3/s for free surface channel. The preliminary experimentations revealed that attainable flow rates for jet configurations range from 0.5×10^{-3} to 3×10^{-3} m^3/s. To enhance measurement accuracy, the minimum flow rate needs to be raised, while the maximum flow rate had to be decreased due to noticeable fluctuations in the free surface observed in configurations featuring an inlet jet.

The roughness height k_s of real reservoirs has been estimated considering the material of the reservoir bottom. In the experimental set up, surfaces are smooth and while the lower limit of the friction number S in Figure 20 can be achieved when H is set to 0.20 m; the upper limit cannot be reached because of the limitation in the minimum water depth.

The selected parameters for both the reference and jet cases are summarized in Table 7. The graph shows that we are covering a wide range of Froude numbers, encompassing those from real basins, previous experiments, as well as a range of high Froude numbers not evaluated in prior experiments. However, the selected hydraulic conditions do not include the minimum values of F nor the maximum values of S. This results in a set of eight configurations for each geometry of the reservoir with inlet channel (two basin lengths × four hydraulic configurations) and six with inlet jet (two basin lengths × three hydraulic configurations). In total, eight (8) configurations are modeled for the reference cases, thirty-two (32) for curved corners, twenty-four (24) for side wall inlet, eight (8) for an outlet weir. And thirty-two (32) configurations are considered for the inlet jet.

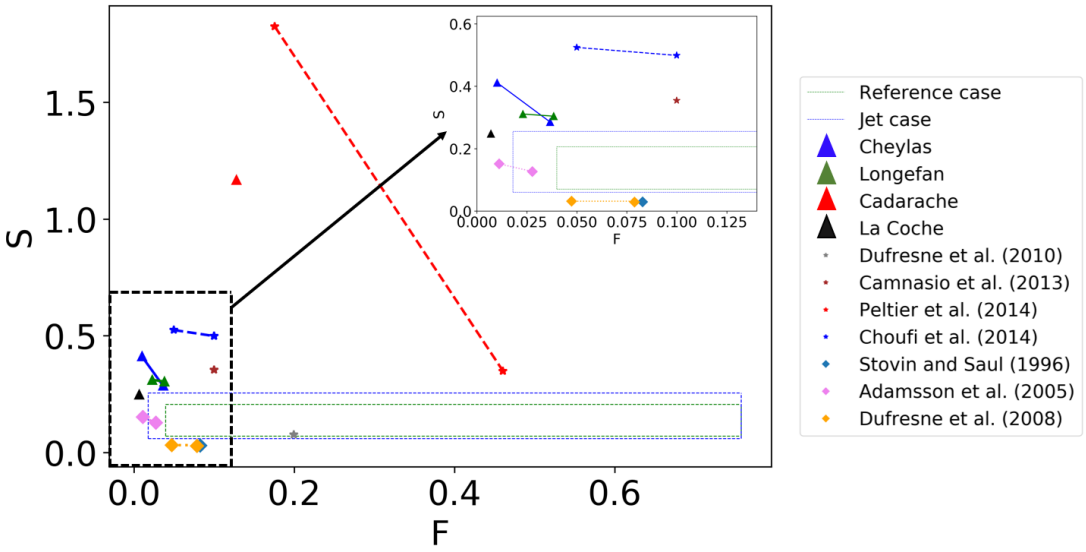

Figure 20: Friction factor S and Froude number F for real reservoirs (points), laboratory experiments with free surface channel inlet (star), and laboratory experiments with jet inlet (diamond)

Table 7: Hydraulic parameters selected parameters for free surface channel and jet inlet configurations

Cases	Configuration Number	b (m)	H (m)	Q (m^3/s) $\times 10^{-4}$	U_{in} (m/s)	$R \times 10^4$	F	S
Free surface inlet channel	1	0.08	0.10	10	0.1250	5	0.126	0.206
	2		0.10	35	0.4375	17.5	0.442	0.159
	3		0.20	10	0.0625	5	0.045	0.103
	4		0.20	35	0.2188	17.5	0.156	0.079
Inlet Jet	5	0.04	0.10	5	0.1250	5	0.126	0.206
	6		0.10	17.5	0.4375	17.5	0.442	0.159
	7		0.10	30	0.7500	30	0.757	0.143
	8		0.20	5	0.0625	5	0.045	0.103
	9		0.20	17.5	0.2188	17.5	0.156	0.079
	10		0.20	30	0.3750	30	0.268	0.071

3.5. Numerical modeling

All the geometrical configurations defined in Section 3.4.2 have been modeled using TELEMAC-2D or TELEMAC-3D, while considering each of the hydraulic condition defined in Section 0. TELEMAC-3D has been preferred to model inlet jet cases due to its capability in representing three-dimensional boundary conditions.

3.5.1. Numerical model parameters

For 2D configurations (reference, curved corner, lateral inlet channel and outlet weir), TELEMAC-2D was applied with a k - ε model and the LIPS (Locally semi-Implicit Predictor-corrector Scheme) for the advection of velocity and turbulence. The 2D mesh is unstructured (mesh size = 0.005 m). A current number (CFL) less than 0.8 was used. Strickler's formula for friction was used with a coefficient of 80 $m^{1/3}/s$ (representing friction of PVC material) which is equivalent to a roughness height $k_s = 10^{-3}$ mm.

For inlet jet cases, TELEMAC-3D is applied with non-hydrostatic pressure distribution, k–ε turbulence model in both horizontal and vertical directions, and LIPS for advection of velocity and turbulence. The 3D model is composed of seven layers uniformly distributed along the vertical, based on 2D unstructured mesh (0.004 m space step) with a total of 930 000 nodes. Figure 21 shows the 2D unstructured mesh and boundary condition positions for reference and jet cases. For the jet case, the inlet pipe is located horizontally at x = 0 and - 0.02 m < y < 0.02 m. Three vertical positions of the jet are studied:

- Inlet flowrate is imposed vertically between plan 1 and 3 (z = 0 is set at the reservoir bottom) for case (t) representing a jet near the bottom,
- Inlet flowrate is imposed between plan 3 and 5 for case (u) representing a jet at the middle-depth,
- Inlet flowrate is imposed between plan 4 and 6 for case (v) for jet near the free surface.

Configurations 3 (Free surface channel) and 8 (Inlet jet) presented in Table 7 are simulated. It is noted that for tested configurations, the 3D inlet condition consists of a rectangle and not a circle.

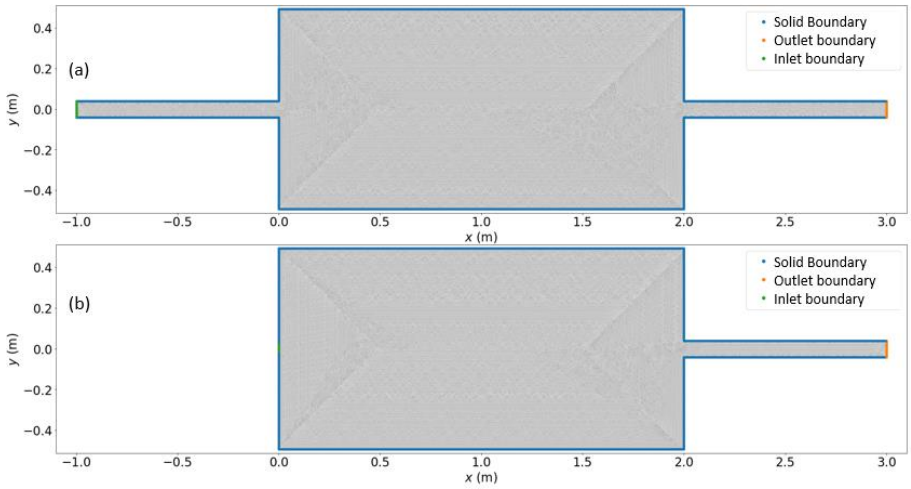

Figure 21: Unstructured 2D mesh and boundary condition positions for (a) reference case, and (b) jet case

3.5.2. Results with TELEMAC-2D

Long and short reservoirs for configurations with free surface channel at the inlet are studied, results are presented at steady state. Velocity magnitude and streamlines are plotted. In the following, indices 1, 2, 3, and 4 on the figure titles correspond to four hydraulic conditions:

- Case 1: Inlet flow rate Q = 0.0010 m^3/s, imposed outlet height H = 0.10 m.
- Case 2: Inlet flow rate Q = 0.0035 m^3/s, imposed outlet height H = 0.10 m.

- Case 3: Inlet flow rate Q = 0.0010 m^3/s, imposed outlet height H = 0.20 m.
- Case 4: Inlet flow rate Q = 0.0035 m^3/s, imposed outlet height H = 0.20 m.

Reference case

Results demonstrate an asymmetric flow pattern for long reservoir (Figure 22) and a symmetric flow pattern for short reservoirs (Figure 23). These results agree with those observed experimentally by Camnasio et al. (2011), Dufresne et al. (2010) and numerically by Dufresne et al. (2012). Steady-state regime is achieved for all tested configurations. Changing Froude number and Friction number while changing the flowrate and the water depth does not affect the results (Figure 22 and Figure 23). It is observed that the side where reattachment occurs changes between configurations (a1) and other configurations. In symmetric geometries, the flow is inherently unstable, and the direction of the jet is heavily influenced by the initial and boundary conditions Dewals et al. (2014).

Curved corners

In Figures 24 and 25, notations (c,d,e,f) and (g,h,i,j) correspond to the configurations R1R2, R2R3, R1R3, and R1R2R3R4 for respectively long and short reservoirs. Results show that there is no noticeable impact of the presence of curved corners compared with rectangular reservoirs. Also, increasing Froude and decreasing Friction number has no impact on the results. We observe an asymmetrical flow typology for long basins and a symmetrical flow typology for short basins, similar to what is observed in rectangular cases. For long basins asymmetric on the inlet side, flow always reattaches on the curved side, while with symmetric basin, flow reattachment occurs either on the left or the right side. Curved corner configurations will not be a priority for conducting physical experiments since they do not show significant differences in flow typologies compared to the reference configurations.

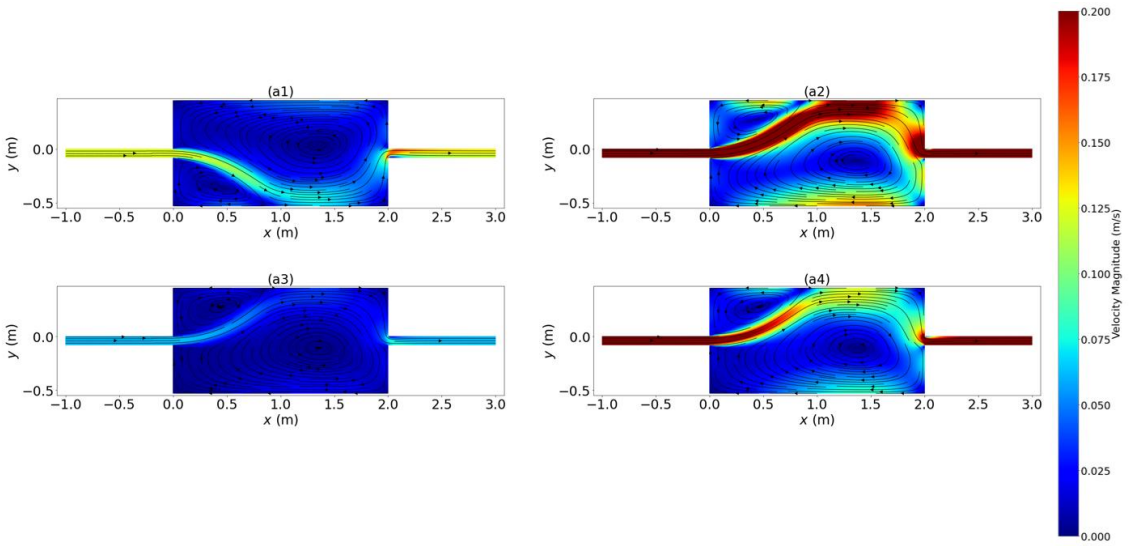

Figure 22: Amplitude of velocities and streamlines modeled with TELEMAC-2D for long reference reservoirs

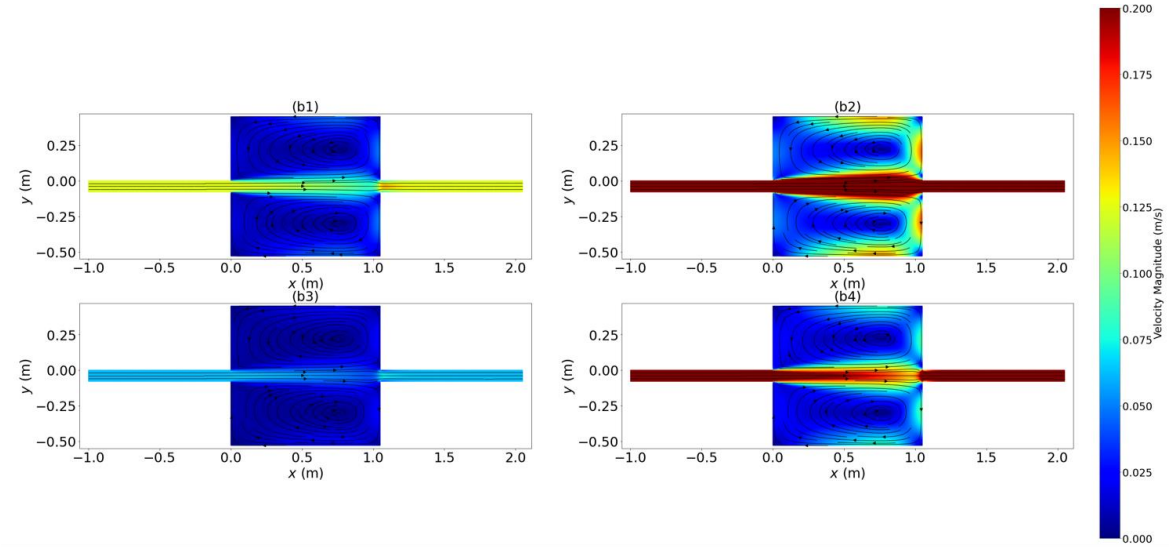

Figure 23: Amplitude of velocities and streamlines modeled with TELEMAC-2D for short reference reservoirs

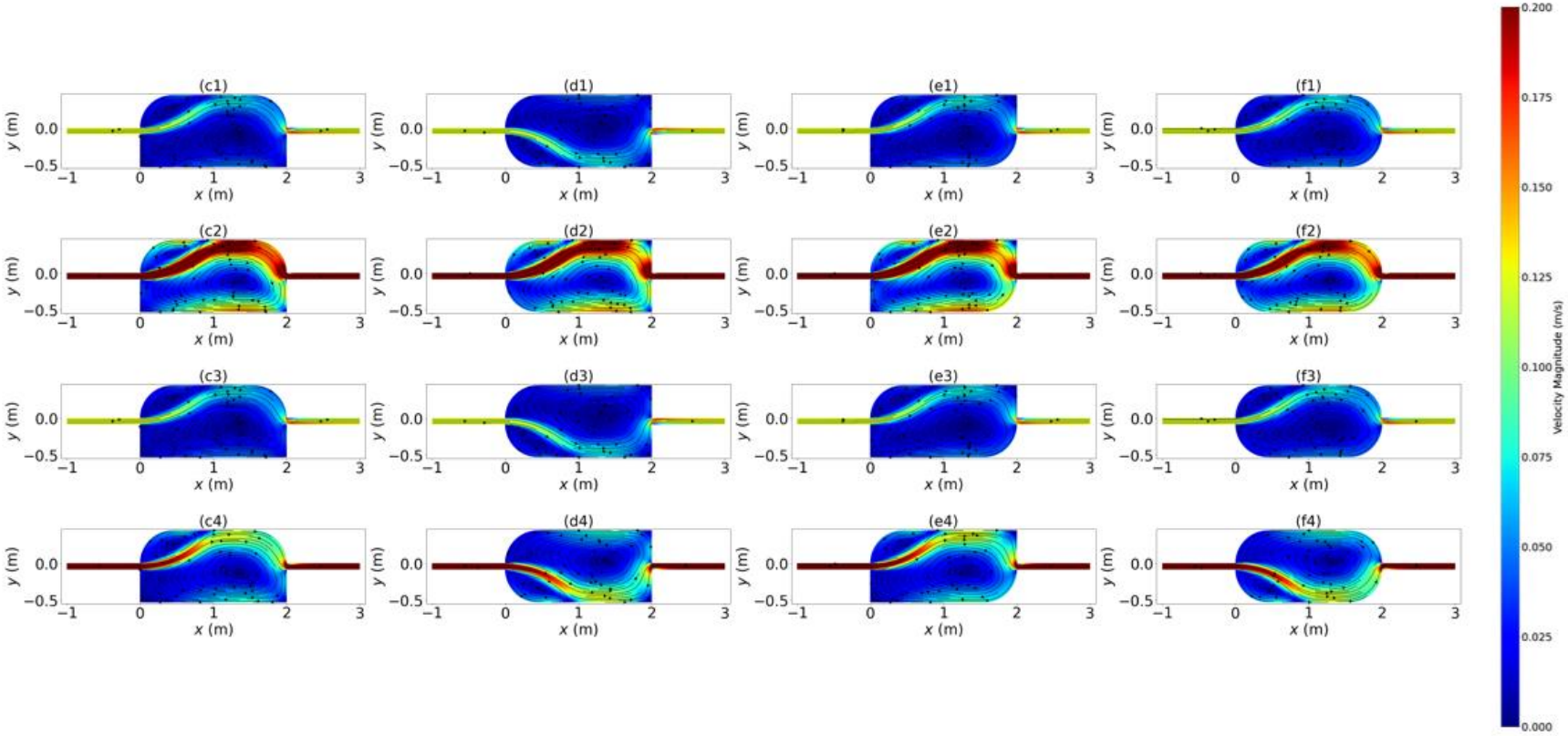

Figure 24: Amplitude of velocities and streamlines modeled with TELEMAC-2D for long reservoirs with inlet at lateral boundary

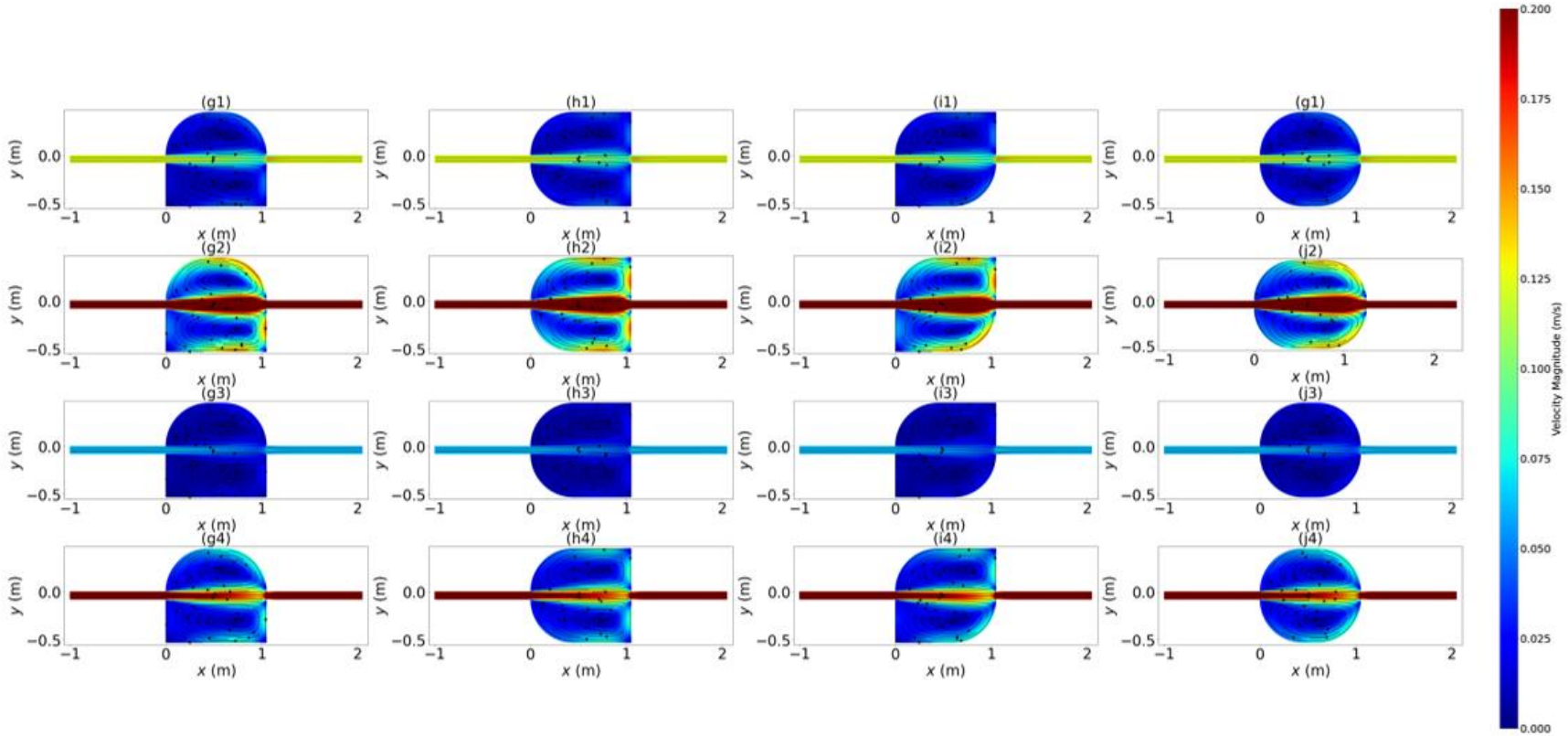

Figure 25: Amplitude of velocities and streamlines modeled with TELEMAC-2D for short reservoirs with curvatures

Inlet on lateral side

In Figures 26 and 27, notations (k,l,m,) and (n,o,p) correspond to the configurations with inlet positioned at *L*/4, L/2, and 3*L*/4 respectively, with long and short reservoirs. In the case of long reservoirs, we can observe two distinct flow patterns: for the (k) and (l) configurations, the jet attaches itself to the opposite wall, resulting in a quasi-symmetrical recirculation for the (l) case and an asymmetrical configuration for the (k) case. However, when the inlet is positioned at 3L/4 (m), we observe a different behavior where the jet flows directly towards the outlet without attaching to the opposite wall. This behavior can be described as a “short-circuit” phenomenon. For short reservoirs, we observe a similar “short-circuit” behavior for the (p) and (l) configurations, where the jet bypasses the recirculation and heads straight towards the outlet. On the other hand, for the (n) configuration, we see that the jet attaches itself to the wall. It appears that the short-circuit configuration is more dependent on the distance between the inlet and the outlet rather than the length ratio.

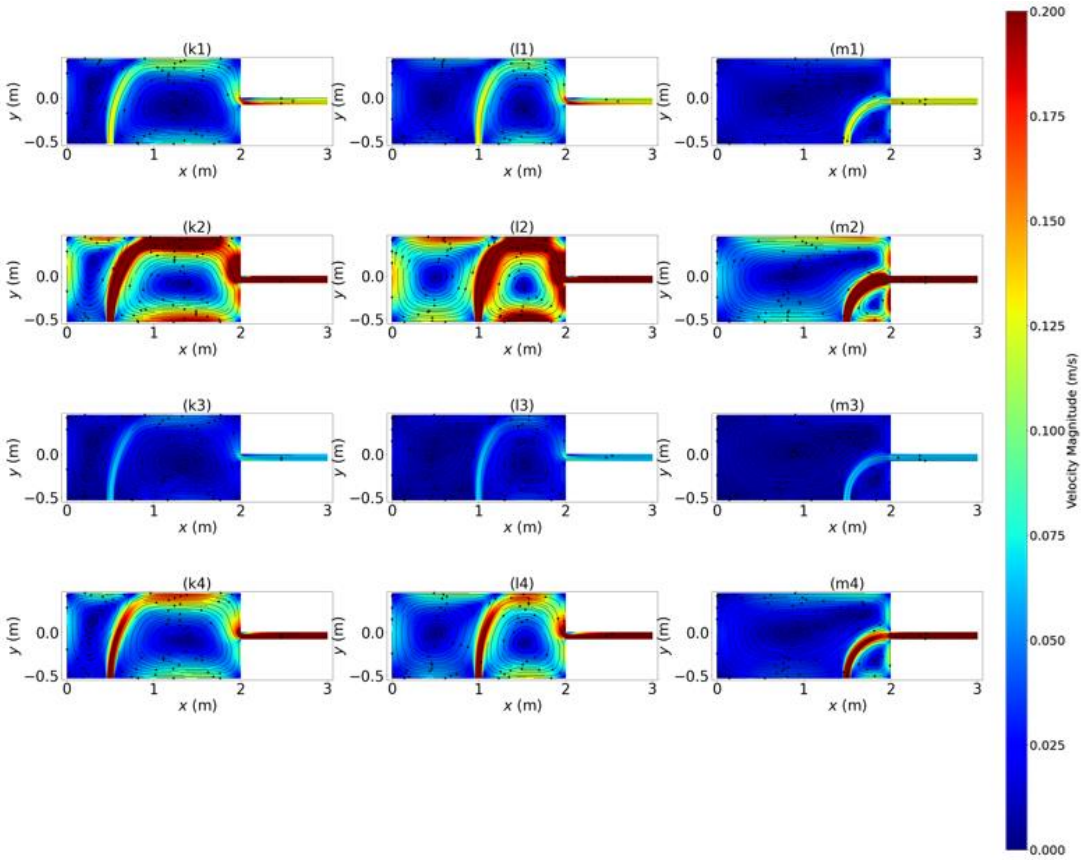

Figure 26: Amplitude of velocities and streamlines modeled with TELEMAC-2D for long reservoirs with inlet at lateral boundary

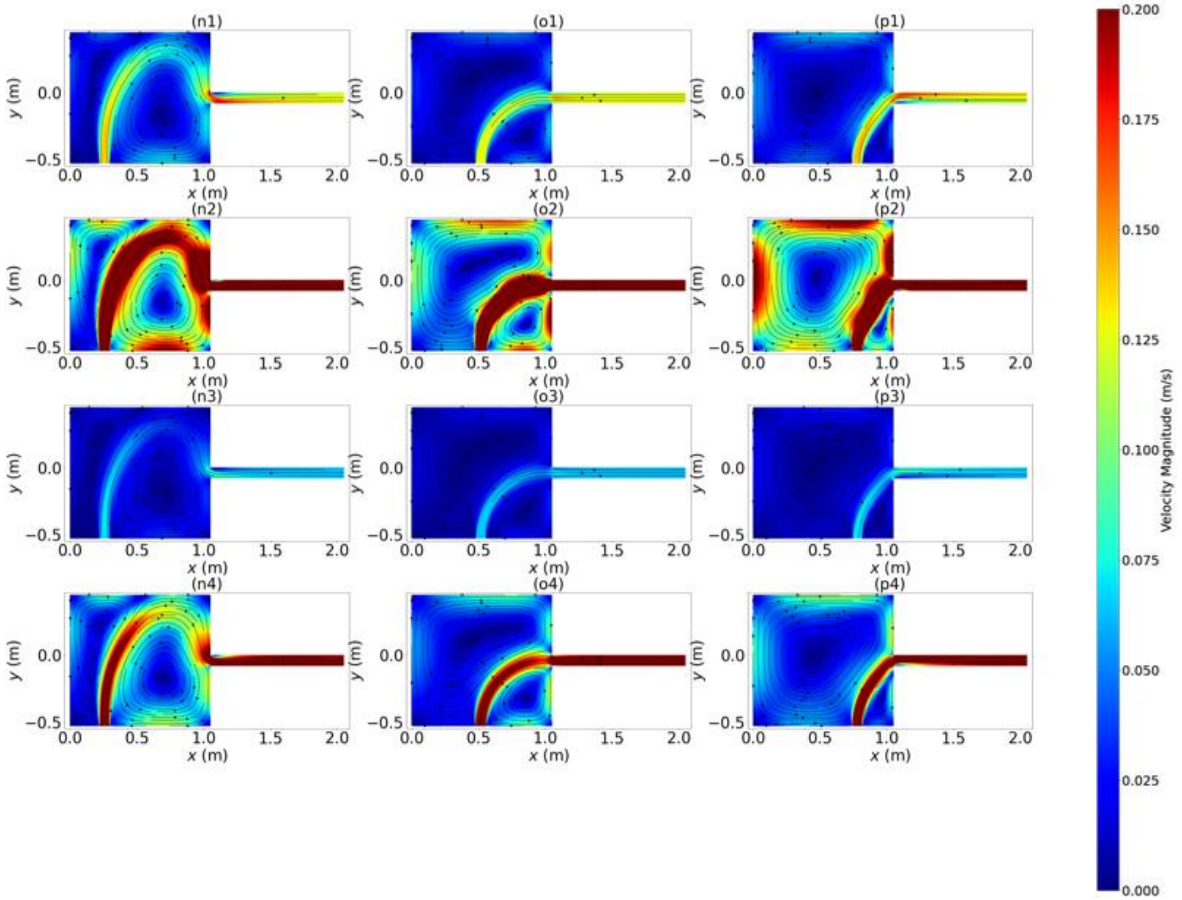

Figure 27: Amplitude of velocities and streamlines modeled with TELEMAC-2D for short reservoirs with inlet at lateral boundary

The occurrence of a short circuit can be related to the distance between the inlet and the outlet. By schematizing the main flow by a line C from the inlet to the outlet (Figure 28), it is found that a short circuit is present when C is less than 0.70 m. The case of reattachment appears when C is greater than 0.89 m, the range (0.70, 0.89) remains to be explored. This could be expanded and validated by examining more positions of the exit condition.

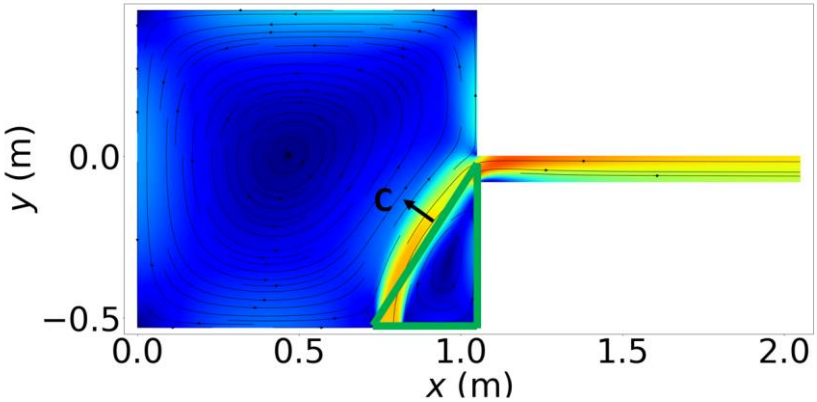

Figure 28: Analysis for short circuit of short reservoir

Weir case

In this case, the downstream side of the rectangular reservoir is a free surface weir, which is represented in TELEMAC(2D using a Thomson exit condition (Hervouet, 2007). Similarly to configurations with curvatures, it is observed that the flow pattern remains unchanged regardless hydraulic conditions and reservoir length, in comparison with the corresponding rectangular configurations. Configurations with a weir at outlet are therefore not a priority.

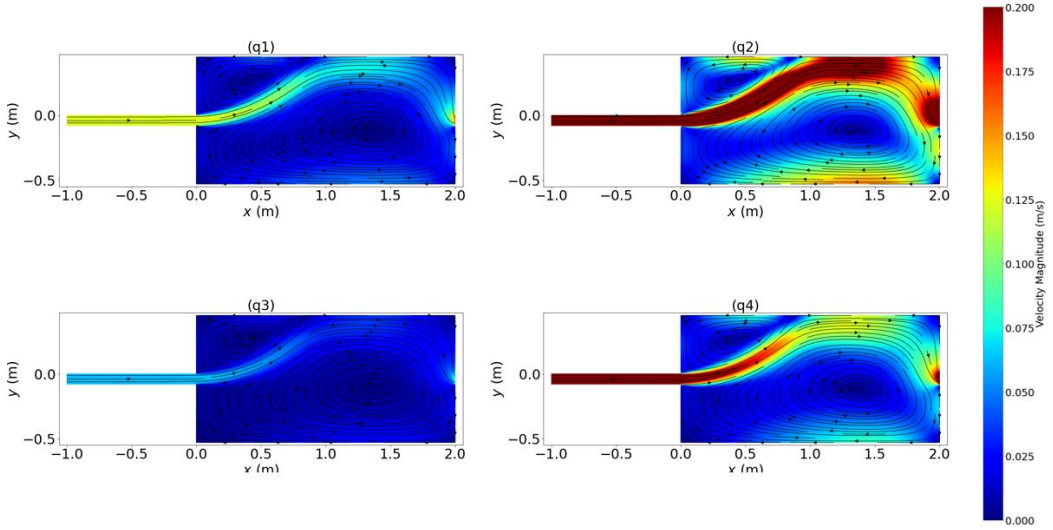

Figure 29: Amplitude of velocities and streamlines modeled with TELEMAC-2D for long reservoirs with inlet at lateral boundary

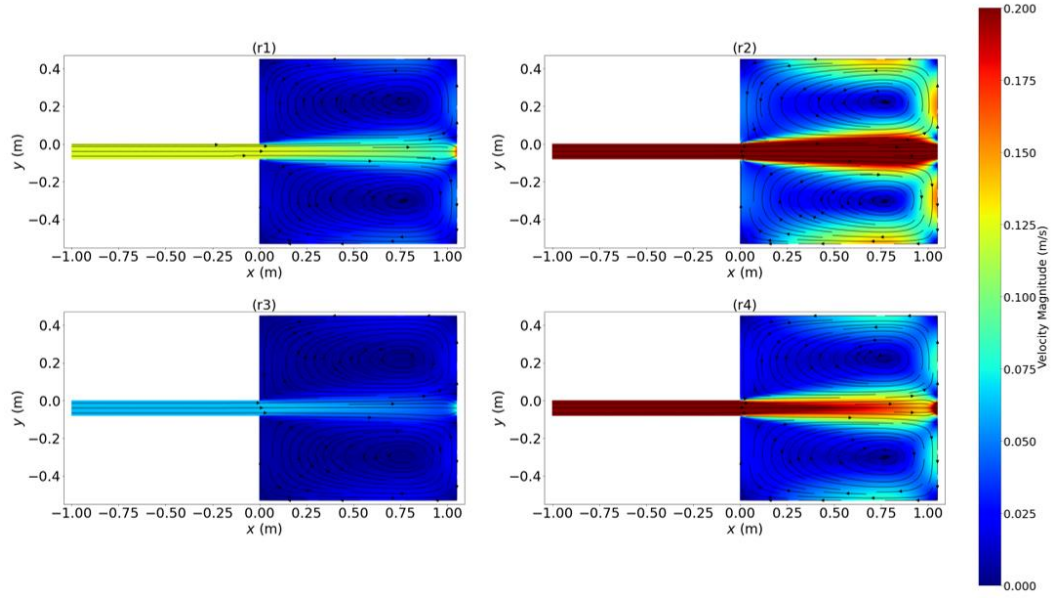

Figure 30: Amplitude of velocities and streamlines modeled with TELEMAC-2D for short reservoirs with inlet at lateral boundary

3.5.3. Results with TELEMAC-3D

TELEMAC-3D was applied to the inlet jet case. Figure 31 shows the depth averaged velocity magnitude and streamlines for three elevations of the inlet jet (located on the center of the reservoir wall opposite to the outlet). Result for the corresponding reference case (s) is also shown. While an asymmetrical pattern is found for the reference case, the jet case yields quasi-symmetrical patterns when the jet is at the bottom(t) and mid- water depth (u) and an asymmetrical pattern when the jet is located on the top (v).

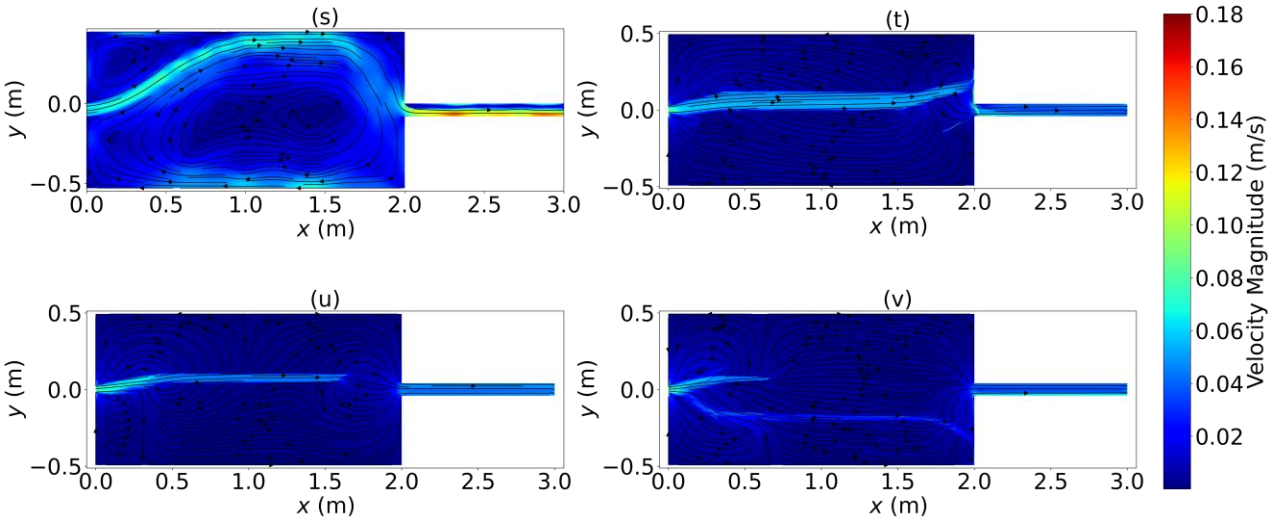

Figure 31: Depth-averaged velocity magnitude and streamlines for (s) Reference case, and inlet jet at (t) bottom position (u) mid water depth and (v) top position. Results are shown at t = 800 s

Comparison of velocity magnitude in a vertical plane at y = 0.0 m (center of jet) shows a decrease in velocity along the reservoir for each case (Figure 32). Figure 33 shows velocity magnitude in a transverse vertical plane at x = 0.1 m (just downstream of the inlet), x = 1.0 m (middle of the reservoir) and x = 2.0 m (reservoir outlet). For reference case and cases (t) and (u), the jet is deflected laterally after a certain distance. Jet does not spread vertically or horizontally. The velocity magnitude is obviously higher for jet case compared to reference case and is mainly localized in the jet direction. For the same hydraulic conditions in terms of F and S, a different flow pattern and distribution are found depending on the inlet flow configuration.

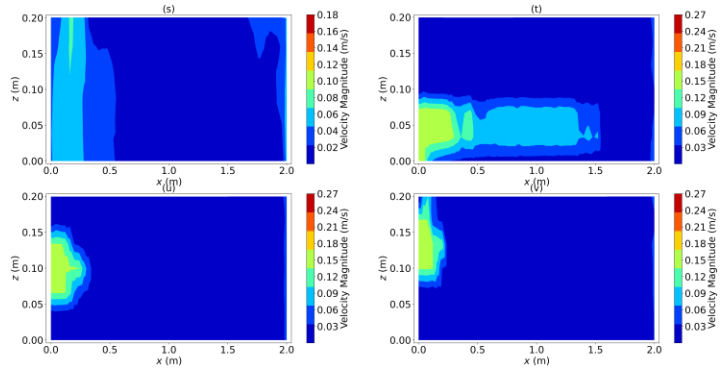

Figure 32: Two-dimensional (2D) velocity magnitude obtained fromTELEMAC-3D numerical simulations for jet case, at y = 0.0 m at t =800 s. s) Reference case, and inlet jet at (t) bottom position (u) mid water depth position, and (v) top position

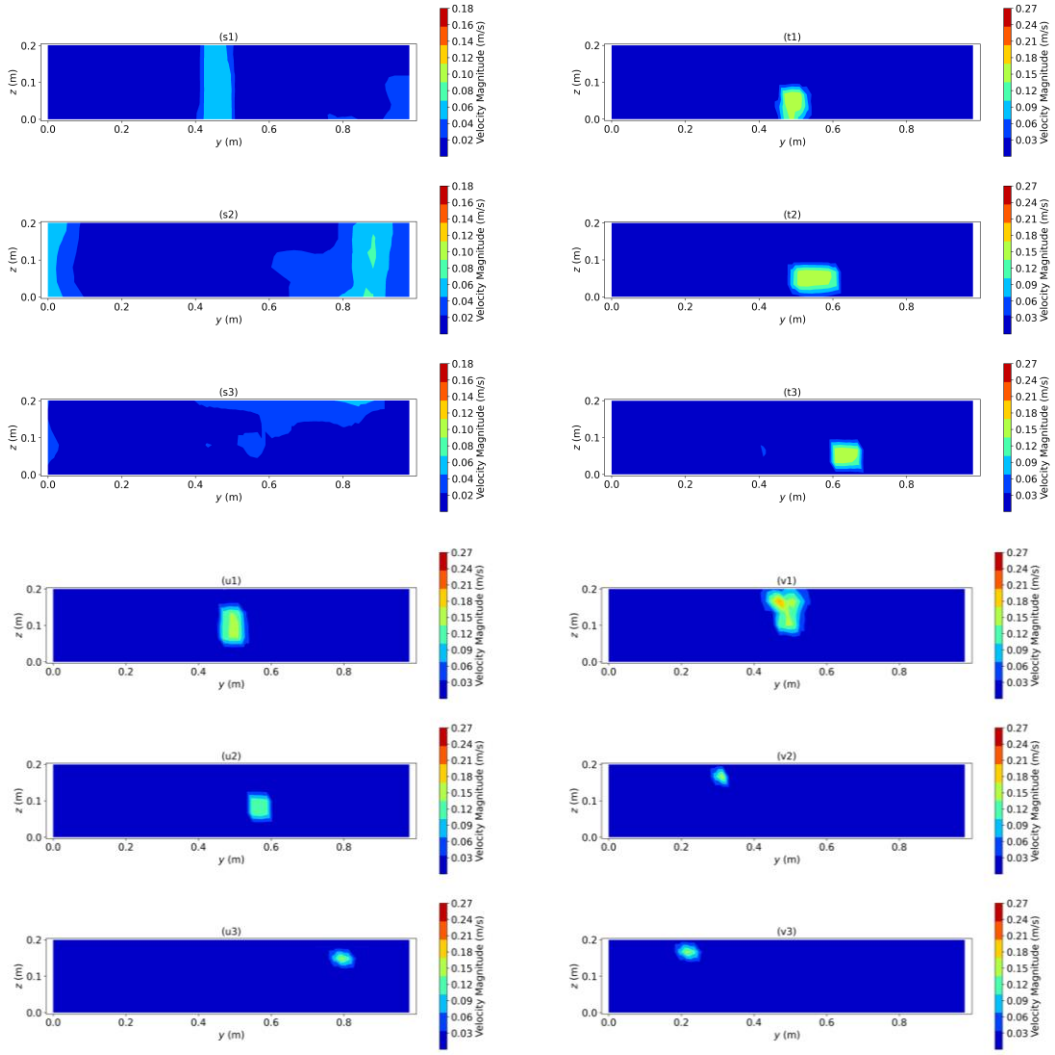

Figure 33: Two-dimensional (2D) velocity magnitude withTELEMAC-3D numerical simulations for (s) reference case, and jet case at (t) bottom position (u) mid water depth position, and (v) top position. (s1), (t1), (u1) and (v1) are results at x = 0.1 m, (s2), (t2), (u2) and (v2) at x = 1.0 m, and (s3), (t3), (u3) and (v3) at x = 2.0 m

3.6. Conclusions

Because of the very low water depth compared to the horizontal dimensions of real shallow reservoirs, scaling real cases according to Froude similitude is often not possible without significant geometrical distortion. Additionally, the shape of real reservoirs is often complex and cannot be accommodated in existing laboratory flumes. By analyzing the geometric specificities of four real reservoirs operated by EDF and considering existing laboratory experiments, the design of new configurations has been proposed. Similarly, hydraulic scenarios representative of real reservoir have been considering the Froude and the Friction numbers, which have a significant influence on flow patterns. All these configurations have been analyzed using TELEMAC-2D or TELEMAC-3D to quantify their influence on main flow features compared to a reference rectangular reservoir case. The ability of both the solvers to correctly represent main flow patterns in rectangular shallow reservoirs has been previously verified considering experimental data from the literature.

Four families of geometric configurations have been defined considering the specificities of shallow reservoirs: inlet jet, curved corners, lateral inlet channel and outlet weir. They have been tested for short and long reservoirs. For each configuration, the specific geometric parameters have been defined considering the constraints of the experimental facility available, while the hydraulic parameters have been adjusted to optimize the maximum and minimum values of the Friction and Froude numbers in accordance with values in real reservoirs. The results of the reference case (inlet and outlet open channels) demonstrate flow patterns that are similar to those observed experimentally by Dufresne et al. (2010b) and numerically by Dufresne et al. (2012). These results remain unaffected by corner curvature and change in outlet condition. In lateral inlet case, two types of flow patterns are obtained numerically: the short-circuit regime and the attached regime. The flow pattern of the short-circuit type depends on the ratio of the horizontal to vertical distances between the outlet and inlet. This could be of interest for sediment deposits management since a reservoir with a short-circuit regime would tend to minimize sedimentation. A jet at reservoir inlet has also been shown to influence flow pattern. This analysis shows that lateral inlet channel and inlet jet are configurations of interest to study the specificities of real reservoirs configurations.

Chapter 4. Experimental study of flow patterns in shallow rectangular reservoirs: effect of inlet boundary condition

This chapter was submitted for publication in International Journal of Sediment Research. The paper is under revision.

This chapter assesses experimentally the effect of the inlet boundary condition on the patterns of clear water flow in rectangular shallow reservoirs. Two distinct inlet boundary conditions were compared: a free surface inlet channel, and a pressurized circular inlet jet positioned at various elevations over the flow depth. The outlet boundary condition was a free surface channel for both cases. Twenty-two steady flow experiments were performed with clear water and velocity fields in the reservoir were measured using large scale particle image velocimetry (LSPIV) and an Acoustic Doppler Velocity Profiler (ADVP). The flow pattern in the reservoir is found greatly influenced by the inlet boundary condition (type and vertical positioning), the reservoir geometry (relatively short vs. long reservoirs) and, to a lesser extent, by the hydraulic boundary conditions (i.e., Froude and friction numbers). For an inlet circular jet located near the reservoir bottom, an unstable flow type, changing randomly over time, was observed regardless of the reservoir length and of the inlet flow rate. The same type of unstable flow pattern was observed for a relatively long reservoir and the lowest tested flow rate, irrespective of the vertical positioning of the inlet jet. In all other tested configurations, a steady reattached jet was found in the reservoir equipped with a pressurized inlet jet. Besides providing new knowledge on flow in shallow reservoirs with an inlet jet, the novel experimental data presented here will prove valuable for evaluating flow computational models. The outline of this chapter is as follows. In Section 4.1, we describe the experimental setup and the test program. Flow patterns and measured velocity fields using LSPIV technique and ADVP probe are presented and discussed in Section 4.2. Conclusions are drawn in Section 4.3.

4.1. Experimental setup and test program

Forty-two (42) experimental tests were performed in a laboratory setup constructed in the hydraulic laboratory of the University of Liege, Belgium. This chapter focuses on the description and analysis of twenty-two (22) experiments conducted with a flow depth H = 0.10 m setup. Additional experiments conducted at a flow depth H = 0.20 m are presented in Appendix I.

The setup is based on the same facility as previously used by Dufresne et al. (2010) and Peltier et al. (2014). The rectangular reservoir was inserted in a 10.4 m long horizontal flume (Figure 34). The reservoir width was kept constant and equal to the flume width: B = 0.985 m, while the reservoir length L_1 was changed by solid blocks (Figure 34a). The flume bottom and walls were fixed and made of glass. In all configurations, the reservoir outlet was a free surface channel of width b_o = 0.08 m. The flow depth H was set at 0.10 m in all tests (i.e., shallowness ratio H / B = 0.10). Two types of inlet boundary condition were considered: either a free surface rectangular channel or a circular jet. The inlet channel and circular inflow pipe were designed long enough to ensure a fully developed flow at the reservoir entrance.

For configurations with a free surface inlet channel, the inlet and outlet channels were located along the reservoir centerline, on opposite sides. The width of the inlet channel was set to b = 0.08 m, leading at the entrance of the reservoir to a sudden lateral expansion of ΔB = 0.4525 m on both sides. In the case of a circular jet at the inlet, the inflow pipe was connected to a PVC tube, of 0.04 m in diameter, fixed perpendicularly to a movable vertical plate (Figure 34). The vertically movable circular tube allows adjusting the positioning of the inlet jet over the flow depth. Three different positions were tested: close to the reservoir bottom (Z_{jet} / H = 0.20), at mid-depth (Z_{jet} / H = 0.50), and close to the water surface (Z_{jet} / H = 0.75), with Z_{jet} the elevation of the inlet pipe centroid above the reservoir bottom. The inlet pipe and outlet channel were aligned with the reservoir centerline.

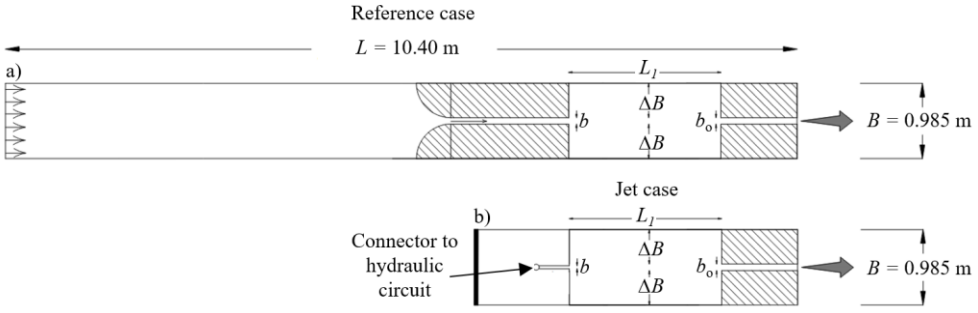

Figure 34: Sketch illustrating experimental flume equipped with (a) a free surface inlet channel and (b) a circular inlet jet (pressurized flow)

The flow in rectangular shallow reservoirs is governed by nine parameters (Peltier et al. , 2014), namely the reservoir length L, the reservoir width B, the inlet channel width or jet diameter b, the flow depth H, the depth-averaged velocity in the inlet channel U_{in}, the roughness height k_s, the kinematic viscosity ν, the gravitational acceleration g, and the elevation Z_{jet} of the centroid of the inlet section. The origin of the z axis is located at the bottom of the reservoir. The inlet velocity is calculated as $U_{in} = Q/(bH)$, with Q the inlet flow rate. According to Vaschy Buckingham theorem,

seven dimensionless parameters can be derived from the nine dimensional ones: relative reservoir width-to-inlet width ratio B / b, reservoir length-to-width ratio L_1 / B, flow depth-to-width ratio H / B (i.e., shallowness parameter), Froude number $F = U_{in} / (gH)^{1/2}$, Reynolds number $R = 4\, U_{in}\, H / \nu$, relative elevation of the inlet section centroid Z_{jet} / H, and relative roughness height k_s / H. Following Peltier et al. (2014), k_s / H and R can be merged into the friction number $S = \lambda\, B / H$, in which the friction coefficient λ is evaluated with Colebrook-White formula. The geometric parameters L / B and B / b may be merged into the reservoir shape factor SF (Dufresne et al., 2010; Peltier et al., 2014).

Table 8 summarizes the experimental conditions, with the corresponding non-dimensional numbers. For each inlet boundary conditions, a short (L_1 = 1.05 m, SF = 4.64) and a long (L_1 = 2.00 m, SF = 8.84) reservoir were studied, considering three steady flow rates Q with a circular inlet jet (0.5 l/s, 1.75 l/s, 3.0 l/s) and two values (1.0 l/s and 3.0 l/s) with a free surface inlet channel. Three inlet jet positions were tested: Z_{jet} / H = 0.20, 0.50, 0.75. The Froude number ranges from 0.13 to 0.76, and the friction number S is in the range from 0.143 to 0.206.

The inflow discharge was measured with an electromagnetic flowmeter, which has an accuracy of 0.04 %. The water level was controlled by a gate downstream of the flume. Its position was adapted for each flow rate to ensure a water depth H = 0.10 m in the reservoir. The water depth was measured using an ultrasonic probe located 0.4 m upstream of the downstream outlet. Large-Scale Particle Velocimetry (LSPIV) technique was used for measuring surface velocity. As shown by Kantoush et al. (2008b) and Peltier et al. (2014), this technique provides accurate results in shallow reservoirs. The underlying principle consists in measuring the motion, between successive images, of visible tracers lying on the free surface. A Panasonic Lumix GH4 camera recording 1920 × 1080 pixels at a rate of 25 Hz was used. Videos were treated with the open-source software Fudaa-LSPIV. Images were orthorectified, and displacements of tracers between the images were calculated through statistical correlations. The floating tracer used was coarse sawdust of 2 mm in diameter.

For a qualitative appraisal of 3D flow features in configurations with an inlet circular jet at, a rod with attached pieces of wool was positioned at different locations in the reservoir. Additionally, 3D velocity profiles were measured with an acoustic Doppler velocity profiler (ADVP) probe (Nortek Vectrino). The probe has a 4-transducer orthogonal plane bistatic geometry. The measurements were performed over a distance of 3 cm staring 4 cm below the transducer head. For each probe location, 8,000 instantaneous velocity values were evaluated with a sampling rate of 100 Hz. To improve the quality of the signal, Glass Microspheres Spherical 110P8 particles were seeded in

the flow. The despiking algorithm of Goring and Nikora (2002) was applied for removing spikes from velocity time series. The LSPIV and ADVP measurements showed a good repeatability of the measurements. A meticulous validation of the Acoustic Doppler Velocity Profiler (ADVP) probe was performed, as detailed in Appendix E, which entailed a two-step procedure. The initial step involved a comparative assessment of the ADVP probe in relation to the Acoustic Doppler Velocimeter (ADV) probe, while the subsequent step was dedicated to evaluating the reproducibility of ADVP measurements (Appendix E). The uniformity of the results confirmed and underscored the accuracy and precision of measurements.

We present here a classification of the flow patterns observed in the twenty-two tested configurations. The main findings are briefly summarized in Section 4.2.1, mostly through Figure 35. For the sake of comparison, Section 4.2.2 displays the flow fields observed for reservoirs equipped with a free surface inlet channel. Next, flow fields encountered in reservoirs with a circular inlet jet are characterized in both relatively short (Section 4.2.3) and long (Section 4.2.4) reservoirs.

4.2. Results

4.2.1. General overview

For reservoirs with a free surface inlet rectangular channel, three types of flow patterns were observed: steady symmetric (detached) jet (S0), steady reattached jet (A1), or meandering jet (i.e., periodically oscillating, O). For the circular inlet jet, only two flow types were observed: either a steady reattached jet, or unstable flow field (i.e., varying randomly over time). For a long reservoir, a flow pattern similar to that of open channels is observed, characterized by a single point located upstream of the reservoir (A1). For short reservoirs, a reattachment of flow with a single point located downstream from the reservoir (A1*) is identified.

Figure 35 provides an overview of the observations. Symbols are filled when a steady reattached jet was observed, and they are empty for unstable and meandering cases. The type of observed flow field depends on the type of inlet boundary condition (jet or channel), the reservoir geometry (length and positioning of the inlet jet) and on the hydraulic boundary conditions (F and S). Cases with a free surface inlet channel are represented by a star at $Z_{jet} / H = 0.50$, while those with an inlet jet are represented by a square. The left and right parts of the symbols correspond to short and long reservoirs, respectively.

Table 8: Program of experimental tests and type of observed flow pattern. S0 stands for symmetric jet without reattachment, O for meandering (oscillating) jet, U for unstable jet, and A1 or A1 for reattached jet in the reservoir*

Inlet	Test ID	L_1 (m)	ΔB (m)	SF	Q (m^3/s) (10^{-4})	U_{in} (m/s)	R (10^4)	F	S	Z_{jet}/H	Flow type
Rectangular channel	1	1.05	0.4525	4.64	10.00	0.13	17.50	0.13	0.21	0.50	S0
	2				35.00	0.44	30.00	0.44	0.16		O
	3	2.00		8.84	10.00	0.13	17.50	0.13	0.21	0.50	A1
	4				35.00	0.44	30.00	0.44	0.16		A1
Jet	5	2.00		8.84	5.00	0.13	5.00	0.13	0.21	0.20	U
	6				17.50	0.44	17.50	0.44	0.16		U
	7				30.00	0.75	30.00	0.76	0.14		U
	8	1.05		4.64	5.00	0.13	5.00	0.13	0.21	0.20	U
	9				17.50	0.44	17.50	0.44	0.16		U
	10				30.00	0.75	30.00	0.76	0.14		U
	11	2.00		8.84	5.00	0.13	5.00	0.13	0.21	0.50	U
	12				17.50	0.44	17.50	0.44	0.16		A1
	13				30.00	0.75	30.00	0.76	0.14		A1
	14	1.05		4.64	5.00	0.13	5.00	0.13	0.21	0.50	A1*
	15				17.50	0.44	17.50	0.44	0.16		A1*
	16				30.00	0.75	30.00	0.76	0.14		A1*
	17	2.00		8.84	5.00	0.13	5.00	0.13	0.21	0.75	U
	18				17.50	0.44	17.50	0.44	0.16		A1*
	19				30.00	0.75	30.00	0.76	0.14		A1*
	20	1.05		4.64	5.00	0.13	5.00	0.13	0.21	0.75	A1*
	21				17.50	0.44	17.50	0.44	0.16		A1*
	22				30.00	0.75	30.00	0.76	0.14		A1*

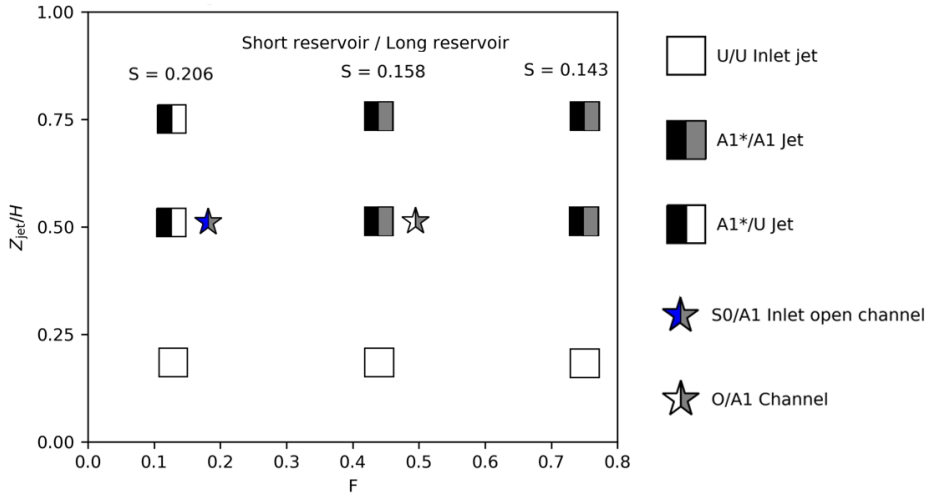

Figure 35: Classification of observed flow patterns in short and long reservoirs: unstable (U), reattached with one point located upstream of the reservoir (A1), reattached with one point located downstream of the reservoir (A1), symmetric without reattachment point*

4.2.2. Free surface inlet channel cases

For inlet free surface channel cases, the observed flow patterns are consistent with those reported in literature, differing according to the reservoir geometry and hydraulic conditions (Figure 35). In relatively short reservoirs (i.e., SF < 6.2), a steady symmetric flow pattern, corresponding to the flow type “S0” reported by Kantoush (2008), Camnasio et al. (2011) and Dufresne et al. (2010) was observed for the lower tested Froude number (Test 1). The corresponding surface velocity field obtained from LSPIV is represented in non-dimensional form in Figure 3a, where the horizontal velocity $U = (u^2 + v^2)^{1/2}$ (u and v are streamwise and transversal components of velocity, respectively) is normalized by a reference velocity at the outlet channel $U_{ref} = Q / (b_0 H)$. The flow type is characterized by a straight jet from the inlet to the outlet, with large symmetric eddies on both reservoir sides and no jet reattachment. When the Froude number is increased (Test 2), the flow jet oscillates (flow type O), in agreement with observations by Dufresne et al. (2010a), Kantoush et al. (2008a,b) and Peltier et al. (2014). In addition, our results are in line with the finding of Peltier et al. (2014) stating that meandering jets form for a F > 0.20 and SF < 6.2.
For the longer reservoir (SF > 6.2, Tests 3 and 4), a steady asymmetric flow pattern was found, characterized by a jet deflecting laterally and reattached to the left sidewall, as shown in Figure 36b-c. This pattern (A1) was described by Kantoush (2008), Dufresne et al. (2010a) and Camnasio et al. (2011). The flow asymmetry was attributed to the Coanda effect (Wille and Fernholz 1965; Miozzi et al., 2010).

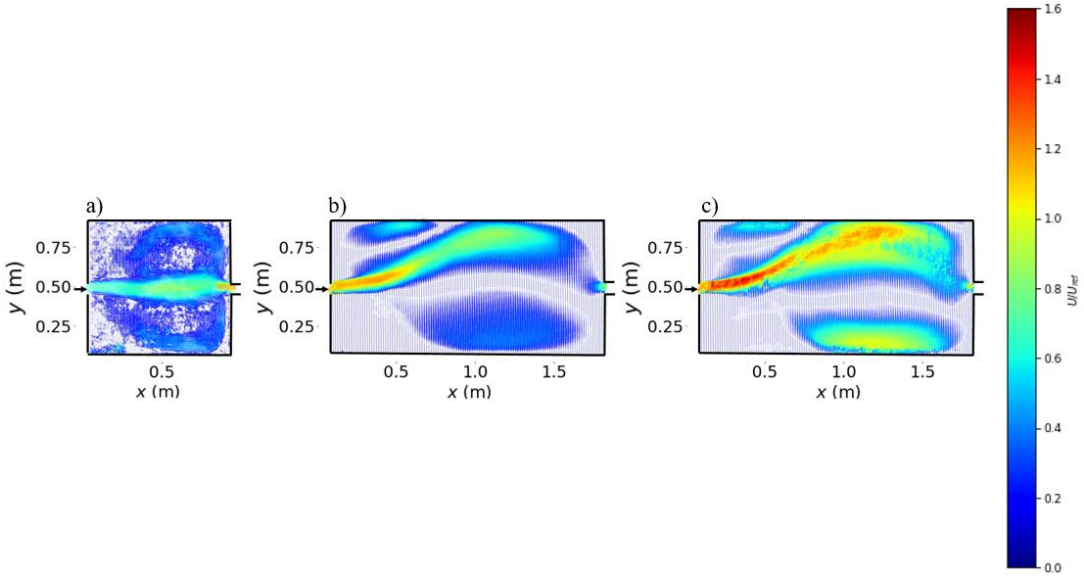

Figure 36: Normalized surface velocity U / U_{ref} for short and long reservoirs with a free surface inlet channel: (a) Tests 1, (b) Test 3 and (c) Test 4

4.2.3. Short reservoirs with a circular inlet jet

In relatively short reservoirs (SF < 6.2) with a circular jet at the inlet, two types of flow pattern were observed depending on the vertical positioning of the inlet jet: either a steady asymmetric pattern, or an unstable pattern (Figure 35).

Steady asymmetric flow pattern

When the inlet jet was positioned either at mid-depth (i.e., $Z_{jet} / H = 0.5$, Tests 14 to 16) or near the free surface (i.e., $Z_{jet} / H = 0.75$, Test 20 to 22), steady asymmetric flow patterns were observed regardless of the hydraulic boundary conditions (i.e., Froude and friction numbers). This flow type is labelled A1* in Figure 35. As revealed by the surface velocity measurements (Figure 37), this flow pattern involves one main recirculation, together with a secondary one and, in most cases, with smaller eddies in the upstream part of the reservoir. It consists of a reattached with one point located downstream of the reservoir. The jet interacts with the free surface only at a certain distance downstream of the reservoir inlet. The magnitude of the normalized surface velocity is systematically greater for cases with an inlet jet closer to the surface than for the inlet jet at mid-depth.

For the lowest Froude number (Tests 14 and 20), the normalized surface velocity magnitude reaches lower values than for the intermediate Froude number (Tests 15 and 21). This may be attributed to a relatively higher jet momentum in the latter case, maintaining the jet more

concentrated below the free surface. In contrast, the normalized surface velocity is relatively lower in Tests 16 and 22 performed under the highest Froude number. This hints at some competition between the increase in momentum and another process, which could be related to enhanced losses due to interactions between the jet and the quiescent water around. In the case of the highest Froude number, the post-processing of the LSPIV measurements was also more challenging due to the presence of air bubbles at the surface and a higher difficulty to ensure a continuous injection of sawdust.

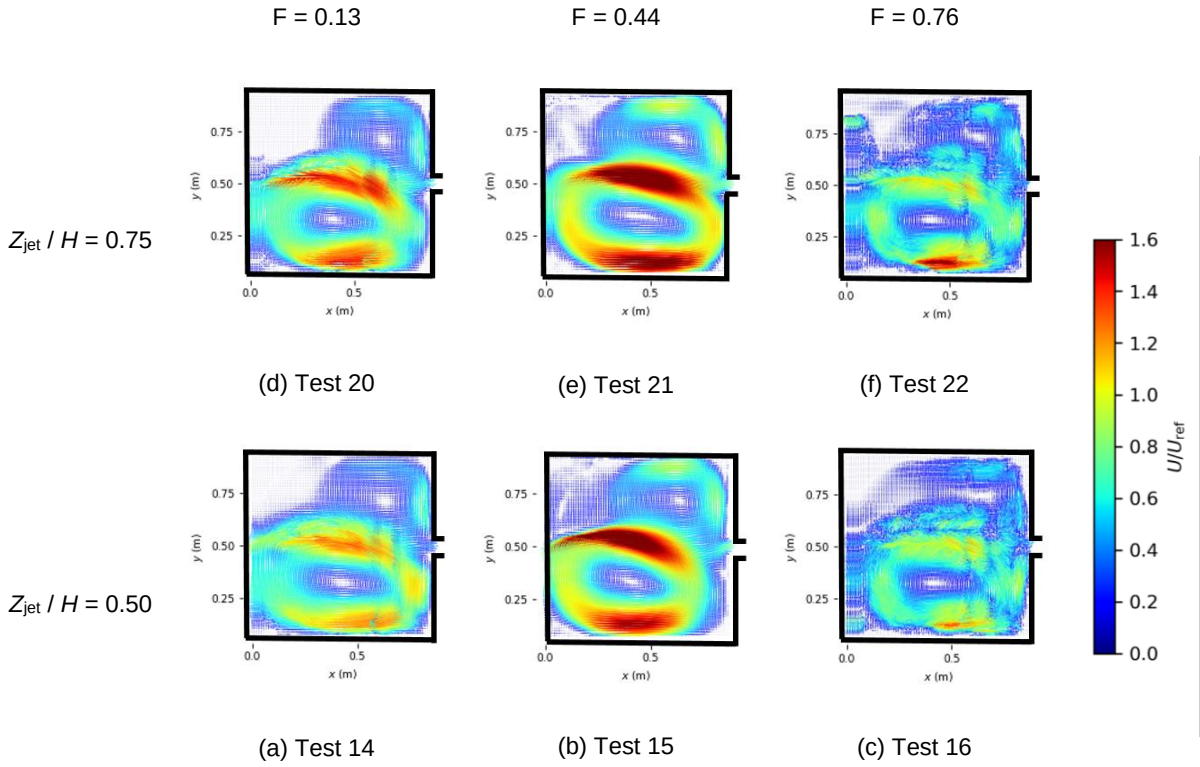

(d) Test 20 (e) Test 21 (f) Test 22

(a) Test 14 (b) Test 15 (c) Test 16

Figure 37: Normalized measured velocities U / U_{ref} for short reservoirs with a circular inlet jet.

Unlike in the case of a free surface inlet channel, reservoirs with an inlet pressurized jet led to highly three-dimensional flow features. This was qualitatively appreciated by placing a rod with wool filaments at different locations. Four filaments were used, uniformly distributed over the flow depth (i.e., positioned at 2, 4, 6 and 8 cm above the reservoir bottom). Similar results are found for configurations of short reservoir with a circular inlet jet; Figure 38 illustrates the case of Test 15. At the reservoir entrance, the filaments located at elevations 0.02 m and 0.04 m follow the direction of the main jet, while the two higher up suggest that the flow velocity is almost zero close to the surface at this location (Figure 38a). In the middle of the recirculation, flow velocity is close to zero and the four filaments wrap around the jet (Figure 38b). Moving the rod toward the downstream end of the reservoir, all four filaments exhibit a similar alignment, which hints a

velocity more uniformly distributed over the flow depth as encountered in the case of a free surface inlet channel (Figure 38c).

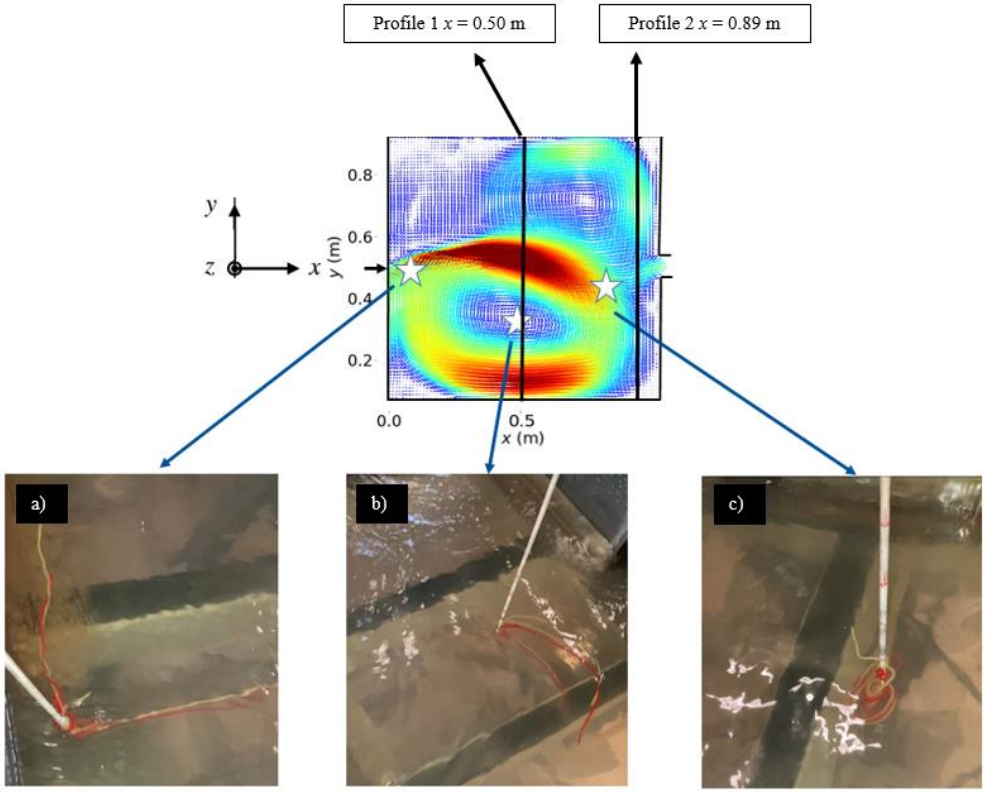

Figure 38: Test 15 - Short reservoir with inlet jet at Z_{jet} / H = 0.5. Images of filaments taken (a) at the reservoir entrance, (b) in the center of the largest eddy, and (c) along the reservoir centerline close to its downstream end.

Measurements were also made with an ADVP probe. Figure 39 depicts transverse profiles of the longitudinal velocity for Tests 14, 15, 20 and 21 along two cross-sections (Figure 38) situated at x = 0.50 m (i.e., x / b = 12.5, Profile 1) and 0.89 m (i.e., x / b = 22.5, Profile 2). These profiles are situated in the intermediate field, found in the range $6 < x / b < 30$ for free jets (Abdel-Rahman, 2010), which is the transition region between the near field region where the flow characteristics are strongly impacted by the characteristics of the outlet nozzle and the far field where an auto-similarity profile could be found. This observation implies that the flow pattern remains unchanged along the vertical in the transition region. In Tests 14 and 20 (i.e., lower Froude number), the ratio of the maximum longitudinal velocity value measured by ADVP exceeds that measured at the surface by LSPIV by up to 20 % in Profile 1 and by 30 % to 40 % in Profile 2. Similarly, in Tests 15 and 21 (i.e., higher Froude number), the surface velocity measured by LSPIV appears to be lower than the measurements obtained through ADVP. This dissimilarity could indicate lower

surface velocities in contrast to the measurements taken at a shallower relative depth, or it could be related to issues with the seeding material.

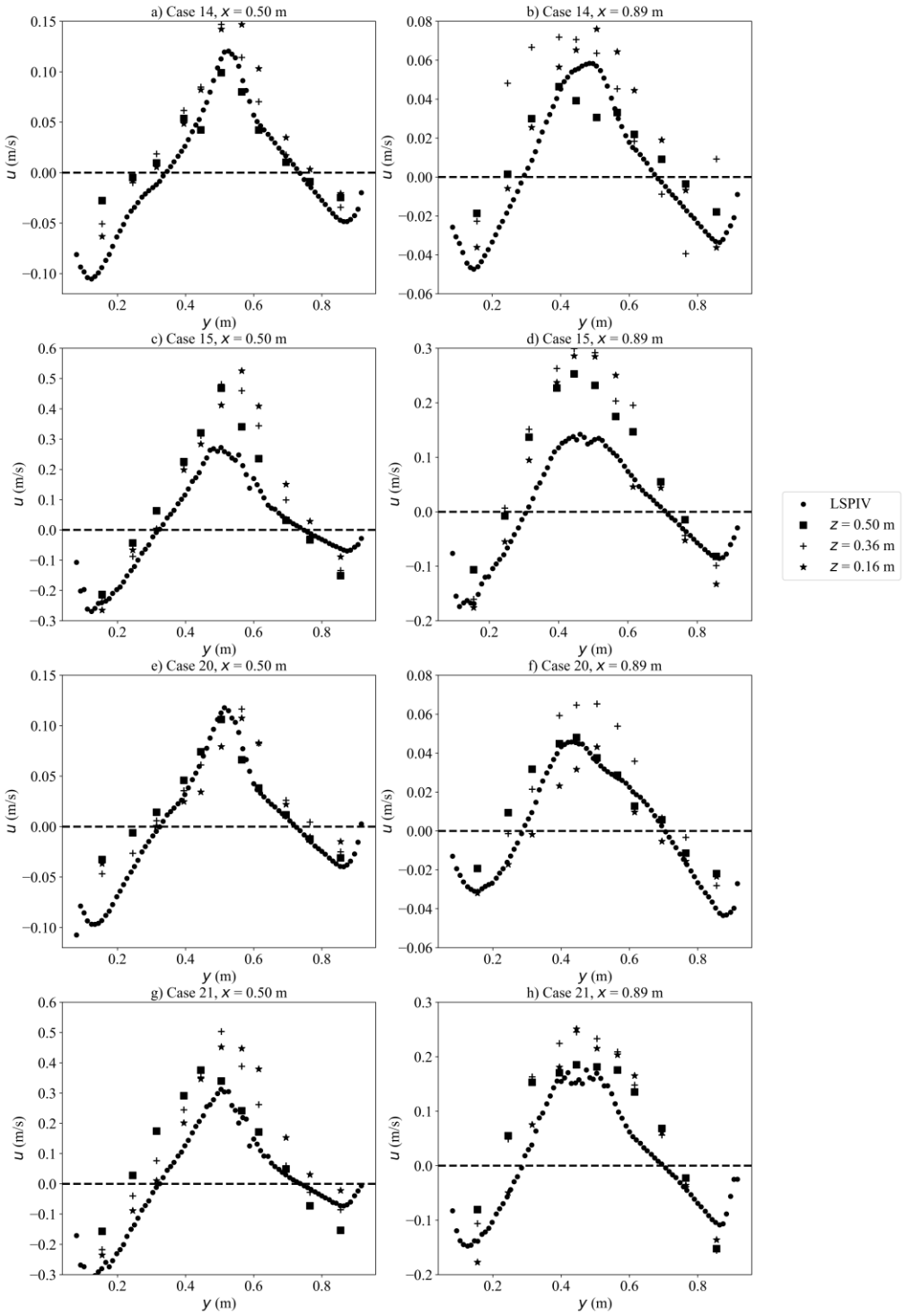

Figure 39: Horizontal velocity profiles in short reservoirs (Tests 14, 15, 20 and 21) along two cross sections (x = 0.50 m and 0.89 m), and for three elevations (z = 0.019 m, 0.036 m and 0.050 m) with ADVP, as well as the surface velocity measured with LSPIV

Unstable flow pattern

When the inlet jet was located close to the reservoir bottom (Z_{jet} / H = 0.20, Tests 8 to 10), an unstable flow pattern was obtained irrespective of the hydraulic conditions. The flow in the reservoir switched randomly over time between different flow types, mostly reattaching alternately to one side wall and to the other. Unstable flow fields were reported by Dufresne (2008) and Dufresne et al. (2009) for rectangular shallow reservoirs equipped with a circular inlet jet, as well as by Camnasio et al. (2011) and Peltier et al. (2014) for reservoirs equipped with a free surface inlet channel. Camnasio et al. (2011) found two configurations with instability for SF equal to 4.09 and 4.48, corresponding to the transition from the symmetrical flow-field region to the asymmetrical flow-field region defined by Dufresne et al. (2010). The unstable regime was observed by Peltier et al. (2014) for 6.2 < SF < 8.1 and F > 0.21. Figure 40 shows surface velocity fields measured by LSPIV for Test 9 at different times. Each velocity field was averaged over a relatively short period (4 s) to capture the time-evolution of the flow. During the first two minutes, the flow heads toward the left wall and two main eddies stand out, with their size changing over time. After running the test one hour, the jet heads toward the right side. The transitions from one state to the other does not occur periodically but the switches seemed random. Other intermediate states were also observed.

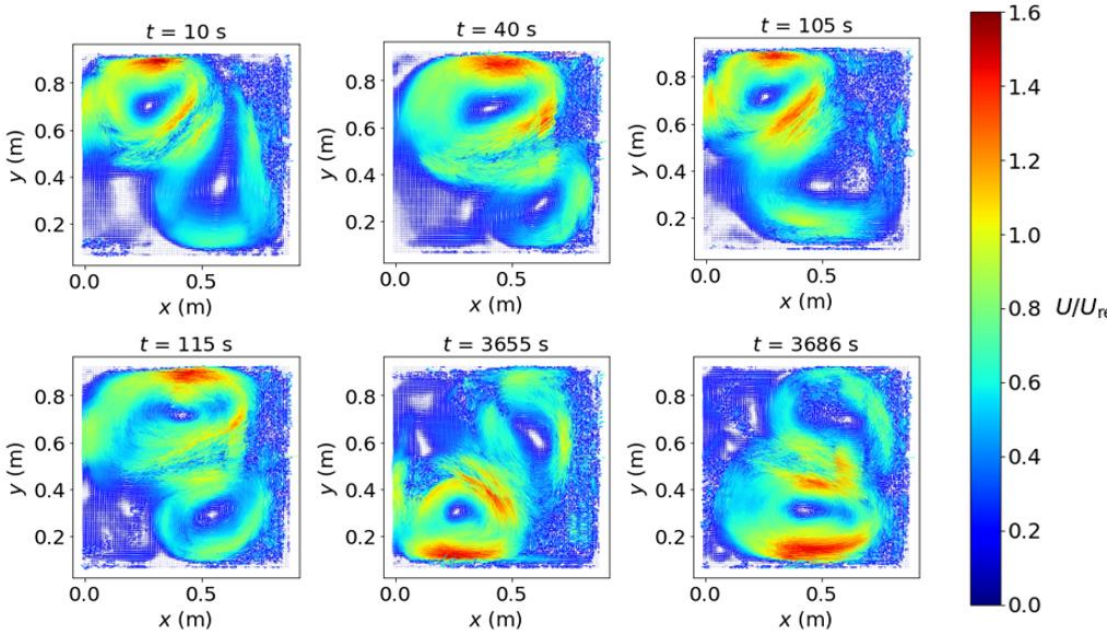

Figure 40: Normalized surface velocity (U / U_{ref}) measured by LSPIV for Test 9. Each displayed velocity was averaged over a short period of 4 s.

4.2.4. Long reservoirs with a circular inlet jet

In long reservoirs (SF > 6.2), when the inlet jet was positioned close to the bottom (Z_{jet} / H = 0.20, Tests 5 to 7), an unstable flow pattern (referred to as U) was observed whatever the hydraulic conditions, like in the case of short reservoirs. When the inlet jet was positioned at mid-depth or close to the surface (i.e., Z_{jet} / H = 0.50 and 0.75, respectively), the flow was also unstable for the slowest flow case (i.e., Tests 11 and 17, F = 0.13), which differs from observations in short reservoirs. Increasing the Froude number (i.e., Tests 12, 13, 18 and 19, F = 0.44 and 0.76), an asymmetric flow pattern with one main recirculation and small eddies in the upper part of the reservoir was found (Figure 41). The ratio of the main recirculation's size to that of the secondary recirculation is greater for flow pattern A1 than for A1*.

Figure 42 shows transverse profiles of the horizontal velocity along two cross-sections, at x = 1.00 m (i.e., x / b = 25, intermediate field) and x = 1.70 m (i.e., x / b = 42.5, far field). Observations in these profiles shows the attachment of the jet to the left sidewall as well as the presence of a recirculation, corresponding to flow pattern A1. For an inlet jet positioned at mid-depth (Test 12 and 13), the ADVP velocity profiles at three vertical positions and the LSPIV profile remain similar in shape but differ in magnitude. In Test 12, the maximum positive longitudinal velocity recorded by ADVP at z = 0.016 m (i.e., close to the bottom) exceeds the surface velocity by a factor of 2.4 at x = 1.00 m, whereas ADVP and LSPIV measurements are mostly similar at x = 1.70 m except for the reverse flow (u < 0) of the profile measured by the ADVP close to the bottom, which still exhibits higher velocity magnitude compared to LSPIV. Compared to the cross-section at x = 1.00 m, the maximum velocity measured by LSPIV and ADVP are more uniform at x = 1.70 m, i.e., at a greater distance from the reservoir entry. Increasing the Froude number (Test 13), the maximum positive velocity recorded by ADVP at x = 1.00 m was found 1.4 times higher than the corresponding value measured by LSPIV. At x = 1.70 m, this difference is again strongly reduced, like in the case of Test 12. LSPIV and ADVP measurements exhibit less consistency, which may be attributed to the difficulty of ensuring a homogeneous presence of sawdust. On the other hand, it is observed that the magnitude of velocities measured by ADVP decreases as one approaches the bottom (z = 0.016m).

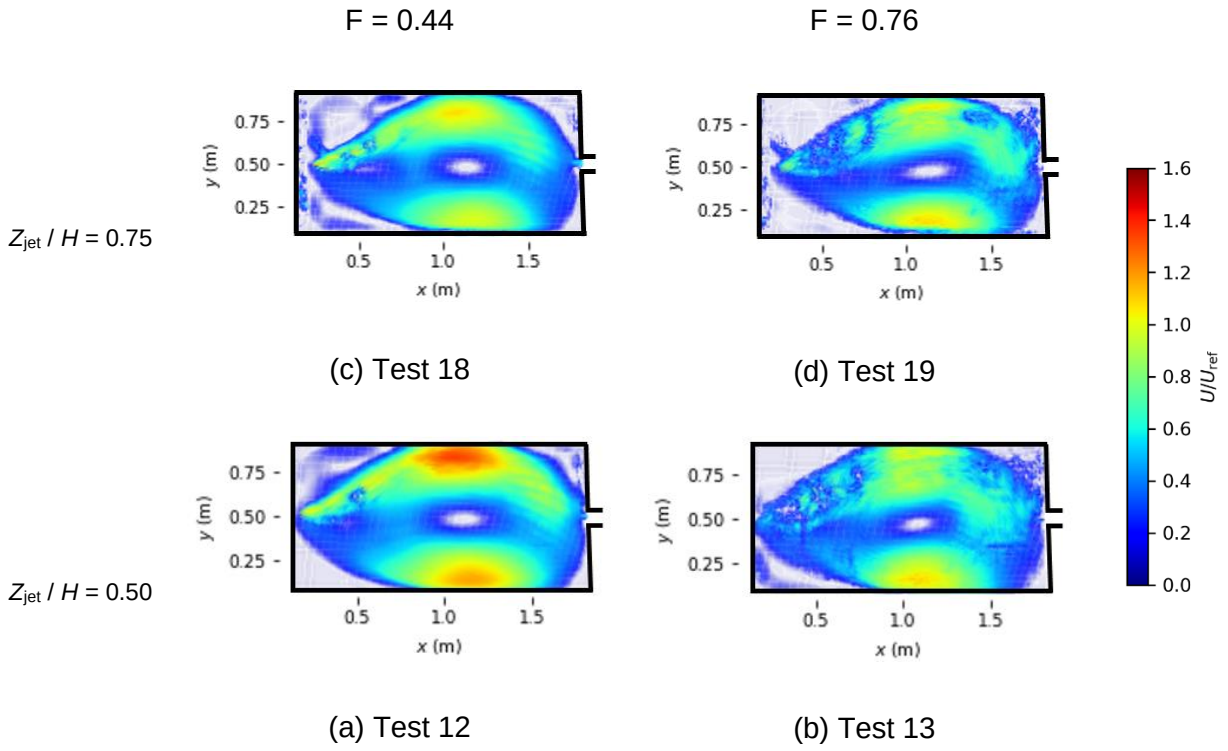

Figure 41: Normalized surface velocity (U / U_{ref}) measured by LSPIV for long reservoirs with inlet jet

Figure 42 shows transverse profiles of the horizontal velocity along two cross-sections, at x = 1.00 m (i.e., x / b = 25, intermediate field) and x = 1.70 m (i.e., x / b = 42.5, far field). Observations in these profiles shows the attachment of the jet to the left sidewall as well as the presence of a recirculation, corresponding to flow pattern A1. For an inlet jet positioned at mid-depth (Test 12 and 13), the ADVP velocity profiles at three vertical positions and the LSPIV profile remain similar in shape but differ in magnitude. In Test 12, the maximum positive longitudinal velocity recorded by ADVP at z = 0.016 m (i.e., close to the bottom) exceeds the surface velocity by a factor of 2.4 at x = 1.00 m, whereas ADVP and LSPIV measurements are mostly similar at x = 1.70 m except for the reverse flow (u < 0) of the profile measured by the ADVP close to the bottom, which still exhibits higher velocity magnitude compared to LSPIV. Compared to the cross-section at x = 1.00 m, the maximum velocity measured by LSPIV and ADVP are more uniform at x = 1.70 m, i.e., at a greater distance from the reservoir entry. Increasing the Froude number (Test 13), the maximum positive velocity recorded by ADVP at x = 1.00 m was found 1.4 times higher than the corresponding value measured by LSPIV. At x = 1.70 m, this difference is again strongly reduced, like in the case of Test 12. LSPIV and ADVP measurements exhibit less consistency, which may be attributed to the difficulty of ensuring a homogeneous presence of sawdust. On the

other hand, it is observed that the magnitude of velocities measured by ADVP decreases as one approaches the bottom (z = 0.016m).

For a jet located close to the free surface and a comparatively low Froude number (Test 18, Figure 42), the profiles measured at x = 1.00 m by ADVP and by LSPIV are all very close to each other, both in terms of shape and magnitude. The maximum velocity recorded by ADVP and by LSPIV differ by no more than 6 %. At x = 1.70 m, the maximum velocity measured by LSPIV exceeds the value obtained by ADVP by about 25 %, revealing greater surface velocities compared to the measurements recorded at a lower relative depth. It is consistently observed that the magnitude of velocities measured by ADVP decreases as one gets closer to the bottom (z = 0.016m). When the inlet Froude number is increased (Test 19, Figure 42), the maximum velocities recorded by ADVP exceed those obtained by LSPIV by almost 40 % at x = 1.00 m. Furthermore, similar to Test 13, the LSPIV measurements exhibit reduced accuracy at this cross-section, the LSPIV measurements exhibit more scatter attributed to the sawdust injection. A general observation that remains available regarding the measurements of profile 2: The velocity intensity rises as one move from the bottom towards the middle of the water column.

The result indicates that a jet within a confined environment loses its self-similarity (Pope, 2000), which is due to the pressure balance, the limitation of amplitude due to confinement and to the effect of flow pattern on the jet evolution (Righolt et al., 2015).

Longitudinal, transversal, and vertical mean velocities were compared across each configuration to evaluate the influence of jet positioning and hydraulic conditions (Appendix F). Furthermore, a comprehensive turbulent analysis was conducted, which included a comparison of Reynolds stress components and an assessment of reservoir anisotropy using the advanced Lumley triangle visualization technique (as described in Appendix G). This analysis revealed that the data points corresponded to two types of axisymmetric turbulence: cigar-shaped and pancake-shaped. Finally, an exploration of spectral analysis of the turbulent signal employing various tools such as Fast Fourier Transformation (FFT), Power Spectrum Density (PSD), and Wavelet analysis with the Morlet function is presented in Appendix H.

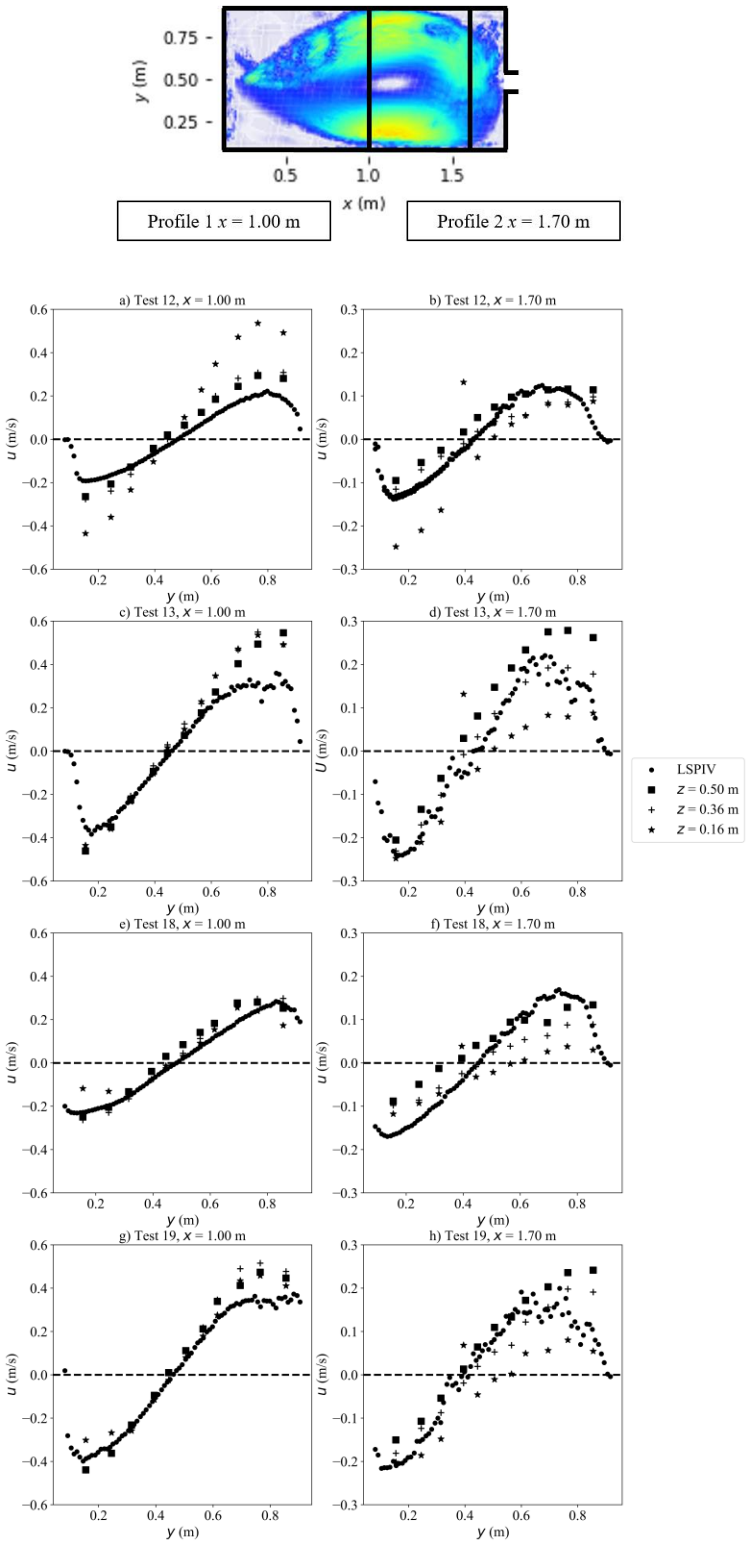

Figure 42: Longitudinal velocity profiles in long reservoirs (Tests 12, 13, 18 and 19), along two lateral cross sections x = 1.00 m and x = 1.70 m, and for three elevations (z = 0.016 m, 0.036 m, and 0.050 m) with ADVP, as well as the surface velocity measured with LSPIV

4.3. CONCLUSION

Flow patterns in rectangular shallow reservoirs were analyzed using laboratory experiments, with particular focus on the effect of inlet boundary conditions: free surface rectangular channel vs circular inlet jet. In both cases, the reservoir outlet was a free surface channel. Twenty-two experimental tests were performed, in which the reservoir length, the hydraulic boundary conditions, and the vertical position of the inlet jet (near bottom, mid-depth or near surface) were varied. For a free surface inlet channel, the observed flow fields agreed with previous studies in similar configurations involving either steady or meandering jets in the reservoir. For a circular inlet jet, our experimental results revealed that the type of flow pattern is influenced by the vertical positioning of the inlet jet, by the reservoir geometry (short vs long) and, in some cases, by the hydraulic boundary conditions (Froude and friction numbers). When the inlet circular jet is positioned near the reservoir bottom, an unstable flow type (i.e., switching randomly over time) was observed irrespective of the reservoir length and of the hydraulic boundary conditions. The same type of unstable flow pattern was observed for a relatively long reservoir under the lowest Froude number condition, regardless of the vertical positioning of the inlet jet. In all other tested configurations, a steady reattached jet was found, distinguishing an asymmetrical flow with reattached point downstream of the reservoir for short reservoir, and an asymmetrical flow with reattached point upstream of the reservoir for long reservoir. Compared to a free surface inlet channel, an inlet jet boundary condition induces a more three-dimensional flow in the near-field of the inlet. The analysis and comparison of ADVP profiles at different vertical positions and LSPIV profiles indicate that the longitudinal velocity along the vertical axis undergoes variations due to the jet position and the inlet Froude number. The present experimental study is an addition to existing works on the complex hydrodynamics of shallow reservoirs. Further laboratory tests are ongoing, paving the way for further analyses on sediment transport and sediment deposition in such reservoirs, as well as on the feedback of morphodynamic evolution on the flow pattern. The new experimental data presented here are valuable for assessing the performance of 2D and 3D computational models.

Chapter 5. Sedimentation in shallow rectangular reservoirs with circular pressurized inlet boundary

This chapter will be submitted for publication in International Journal of Sediment Research.

5.1. Introduction

Limited research has been published on clear water flow patterns in shallow reservoirs with an inlet circular jet condition (see review in Chapter 2). Asymmetrical, symmetrical stable or pseudo-periodic regimes were identified under certain conditions in inlet jet cases (Adamsson et al., 2005; Dufresne, 2008). In Chapter 4, we presented our experimentally study on the effect of inlet boundary condition on the flow patterns in rectangular reservoirs, considering two configurations: an open channel, and a pressurized flow jet at the inlet; the outlet boundary condition was a free surface channel for both cases. We found that compared to free surface inlet channel, the inlet jet boundary condition induced a more three-dimensional flow in the near-field of the inlet. We also highlighted two flow patterns for the inlet jet case: a steady reattached jet and an unstable flow field varying randomly over time. The type of flow pattern depends on the vertical positioning of the inlet jet, the reservoir geometry (short vs long) and, in some cases, on the hydraulic boundary conditions (i.e., Froude and friction numbers) (see Figure 35). Regarding sedimentation in shallow reservoirs, few experimental studies have been published, and most of them were conducted in rectangular reservoirs, mainly under permanent flow conditions. Table 9 summarizes the existing laboratory experiments, including the hydraulic conditions (inlet Reynolds number R, inlet Froude number F), type, diameter and settling velocity of used materials. These studies used non-cohesive, lightweight, and homogeneous materials of different median diameters, densities and settling velocities. Using crushed olive stones, Stovin and Saul (1994) confirmed that sedimentation pattern in storage chambers with inlet and outlet pipes predominantly depends on the flow field (i.e., bed shear stress distribution), and the distribution of deposited sediment can be predicted from the flow velocity distribution in the reservoir and the values of critical bed shear stress for deposition (0.03~0.04 Pa) and erosion (0.062 Pa). However, values of these critical bed shear stresses are specific for the experimental conditions tested by Stovin and Saul (1994). Using sediment with different grain sizes and densities, Luyckx et al. (1999) proposed trapping efficiency curves in a rectangular chamber equipped with inlet and outlet pipes and a high side weir overflow. The trapping efficiency for a certain sediment fraction was found to depend solely on its settling

velocity, and overall, the trapping efficiency depends on the Froude number at the inlet and the settling velocity to flow velocity ratio in the inlet pipe. Kantoush (2008) conducted suspended sediment experiments in rectangular, lozenge, and hexagon-shaped reservoirs with inlet and outlet open channels and high inlet sediment concentrations. He observed changes in the flow field when the deposit thickness exceeded about 15% of the water depth and proposed empirical relationships to predict the trapping efficiency according to the reservoir shape factor (Kantoush et al., 2008). Nevertheless, the flow pattern was not steady, probably because of the large sediment deposit observed near the inlet that changed the flow direction into the reservoir. Using granular plastic particles, Dufresne et al. (2010a) performed experiments with sediment inflows lower than the transport capacity of the flow at the inlet channel and observed an abrupt increase in the trapping efficiency of the reservoir due to the transition between symmetric to asymmetric flow patterns. According to Camnasio et al. (2013), the flow pattern changes with a deposit height of no more than 10% of the water depth, and the position of the inlet and outlet open channels highly influenced the location of sediment deposits. Camnasio et al. (2013) observed in all tested configurations that the maximum thickness of deposit was along the main jet, because the sediment inlet rate was higher than the transport capacity of the flow in the main jet.

Herein we propose a detailed experimental study of sediment deposition in rectangular shallow reservoirs with a turbulent circular inlet jet and a free surface channel at the outlet. The present study differs from those of Stovin and Saul (1994) and Dufresne et al. (2009) in terms of the type of position of the inlet jet, the outlet condition, shape factor and hydraulic conditions. In addition, different hydraulic conditions and reservoir lengths have been investigated. The outline of the chapter is as follows: in Section 5.2, we describe the experimental setup. In Section 5.3, results are analyzed and discussed, followed by concluding remarks in Section 5.4.

Table 9: Summary of existing laboratory experiments

Authors	Type of basin	Inlet boundary	Outlet boundary	R (10^4)	F	Sediment particles	Median diameter d_{50} (µm)	Density (Kg/m^3)	Settling velocity W_s (m/h)	Inlet concentration (g/l)
Stovin and Saul (1994)		Circular jet	Gate	33.4	0.30	Crushed olive stone	47	2500	1.3	0.25
Luyckx et al. (1999)		Rectangular channel	Weir	-	0.20 -1.00	Bakelite	400 to 2000	1400	70.6 to 131.4	-
Luyckx et al. (1999)				-	0.20 -1.00	Nylon	2000	1050	242.5	-
Kantoush (2008)	Rectangular	Rectangular channel	Rectangular channel	5.6-11.2	0.05-0.10	Crushed nuts	50	1500	3.6	3
Dufresne et al. (2009)		Circular jet	Circular jet +Weir	15 -25	0.04 -0.08	Polystyrol sediment	750	1030	37	-
Dufresne et al. (2010b, 2012)		Rectangular channel	Rectangular channel	21.0 -22.8	0.19 -0.21	Granular plastic	2400	1020	90	0.5
Camnasio et al. (2013)		Rectangular channel	Rectangular channel	11.2	0.1	Crushed walnut shells.	89	1500	3.6	2
Present study		Circular jet	Rectangular channel	5-30	0.13-0.76	Granular plastic	2400	1020	90	1.16-1.98

5.2. Experimental setup and methodology

Following the experimental work presented in Chapter 4 with clear water flow patterns in shallow reservoirs, we used the same laboratory setup to perform twelve (12) experiments with sediment inflow. The glass-made, rectangular reservoir was designed in a 10.4 m long horizontal flume; the reservoir width was B = 0.985 m in all tests, while its length L_1 was changed by solid blocks (Figure 43). The inlet jet water flows through a circular PVC tube, 0.6 m long and 0.04 m in diameter. The pipe was connected to a vertical, moveable plate located at the upstream wall of the reservoir, so that the elevation of the inlet pipe axis above the reservoir bottom Z_{jet} could be adjusted. The outlet boundary was a free surface channel, b_0 = 0.08 m wide and 0.6 m long. The inlet and outlet were on the opposite sides of the reservoir, parallel to the reservoir longitudinal axis. The flow rate was measured with an electromagnetic flowmeter (Siemens Magflow, accuracy of 0.04%). Water level in the reservoir was measured with an ultrasonic probe (microsonic, accuracy of 1%), which was placed at the mid-width of the reservoir and 0.4 m upstream of the reservoir outlet.

Elliptical, granular plastic (Styrolux 656 C) particles, with a density of 1,020 kg/m^3 and a characteristic median diameter d_{50} = 2.4 mm, were used. To avoid flocculation, particles were wetted and subsequently dried prior to each test. The use of granular plastic particles derived from both the feedback of Dufresne et al. (2010a) and our preliminary tests indicating that these particles did not settle in the inlet pipe, while having the potential to settle in the reservoir.

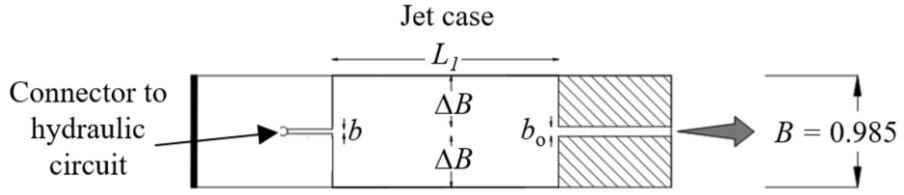

Figure 43: Sketch illustrating the existing experimental setup (not to scale)

Shape factor is defined as SF = $L_1/(\Delta B^{0.6}\ b_0^{0.4})$, with L_1 the reservoir length, b_0 the inlet channel width, and $\Delta B = (B - b_0)/2$. Long and short reservoirs were studied with a SF equal to 8.84 and 4.64, respectively. The inlet flow rate was changed, while keeping the flow depth H in the reservoir set at 0.10 m in all tests, so that the shallowness parameter remained constant (i.e., $H/B \approx 10$). The flow was turbulent as the Reynolds number was between 5×10^4 and 30×10^4; the Froude number was in the range 0.13 - 0.76 and friction number S between 0.14 and 0.21. Two jet positions were tested: at mid-depth (Z_{jet} / H = 0.50) and close to the water surface (Z_{jet} / H = 0.75).

Table 10 summarizes the test program, indicating for each case the corresponding clear water test. The reference inlet particle concentration C_{in} was set at 1.16 g/l based on the material dry weight, but a sensitivity analysis was made by testing a concentration of 1.98 g/l for the long reservoir case. Particles were injected into the inlet pipe carefully: for instance, for inflow discharge Q = 3.0 l/s the total mass of 2500 g was divided into discrete batches of 50 g each injected over 14.4 second per batch. The total period of injection was fixed at 12 minutes for all the cases, following preliminary tests. Shorter injection durations were not sufficient to draw conclusions on the evolution of trapping efficiency. To measure the mean outflow concentration, particles were collected using a net placed in the free jet downstream from the outlet channel each two minutes. The net was systematically replaced to ensure continuity of measurements. Each test had a duration of one hour. Tests 8, 9, 11 and 12 showed a complex sediment transport behavior due to high turbulence, measurements of trapping efficiency over time have been repeated several times, and any discernible trend could be identified, thus only final trapping efficiency was measured for these tests. To assess the measurement uncertainty, Tests 1, 3, and 4 were repeated. The comparison between long and short reservoirs at (S, F) = (0.21, 0.13) is unavailable due to flow instability in the long reservoir cases (see- TEST ID 11 and 17- Table 8, Chapter 4).

Similarly to the experimental procedure for clear water tests (Chapter 4), a 3D velocity profile using ADVP probe, Nortek Vectrino, was performed. For each point, 12,000 instantaneous velocity values were evaluated with a sampling rate of 100 Hz. To improve the quality of the measured data, Glass Microspheres Sphericel 110P8 particles were seeded in the flow. Joint probability density function of velocity fluctuations was calculated in Matlab (v2017b) using 2-D kernel density estimation. Coherent structures were treated using Quadrant analysis. The Panasonic Lumix GH4 camera 1920x1080 pixels at frequency of 25 Hz was used for recording the horizontal evolution of sediment deposits in the reservoir. Videos, treated by the free software Fudaa-LSPIV, were orthorectified to remove perspective-induced distortion, and polylines around the deposit zone were extracted. A Mini-echo-sounder UWS was used for measuring the sediment thickness and total volume of sediment deposited, as recommended by Kantoush (2008). The probe emits an ultrasound impulse, which is reflected by the bottom and then received by the ultrasound sensor. A calibration step validated its use on plastic particles. Multiple reference points with different shapes were manually established. A remarkable precision of ±2 mm was found. Measurements were performed after one hour on a grid covering the entire deposition zone by a step of 0.05 m. The flow rate was gradually decreased while maintaining a constant water depth and flow pattern, thus preventing significant particle movement caused by high velocities. In contrast, a sudden pump shutdown could have led to the generation of waves and hence sediment remobilization.

Table 10: Program of experimental tests. Geometrical, hydraulic and sediment parameters are given. R for repeated test.

	Cases	TEST ID (clear water)	L	SF	Q (m^3/s) (10-4)	U_{in} (m/s)	R (10^4)	F	S	Z_{jet}/H	Particle mass injected (g)	Inlet Concentration C_{in} (g/l)
Long reservoir	1- R	18	2	8.84	17.5	0.44	17.5	0.44	0.14	0.75	2500	1.98
	2	18			17.5	0.44	17.5	0.44	0.16	0.75	1459	1.16
	3 – R	19			30	0.75	30	0.76	0.14	0.75	2500	
	4 - R	12			17.5	0.44	17.5	0.44	0.16	0.5	2500	1.98
	5	12			17.5	0.44	17.5	0.44	0.16	0.5	1459	1.16
	6	13			30	0.75	30	0.76	0.14	0.5	2500	
Short reservoir	7	20	1.05	4.64	5	0.13	5	0.13	0.21	0.75	417	1.16
	8	21			17.5	0.44	17.5	0.44	0.16	0.75	1459	
	9	22			30	0.75	30	0.76	0.14	0.75	2500	
	10	14			5	0.13	5	0.13	0.21	0.5	417	
	11	15			17.5	0.44	17.5	0.44	0.16	0.5	1459	
	12	16			30	0.75	30	0.76	0.14	0.5	2500	

5.3. Results and discussion

5.3.1. General overview

Except Tests 3 and 4, all other configurations showed a steady regime, and no significant time-dependence of the mean flow patterns was observed as sediments were introduced in the setup and deposits accumulated in the reservoir. In these steady-state tests, locations of sediment deposits were almost the same, and maximum deposit thickness can reach up to 64% of flow depth for long basins and 28% of the flow depth for short basins. This contrasts with findings in the literature, where a possible change in flow pattern was reported to occur at a threshold of 10% to 15% of the water depth, particularly in studies by Kantoush (2008) and Camnasio et al. (2013). This can be primarily attributed to different test conditions and, most importantly, to the fact that in the current experiments, deposits did not form in the main jet axis but rather in the center of recirculation zones, resulting in less influence of the deposits on the main jet.

Tests 3 and 4 with clear water (i.e., Tests 19 and 12, respectively, in Chapter 4) showed a stable regime characterized by a primary recirculation with a reattachment point. However, upon introducing sediment injection, an unsteady regime was observed within a span of two minutes, the flow pattern moved from one reattachment point on the left sidewall of the reservoir to another one on the right sidewall, with a transition involving a jet approximately aligned with the reservoir centerline (Figure 44). After this unsteady episode, the flow returned to a quasi-stationary state. Tests 3 and 4 were retested, and the shift of the left-to-right jet did not occur during the 3-R and 4-R tests, demonstrating that the experiment is highly sensitive to even slight disturbances in main flow caused by the presence of the sediment deposit.

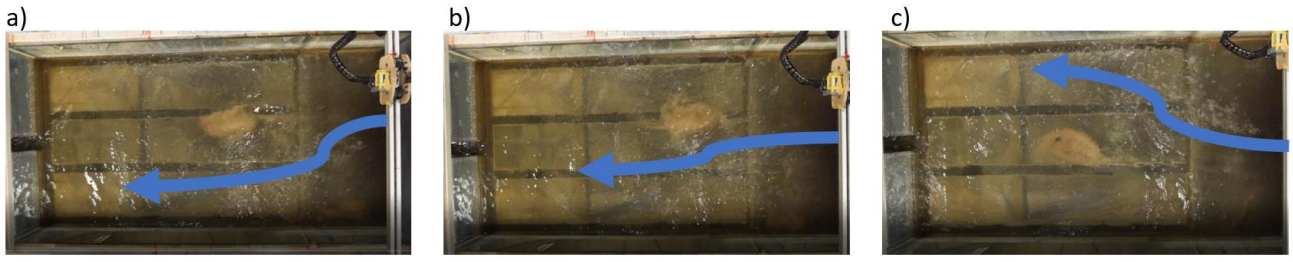

Figure 44 : Case 4 - Flow pattern changes over time at t =25 min (a), t =25.4 min (b) and t =26.5 min (c)

5.3.2. Trapping efficiency

The trapping efficiency indicates the ability of the reservoir to cause deposition of the inflowing sediments. Using the collected material mass at the outlet, the concentration C_{out} was calculated, and the trapping efficiency time-evolution was deduced as $100\times(C_{in}-C_{out})/C_{in}$. The main findings are shown in Figure 45:

- Cases 1, 3, and 4 were repeated to assess the uncertainty of the results. The average differences are 3%, 5.6%, and 5.4%, respectively, with standard deviations of 1.9%, 3.9%, and 3.2%, respectively. Overall, the average error for these experiments is 4.7%.
- A decrease in trapping efficiency was observed for all cases between t = 2 min and 4 min.
- Trapping efficiency in Cases 7 and 10, as displayed in Figure 45, is higher than in all other cases. These two tests were conducted in the long reservoir, with a low inflow discharge.
- High flowrates led to a lower trapping efficiency, as can be seen by comparing Cases 2 and 3, as well as Cases 5 and 6. Comparisons revealed an average difference of 20% (with a standard deviation of 6.5%) between Cases 2 and 3, and a 9% decrease in the trapping efficiency (with a standard deviation of 3.67%) between Cases 5 and 6.
- Concentration has a significant impact on the results. Higher concentrations decrease the trapping efficiency. An average difference of 10.5% (with a standard deviation of 3%) was observed when comparing Cases 1 and 2. A difference of 11.5% (with a standard deviation of 4.3%) was observed when comparing Cases 4 and 5.
- The jet position generally has a slight effect on the results, except for the highest tested flow rate. A higher trapping efficiency was observed for the jet located at Zjet/H = 0.50. This result was substantial only for the higher flow rate. In this case, an average difference of 12% (with a standard deviation of 5%) was found when comparing Cases 3 and 6. The difference was less significant for configurations with lower flow rates (i.e., Cases 2 and 5), for which an average difference of 1% with a deviation of 0.7% is observed.

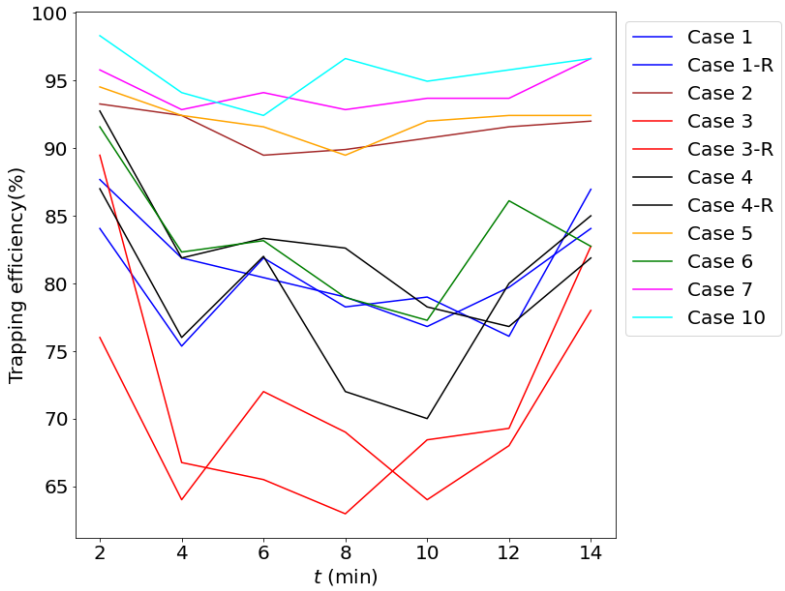

Figure 45: Evolution of trapping efficiency during injection time

In each test, the final deposition mass after 1h was dried during 72h and then weighted. The final trapping efficiency is calculated as the ratio between the deposited mass in the reservoir to the total entering sediment mass (Figure 46). This indicator allows us to compare the different configurations and classify them in terms of trapping efficiency. For long reservoirs, analysis of videos after the injection phase revealed that the injected sediment remained trapped in the eddy zone without reaching the outlet channel. The long reservoir Case 2 was repeated over a duration of 12h instead of 1h, and results showed that the amount of sediment reaching the outlet only represented 8% of the mass deposited after 1h. We conclude that at certain moment and because of the eddy intensity, trapped sediment cannot get out of the eddies. On the hand, comparing Cases 1 and 1-R shows a slight difference in terms of percentage (2%), which provides confidence in the subsequent results. Cases 3 and 4 show a more significant difference of approximately 8% and 11% in terms of final trapping efficiency, which may be attributed to the previously discussed unsteady episode.

A comparison between the long and short reservoirs with the same friction factor and Froude number and jet position (S, F, Z_{jet}/H) showed that the long reservoir (SF = 8.84) presents more interesting trapping characteristics than the short reservoir (SF = 4.64). Results agree with the conclusions of Dufresne et al., (2012) who found that the sediment deposition is minimized in reservoirs with SF<6.2 and maximized for SF>6.8. However, this study contributes to extending these findings because the three rectangular reservoirs examined by Dufresne et al. (2012) did not account for the influence of hydraulic parameters or boundary conditions. Additionally, unlike

the short reservoir configurations characterized by symmetrical patterns studied by Dufresne et al. (2012), the current configurations exhibit an asymmetry in flow patterns. The short reservoir Cases 8 and 11 (i.e., (S,F) = (0.16, 0.44)), and Cases 9 and 12 (i.e., (S,F) = (0.14,0.76)), showed significant low trapping capacity irrespective of the inlet jet position. For those cases, the main and secondary eddies interact with the main jet, which cause the transport of trapped particles to the reservoir outlet. The results reveal a slight impact of the jet position on the trapping capacity (e.g., Cases 1 and 4, Cases 2 and 5, Cases 7 and 10). However, the difference is very subtle, and due to the uncertainty in the measurements, no definitive conclusions can be drawn. Nevertheless, the influence of hydraulic conditions remains significant for the final trapping capacity: experiments with high flow rates, (S, F) = (0.14, 0.76) (i.e., Cases 3, 5, 6, and 12), exhibit a lower trapping capacity. This is particularly evident in long reservoir tests: for example, the trapping efficiency is 33.5/ lower in Case 3 compared to Case 2 ((S, F) = (0.16, 0.44), and is 38% lower in Case 6 compares to Case 5 ((S, F) = (0.16, 0.44)).

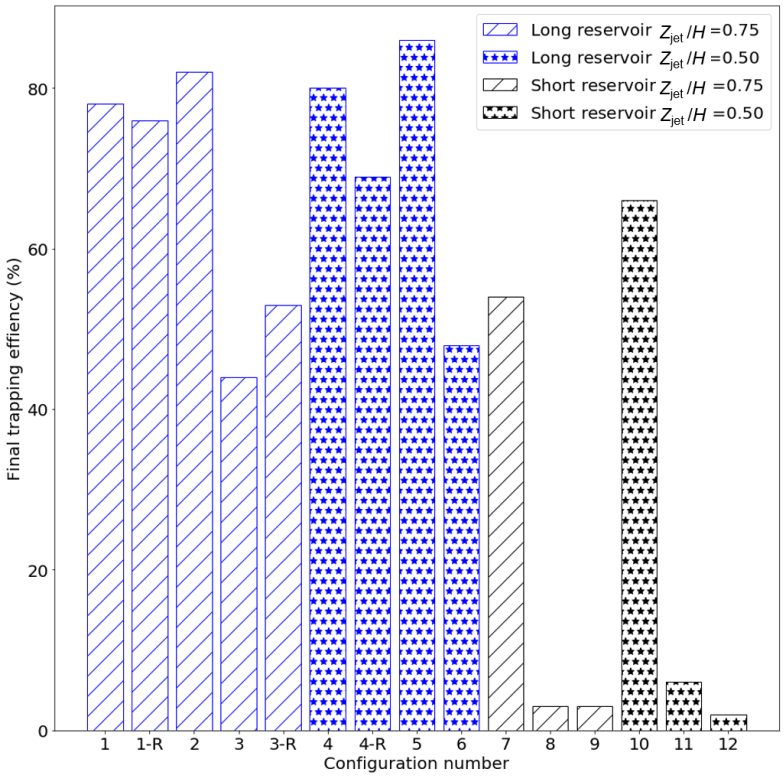

Figure 46: Final trapping efficiency

5.3.3. Horizontal and vertical evolution of sediment deposit

Images taken from a camera positioned above the flume were used to analyze the evolution of the sediment deposits extent (see examples of images in Appendix L). A continuous motion of sediments was observed during the whole duration of the tests, essentially due to the presence of unsteadiness in the jet as well as the presence of coherent structures. Nonetheless, the sediment deposition area generally remains unaltered. Results during the injection period are presented in Figure 47, showing the temporal evolution of the deposit area. The results from all tests indicate a progressive increase in the area over the injection time. Nevertheless, certain deviations from this trend become apparent after six minutes. For instance, in Case 3, characterized by the highest Froude number and lowest Friction number, fluctuations are observed between the sixth and twelfth minutes. A drop in the horizontal extent of sediment deposits does not necessarily imply a decrease in the amount of trapped sediment but could be explained by an increase in the vertical thickness of the deposits and a reduction in its horizontal spread. Indeed, the sediment trapping efficiency curves presented earlier maintain a relatively stable trend throughout the duration of the injection.

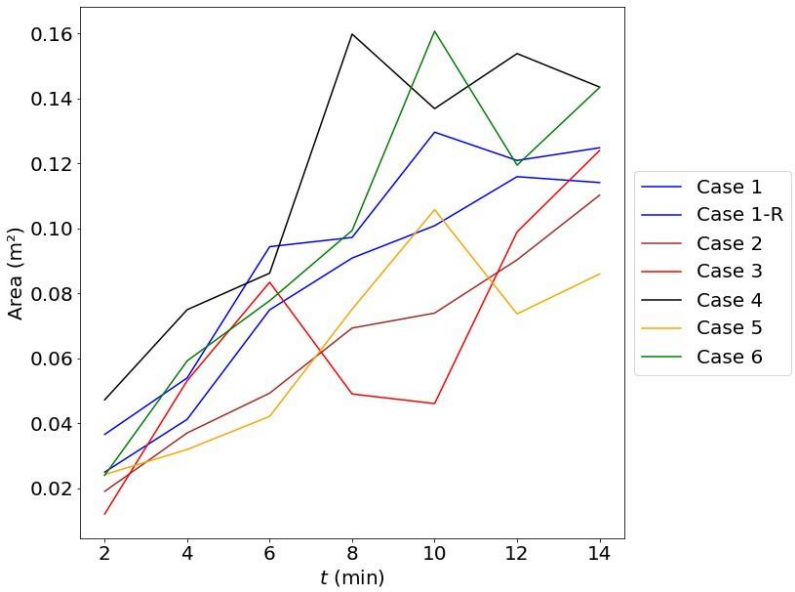

Figure 47: Evolution of horizontal area during injection time

Regarding the post-injection phase, images taken every 10 minutes (between 20 and 60 minutes from the beginning of the test) reveal that the deposition areas are consistent with those described during the injection phase: they remain located at the center of the eddies (Figure 48: Description of horizontal deposition area for long (Case 1) and short (Cases 7 and 10) reservoirs). Cases 1

and 1-R demonstrate that the deposition areas remain consistent over time, maintaining an oval shape. Variations in deposition areas for long reservoirs were more significant for high flow rate, i.e., Cases 3 and 6 (Appendix A) corresponding to (S, F) = (0.14, 0.76). Higher Reynolds numbers lead to increased turbulence, resulting in more coherent structures and higher bed shear stress, thus enhancing the transport capacity. For short reservoirs, variations in deposit areas along the horizontal axis are more pronounced compared to long reservoirs. These results are particularly observed in Cases 7 and 10, which correspond to the lowest flow rate with (S, F) = (0.21, 0.13). Video analysis was not feasible for short reservoir Cases 8, 9, 11, and 12 under much higher flow rates (i.e., (S, F) = (0.16, 0.44) and(S, F) = (0.14, 0.76)), owing to the highly turbulent character of the flow and its influence on sediment motion.

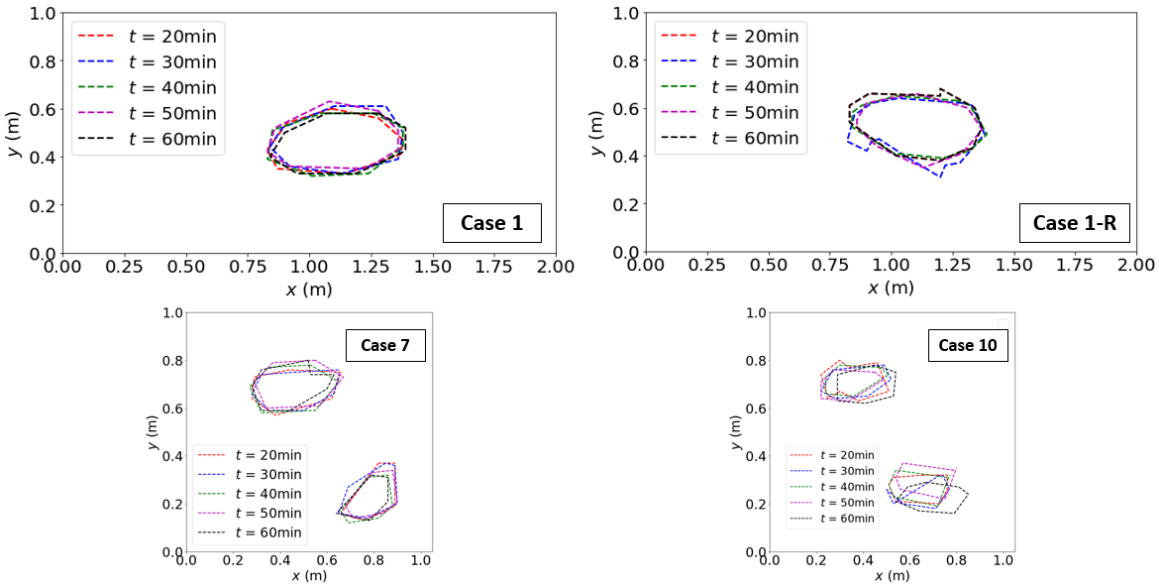

Figure 48: Description of horizontal deposition area for long (Case 1) and short (Cases 7 and 10) reservoirs

Mean values and standard deviation of deposition areas for selected long and short reservoir tests are presented in Figure 49. Standard deviation remains similar for all cases, while mean values show important variability from a case to another. Results for short reservoirs and variation of barycenter of the deposit area for all cases are presented in Appendix A. It is found that barycenter remains located at the core of principal recirculation with negligible variability for long reservoir cases and more important variability for two short reservoir tests.

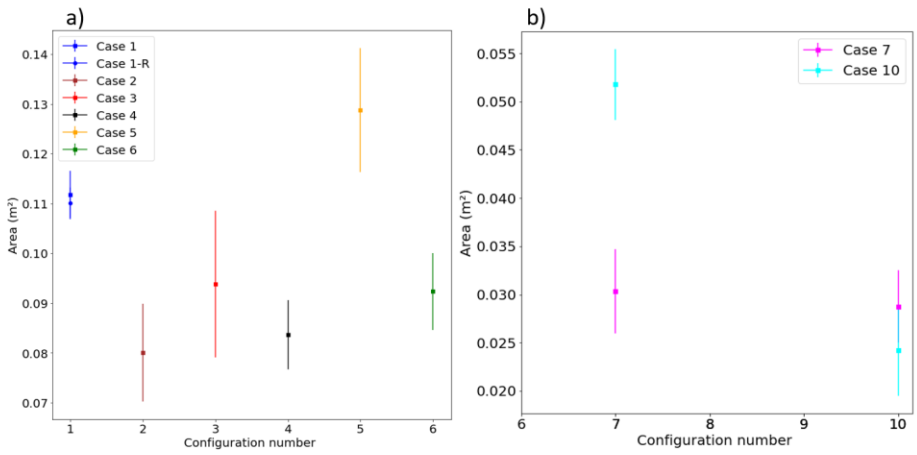

Figure 49 : Mean and standard deviation of horizontal areas for long (a) and short (b) reservoirs.

It was also observed that the thickness of the deposit changes with time due the presence of coherent structures. Deposition zones remain at the same areas but could become flatter (e.g., t = 20 min), or more concentrated with a higher peak elevation (e.g., t = 10 min) compared to other instants, as illustrated for Case 3 in Figure 50. As mentioned for the horizontal evolution, the variability changes from one configuration to another.

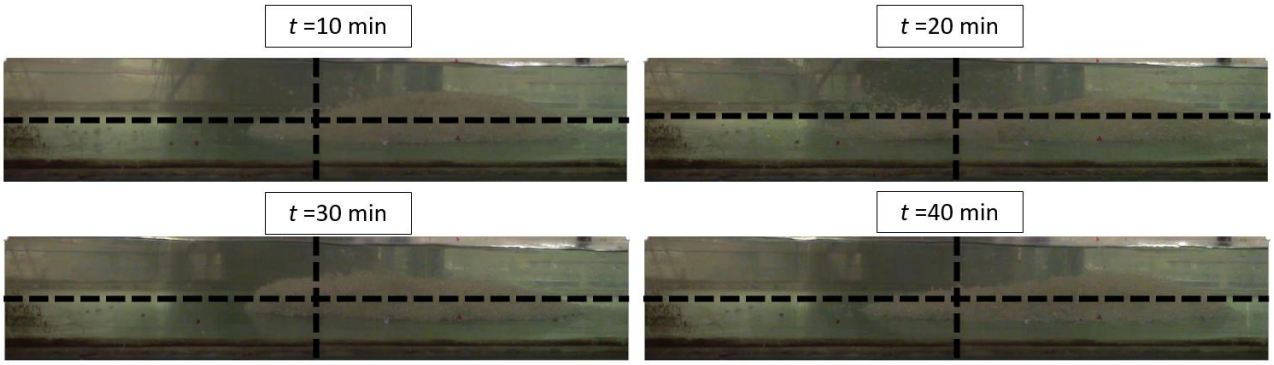

Figure 50: Case 3 -Vertical view of deposition over time

The thickness of the deposits s, as determined through UWS measurements, reveals a consistent 'bump' shape in all cases. In Case 1, there is a distinct peak thickness at the center, which gradually decreases toward the periphery of the “bump”. Notably, the thickness can reach values as high as 0.064 m (Figure 51), corresponding to a high s/H ratio of 64%. Further analysis demonstrates that the thickness of the deposits is more significant in configurations with higher concentration, specifically Cases 1 and 4. Conversely, configurations characterized by low flow conditions (i.e., (S, F) = (0.21, 0.13)) and a low concentration (i.e., 1.16 g/l) exhibit comparatively

weak deposit intensities, with *s*/*H* ratios not exceeding 40%. Cases 1-R, 2, and 5 show similar sediment deposit behavior as presented in Appendix B.

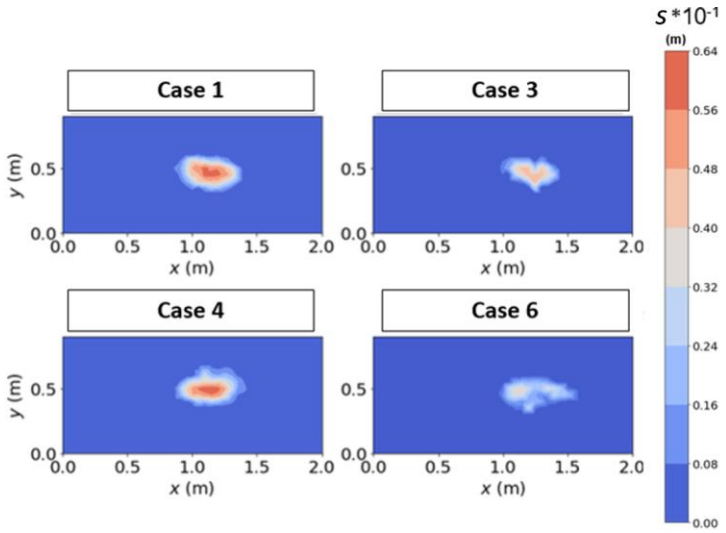

Figure 51: Thickness of sediment deposits after 1 h for long reservoir cases

5.3.4. Bursting phenomena:

In accordance with the definitions provided by Kline (1967) and Nezu and Nakagawa (1993), the turbulent eddies that exhibit burst-like behavior tend to manifest randomly in both space and time near the bottom. Nevertheless, their actions exhibit an organized and coherent nature, characterized by a cyclic sequence of ejections and sweeps. Analysis of our videos for tests showed the extensive presence of coherent structures and bursting phenomena (Figure 52).

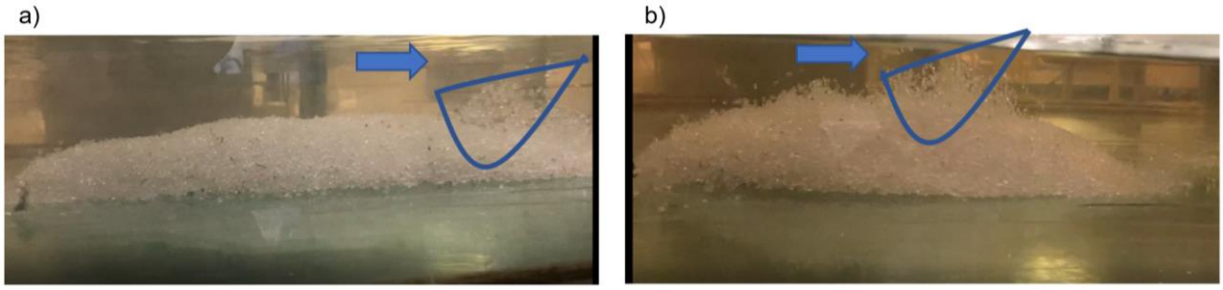

Figure 52: Case 6 -Coherent structures and bursting phenomena at t = 724 s(a) and t = 840 s (b). The arrow indicates the direction of flow, and the closed contours indicate the presence of bursts

Model of bursting process were described by Theodorsen (1955) through Horseshop-hairpin model or a conceptual model of cyclic bursting by Wallace (1985). Nezu and Nakagawa (1993) give an overview about bursting phenomena and the role they play on sediment transport process (erosion, deposition, transport). Practical techniques based on statistical tools allow a good

description of the phenomena (Nezu and Nakagawa, 1993). Quadrant analysis of Reynolds shear stress stands out as one of the most used tools on this subject (for details, reader may refer to Wallace (2010)). The analysis allowed estimating the fractional contributions of the Reynolds stress tensor to the -<*u*'*w*'> component from bursting events. It consists of four quadrant namely Q_1(*i*=1; *u*'>0, *w*'>0), Q_2(*i*=2; *u*'<0, *w*'>0), Q_3(*i*=3; *u*'<0, *w*'<0) and Q_4 (*i*=4; *u*'>0, *w*'<0). Q_1 and Q_3, named ejections and sweep events, respectively, are related to energy dissipation. Q_3 and Q_4, named outward and inward correlations, respectively, are related to energy production. To distinguish weak and strong events from Reynolds shear stress, a threshold value named the "hole" H_o is bounded by the curve $|u'v'| = H_o(\langle u'u'\rangle)^{0.5}(\langle v'v'\rangle)^{0.5})$. The hole size $H_o = 0$ means that all data pairs (*u*', w') are considered. The shear stress fraction distribution is defined as $S^f_{i,H0} = \langle u'v'\rangle_{i,H0}/\langle(u'v')\rangle$. To calculte the shear stress fractional contribution per quadrant, a detection function is involved with $I_{i,Ho}(u',v') = \{1, \text{ if } |u'v'| \geq H_o(\langle u'u'\rangle)^{0.5}(\langle v'v'\rangle)^{0.5}\}$; and 0 otherwise}. The contribution of each quadrant $\langle u'v'\rangle_{i,Ho}$ is calculated as a function of $I_{i,Ho}(u',v')$. The choice of H_o, number *N* of total bursting events and number *n* of instantaneous bursting events is defined as follow:

$$\langle u'v'\rangle_{i,Ho} = \sum_{n=1}^{N} u'(n)v'(n)\ I_{i,Ho}(u',v')$$

Cellino and Lemmin (2004) studied the effect of coherent structures on sediment transport in an open channel flow through measurements with clear water and with sediment laden and showed that a study with clear water is sufficient to draw conclusions about the burst-cycle. Following Cellino and Lemmin (2004), we opted for clear water measurements, which allows a better data quality of acoustic doppler technique. The hole H_o was set at zero. Figure 53 illustrates the joint PDFs for *u*' and *w*' for four points from Case 6. Those points, selected along the jet direction, are located far from the boundary layer and between 1.0 m and 1.7 from the jet origin. Joint PDFs shows an elliptical or circular shape which relates to isotropic characteristics of turbulence. Analysis made for points near the bottom shows different behavior, where an anisotropy of turbulence is found (Appendix C).

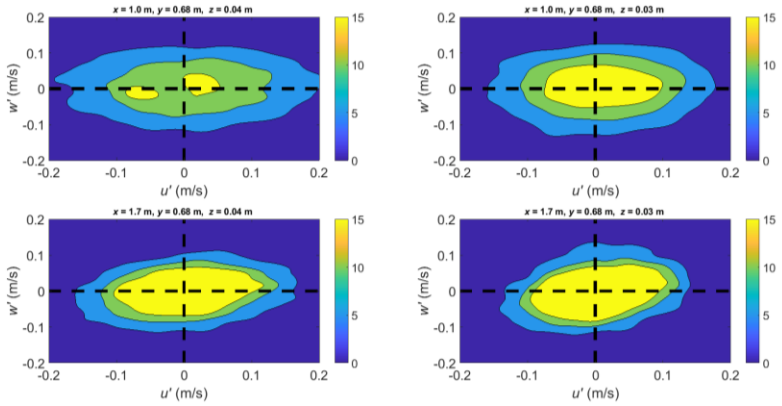

Figure 53: Case 6 - Joint probability density function of fluctuations (u',w') for four points (x, y, z).

The contribution of each quadrant with respect to the total shear stress is calculated for long reservoirs with the following four points (*x*, *y*, *z*) (1.0, 0.68, 0.04), (1.0, 0.68, 0.03), (1.7, 0.68, 0.04), and (1.7, 0.68, 0.03) (Table 11) and for short reservoir with the four points (*x*, *y*, *z*) (0.50, 0.68, 0.04), (0.50, 0.68, 0.03), (0.89, 0.68, 0.04), and (0.89, 0.68, 0.03) (see Appendix C). For Z_{jet}/H =0.75 (Cases 1, 2 and 3), similar results are found in terms of quadrant percentage, with Q_1 and Q_3 representing around 60% of the total Reynolds shear stress. Q_1 and Q_3 contribute to a negative distribution of Reynolds shear stress, resulting in energy dissipation. For Cases 4, 5 and 6, quadrants Q_1, Q_2, Q_3, and Q_4 are all nearly equal to 25%, which suggests that sediment transport is evenly distributed among the four quadrants, with each quadrant contributing equally to the overall distribution. This observation may indicate a degree of regularity or symmetry in the sediment transport pattern.

Table 11: Occurrence probability of each quadrant for long reservoir tests at a: (1.0, 0.68, 0.04), b): (1.0 , 0.68, 0.03), c: (1.7, 0.68, 0.04), and d: (1.7, 0.68, 0.03)

	Cases 1 and 2				Cass 3				Cases 4 and 5				Case 6			
(%)	a	b	c	d	a	b	c	d	a	b	c	d	a	b	c	d
Q1	26.4	23.8	30.7	30.2	27.3	27.1	28.1	29.0	24.3	27.2	26.6	26.7	24.6	27.9	27.9	26.2
Q2	24.0	24.2	20.2	19.7	23.4	24.5	21.7	20.7	24.6	23.9	23.1	22.2	25.3	23.1	29.4	23.6
Q3	25.1	27.7	29.3	31.0	25.8	24.0	28.4	29.5	26.5	25.3	26.5	26.7	26.9	25.5	21.2	26.2
Q4	24.4	24.3	19.8	19.1	23.5	24.3	21.8	20.9	24.6	23.7	23.9	24.3	23.2	23.5	21.5	23.9

5.3.5. Conclusions

Flow patterns and sedimentation in rectangular shallow reservoirs, with circular inlet jet and free surface channel at the outlet, were analyzed using laboratory experiments. Twelve experimental tests were performed, in which the reservoir length, the hydraulic conditions, the vertical position of the inlet jet (mid-depth or near surface), and the inlet sediment concentration were varied. Overall, the deposition zone tends to be located at the center of the large flow recirculations for all the configurations. Long reservoirs demonstrate higher trapping efficiency compared to shorter ones, supporting previous findings by Dufresne et al. (2012) using free surface channel at the inlet. The flow rate noticeably affects trapping efficiency in both long and short reservoirs. It is observed that high flowrate (high Froude number and low friction number S) decreases the trapping efficiency. The horizontal surface of the deposition area evolves during the injection period and varies from a configuration to another, although the standard deviation of this time evolution remains barely important. Notably, the calculation of the barycenter of the deposition zone consistently aligns across all configurations for long reservoirs. Despite the high thickness of the deposits reaching 64% of the flow depth, the sediment deposit does not affect the flow typologies because it is not located in the main direction of the jet. Concerning the bursting phenomena, the joint probability density functions (PDFs) exhibit an elliptical or circular shape, indicating the isotropic nature of turbulence. The data obtained from the present sturdy can be employed to assess the ability of a hydro-sedimentary numerical model to reproduce the sediment transport in shallow reservoirs at laboratory scale.

Perspectives of this study are numerous: a 3D description of the evolution of sediment deposition in space and time which will allow a better appraisal of sediment transport process. Also, evaluating the influence of various factors such as geometrical shapes, boundary condition types and positions, and sediment characteristics is needed. A much longer injection time and higher concentration will allow extending the current results by involving more substantial morphodynamic changes in the reservoir. Meandering, bi-stable and unstable flow patterns should also be studied.

Chapter 6. Numerical modeling of laboratory experiments

After several attempts, we were unable to validate TELEMAC-3D with the new 3D experiments of a pressurized inlet jet. TELEMAC-3D simulations have intrinsic limitations in accurately representing inlet boundary conditions of a circular jet type. Due to time constraints, we decided to use code_saturne. This numerical model was applied to selected experimental tests performed. The aim of the numerical modeling is to assess the performance of the code and particularly its turbulence models. The following experimental tests with clear water and using inlet jet condition were simulated:

- Test 9: short reservoir, L_1 = 1.05 m, H =0.100 m, Z_{jet}/H = 0.20, Q = 0.0175 m^3/s;
- Test 12: long reservoir, L_1 = 2.00 m, H =0.100 m, Z_{jet}/H = 0.50, Q = 0.0175 m^3/s;
- Test 15: short reservoir, L_1 = 1.05 m, H =0.100 m, Z_{jet}/H = 0.50, Q = 0.0175 m^3/s;
- Test 29: short reservoir, L_1 = 1.05 m, H =0.200 m, Z_{jet}/H = 0.10, Q = 0.0175 m^3/s.

The simulation of Test 9 focused on identifying and characterizing an unstable flow regime. The simulations of Tests 12 and 15 aimed at replicating steady-state conditions, referred to as A1 and A1*, respectively. Meanwhile, simulation of Test 29 aimed at accurately modeling and depicting the flow pattern known as 'Back flow' (BF).

For each test, three high Reynolds number turbulence models (Standard K-ε, Linear K-ε, Rij-ε SSG) and four low Reynolds number models (Spalart-Allmaras, Bl-v2/k, K-w SST, Rij-ε EBRSM) have been tested. Computed flow patterns at the surface as well as longitudinal and transversal profiles of velocity at different vertical positions were compared to measurements for Test 15. Furthermore, an exploratory simulation with Large Eddy Simulation (LES) using the Smagorinsky model was carried out for Test 15.

6.1. Reminder of observed patterns

Before going into the details of numerical simulations, the flow patterns identified experimentally (Chapter 4) are reminded herein (Figure 54):

- Test 9 is a short reservoir where an unstable flow pattern was observed. In the initial two minutes, the flow directed itself toward the left wall, and two primary patterns became apparent, with their sizes evolving over time. After running the test for one hour, the jet

shifted its direction toward the right side. The transitions between these two states did not follow a regular pattern. Additionally, intermediate states were noted during this test;

- Test 12 is a long reservoir with a steady asymmetric flow pattern (A1) characterized by one main recirculation and small eddies in the upper part of the reservoir;

- Test 15 is a short reservoir case with an asymmetric flow patter (A1*) consisting of one main recirculation, along with a secondary one;

- Test 29 is a short reservoir where a jet remains localized at the bottom with the presence of surface Back Flow (BF) return currents emerging at the outlet channel.

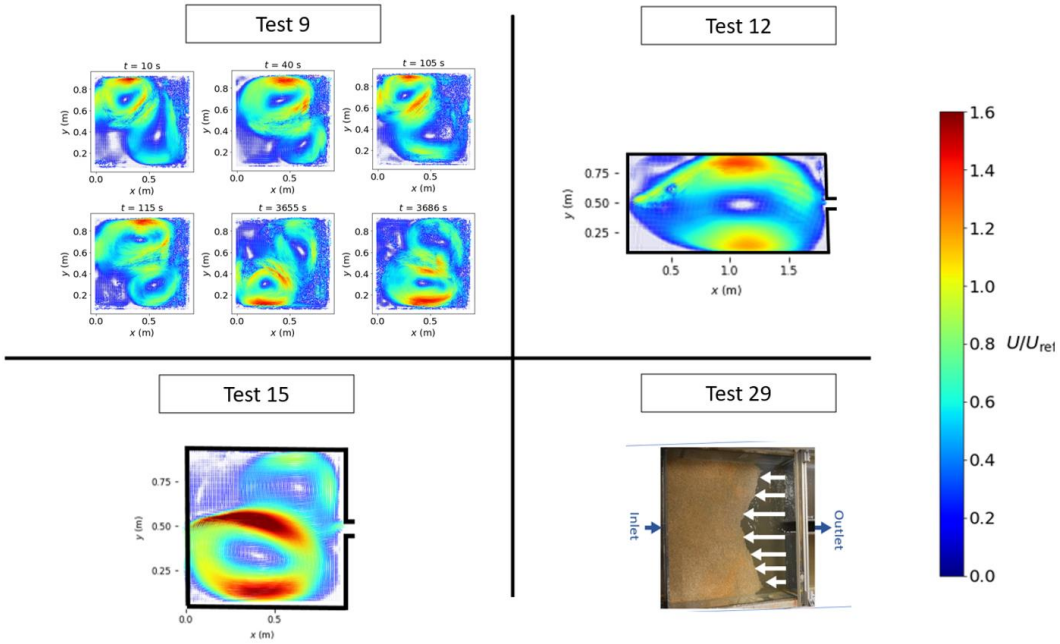

Figure 54*: Experimental flow patterns at free surface for Tests 9, 12, 15* and 29

6.2. Mesh choice

Creating an appropriate mesh for the present geometry posed challenges, as both the inlet jet pipe and reservoir required different meshing approaches. A preliminary study was conducted to select the appropriate mesh type, including polyhedral, Cartesian, and tetrahedral meshes. However, extruding a prism in the present case with a tetrahedral mesh proved to be complex in the mesh module of SALOME (SMESH User Guide) and code_saturne. Ansys Mesh Student Version was used to generate the required mesh. The attempt to create a structured hexahedral mesh for the reservoir did not yield satisfactory outcomes, even when experimenting with prism

extrusion. On the contrary, using an extruded tetrahedral mesh transformed into prisms improved the results. An illustrative representation of those meshes for three configurations is provided in Figures 55-57. It is noteworthy that the mesh type remains similar across the four tested cases. However, variations in mesh density and the y+ parameter were introduced to accommodate the specific characteristics of each case, as detailed in Table 12.

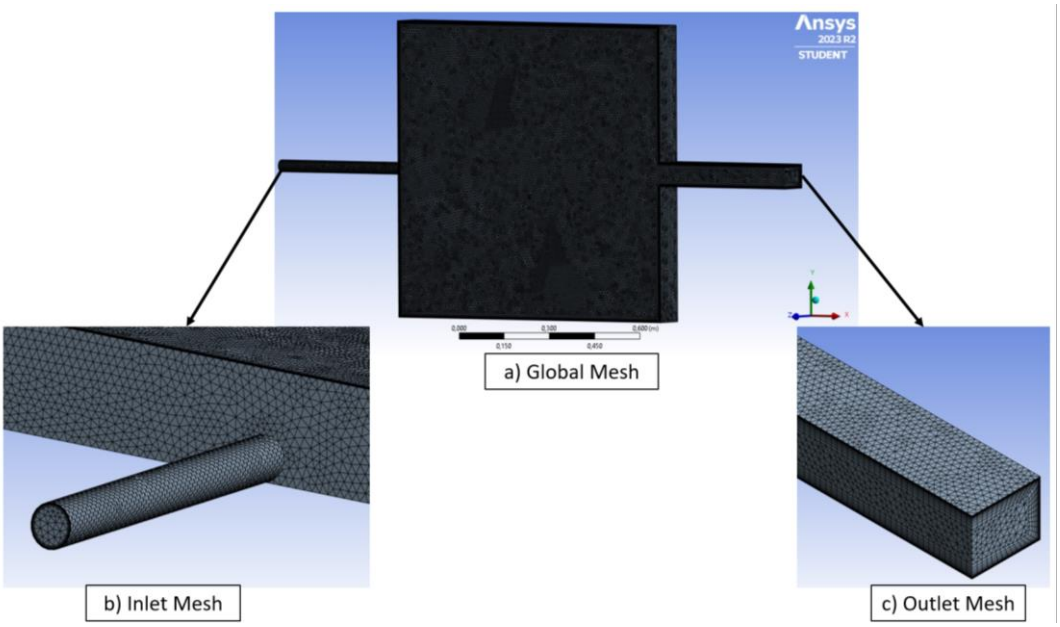

Figure 55: Example of a tetrahedral mesh extruded into prism for short reservoir with $Z_{jet}/H = 0.20$ (Test 9)

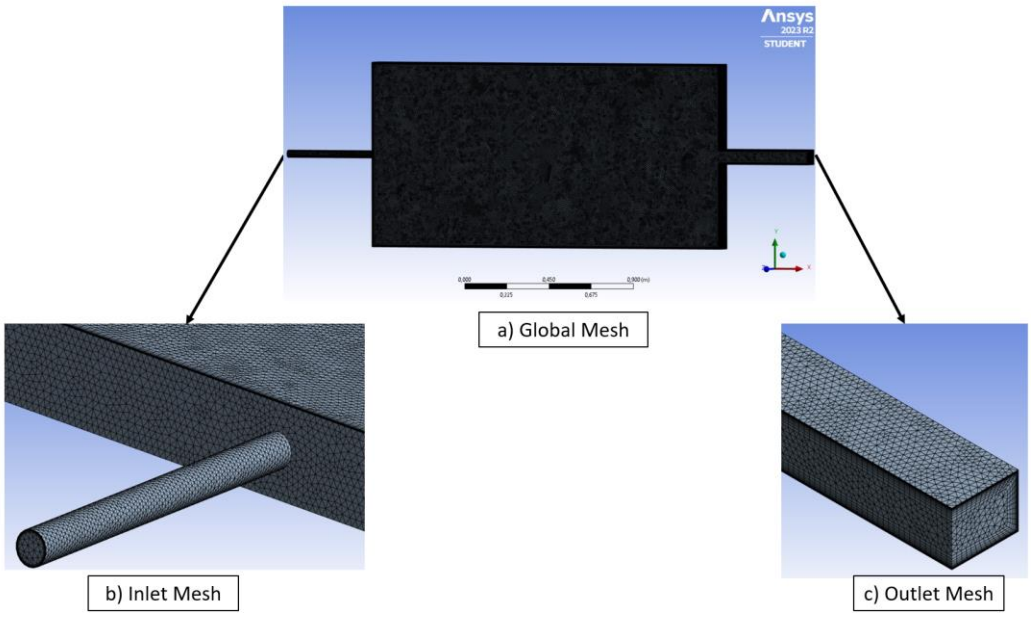

Figure 56: Example of a tetrahedral mesh extruded into prism for short reservoir with $Z_{jet}/H = 0.50$ (Test 12)

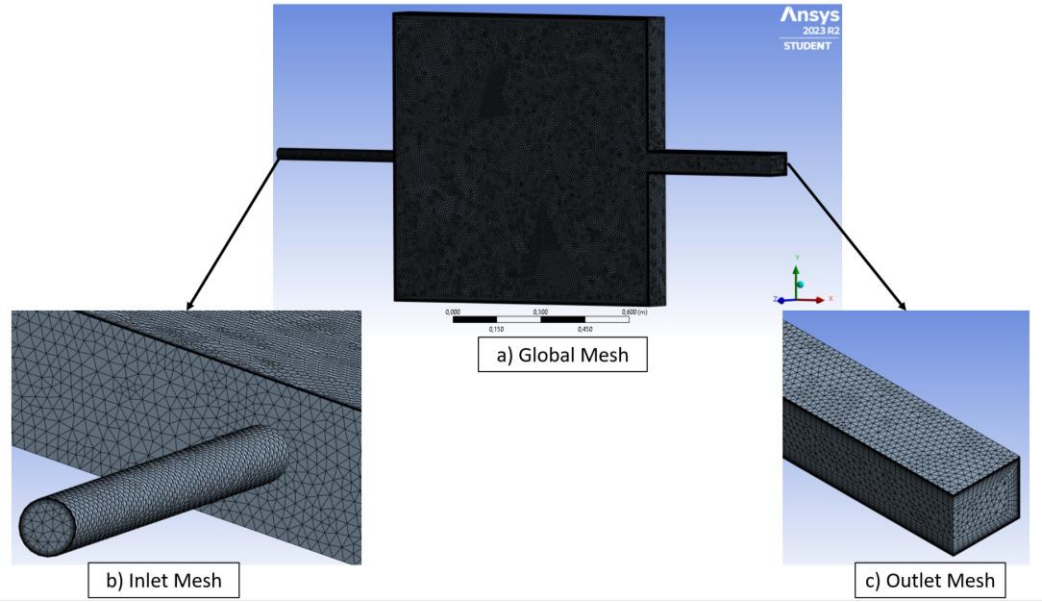

Figure 57: Example of a tetrahedral mesh extruded into prism for short reservoir with $Z_{jet}/H = 0.5$ (Test 15)

6.3. Numerical setup

For all configurations, an inlet flow Q = 0.00175 m³/s was imposed, with a Reynolds number at the jet inlet set to R = 139,331. The outlet boundary condition was specified as open boundary with pressure outlet, while a symmetric condition was applied to the fluid free surface. The simulation adopted a standard Eulerian single-phase model. The fluid is considered incompressible. The second-order centered convection scheme is employed for solving advection step for velocity and for turbulent quantities. The reconstruction of velocity gradients utilized the least square method, and the option for extended neighbor connectivity across all vertices was activated. The velocity-pressure resolution is a SIMPLEC predictor/corrector with a Rhie & Chow filter, as the variables are all co-located in space (as described in code_Saturne v8.0 Theory Guide). The total duration of the simulation was 300 seconds for steady-flow pattern cases (Tests 9, 12 and 29) and 210 seconds for the unstable case (Test 9). For the steady-state cases, velocity fields were averaged starting from the 150 seconds. For all the simulation a CFL < 1.0 in the reservoir was fulfilled.

Table 12 provides a summary of the key features of the tested configurations, by rearranging configurations into two categories: short *vs* long reservoirs. For the short reservoirs, a first series of numerical simulations aimed to assess the code ability to replicate steady-state asymmetric flow pattern A1* corresponding to Test 15. To achieve this, mesh convergence was performed using the Rij-ε EBRSM model. Subsequently, an analysis of different high and low Reynolds

models was carried out. Finally, an exploration with LES and the Smagorinsky model was conducted for Test 15. Tests 9 and 29, representing an unstable patten and a back flow pattern, respectively, were also modeled using both low and high Reynolds turbulence models. Additional tests to explore transition between stable and unstable flow were conducted by reducing the water depth H to 0.095 m. For the long basin Test 12, representing a flow pattern of type A1, numerical simulations were done both with low and high Reynolds turbulence models.

Table 12: Summary of numerical simulations and turbulence models used. Observed flow patterns are also reminded. A1 or A1 for reattached jet in the reservoir, U for unstable jet, and BF for backflow configuration.*

	TEST ID (clear water)	Num. Run	Z_{jet}/H	H (m)	Exp. flow pattern	y+	Mesh number (Millions)	Turbulence models
Short reservoirs	15	1 (mesh convergence)	0.50	0.100	A1*	0.5/1.0	14/2.4	Rij-ε EBRSM
		2				31.0	1.7	K-ε Standard / K-ε Linear production / Rij-ε SSG
		3				1.0	2.4	K-w SST/ BL-v2/k / Spalart- Allmaras / Rij-ε EBRSM
		4	0.50	0.100		0.5	14	LES - Smagorinsky Model
	29	5	0.10	0.200	BF	31.0	2.2	K-ε Standard / K-ε Linear production / Rij-ε SSG
		6				1.0	3.5	K-w SST/ BL-v2/k / Spalart- Allmaras / Rij-ε EBRSM
	9	7	0.20	0.100	U	31.0	1.7	K-ε Standard / K-ε Linear production / Rij-ε SSG
		8				1.0	2.4	K-w SST/ BL-v2/k / Spalart- Allmaras / Rij-ε EBRSM
	9-bis	9	0.21	**0.095**	U	31.0	1.5	K-ε Standard / K-ε Linear production / Rij-ε SSG
		10				1.0	2.3	K-w SST/ BL-v2/k / Spalart- Allmaras / Rij-ε EBRSM
Long reservoir	12	11	0.50	0.100	A1	31.0	2.4	K-ε Standard / K-ε Linear production / Rij-ε SSG
		12				1.0	3.8	K-w SST/ BL-v2/k / Spalart- Allmaras / Rij-ε EBRSM

6.4. Mesh sensitivity

A mesh sensitivity analysis was conducted for Test 15 using the Rij-ε EBRSM model, and the results were compared to a steady-state regime. Two numerical runs were performed, one with y+ = 1 and one with y+ = 0.5. Figure 58 presents the computed and measured flow patterns, indicating that the mesh criteria have a minor impact on the flow pattern (i.e., A1*). When compared to experimental results, the velocity near the wall, the size of the secondary pattern, and the jet width are better represented for y+ = 0.5. Also, the longitudinal and transverse velocity profiles extracted at x = 0.50 m and z = 0.050 m reveal slightly improved results for y+ = 0.5 (Figure 59). The RMSE between computed and measured velocities u are 0.074 and 0.076 m/s for y+ = 0.5 and y+ = 1, respectively. For transverse velocity v, values of 0.038 and 0.043 m/s are obtained for y+ = 0.5 and y+ = 1, respectively. For the remainder of the study, and due to mesh size constraints, we decided to maintain y+ = 1 for all low Reynolds turbulence models simulations.

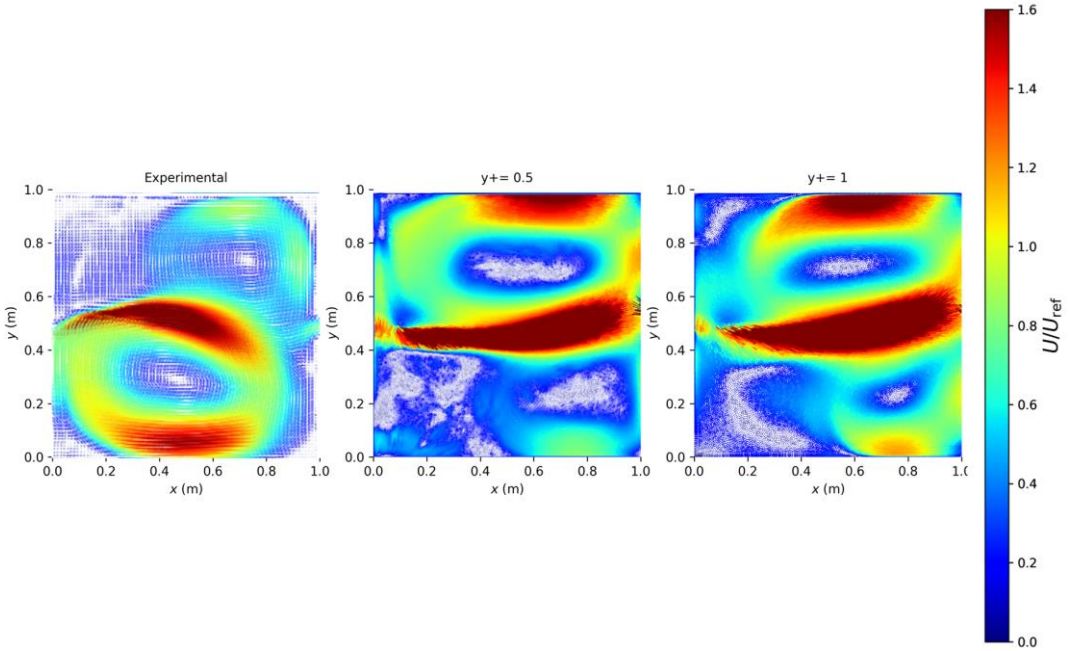

Figure 58: Test 15 -Run 1. Comparison of experimental and computed flow fields at the surface using EBRSM turbulence model and different values of y+

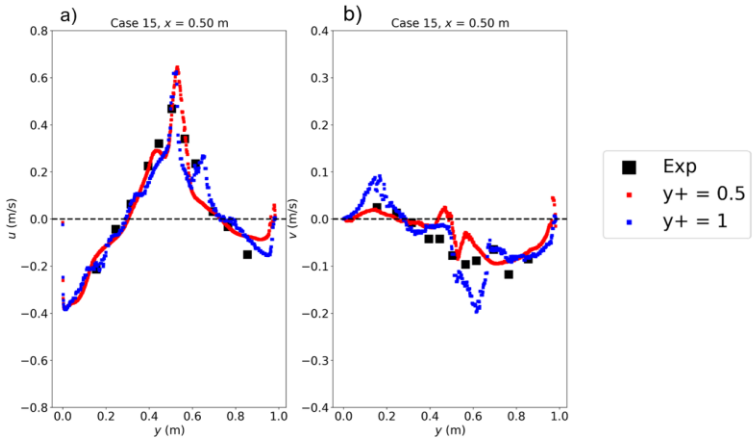

Figure 59: Test 15 - Run 1. Comparison of computed and measured (a) longitudinal and (b) transversal velocities extracted at x = 0.50 m and z = 0.050 m. EBRSM turbulence model and two values of y+

6.5. Simulation of short reservoir cases

6.5.1. Results for Test 15

Figure 60 compares the observed flow pattern at the surface using LSPIV with the numerical results extracted at z = 0.010 m. It can be observed that the three high Reynolds number models replicate the flow asymmetry. However, the Standard K-ε and Linear Production K-ε models fail to reproduce the size of the secondary recirculation. These two models are isotropic and do not account for directional variations in turbulence, while the boundary layer near the wall is highly anisotropic. In contrast, the Rij-ε SSG model provides a more accurate representation of the secondary recirculation size. Of particular interest, the three models are not valid very close to the wall due to the presence of a large velocity gradient in the near-wall region, necessitating the use of a simplified momentum balance-based wall function model. Also, it is observed that computed velocity intensities provided by the three high Reynolds number models are higher than in the experimental measurements. This phenomenon can be elucidated by the imposed symmetry condition at the surface by *code_saturne*.

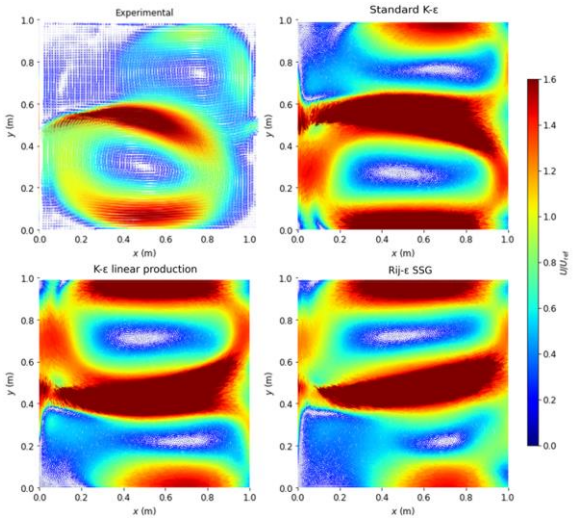

Figure 60: Test- 5 - Run 2. Comparison of experimental and computed flow field at surface using high Reynolds turbulence models for y+=31.

Figure 61-62 depict the model-data comparisons of horizontal velocity profiles (*u* and *v*) at *x* = 0.50 m and *x* = 0.89 m. As describe in Chapter 4, these profiles are situated in the intermediate field. For each position, horizontal profiles extracted at *z* = 0.050 m, *z* = 0.036 m, and *z* = 0.016 m are compared, showing a good model-data agreement. The shape and magnitude of velocities are accurately reproduced. These results demonstrate that despite the suboptimal reproduction of the surface flow characteristics, the profiles extracted at specific vertical positions below half-flow depth are satisfactory in terms of jet amplitude and spread.

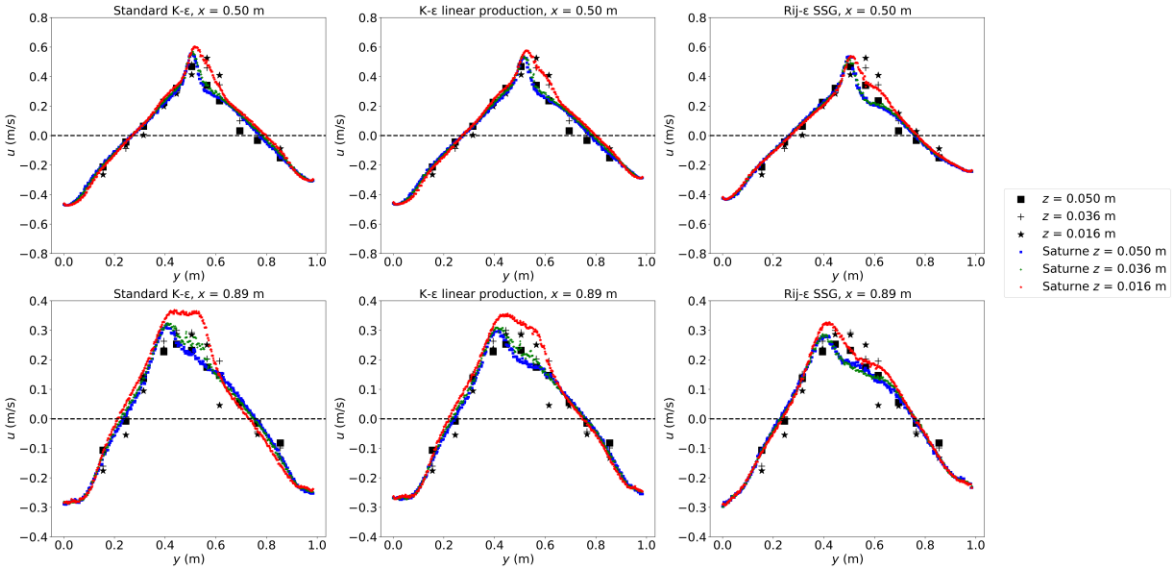

Figure 61: Case 15, Run 2. Measured and computed cross-sectional profiles of longitudinal velocity at x = 0.50 m and x = 0.89 m using high turbulence models for y+=31

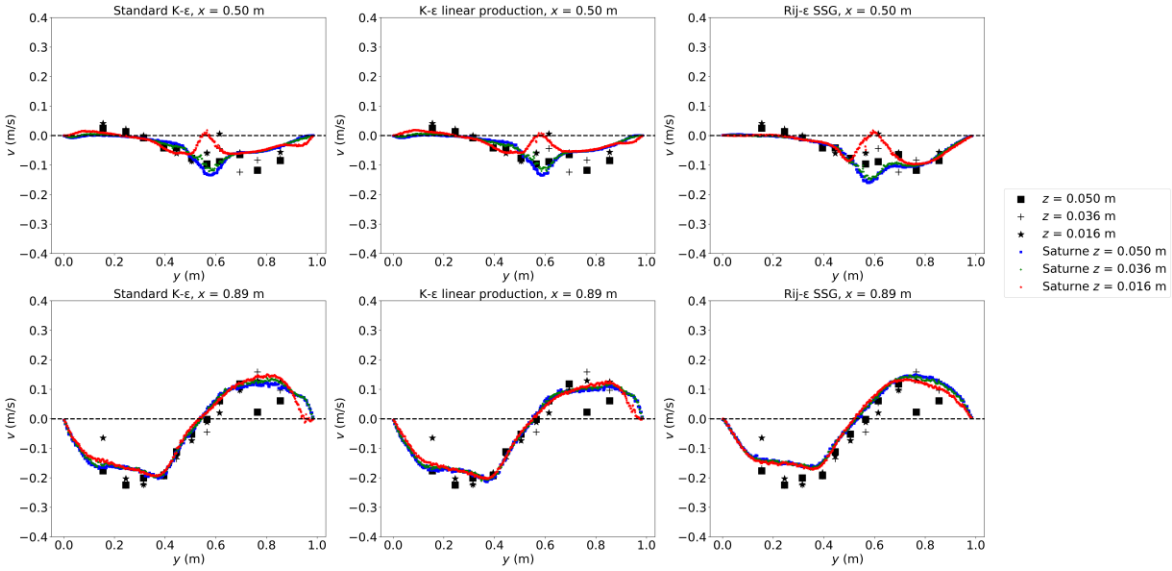

Figure 62: Case 15, Run 2. Measured and computed cross-sectional profiles of transversal velocities at x = 0.50 m and x = 0.89 m using high turbulence models for y+=31

Figure 63 compares the observed flow pattern at the surface using LSPIV with the numerical results obtained at z = 0.010 m. Using the low Reynolds turbulence models K-w SST, BL-v2/k and Rij-ε EBRSM, the flow pattern is replicated more accurately compared to the high Reynolds turbulence models, with a better representation of the secondary recirculation zone size. These three low turbulence models reproduce accurately the damping of eddy viscosity near the wall. The Spalart- Allmaras fails to reproduce well the secondary currents, as this model contains an additional nonlinear term for diffusion, which is important at the edge of turbulent region where diffusion dominates (wake edge). This additional term allows an accurate spreading of the jet profile, but it is possible that it could impact the recirculation zone. The presence of the lateral wall destroys turbulence by a combination of inviscid blocking pressure fluctuation and viscous damping very close to the wall. In the Spalart-Allmaras model, destruction of turbulence occurs while considering only the viscous damping. A source term plays a role in reducing the value of ν (turbulent eddy viscosity) and considers the distance to the nearest wall. As we get closer to the wall, we expect the destruction of turbulence to increase because of viscous damping (Kalitzin et al. 2005). A possible reason explaining the less good reproduction of the secondary currents could be the important weight of the destruction term in the equation.

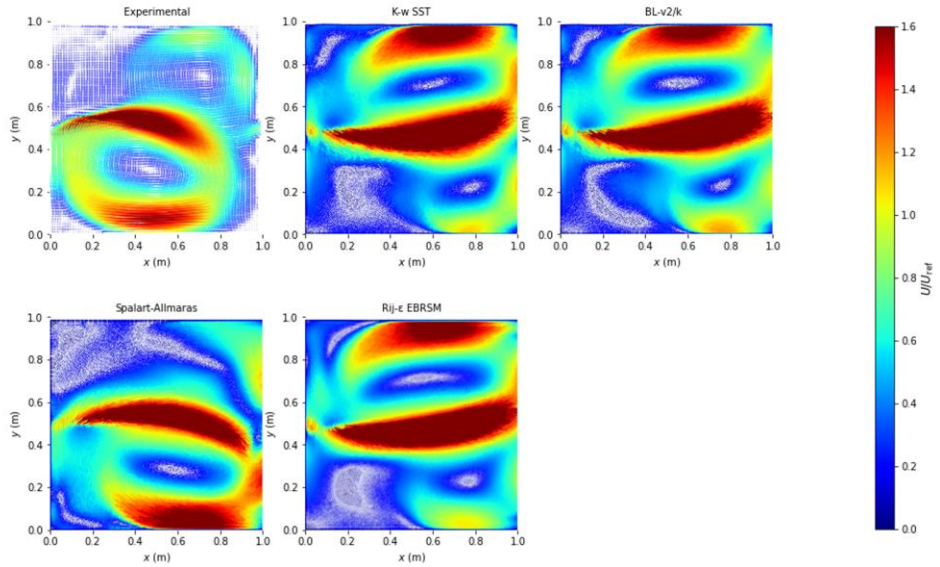

Figure 63: Case 15, Run 3. Comparison of experimental and computed flow fields at surface using low Reynolds turbulence models

Figure 64 and 65 illustrate profiles of horizontal velocities (*u* and *v*) at two positions, *x* = 0.50 m and *x* = 0.89 m. For each position, horizontal profiles extracted at *z* = 0.050 m, *z* = 0.036 m, and *z* = 0.016 m are shown, demonstrating good agreement with measurements. Overall, the magnitude and spread of velocities are accurately reproduced. The BL-v2/k model performs well, replicating both longitudinal and transverse profiles. The Spalart-Allmaras model yields a slight overestimation of velocities near the bottom due to a term responsible for jet spreading. The K-w SST model shows less accurate results for the transverse velocities *v*, due to increased diffusion.

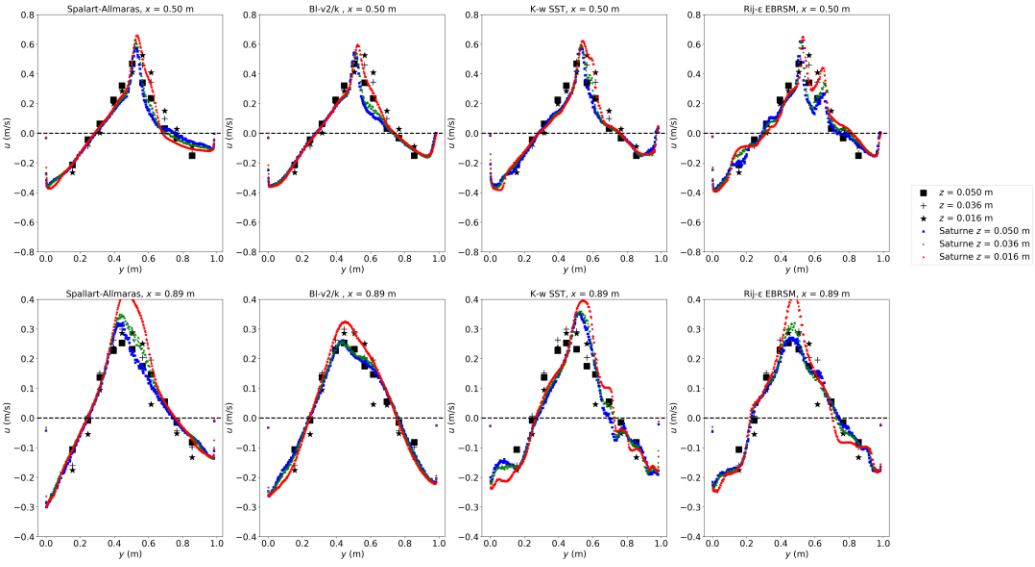

Figure 64: Case 15, Run 3. Measured and computed cross-sectional profiles of longitudinal velocity u at x = 0.50 m and x = 0.89 m using low turbulence models for y+=1

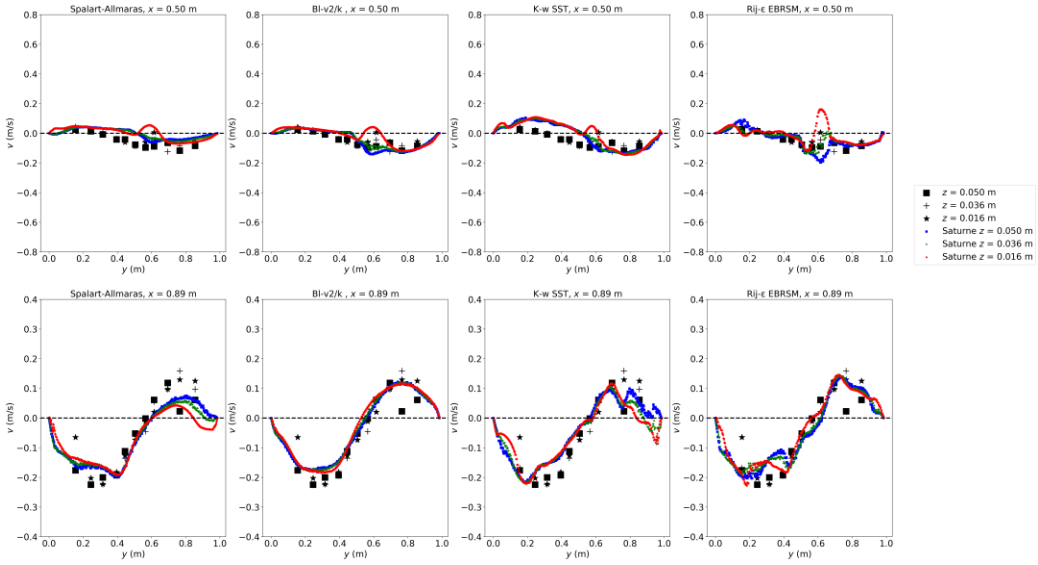

Figure 65: Case 15, Run 3. Measured and computed cross-sectional profiles of transversal velocity v at x = 0.50 m and x = 0.89 m using low turbulence models for y+=1

6.5.2. Results for Test 29

All high Reynolds number turbulence models successfully replicate the flow characteristics, i.e., back flow pattern. This implies that, to some extent, the damping effect due to the turbulence model is negligible when compared to the advection term. The standard K-ε model and the K-ε model with linear production models produce very similar results. Both the nonlinear and linear components of the production term in these models have minimal impact on the results. The Rij-ε SSG model exhibits similar outcomes, particularly for the spreading of the jet toward the bottom and the intensity of surface back flow at z = 0.20 m. For all three turbulence models the velocity intensity is negligible within the central plane located at z = 0.10 m. Thus, the back flow currents predominantly take place in the vicinity of the outlet channel.

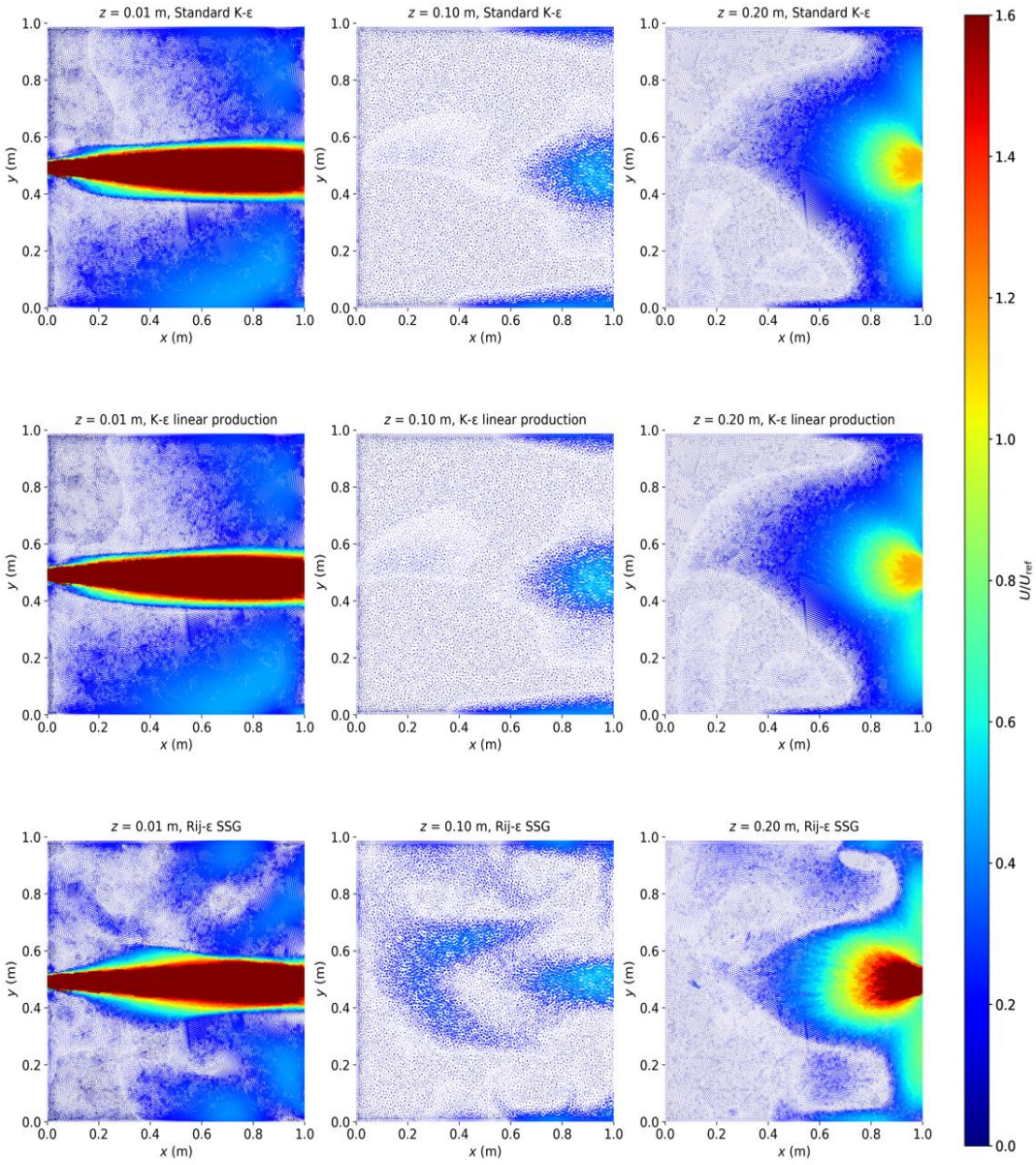

Figure 65: Case 29, Run 5. Flow patterns near bottom (z = 0.01 m), middle (z = 0.10 m), and surface (z = 0.20 m) for high Reynolds turbulence models at t = 300 s

Low Reynolds models also successfully reproduce the flow characteristics. Differences are observed in terms of the jet spreading at the bottom. Additionally, the central plane exhibits the presence of backflow currents, unlike the high Reynolds number models. These currents extend beyond half the length of the reservoir for the K-w SST and Spalart-Allmaras models. The intensity and shape of surface backflow currents vary from one model to another. For instance, in the K- w SST and Spalart-Allmaras models, these currents spread across the entire width of the jet, whereas in the BL-v2/k and Rij-ε EBRSM models, they are more concentrated towards the center

of the jet. Indeed, experiments do indicate that backflow currents are more pronounced in the middle of the basin compared to the sides. The Rij-ε EBRSM model appears to better capture the flow characteristics of this configuration. However, this assertion requires confirmation through a quantitative comparison of velocity measurements.

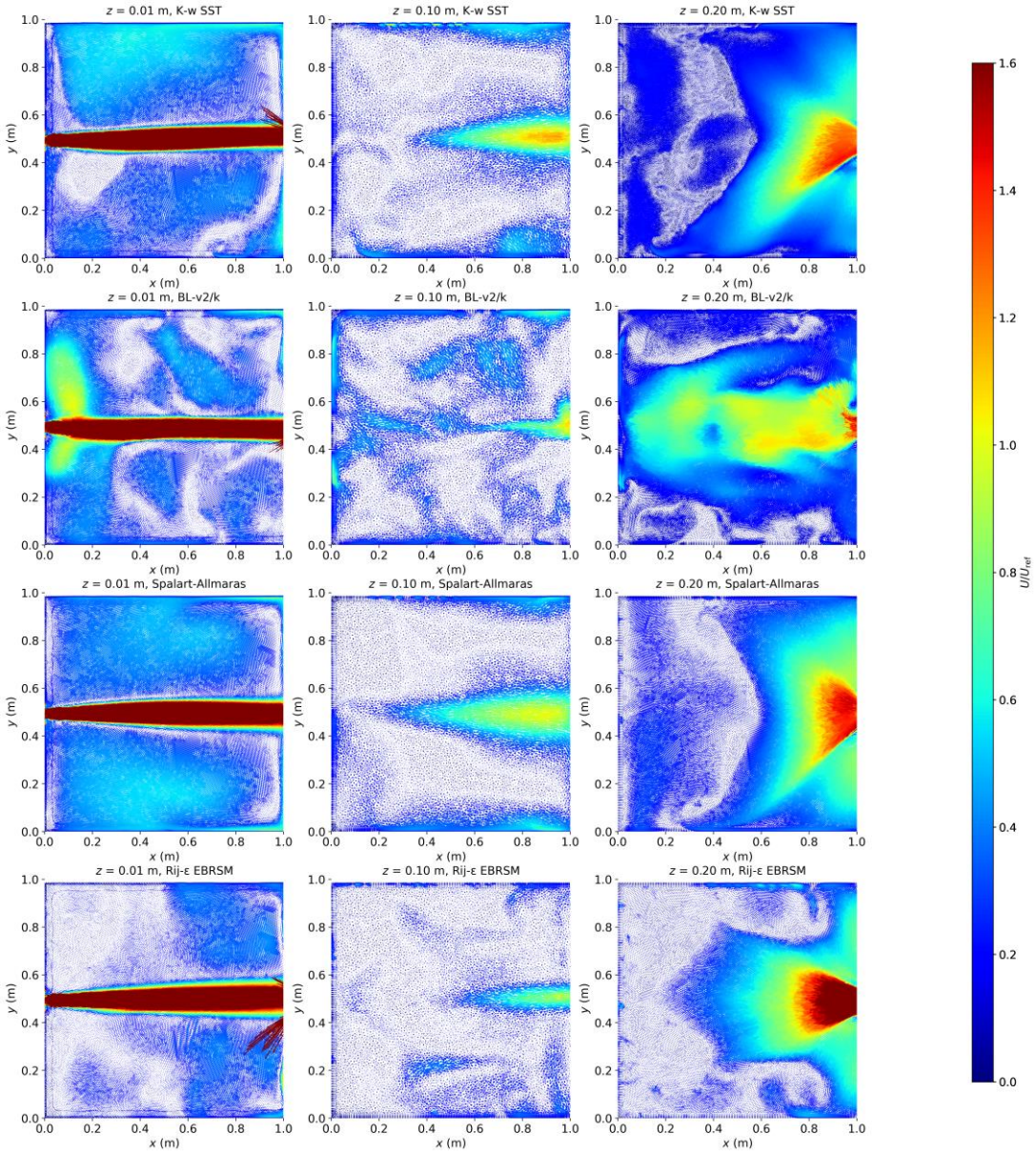

Figure 66: Case 29, Run 6. Flow patterns at bottom (z = 0.01 m), middle (z = 0.10 m), and surface (z = 0.20 m) for Low Reynolds turbulences models at t = 300 s

6.5.3. Results for Test 9

Test 9 is a challenging case, as it exhibited experimentally inherent flow instability. When instability is observed, a qualitative comparison between the numerical and experimental flow states is carried out. All three high Reynolds number turbulence models successfully capture the presence of flow instability. Figure 67 shows computed flow patterns at various time for Standard K-ε model. Initially, back flow currents at the surface appear numerically at t = 37.5 s. From t = 52.50 s, three distinct flow states emerge: the first one at t = 52.50 s features the creation of a large recirculation zone with a secondary recirculation. The second one at t = 60 s demonstrates the jet attaching more closely to the lateral wall, facilitating the enlargement of the secondary recirculation. The third state at t = 82.50 s represents an intermediate state between the first and second ones, and recurs at multiple times, including 90 s, 120 s, 127.50 s, 142.5 s, 150 s, 157.5 s, 165 s, 195 s, and 206 s. Experimentally, the instability appeared at two distinct apparent states, one occurring at t = 10 s, 40 s, and t = 3655 s, and the other at t = 40 s, 115 s, and t = 3686 s. Additionally, the experimental jet underwent transition states. The velocity intensity in the experimental data is lower compared to the numerical results. Similar results are observed for the linear K-ε model, although these states occur at different times compared to those in the experiment. The Rij-ε SSG model reproduces instability but, in a manner, distinct from the K-ε models. It provides enhanced visualization of the instability creation process. Up to 60 seconds, similar flow states as K-ε are observed, characterized by the presence of backflow currents at the surface and a small recirculation that increases in intensity over time. This recirculation subsequently decreases in intensity, giving rise to a second recirculation, ultimately leading to the formation of two nearly symmetrical small patterns around the principal jet direction. Asymmetry begins to manifest at t = 111.25 s, resulting in the jet reattachment to the opposite wall (t = 150 s) and subsequently to the lateral wall (t = 165 s). It is noteworthy that the jet does not return to its state at t = 150 s thereafter. The Rij-ε SSG model reproduces the experimentally identified flow patterns less accurately.

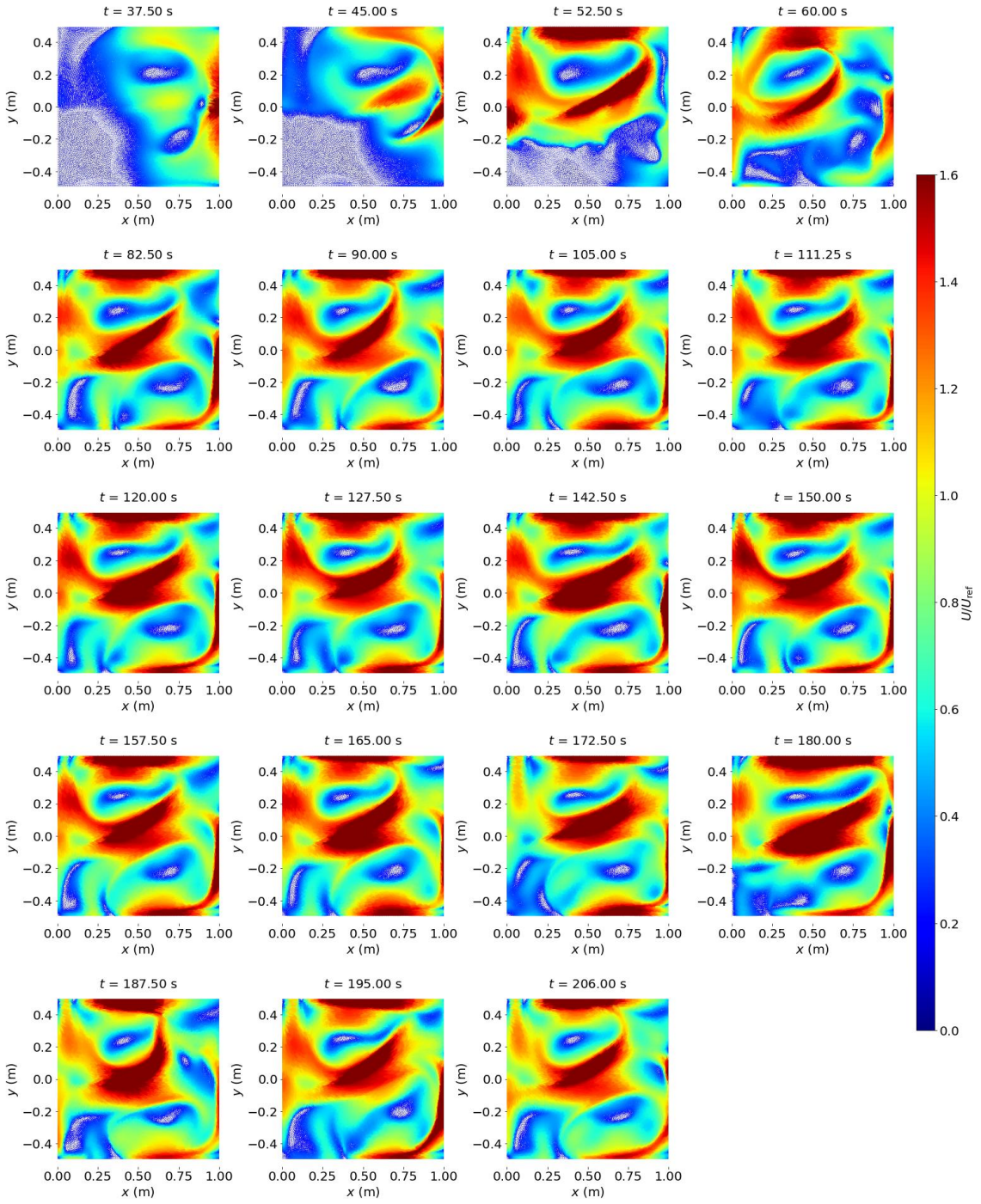

Figure 67: Case 9, Run 7. Flow patterns at surface (z = 0.010 m) for Standard K-ε turbulence model at different times

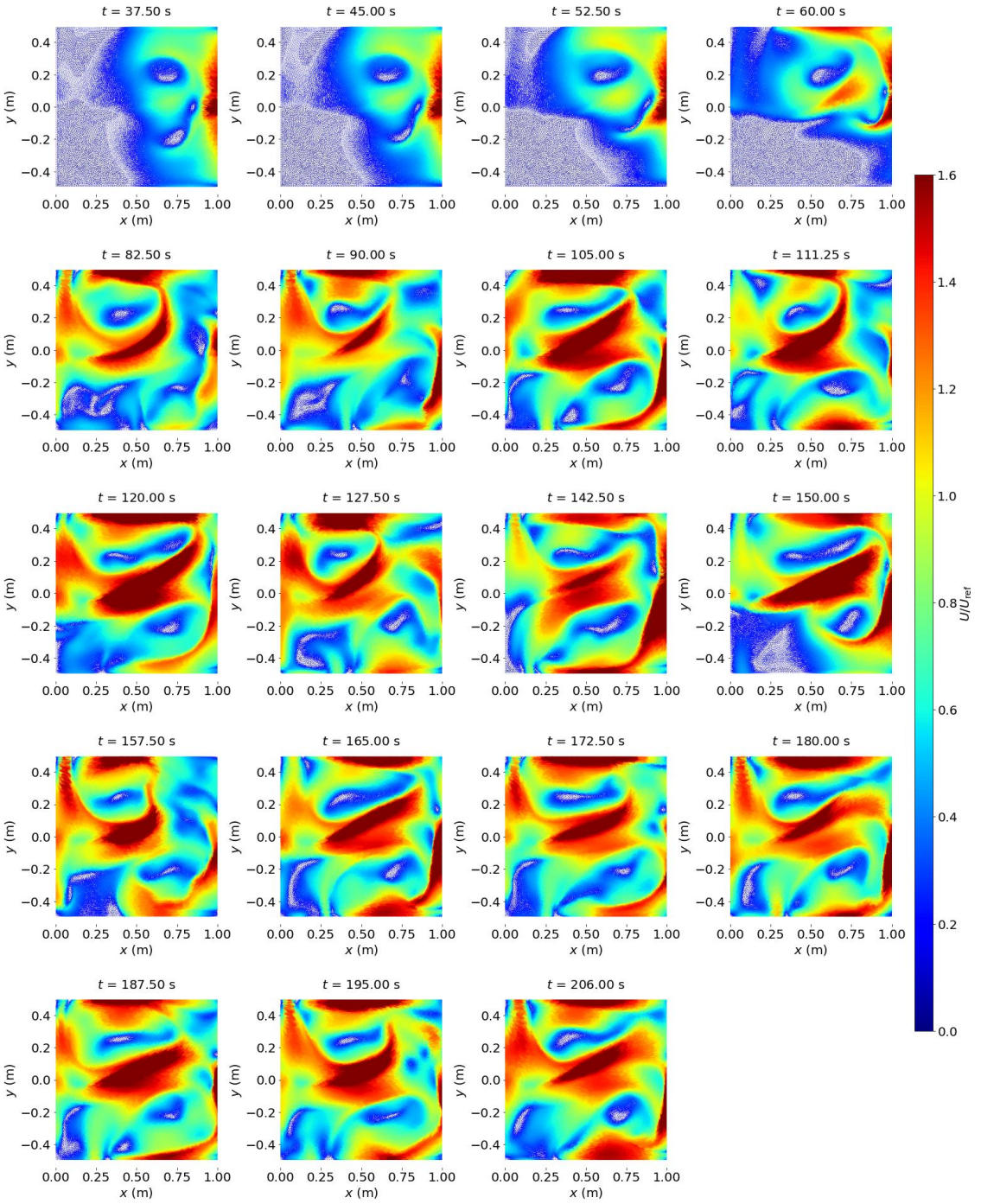

Figure 68: Case 9, Run 7. Flow patterns at surface (z = 0.010 m) for K-ε linear production turbulence model at different times

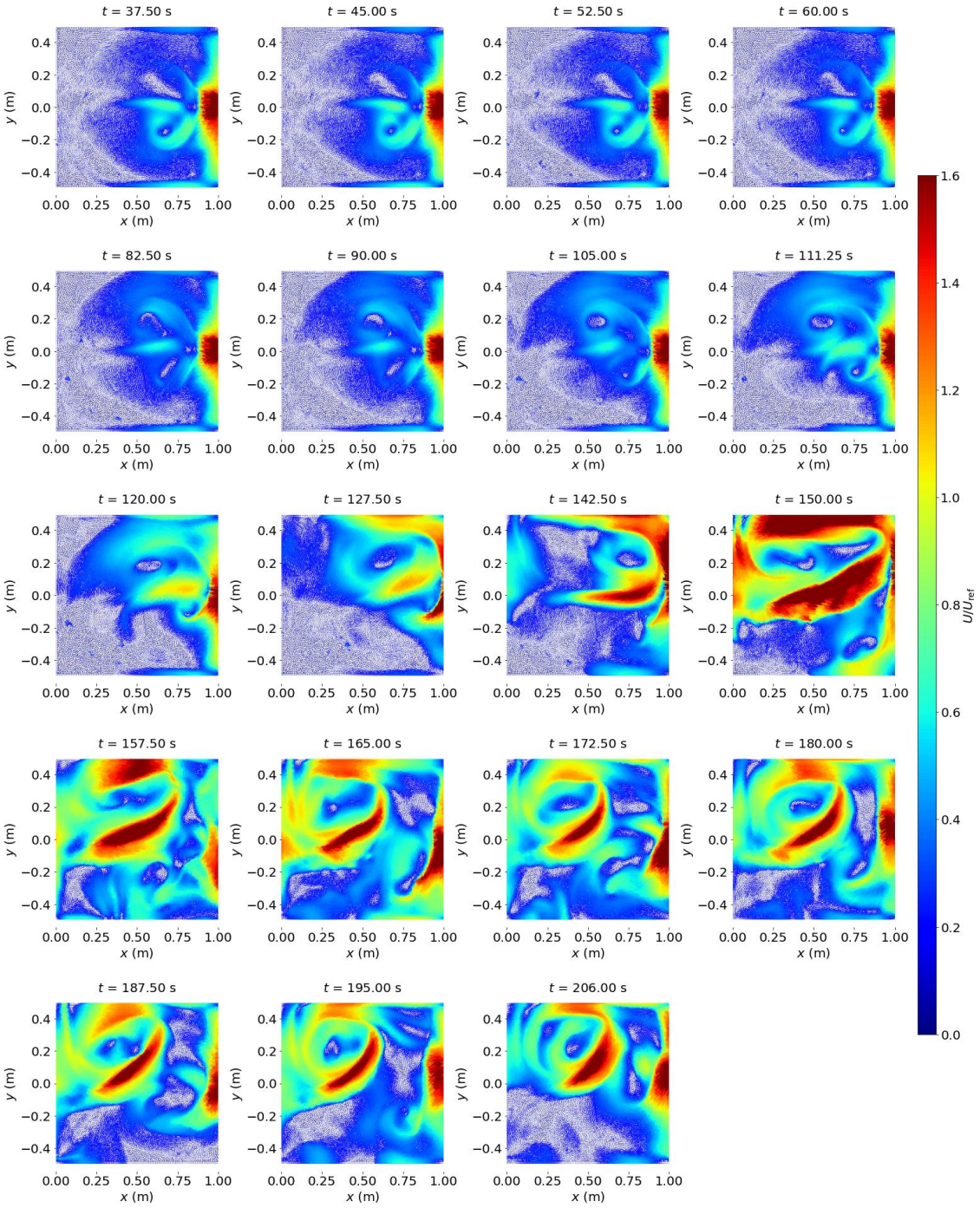

Figure 69: Case 9, Run 7. Flow patterns at surface (z = 0.010 m) for Rij-ε SSG turbulence model extracted at different times

Low Reynolds models fail to capture the instability. Figure 70 shows flow patterns at bottom (z = 0.01 m), middle (z = 0.05 m), and surface (z = 0.010 m) extracted at t = 300 s. It is observed that the jet remains located at the bottom and backflow currents are visualized at the surface. However, unlike Test 29, the turbulence models yield jets at the median plane with significant intensity.

Presence of two small vortices generated due to the shear layer around the jet is observed for all the models. The Rij-ε EBRSM model provides a similar state as the high Reynolds number Rij-ε SSG model before the jet reattaches in the lateral wall (at *t* = 82.50 s).

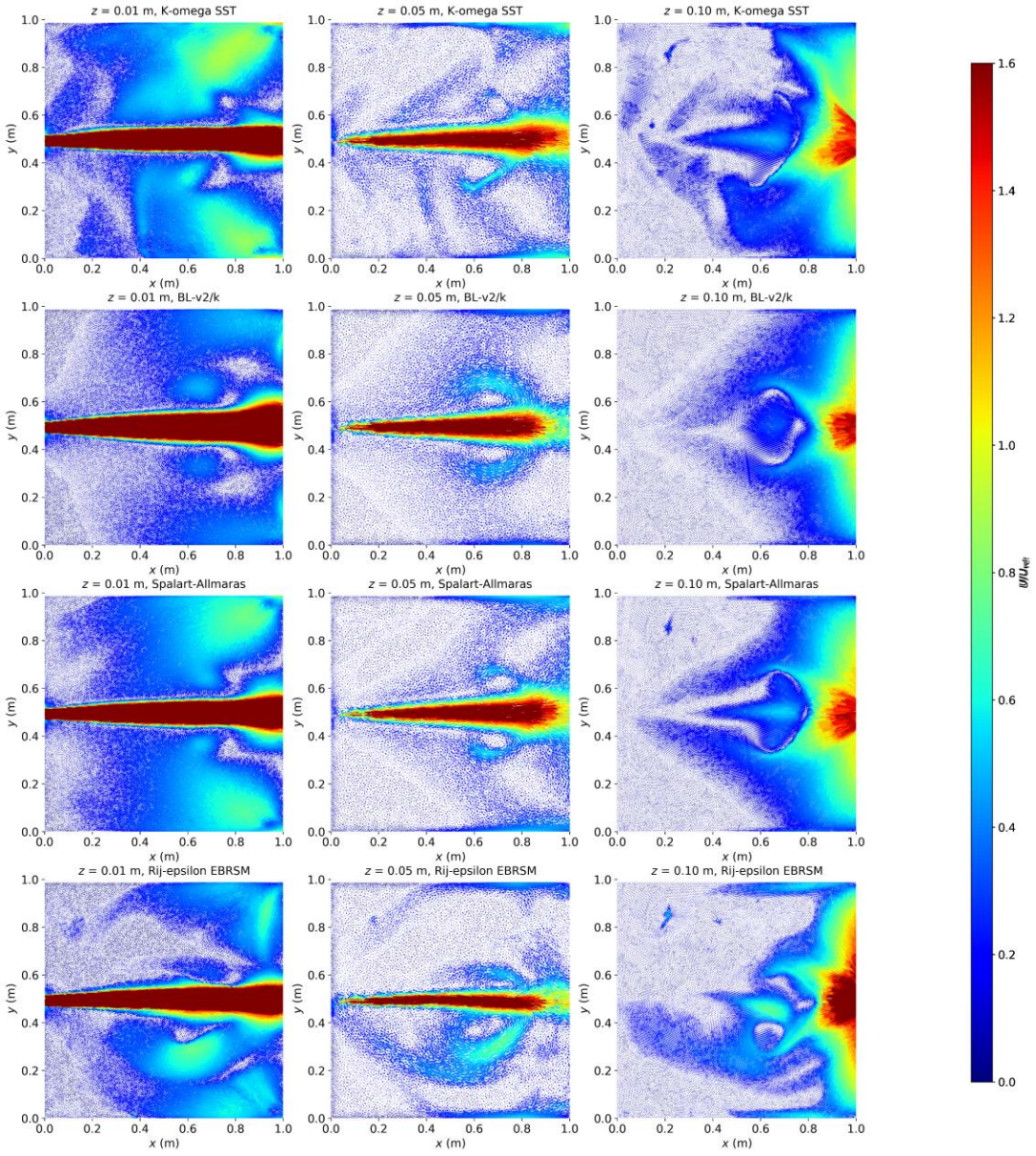

Figure 70: Case 9, Run 8. Flow patterns at bottom z = 0.01 m, middle z = 0.05 m, and surface z = 0.010 m for Low Reynolds turbulences models at t = 300 s.

Figure 71 depicts the 3D velocity distribution using the K-w SST model. As previously described, we can readily discern the phenomenon of surface secondary currents coexisting with a localized jet at the bottom.

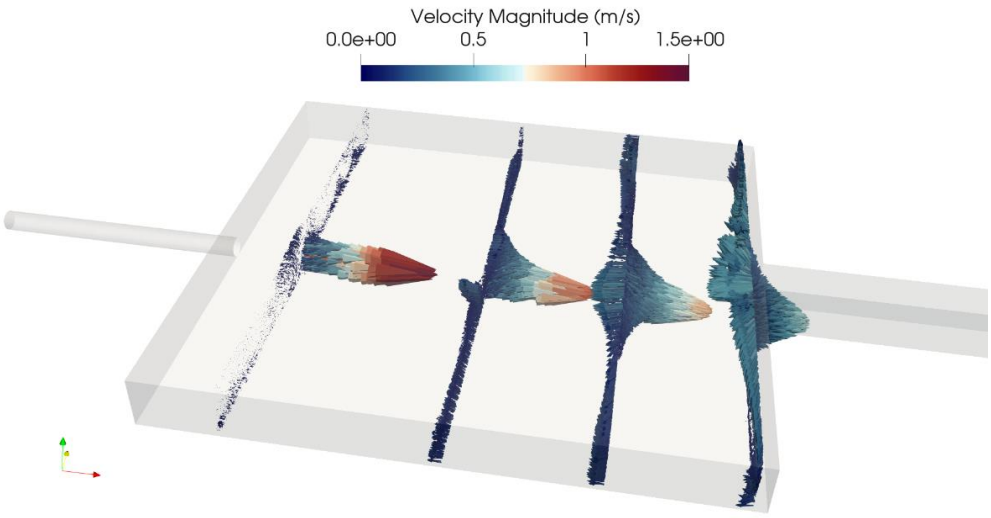

Figure 71: Case 9, Run 8. 3D flow fields in the reservoir extracted at different plans using K-w SST turbulence model

6.5.4. Influence of water depth

Using Test 9, additional simulations were conducted with a water depth H = 0.095 m instead of 0.10 m, to asse the influence of water depth on the instability characteristics. the high Reynolds turbulence models can replicate this instability. The Standard K-ε model, as illustrated in Figure 72, yields similar results as the numerical run using H =0.10 m. However, the flow states do not occur at the same times.

The Linear production model also yields results like those observed using H = 0.10 m, although the various states appear at varying time intervals. Nevertheless, this model has the capability to reproduce the transition observed in experiments (t = 206 s), where the jet changes its direction while maintaining the same flow pattern as at t = 45 s. This model is a modification of the standard k-ε model, the aim of the model is to mitigate the overestimation of energy by linearizing the production term when the strain rate is significant. This is achieved by incorporating a variable constant (Guimet and Laurence, 2002). It can be inferred that the production term plays a significant role in the jet's transition from one side to another.

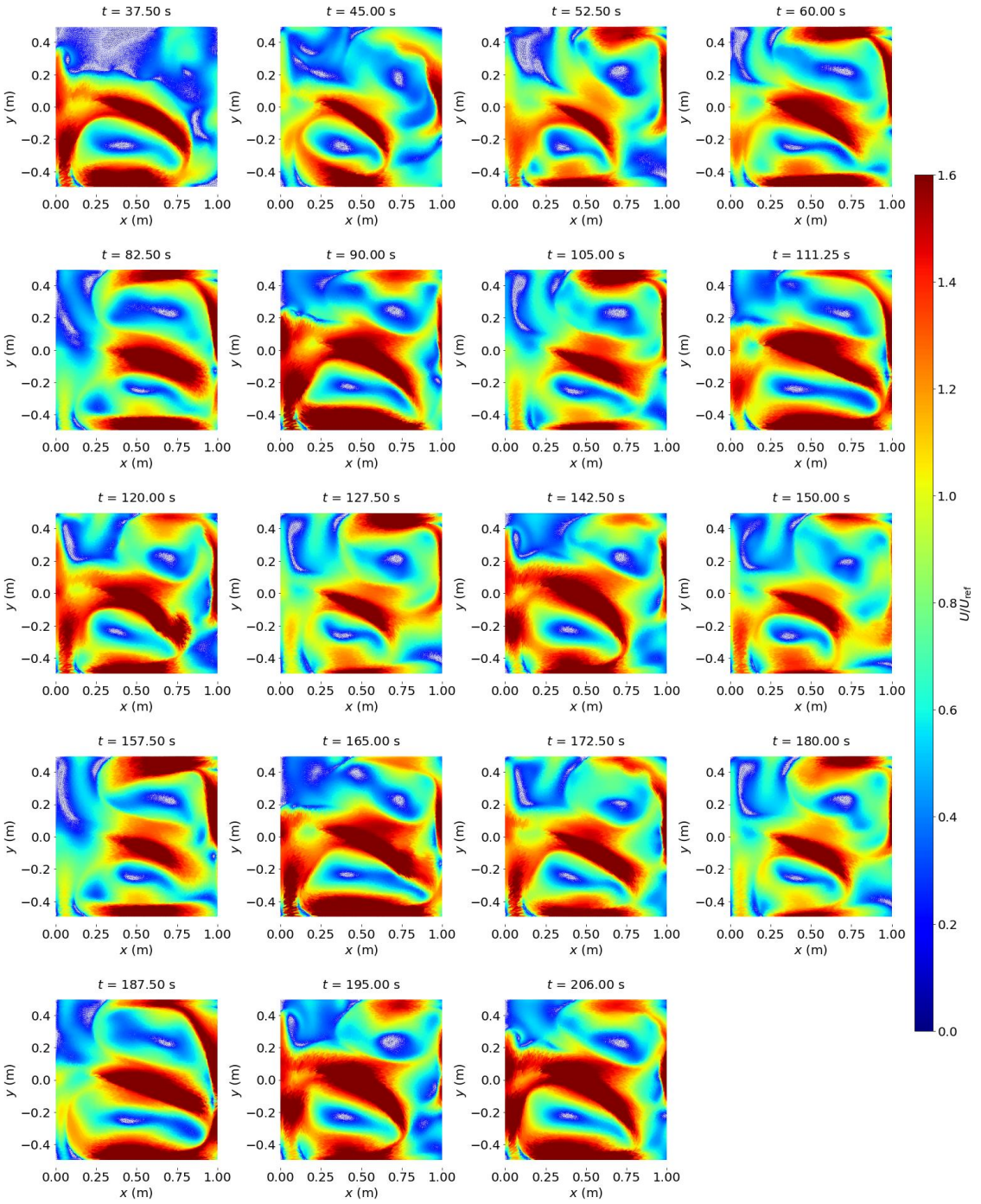

Figure 72: Case 9-bis, Run 9. Flow patterns at bottom (z = 0.010 m) for Standard K-ε turbulence model at different times

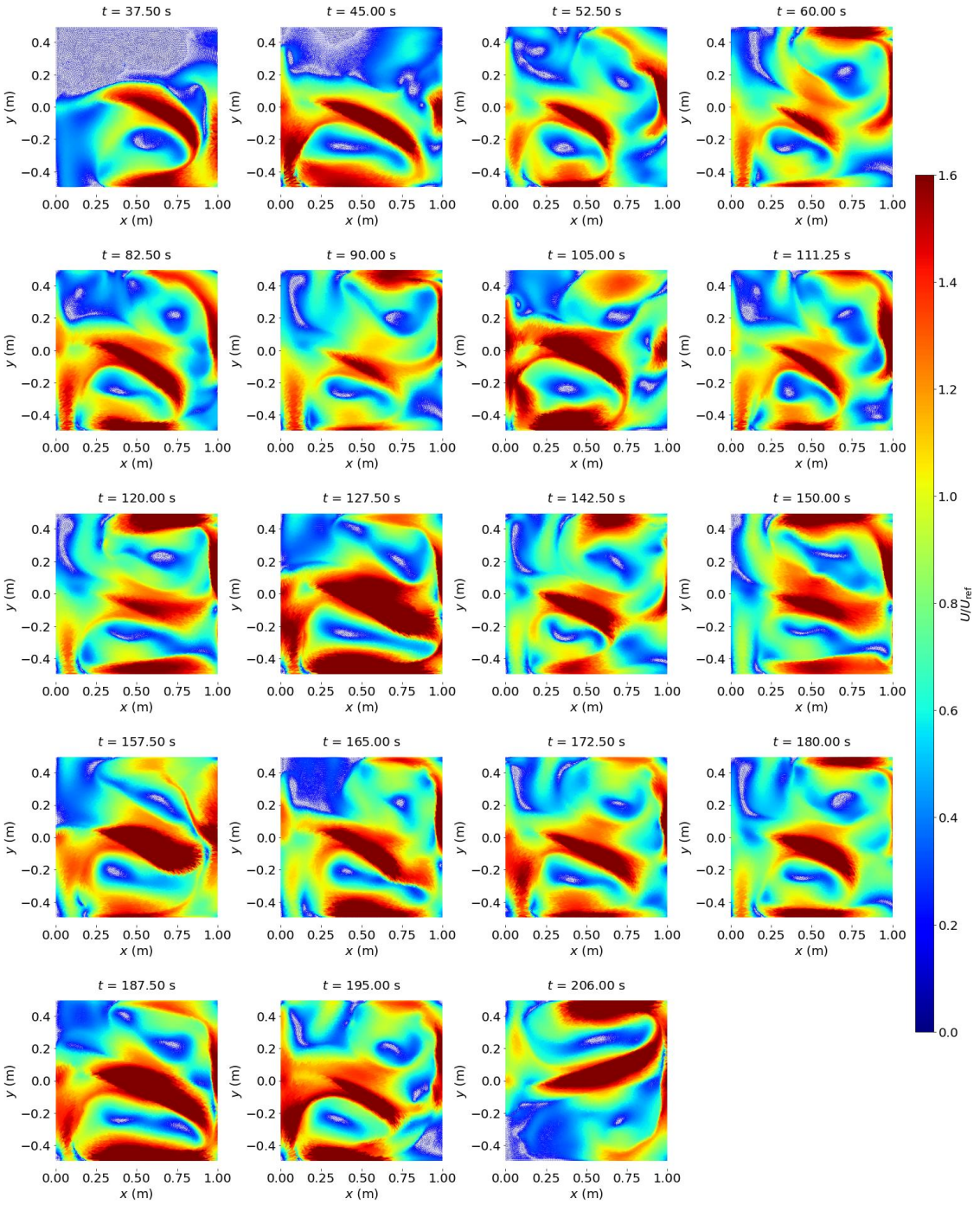

Figure 73: Case 9-bis, Run 9. Flow patterns at bottom z = 0.10 m for K-ε linear production turbulence model at different times

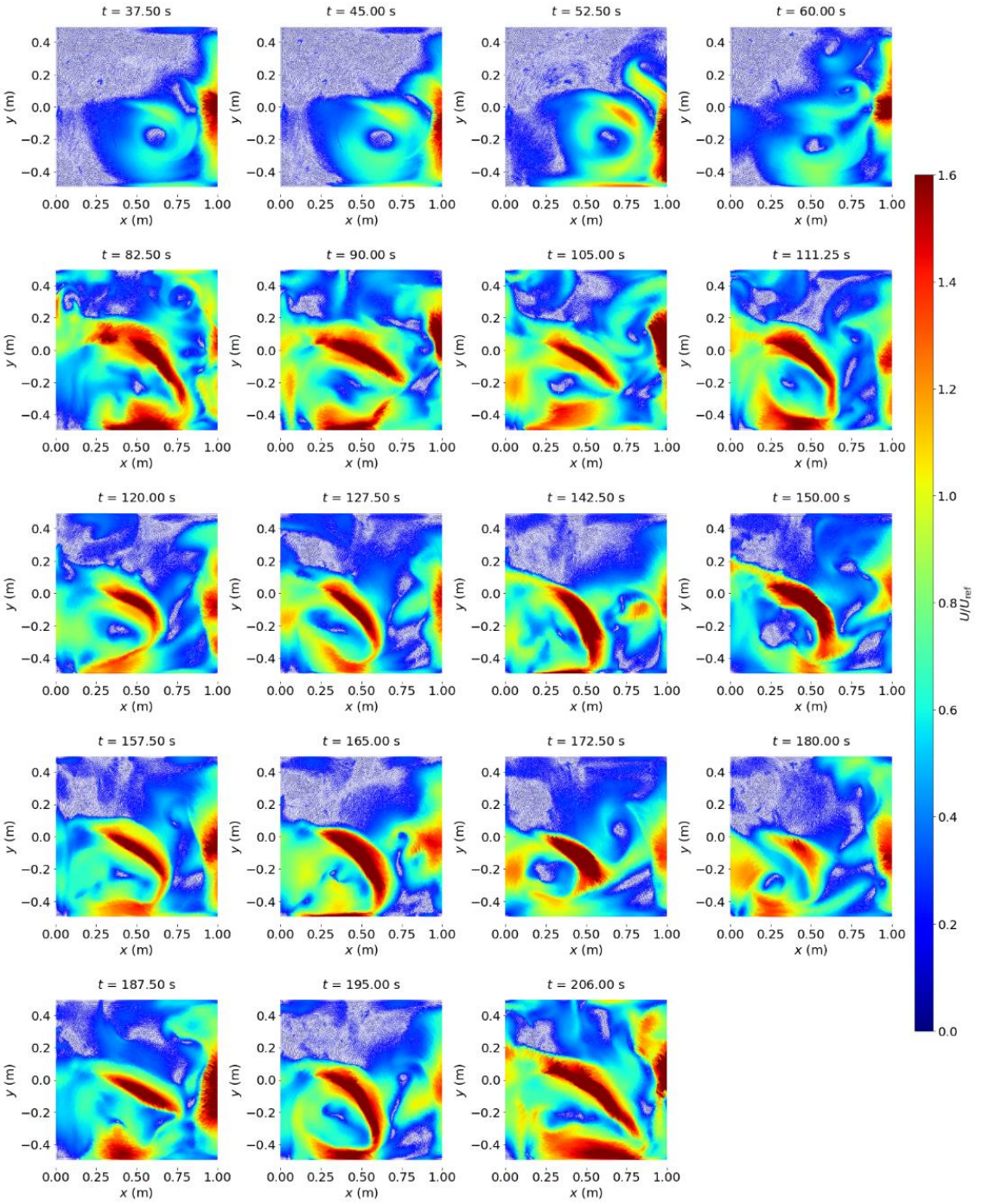

Figure 74: Case 9-bis, Run 9. Flow patterns at bottom z = 0.010 m for Rij-ε SSG turbulence model extracted at different times

K-w SST model reproduces the instability, with four distinct patterns. At *t* = 37.50 s, there is a large main recirculation with two secondary recirculations, characterized by a pressure minimum, causing the fluid jet to bend or curve to the right (or left). As the fluid jet continues to bend towards the right, it eventually impinges on the side wall of the reservoir. At *t* = 45.00 s, a second state is obtained with a large main recirculation and a smaller similar recirculation. It appears that the large main recirculation continues, but there is a secondary recirculation of lesser significance. At *t* = 52.50 s, the jet starts to attach more to the lateral wall, reducing the size of the main recirculation. This allows the secondary recirculation to grow due to the weak depression (low pressure). At *t* = 60 s, the system reaches an almost symmetrical state where two large recirculations form with slightly similar sizes. State 2 reappears at 82.50 s, 111.25 s, and 120 seconds. A third state is found at *t* = 90, 120 s, and fourth one at *t* = 105 s. Subsequently, the jet will switch to the opposite side. At *t* = 127.50 s, this switch occurs just after the jet is reattached to the wall, due to the significant depression in the main recirculation and the weak depression in the secondary recirculation. As time progresses, the recirculation zone becomes stronger, resulting in an increasing pressure difference between the jet and the center of this recirculation area. With the growing pressure difference, the jet is pulled toward the left, opposite to its initial direction. This movement implies the presence of a dynamic feedback mechanism or a force influencing the jet direction (Kalter, 2014). The entire process repeats cyclically until returning to *t* = 206 s, at the state encountered at *t* = 40 s. Comparing the results with the experimental data reveals the presence of intermittency, which manifests as two distinct apparent states (State 2) occurring at *t* = 10 s, 40 s, and *t* = 3655 s, and State 3 corresponding to *t* = 40 s, 115 s, and *t* = 3686 s in the experiment. Additionally, the jet undergoes a positional switch in the experiment. However, it is noteworthy that the velocity intensity in the experimental data is observed to be lower when compared to the numerical results. This difference can be attributed to a reduction in the flow height, from 0.1 m in the experiment to 0.095 m in the numerical simulation, and also to the surface-to-surface boundary conditions imposed in the code_saturne, which introduce a symmetry condition.

The oscillation is initiated by the jet's flow and the resulting formation of a pair of recirculating eddies, which establish the entrainment field within the enclosed space. Confined oscillation arises from a dynamic balance between the pressure differential across the jet and the momentum of the recirculating currents.

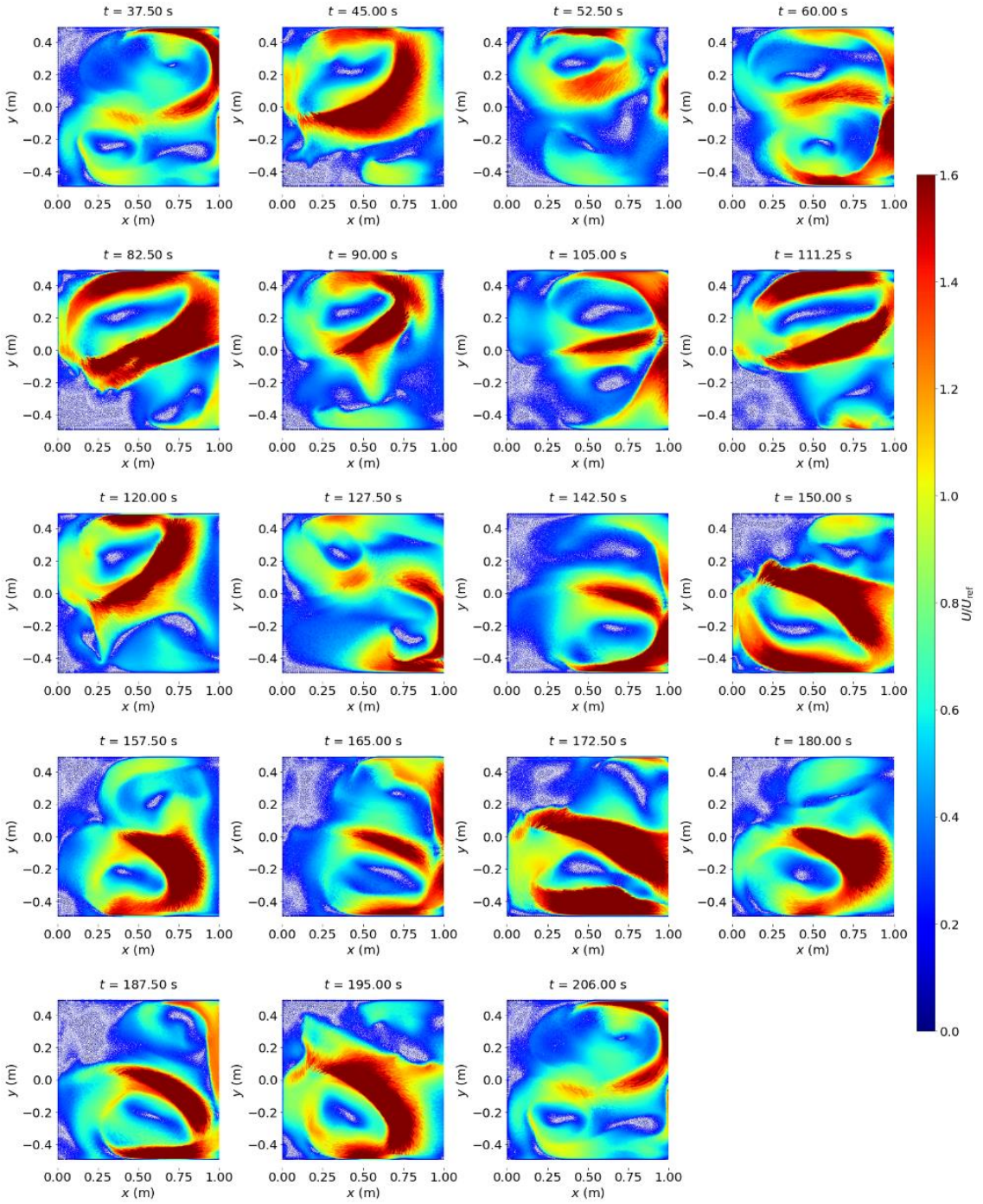

Figure 75: Case 9-bis, Run 10. Flow patterns at bottom z = 0.010 m for K-w SST turbulence model extracted at different times

Using H = 0.0095 m, the Rij-ε EBRSM model reproduces instability, with the flow switching from symmetry to asymmetry with an approach towards the wall starting at t = 82.50 s and then returning to a symmetrical state at t = 187.50 s. When comparing the different states obtained, it is observed that this model fails to replicate the typologies observed experimentally.

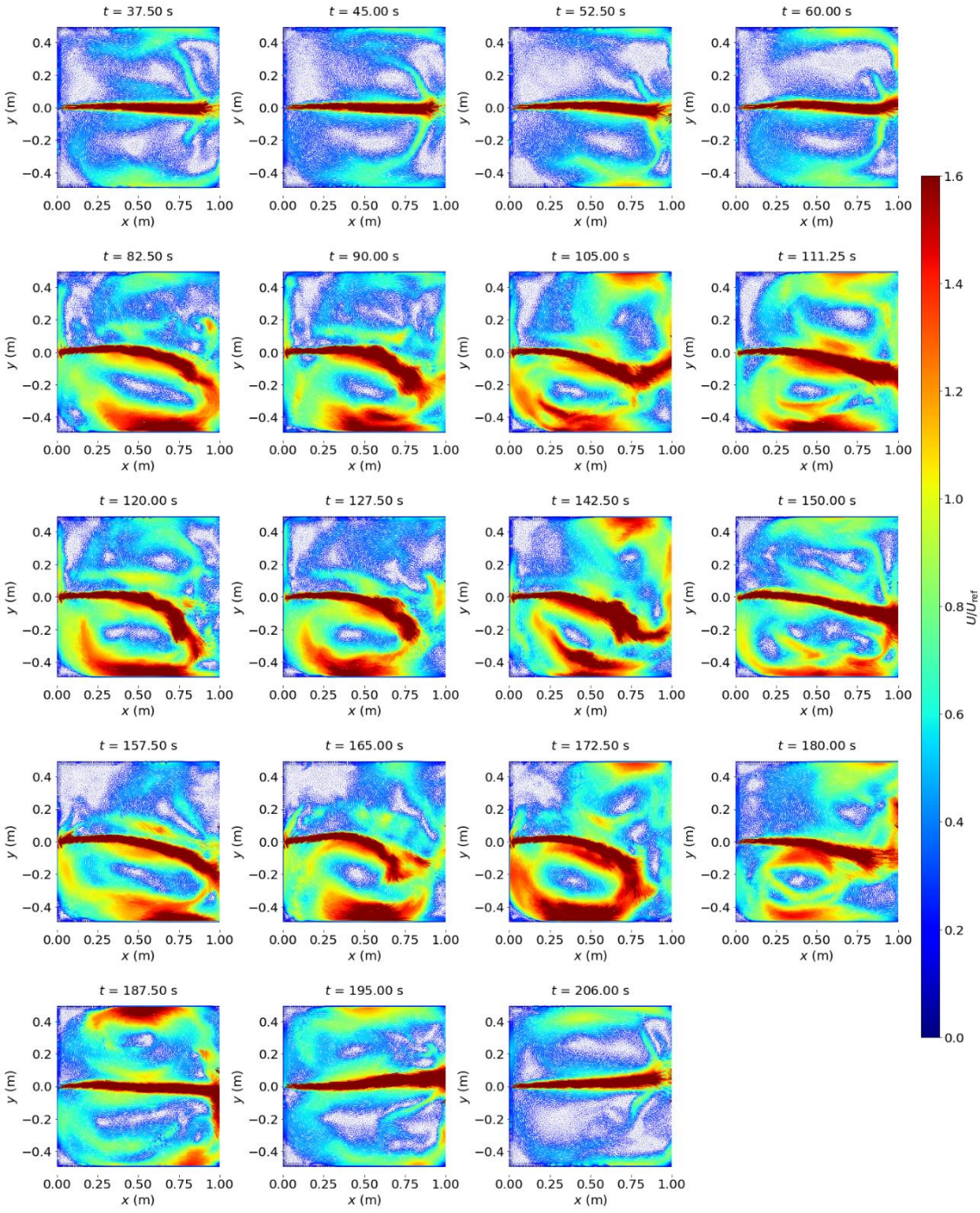

Figure 76: Case 9-bis, Run 10. Flow patterns at bottom z = 0.01 m for Rij-ε EBRSM turbulence model extracted at different times

Figure 77 depicts flow patterns at different depths for the BL-v2/k and Spalart-Allmaras turbulence models t = 300 s. It is evident that, for both models, decreasing the flow depth fails in reproducing the observed instability. However, the BL-v2/k model does exhibit some surface recirculation, suggesting that a longer computational duration may be necessary for it to transition. In contrast,

the Spalart-Allmaras model yields the surface backflow currents prevailing, with their extent surpassing half of the channel length.

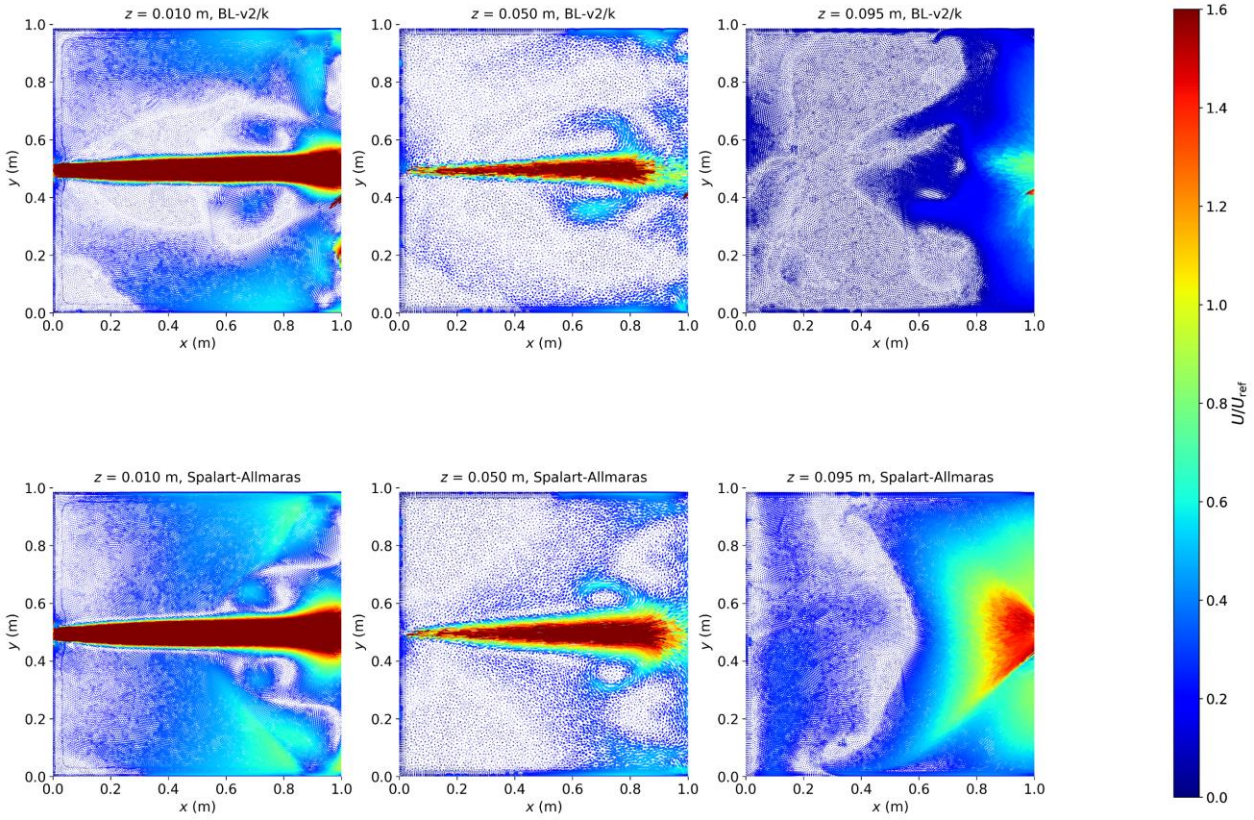

Figure 77: Case 9-bis, Run 10. Flow patterns at bottom z = 0.01 m, middle z = 0.05 m, and surface z = 0.10 m for BL-v2/k and Spalart-Allmaras turbulences models extracted at t = 300.

6.5.5. Large Eddy Simulation

An exploratory study with LES was carried out for Test 15 which showed stationary behavior. To model the turbulence, the large eddy simulation (LES) method with the Smagorinsky subgrid-scale (SGS) is used. LES is based on solving large eddies and modeling small eddies, which are done by imposing filters on the governing equations. The Smagorinsky subgrid-scale operates under the assumption that there is an equilibrium between the production and dissipation of small-scale eddies. A mesh with y+ =0.5 near the wall was used for this configuration. A tetrahedral mesh extruded with near walls a prism extension with a geometric progression was necessary to ensure a smooth transition in the mesh size, with a mesh size of 22 million nodes. Numerical convergence was achieved with the following options, least squares with opposite adjacent cell centers completed on boundaries (immediate neighborhood) and SOLU scheme. Figure 78 shows the

LES results at t = 50 s, t =100 s and t =150 s on two planes, namely a bottom plane z =0.01 m, and a middle plane z =0 .05 m. It is observed that the flow typologies at the bottom and middle planes correspond well to the observed patterns. Main and secondary recirculations are found. Velocity fluctuations from a certain distance from the jet show the presence of coherent structures. LES results are averaged over 200 s to allow a comparison with measurements. Results corresponds well to the flow typology found in the experiment (A1*, see Chapter 4). This exploratory study shows promising results in terms of flow typologies, but the use of the SOLU numerical scheme is not the most suitable because of the high diffusivity it generates. Also, inlet conditions are constant, and this could potentially influence the results.

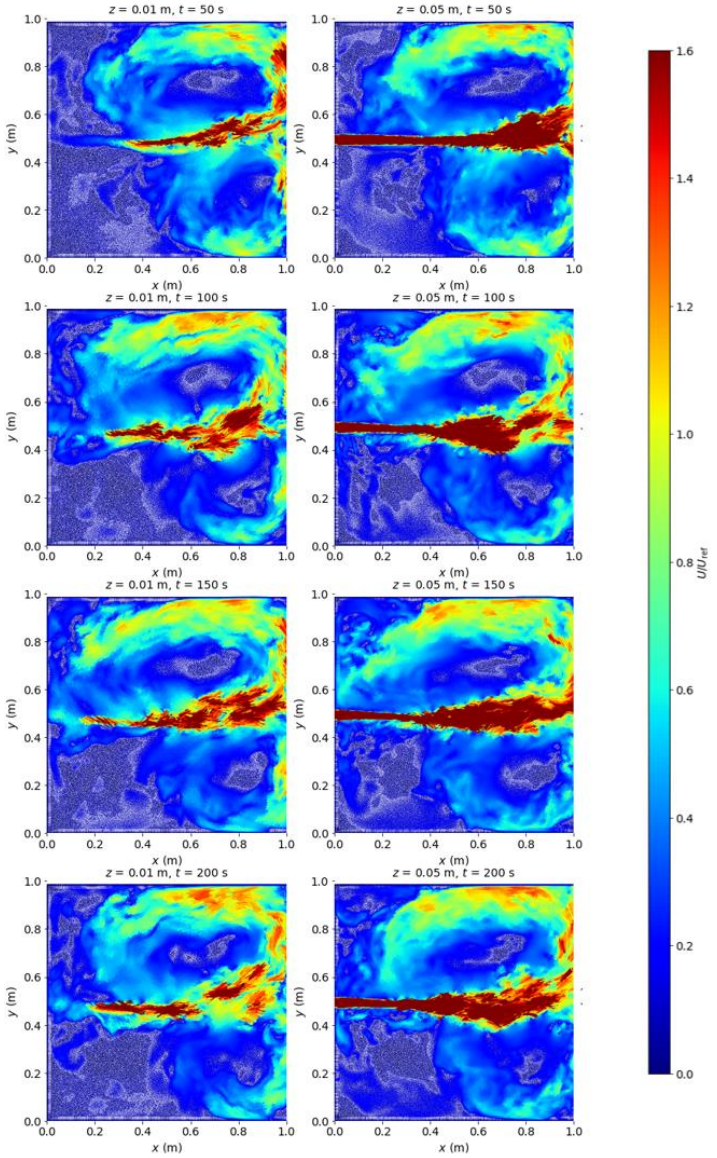

Figure 78: Case 15, Run 4. Flow patterns at bottom z = 0.01 m, middle z = 0.05 m, and surface z = 0.10 m for LES using Smagorinsky model extracted at different times

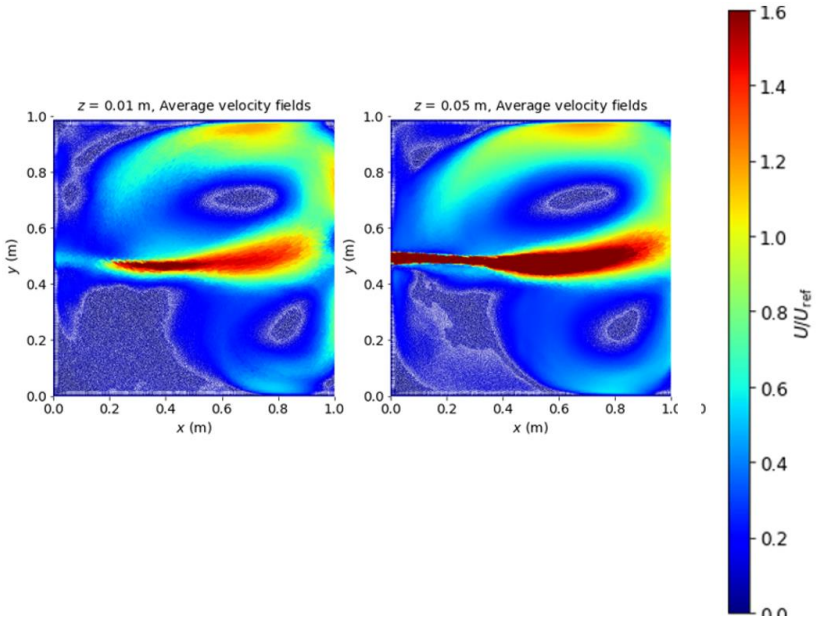

Figure 79: Case 15, Run 4. Average flow patterns at bottom z = 0.01 m, middle z = 0.05 m, and surface z = 0.10 m for LES using Smagorinsky model.

6.6. Simulation of a long reservoir case

6.6.1. Results for high Reynolds number turbulence models

Figure 80 illustrates a comparison between experimental and computed flow fields at the surface using high Reynolds turbulence models for Test 12. All three models fail to reproduce both the asymmetry and the attachment point. The two K-ε models produce nearly perfect symmetrical results, while the Rij-ε SSG model exhibits slight asymmetry, with no representation of the attachment point. There are several potential reasons for these discrepancies. Firstly, we did not conduct mesh convergence for long reservoirs but relied on the conclusions found for short reservoirs. Given the distinct typologies, it would be interesting to analyze these cases with finer mesh sizes. Secondly, ignoring the free surface can impact the results. Furthermore, we observe that the jet appears at the surface numerically only after a greater distance than what was observed experimentally, which can strongly impact its reattachment. In the present study, we were expecting to find an asymmetric pattern of type A1, but instead, we have observed a symmetrical flow pattern. In this context, the transition between symmetrical and asymmetrical configurations has been previously explored by Westhoff et al. (2018), with particular attention given to the shift between symmetrical and asymmetrical recirculation zones on both sides of the primary jet. It has been established that, for a specific flow regime, the momentum transfer from

the jet to the recirculation zone is optimized to achieve maximum energy dissipation within the shear layer between the jet and the recirculation zone. It is noteworthy that this optimized energy dissipation is greater for a symmetrical flow configuration compared to an asymmetric one.

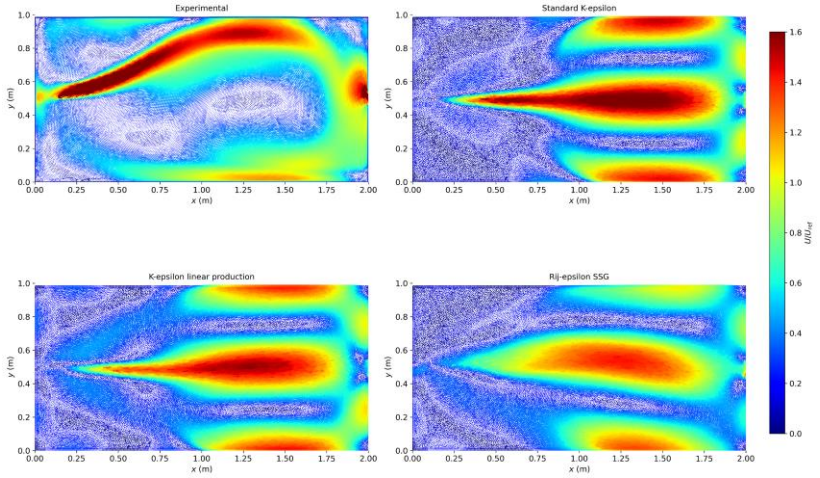

Figure 80: Case 12, Run =11. Comparison of experimental and computed flow pattern at surface using high Reynolds turbulence models

6.6.2. Results for low Reynolds number turbulence models

Spalart-Allmaras model is the only model that correctly reproduces well the reattachment point. The K-w SST model exhibits some asymmetry but fails in replicating the correct recirculation observed experimentally. The BL-v2/k and Rij-ε EBRSM models, which are extensions of the K-ε and Rij-ε SSG models, do not improve the results. The same reasons, namely, the influence of mesh refinement, free surface effects, and the maximum energy dissipation between the jet and the recirculation zone discussed for the high Reynolds number models remain valid for the low Reynolds number models. However, it is worth noting that all low Reynolds number models show significant velocity intensities at the surface compared to experimental results. Modeling with the Volume Of Fluid (VOF) method would potentially lead to a considerable improvement of the results.

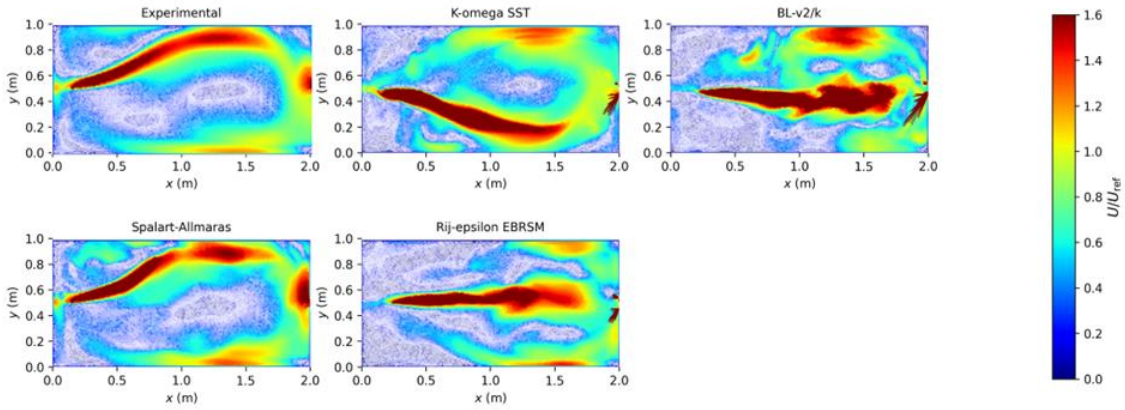

Figure 81: Case 12, Run =12. Comparison of experimental and computed flow field at surface using low Reynolds turbulence models

6.7. CONCLUSIONS

In this study, numerical modeling of four laboratory experiments with clear water and inlet jet condition was carried out using the code_saturne. Seven turbulence models were evaluated for each configuration, and their results were compared against experimental data. For the short reservoir configurations with Z_{jet}/H = 0.50, it was observed that all turbulence models were capable of adequately reproducing the asymmetry within the reservoir. However, it was noted that the low Reynolds number models provided a more accurate description of flow pattern, notably by reasonably replicating the size of the secondary recirculation. Comparison of longitudinal velocity profiles indicated good agreement between most models and the data. Regarding the long basin configuration with Z_{jet}/H = 0.50, the low Reynolds number models were unable to accurately reproduce flow typologies within the reservoir, while the low Reynolds number models performed adequately.

For test 12, At high Reynolds numbers, only the Spalart-Allmaras model exhibits a reattachment point. The K-w SST model displays some asymmetry but fails to accurately reproduce the observed recirculation. The BL-v2/k and Rij-ε EBRSM models, which are extensions of the K-ε and Rij-ε SSG models, do not offer any improvements in the results.

For Test 29 with H = 0.20 m, both high and low Reynolds number models successfully replicate the back flow pattern. However, variations are noticeable in terms of the jet spreading of back flow currents.

For Test 9, high Reynolds models effectively capture the presence of instability, but in comparison to experimental observations, they do not faithfully reproduce the identified flow patterns. Low

Reynolds models are unsuccessful in capturing the instability and results showed flow patterns similar to Test 29 with surface backflow currents. Using H = 0.095 m instead of 0.10 m, high Reynolds turbulence models remain capable for reproducing this instability, but not the flow patterns. For the Standard k-ε model, results resembling those obtained using H = 0.10 m. However, it is important to note that these flow states do not occur simultaneously. On the other hand, low Reynolds models, such as BL-v2/k and Spalart-Allmaras models displayed backflow at H = 0.010 m switch to unstable flows while reducing the water depth.

Overall, in order to replicate the various flow patterns observed experimentally, the standard K-ε, linear production K-ε, and K-w SST models exhibit satisfactory results in reproducing the A1* (Test 15), the unstable flow (Test 9) and the Backflow (Test 29) in short basins. The K-w SST model stands out for providing a more accurate representation of flow typologies, especially in asymmetric configurations with a steady-state. A more detailed comparison involving turbulent kinetic energy and Reynolds tensor would provide further insight into turbulence models and exploring applications like Large Eddy Simulation (LES) or Detached Eddy Simulation could be valuable for capturing and analyzing coherent structures.

Chapter 7. NUMERICAL MODELING OF FIELD CASE

In this chapter, we undertake an exploratory study to investigate the potential optimization of trap efficiency of the Cheylas basin by incorporating deflectors. The primary goal behind adding deflectors is to promote sediment deposition in the northern section of the basin. The present study does not address an existing operational need. It serves as an opportunity to explore optimization possibilities utilizing numerical models.

The shallow basin under investigation is the Cheylas reservoir, situated in the French Alps and a constituent of the Arc-Isère hydroelectric complex. Cheylas reservoir is the lower reservoir of the Pumped Storage Hydropower Stations (PSHS) at Cheylas-Flumet. A PSHS consists of two reservoirs, one lower and one upper, interconnected. The capacity of Cheylas real basin to be used as a sediment transit basin has been studied by Claude et al. (2019) using in-situ measurements and 2D and 3D numerical models. The ability of TELEMAC-2D-SISYPHE and TELEMAC-3D-SEDI3D (SISYPHE and SEDI-3D are, respectively, the 2D and 3D old sediment transport modules in the TELEMAC-MASCARET chain) to reproduce the flow structure and sediment transport in this basin was studied.

In the present work, the numerical setup by Claude et al. (2019) has been adapted to TELEMAC-2D and GAIA (the new sediment transport module in TELEMAC-MASCARET suite). The mesh is unstructured with a total number of nodes equal to 155 000 (Figure 82). For TELEMAC-2D module, k–ε turbulence model and LIPS scheme are used, a CFL <0.8 was chosen. A flow discharge of 98 m^3/s was imposed at the inlet boundary and a water level of 242.33 m was prescribed at the outlet boundary. According to Claude et al.'s (2019) calibration set-up, a Strickler formula was used with a coefficient equal to 55 $m^{1/3}\,s^{-1}$.

The basin we fed with cohesive material (D_{50}= 0.01 mm, density equal to 1600 kg/m^3). According to Claude et al. (2019) the diffusion of suspended sediment was set to zero, the volumetric concentration of the bed was fixed at 1000 kg m^{-3}, the critical erosion stress as τ_{ce} = 1 Pa, and the Partheniades constant M = 0.01 kg m^{-2} s^{-1}. The settling velocity was computed according to concentration from in-situ measurements (Claude et al., 2019). A concentration of 0.25 g/l was imposed at the inlet boundary, which is an operating value. The physical time was equal to 10 hours. In the first scenario, Deflector 1 was added at the entrance, while in the second option Deflector 2 was placed perpendicular to the right bank (i.e., flow direction) (Figure 83). Figure 83 Also depicts the initial flow depth in the reservoir. The water depth at the entrance is higher (+17.5

m) than the average water-depth in the basin, which could be explained by the erosion effects due to high flowrate from the inlet jet.

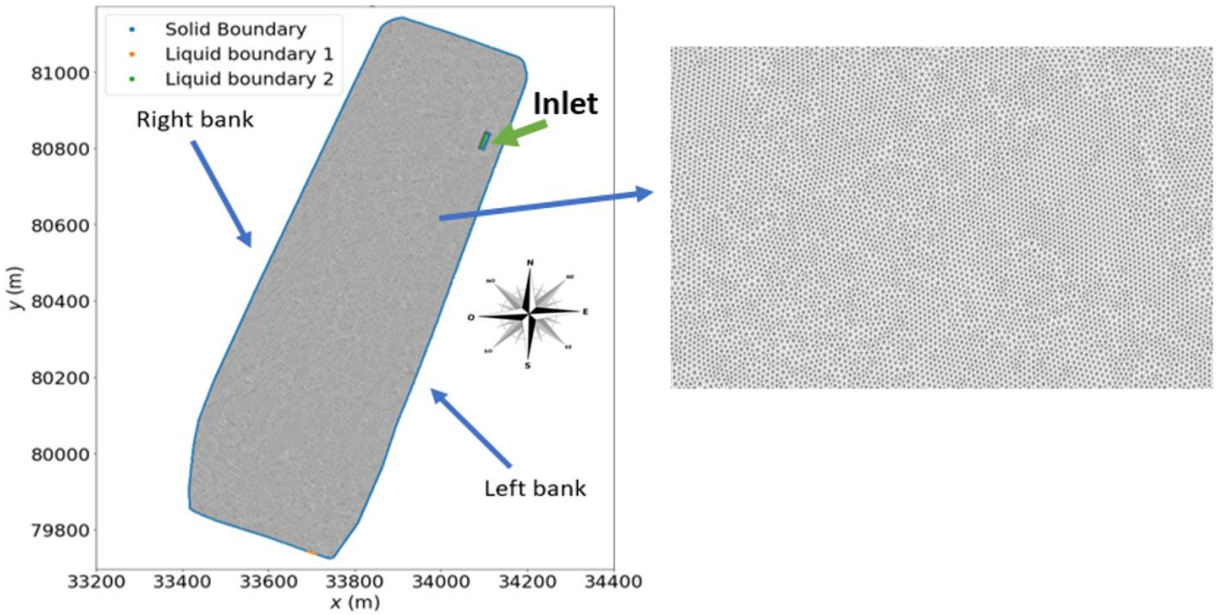

Figure 82: Unstructured 2D mesh and boundary conditions positions for Cheylas real basin

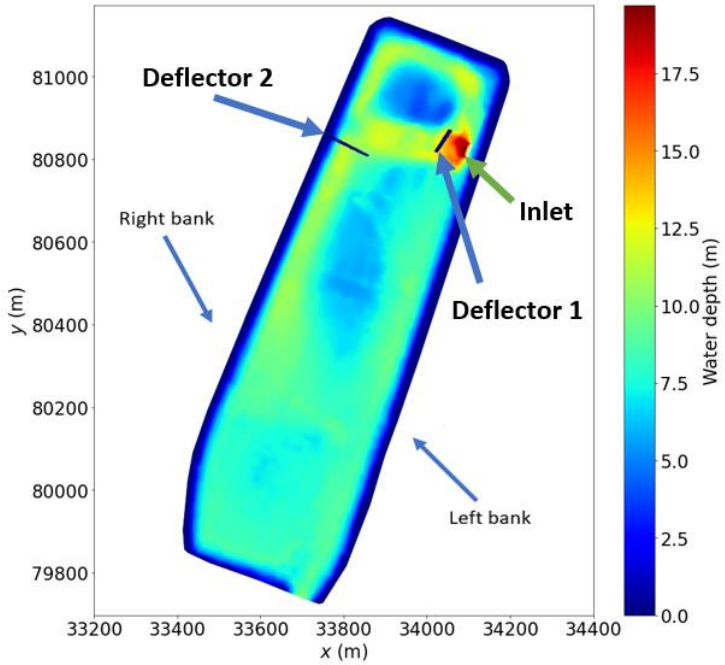

Figure 83: Initial flow depth and position of deflectors: Deflector 1 (at the entrance) and Deflector 2 (perpendicular to right bank)

Without any deflector (Figure 84a), the numerical results show a recirculation in the north, generated by the outflow from the inlet jet in a direction perpendicular to the basin length axis. The main inlet jet splits in two at the right bank of the basin. A major part of the jet leaves toward the south and sticks to the bank before joining the outlet of the basin, generating a large recirculation on the left bank of the Cheylas reservoir. As displayed in Figure 84b and c, deflectors allow a change in the position of spiling flow point which implies a change in main jet direction. The recirculation in the north is impacted by the deflectors. Its size, shape and magnitude change specifically for case with Deflect 1 (placed at the reservoir inlet). A meandering jet is found for the three studied configurations.

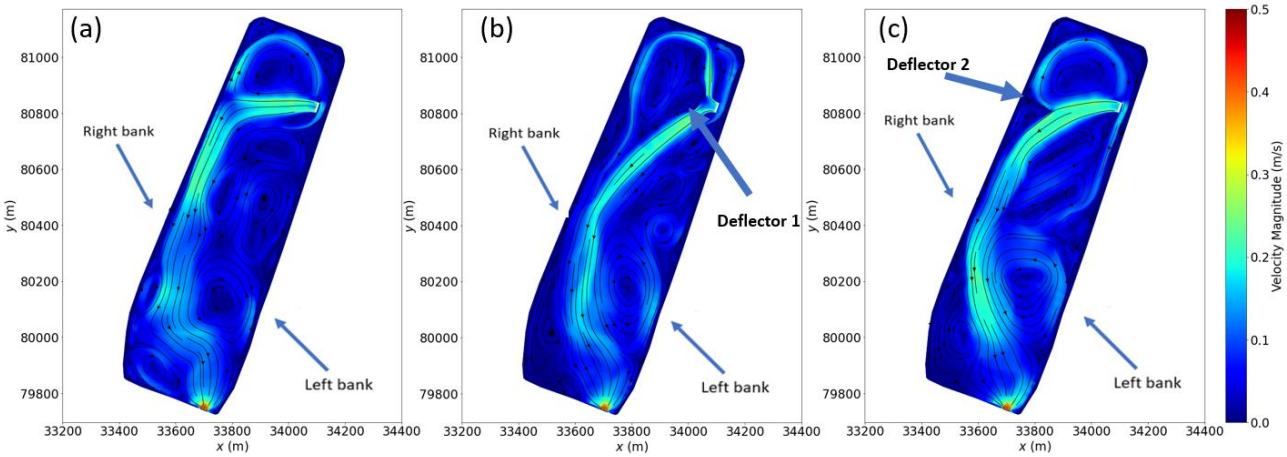

Figure 84: Simulated velocity for (a) real case, (b) Deflector 1 at entrance, and (c) Deflector 2 at right bank. Results are shown at the end of the simulation (10 h)

Figure 85 shows the bottom bed evolution due to sediment deposits after 10 hours of simulation; the negative evolution of the bathymetry due to erosion is not presented. The deposit of interest is in the northern part of the yellow bar presented on Figure 85. The results show that areas of sediment accumulation are closely related to the flow pattern, as sediment is deposited in the jet principal direction. The placement of Deflector 1 at the level of the entrance of the jet promotes deposition in the northern part of the reservoir, where dredging operation could be conducted easily. The flow splits at the deflector level, diverting the flow directly to the northern part of the basin where flow velocities are low. On the other hand, Deflector 2, placed close to the right bank and perpendicular to the flow direction, yields similar results as the original configuration.

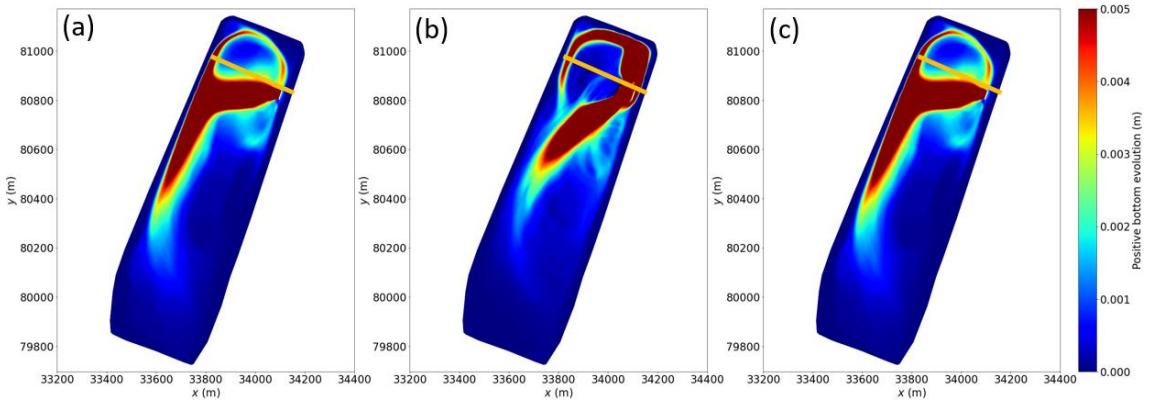

Figure 85: Bed changes due to deposition for (a) real case, (b) Deflector 1 at entrance, and (c) Deflector 2 at bifurcation right bank. Results are shown at the end of simulation (10 h). Yellow line indicates the limit of north area

To quantitively evaluate the impact of adding a deflector on sediment deposits, the net volume of deposition in the northern part of the reservoir after 10 h of simulation was calculated (Figure 86). The scenario with Deflector 1 gives better results, with higher sediment deposits and clearly stands out from the other scenario. The addition of a deflector at the inlet boundary condition allows increasing the sediment deposits in the northern part of reservoir by more than three times. A more judicious choice of the position and size of the deflector with geometrical optimization methods would certainly allow further improving of these results.

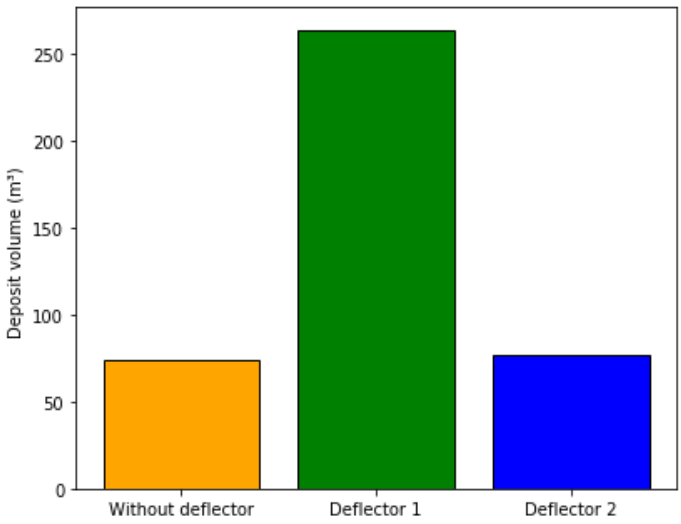

Figure 86: Deposit volume at the north of the Cheylas reservoir according to three scenarios

Chapter 8. Conclusions and perspectives

8.1. Conclusions and findings

The aim of this thesis was to enhance our understanding of flow and sedimentation in shallow reservoirs using experimental and numerical modelling. The two-dimensional (2D) depth averaged model TELEMAC-2D was first applied to simulate four laboratory experiments performed by Camnasio et al. (2013) in rectangular reservoirs with open rectangular channels as inlet and outlet boundaries. For the laboratory experiments with clear water, the TELEMAC-2D model reproduced the experimental observation and measurements accurately well. The effect of numerical scheme on the results was weak. The best data-agreement was achieved using the Spalart-Allmaras turbulence model. The k-ε, Elder, and a constant viscosity (10^{-3} m^2s^{-1}) turbulence models also demonstrated reasonable conformity with experimental data, except for one configuration (L-R) where the observed attachment point was not numerically replicated. Using TELEMAC-3D, the standard k-ε model accurately replicated the observed velocity vector field for two configurations (C-C and C-R), but failed to replicate the point of reattachment for the two configurations L-L and L-R.

The numerical model TELEMAC-2D was then involved in the design of an experimental setup, drawing inspiration from real basins and previous studies. Real shallow reservoirs are characterized by significantly smaller water depths compared to their horizontal dimensions. Design of corresponding physical models according to the Froude number similarity calls for a considerable scale geometric distortion. Additionally, the complex and varying shape of real reservoirs is usually challenging to faithfully be reproduced within the space limitations encountered in existing laboratory flumes. Using data from real reservoirs and existing laboratory experiments, the Froude and Friction numbers which have been seen to significantly impact the flow patterns, have been retained for the design of new laboratory experiences representative of real cases. Following this analysis, a reference case involving a rectangular channel with an inlet and outlet in a free-surface channel, along with four additional preliminary configurations, has been identified for further study. Numerical pre-simulations were conducted to choose two novel flow patterns for experimental investigation, specifically involving a jet at the inlet and an inlet positioned at the lateral boundary.

An experimental setup was constructed and put into operation at the University of Liège. The primary emphasis was on clear water entering a rectangular reservoir, while focussing on the

study of the effect of the inlet boundary condition. Two types of inlet boundary were tested: open rectangular channel and pressurized pipe (i.e. jet); an open channel was used at the reservoir outlet. Furthermore, the inlet jet position was subject to variation to evaluate its influence on the results. The reservoir length was also adjustable. An extensive range of Reynolds, Froude and Friction numbers was explored. In total forty-two (42) experiments were performed. The first twenty-two (22) experiments were conducted with a water depth in the reservoir fixed at H = 0.10 m, involving variations in reservoir length, hydraulic boundary conditions, and vertical position of the inlet jet (near the bottom, mid-depth, or near the surface). For the case of a free surface inlet channel, the observed flow patterns aligned with earlier investigations in analogous setups that involved steady or meandering jets within the reservoir. In contrast, when employing a circular inlet jet, our experimental findings unveiled that the nature of the flow pattern was influenced by several factors: vertical positioning of the inlet jet, reservoir geometry (short versus long), and hydraulic boundary conditions (Froude and friction numbers). When the circular inlet jet was positioned close to the reservoir bottom, an unstable flow pattern characterized by random switching over time was observed, regardless of the reservoir length or hydraulic boundary conditions. This unstable flow pattern was also observed for long reservoirs under the lowest Froude number condition, irrespective of the vertical positioning of the inlet jet. In all other tested configurations (long and short reservoirs, with (F,S) values of (0.76, 0.14) and (0.44, 0.16), and Z_{jet}/H equal to 0.50 and 0.75, and to short reservoirs with (F,S) = (0.13, 0.21) at Z_{jet}/H equal to 0.50 and 0.75) a steady flow pattern emerged. A steady reattached jet was identified, which indicated asymmetrical flow. This asymmetry manifested as a reattached point downstream of the reservoir for short reservoirs and as a reattached point upstream of the reservoir for long reservoirs.

Subsequently, intrusive measurements were taken vertically across different configurations, providing a deeper understanding of the vertical flow dynamic and facilitating a thorough analysis of turbulence. This was preceded by a careful validation of the ADVP probe, as outlined in Appendix E, which consisted of two steps. The first step involved comparing the ADVP probe with the ADV probe, while the second step focused on evaluating the repeatability of the ADVP measurements (Appendix E). Nevertheless, the consistency of the results ensured the stability and accuracy of our measurements. Longitudinal, transversal, and vertical mean velocities were extracted and compared for each configuration to assess the effect of jet position and hydraulic conditions (Appendix F). Furthermore, an evaluation of the reservoir anisotropy was conducted utilizing the Lumley triangle visualization (Appendix G), which revealed that the points belonged to two states of axisymmetric turbulence: cigar-shaped and pancake-shaped. Lastly, the turbulent signal underwent analysis using a range of spectral analysis tools. A second set of twenty (20)

configurations was carried out with a fixed water depth of H = 0.20 m (Appendix I). In the case of a jet situated near the bottom, the flow pattern underwent a transition from instability when H = 0.10 m to stability when H = 0.20 m, manifesting a Blackflow (BF) pattern distinguished by surface return currents. In the scenario of a mid-depth jet with Z_{jet}/H = 0.50, consistent flow pattern (A1*) characteristics were observed for short reservoir (H = 0.10 m), while long reservoir with H = 0.10 m witnessed a shift from asymmetric flow(A1) stability to instability. When examining a jet with Z_{jet}/H = 0.75, the flow pattern (A1*) remained unaltered for short basins comparing to results with H = 0.10 m , except for a specific configuration with the highest Froude number, which resulted in a transition to a symmetric configuration (S0). For long reservoir, a comparable change in flow pattern occurred as observed with Z_{jet}/H = 0.50, involving a transition from asymmetric stable flow with an reattachment point (A1) to unstable flow.

Flow patterns and sedimentation in rectangular shallow reservoirs, featuring a circular inlet jet and a free surface channel at the outlet, were investigated through a series of laboratory experiments. A total of twelve (12) tests were conducted, wherein we systematically varied parameters such as reservoir length, hydraulic boundary conditions, vertical position of the inlet jet (mid-depth or near surface), and inlet sediment concentration. The thickness of the deposits was measured using an UWS probe. In all configurations, the deposition zone tended to be centrally located within the flow pattern. Except for Test 3 and 4 (with sediment), where a momentary shift in flow typology occurred as the jet switched from the right side to the left side, no significant time-dependent variations in mean flow patterns were observed during the introduction of sediments into the setup and the subsequent accumulation of deposits in the reservoir. Long reservoirs exhibited high trapping efficiency compared to short reservoirs, which agrees with previous findings by Dufresne et al. (2012) who utilized a free surface channel at the inlet. Notably, the flow rate had a noticeable impact on trapping efficiency in both long and short reservoirs, with higher flow rates (characterized by a high Froude number and low Friction number) leading to decreased trapping efficiency. The shape of the horizontal surface of the deposition area evolved during the injection period and varied between different configurations. However, the standard deviation of this temporal evolution remained relatively consistent. Importantly, the calculation of the barycenter of the deposition zone consistently aligned across all configurations for long reservoirs. Despite sediment deposits reaching up to 64% of the flow depth, they did not significantly affect the flow patterns, as they were not located in the main direction of the inlet jet. Regarding the observed bursting phenomena in configurations with (F, S) = (0.44, 0.16) and (0.76, 0.14), probability density functions (PDFs) displayed either elliptical or circular shapes, indicating the isotropic nature of turbulence.

Numerical simulations were conducted to simulate clear water flow in shallow rectangular reservoirs with four configurations using the code_saturne software. Seven turbulence models were assessed for each configuration, and their results were compared to experimental data. The main findings are:

- For the short reservoir case with H = 0.10 m and Z_{jet}/H = 0.50, all turbulence models adequately reproduced the asymmetry within the reservoir. However, low Reynolds number models provided a more precise representation of flow characteristics, especially regarding the size of secondary recirculation. Longitudinal velocity profiles showed good agreement between most models and the data, but the high Reynolds number Rij-epsilon -SSG model and the low Reynolds number K-omega SST model had some difficulties to provide accurate transverse velocity profiles.
- For the short reservoir case with H = 0.20 m and Z_{jet}/H = 0.10, both high and low Reynolds number models successfully replicated flow characteristics, but variations were observed in the spreading of back flow currents.
- For short reservoir case with H= 0.10 m and Z_{jet}/H =0.20, high Reynolds models captured instability but did not faithfully reproduce the observed flow patterns. Low Reynolds models were unsuccessful in capturing the instability, resulting in flow patterns similar to the previous case with surface back flow currents. Testing H = 0.095 m instead of 0.10 m, high Reynolds turbulence models still reproduced the instability, with the Standard k-epsilon model yielding similar results as with H =0.10 m. However, these flow states did not occur simultaneously. On the other hand, low Reynolds models such as Rij- ε EBRSM and K-w SST exhibited backflow at H = 0.10 m and shifted to unstable flows as the water depth decreased. Spalart-Allmaras and BL-v2/k failed to capture the instability even when the water depth is reduced.
- For the long basin case with H= 0.10 m and Z_{jet}/H = 0.50, low and high Reynolds number models struggled to accurately reproduce flow patterns. At high Reynolds numbers, only the Spalart-Allmaras model displayed a reattachment point. The K-w SST model showed some asymmetry but could nott accurately replicate the observed recirculation. Models such as BL-v2/k and Rij- ε EBRSM, extensions of the K- ε and Rij- ε SSG models, did not improve the results.

In a general context, and with the aim of modeling the diverse flow patterns observed in experiments, it can be noted that the standard K- ε, linear production K- ε, and K-w SST models demonstrated effective performance in replicating the three flow patterns found in short basins,

including both stable and unstable scenarios. Notably, the K-omega SST model provided a better representation of flow patterns, particularly in cases of asymmetric configurations characterized by a steady-state.

The hydro-sedimentary numerical model TELEMAC-2D, coupled with its sediment transport module GAIA, was used to simulate flow and sediment transport processes in a real reservoir.. Even though this configuration differs from the series of experiments conducted in the laboratory in terms of reservoir size, the presence of cohesive sediments, and the position of upstream and downstream boundary conditions, it serves as an exploratory approach for engineering applications. The introduction of deflectors was undertaken to investigate potential optimization of trap efficiency in the north area, where dredging operation could be conducted easily. Three scenarios were evaluated, and the addition of a deflector at the reservoir inlet leads to increased sediment accumulation in the northern reservoir area.

8.2. Perspectives

Methodology

Initially, a persistent research question revolves around the meticulous development of methods to design idealized representations of real basins. These representations would serve for laboratory testing, accounting for the specific constraints of these environments, while preserving the phenomenological characteristics inherent to actual basins, particularly the various flow patterns. The work conducted on the Cheylas basin illustrates this approach. The objective thus involves extending this methodology to several other basins. One potential perspective involves delving deeper into the analysis of conformal transformations, a subject explored across various domains linked to modeling issues in numerical mechanics. These transformations have already demonstrated their efficacy in diverse engineering fields such as aerodynamics, hydrodynamics, thermodynamics, and numerical methods, achieving significant success. The perspectives aim to leverage these advantages for small-scale hydraulic applications.

In the current approach, we have delineated the evolution of flow typologies into three stages. The initial step is essential for isolating the effects of each stage on flow typology and ensuring the code's capability to accurately replicate these distinct stages. Once this step is accomplished, it becomes pertinent to evaluate more intricate configurations, involving linear combinations of the studied setups, which would better resemble real-world basins. For instance, a more

representative scenario could involve a jet-like inlet on a lateral wall accompanied by curvature and an outlet in the form of a spillway.

Experimental investigations

Due to time constraints, certain experiments could not be conducted, particularly those involving an inlet located on the lateral wall. The outcomes of the performed numerical pre-simulations underscore the significance of investigating this boundary condition experimentally.

From an experimental standpoint, particularly concerning the clear water segment, the incorporation of alternative measurement techniques can complement the research. Utilizing Particle Image Velocimetry (PIV) would offer a more detailed depiction of flow behavior along the vertical axis, particularly for cases of periodic or pseudo-periodic flows. These techniques would also facilitate a more comprehensive exploration of the flow, enhancing understanding of coherent structures. Additionally, leveraging PIV results, Proper Orthogonal Decomposition (POD) could be employed to effectively discern dominant modes in fluid dynamic data, enabling streamlined analysis and reduced-order modeling. POD presents a robust framework for diminishing dimensionality and revealing pivotal flow characteristics in fluid dynamics.

Another perspective involves examining transient regimes using hydrographs with an inlet jet (e.g., flushing sediment type). However, this requires careful consideration of the post-processing to be applied to the ADVP data.

In the context of sediment-related investigations, it is necessary to augment the existing experiments carried out at H = 0.20 m by incorporating sediment-laden tests. Furthermore, especially in the context of non-cohesive sediments, for the purpose of achieving a more comprehensive representation of real-world basin dynamics, it becomes essential to study experiments using sediment mixtures covering a wider spectrum of particle diameters, encompassing both cohesive and non-cohesive sand mixtures.

Numerical investigations:

In the sediment-related aspect, the investigation into various sediment transport parameters (such as settling velocity, diffusion coefficient, and equilibrium near-bed concentration formulas) demonstrates their significant sensitivity and the challenges associated with manual calibration. The possibility of an automatic calibration of the Camnasio et al. (2013) experiments can be considered. This would involve initially assessing the impact of each parameter using a global sensitivity analysis and subsequently conducting an automated calibration through the optimization of a defined cost function.

TELEMAC-2D facilitated the validation of both the Camnasio et al. (2013) experiments and the pre-simulation of experiments carried out during this thesis. However, TELEMAC-3D encountered certain challenges in replicating the inlet condition. A prospective of this work involves enhancing the fidelity of reproducing this inlet condition and refining the treatment of turbulence within TELEMAC-3D, encompassing turbulence models and wall laws. Indeed, the results achieved with code_saturne provided guidance on turbulence models that best replicate the experimental outcomes.

In the context of code_saturne, there is a compelling opportunity to delve deeper into the analysis of turbulent quantities, specifically the Reynolds tensor and Lumley triangle, especially within configurations that encompass Large Eddy Simulation (LES). Conducting a comprehensive exploration of these turbulent parameters under LES conditions could offer a more intricate understanding of the flow dynamics and turbulence characteristics, thereby enriching the insights gained from the simulations. Moreover, the incorporation of Proper Orthogonal Decomposition (POD) presents an intriguing way for enhancing the analysis of fluid dynamics within these simulations. Applying POD can aid in dissecting the complex flow field into its dominant modes, allowing for a clearer identification of coherent structures. By extracting these coherent patterns, researchers can gain deeper insights into the underlying mechanisms driving the fluid behavior, leading to improved understanding and potential predictive capabilities. By pursuing these avenues of investigation within the framework of code_saturne, researchers stand to uncover valuable insights into the turbulence and flow structures, thus contributing to the broader understanding of fluid dynamics and turbulence modeling.

Appendix A: Horizontal evolution of sediment deposit (Chapter 5)

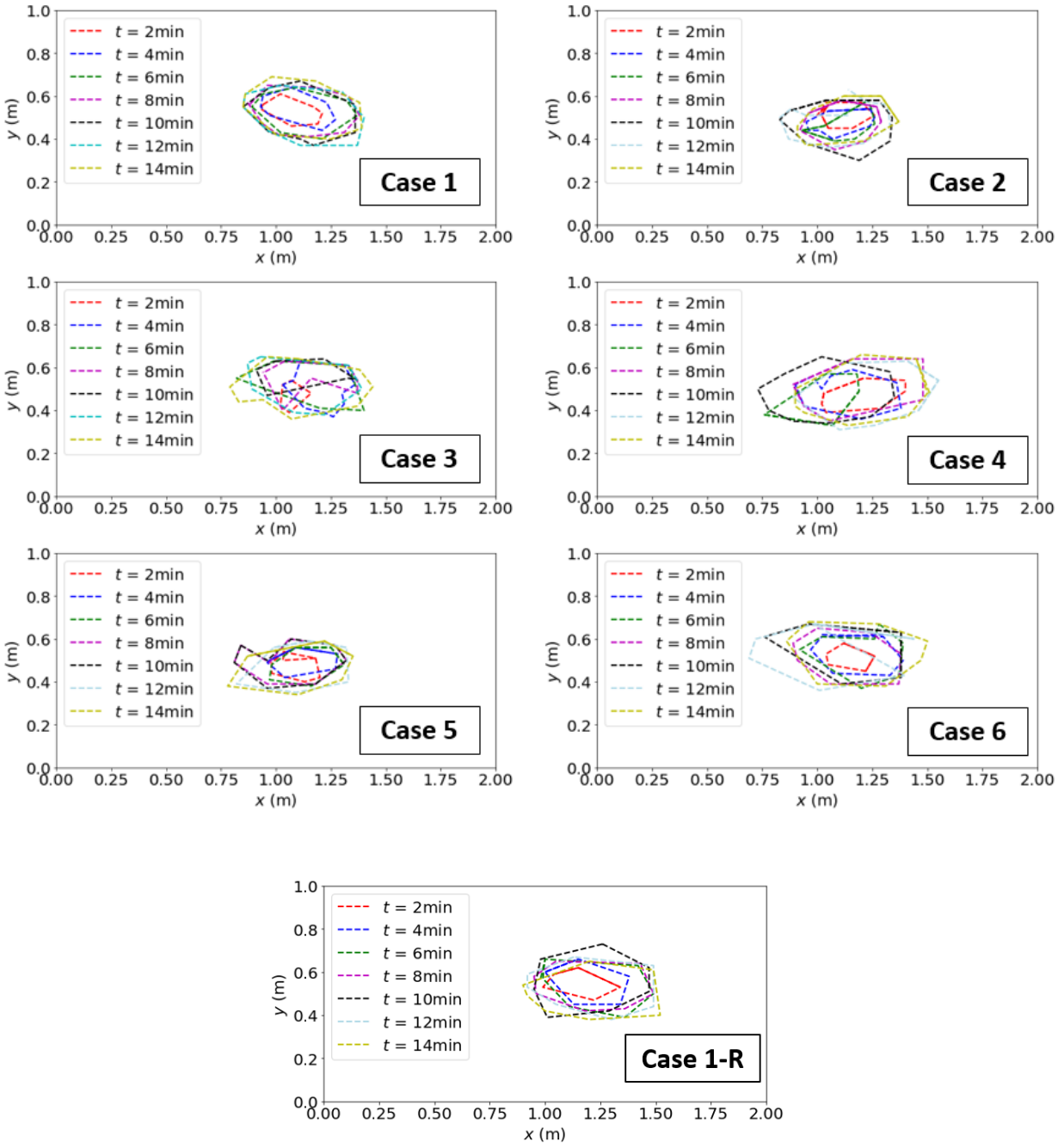

Figure A1: Long reservoir tests - Evolution of Horizontal deposition during time injection

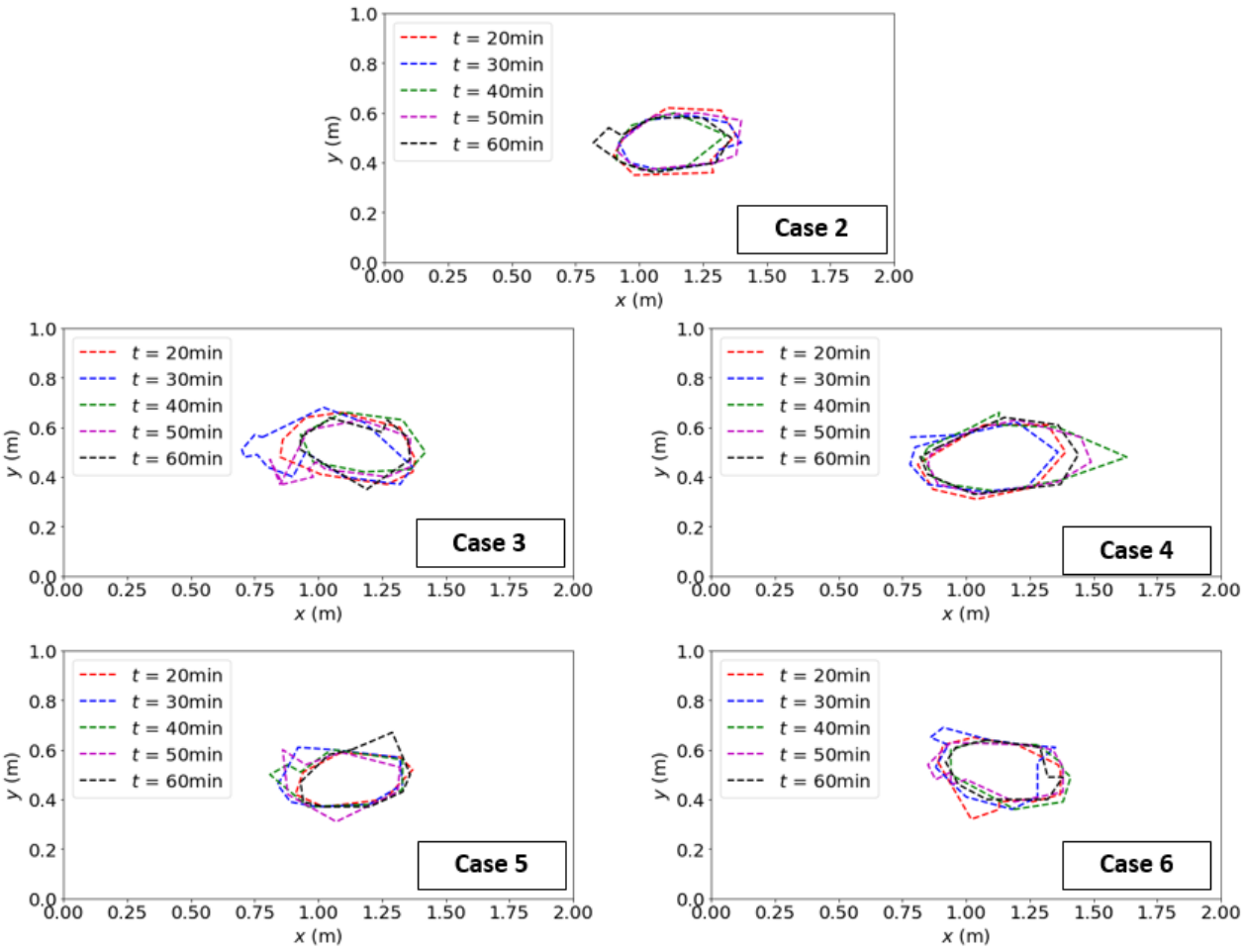

Figure A2: Long reservoir tests - Evolution of horizontal areas of deposits after the end of sediment injection

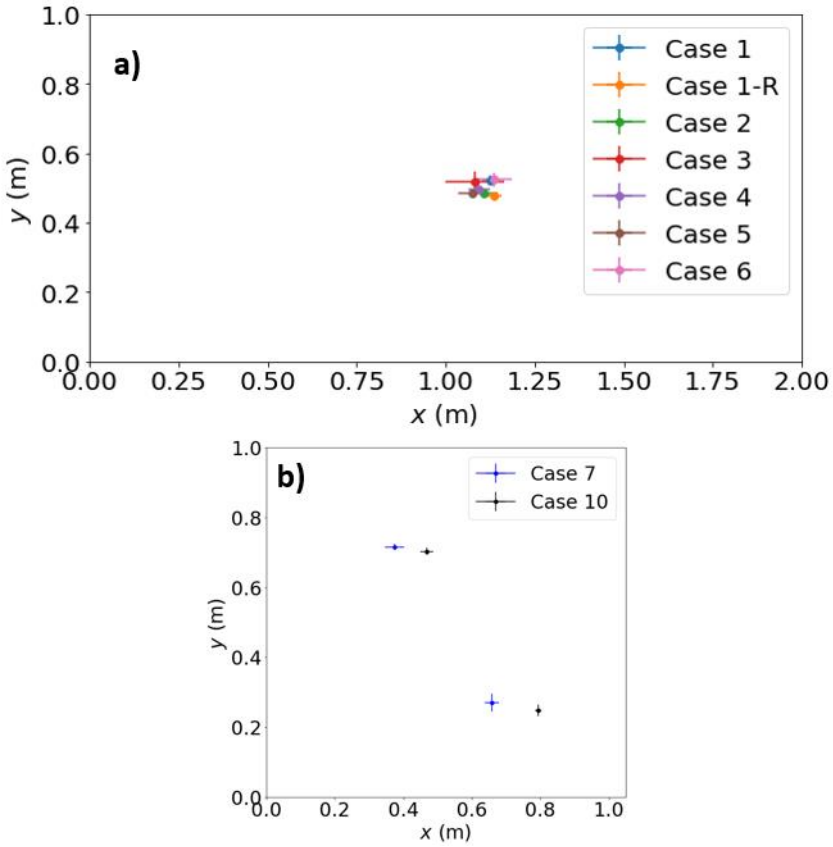

Figure A3: (a) Mean and standard deviation for barycenter of eddies of long reservoir cases, (b) Mean and standard deviation for barycenter of eddies of short reservoir cases

Appendix B: Mapping of sediment deposit (Chapter 5)

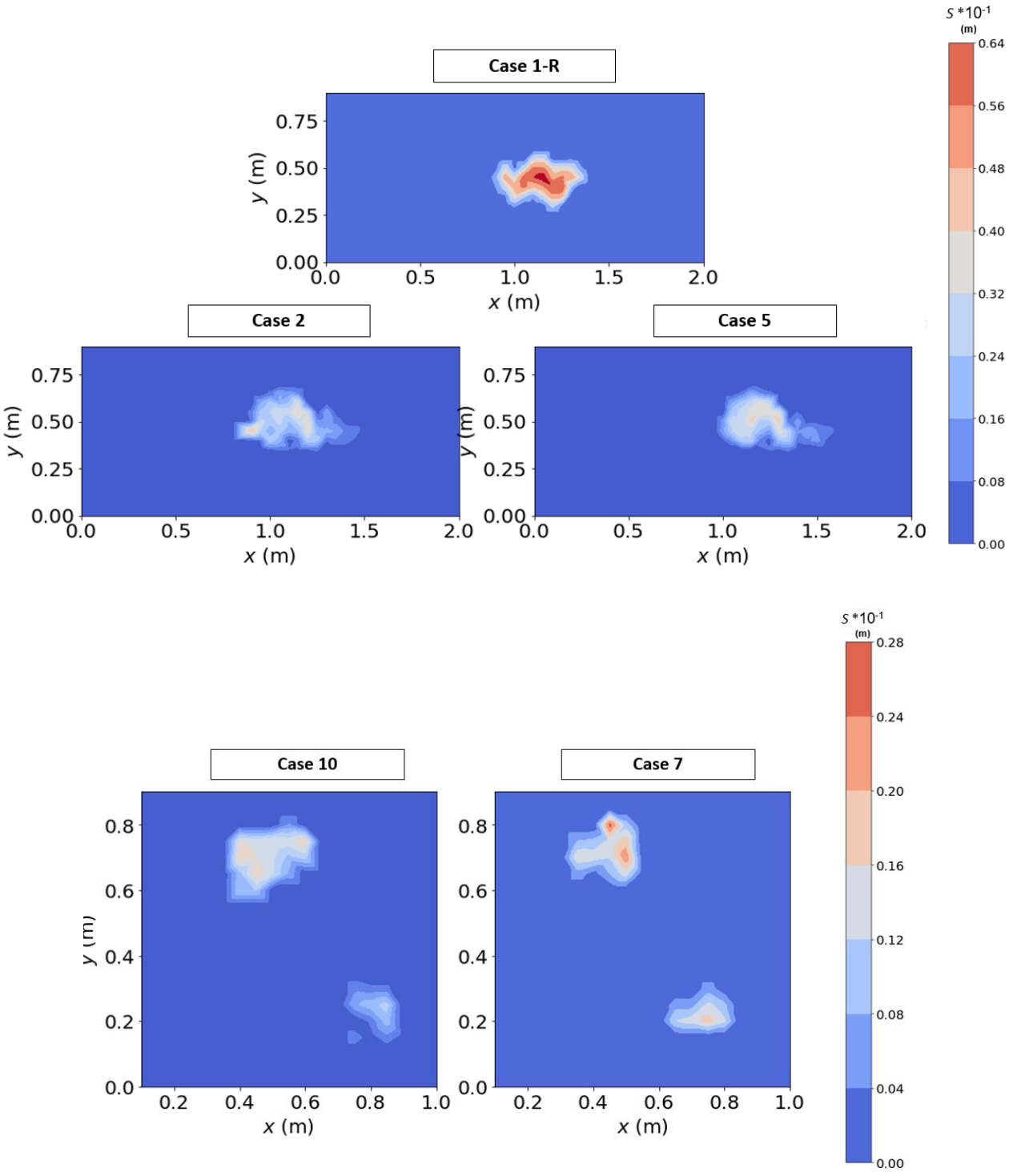

Figure B1: Thickness of sediment deposits after 1 h of experience

Appendix C: Quadrant analysis (Chapter 5)

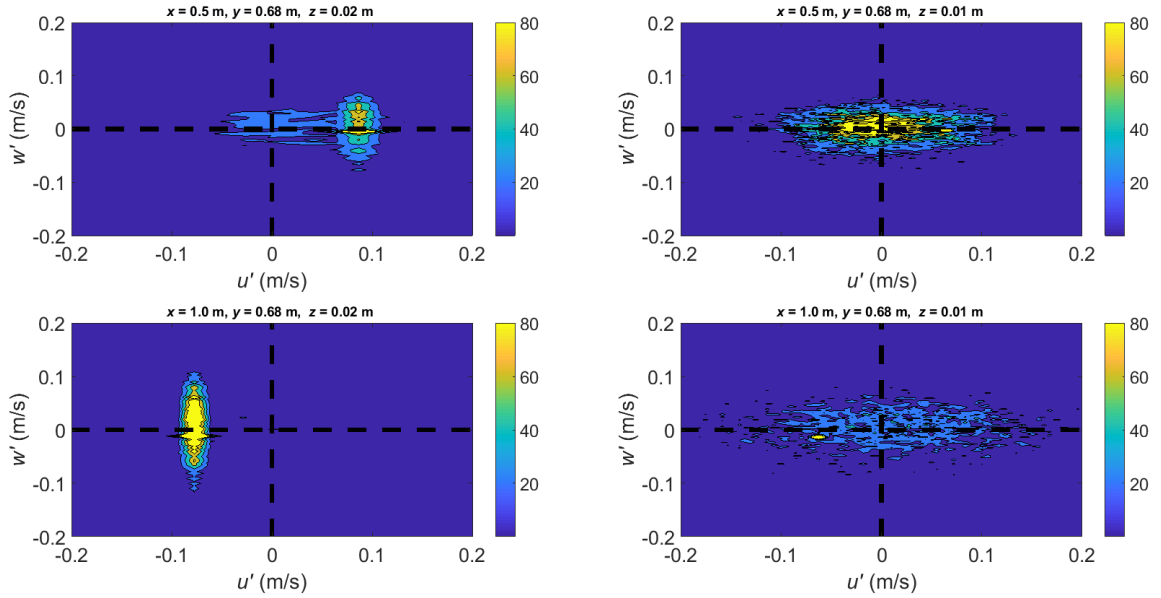

Figure C1: Case 6 -Joint probability density function of fluctuations (u',w') for four points near bottom

Table C1: Occurrence Probability of each quadrant of short reservoir cases at e (x= 1.00 m, y=0.68 m, z=0.02 m), f (x=1.00 m, y=0.68 m, z=0.01 m), g (x=1.70 m, y=0.68 m, z=0.02 m), h (x=1.70 m, y=0.68 m, z=0.01 m).

	Cases (1,2)				Case 3				Cases (4,5)				Case 6			
(%)	e	f	g	h	e	f	g	h	e	f	g	h	e	f	g	h
Q1	26.7	29.2	23.9	29.2	21.6	27.1	25.8	22.9	17.0	22.3	24.7	24.0	23.3	30.0	22.3	24.3
Q2	22.6	22.7	24.1	22.7	22.3	30.8	25.7	29.1	30.0	25.8	25.6	27.1	25.9	35.6	28.2	28.7
Q3	17.4	18.6	28.1	18.6	33.2	22.8	26.7	23.7	38.0	31.1	24.2	25.1	27.9	19.1	23.5	25.1
Q4	33.3	29.6	23.8	29.6	22.9	19.3	21.7	24.2	15.0	20.7	25.5	23.8	22.9	15.3	26.0	21.9

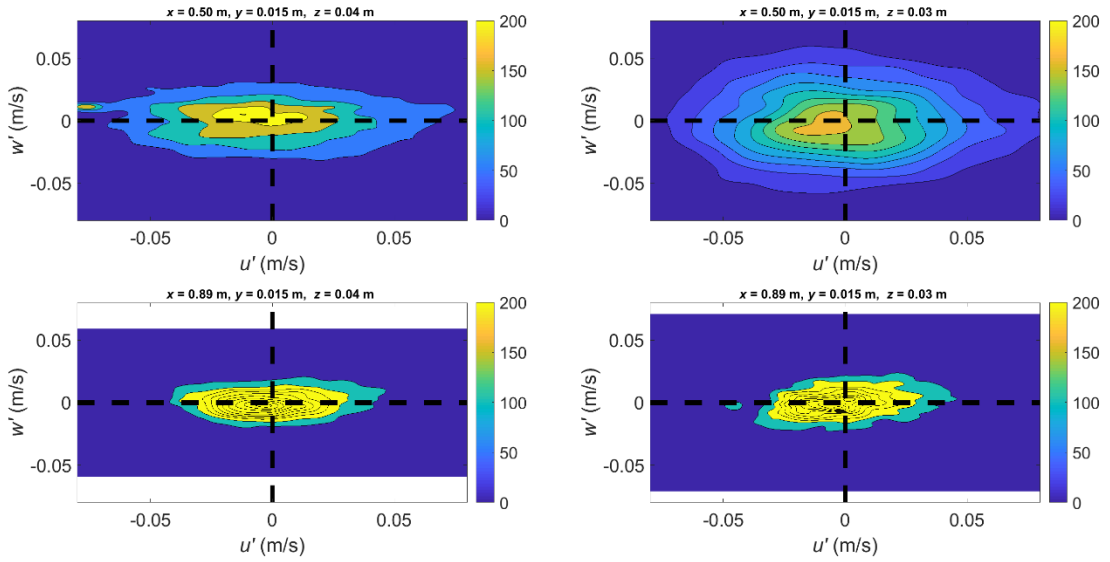

Figure C2: Case 7-Joint probability density function of fluctuations (u',w') for four points near bottom

Table C2: Occurrence Probability of each quadrant of short reservoir cases at e (x= 0.50 m, y= 0.68 m, z= 0.04 m), f (x= 0.89 m, y= 0.68 m, z= 0.03 m), g (x= 0.50 m, y= 0.68 m, z= 0.04 m), h (x= 0.89 m, y= 0.68 m, z= 0.03 m)

	Case 7				Case 8				Case 10				Case 11			
(%)	a	b	c	d	a	b	c	d	a	b	c	d	a	b	c	d
Q1	24.9	28.6	29.0	29.0	25.6	25.7	28.1	30.2	25.5	25.5	25.6	26.7	24.3	26.1	27.2	26.5
Q2	25.4	23.0	20.7	22.6	25.2	25.8	21.7	19.7	25.6	27.8	25.3	24.8	25.8	23.7	25.2	25.8
Q3	24.2	27.7	29.5	20.4	26.5	27.1	28.4	31.0	25.6	22.5	24.7	25.2	25.2	25.8	22.5	23.3
Q4	25.4	20.7	20.9	28.6	22.6	21.5	21.8	19.1	23.3	24.3	24.4	23.3	24.7	24.4	25.1	24.4

Appendix D. Review of turbulent jet (Chapter 4)

What is the current state of the art in the literature regarding jets in general, spanning from free jets to shallow water jets?

Jet flows are a common occurrence in various engineering applications, such as pollutant discharge, heating, cooling, ventilation, airfoil design and chemical engineering. Numerous experimental (Davies, 1966), analytical (Townsend, 1987) and numerical investigations have enhanced scientists understanding of the complex processes and physics involved. The literature has focused on investigating various parameters that can affect jet flows, including Reynolds number, nozzle exit and boundary conditions, as studied by Abdel-Rahman (2010). One of the key areas of interest has been understanding the physics of a round axisymmetric turbulent jet, which serves as a classical prototype of the shear flow family (which includes wakes and mixing layers). This type of jet is produced when a fluid is ejected at a velocity through a circular nozzle of diameter, into a receiving environment, which could have different temperature, velocity and pressure depending on the application. At the jet exit, a shear layer is formed as the flow interacts with the surrounding environment, which is dominated by Kelvin-Helmholtz instabilities, resulting in the formation of azimuthally coherent vortices. These coherent structures are highly inhomogeneous and dominate the flow field and are on the order of magnitude of the geometry, as depicted in Figure D1. According to A.K.M.F Hussain (1983), they can be defined as "a connected, large-scale turbulent fluid mass with phase-correlated vorticity over its spatial content".

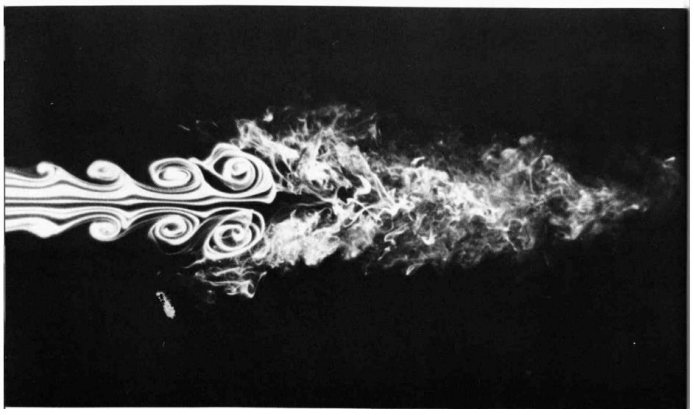

Figure D1: Development of axisymmetric oscillations in the near-field region of a round jet, rolling up into vortex rings and then abruptly becoming turbulent (from Van Dyke, 1982)

Two main categories of jets can be distinguished: the free and the bounded jets. Free jets results when the kinetic energy is driven into receiving environment without obstruction or restriction.

Three different regions can be defined in the free jet (Figure D2): the near-field, the intermediate-field and the far-field. The near-field region is located immediately downstream of the ejection section. It covers a length of a few diameters (and is usually found within 0 <x/d< 6) and has been the subject of numerous studies. This region is also called the potential zone. The flow characteristics in the near field region is strongly impacted by the characteristics of the exit-nozzle (temperature, salinity, position, angle of exit…). The intermediate region (or region of the transition, found within 6<x/d<30) which extends from the end of the potential core to the beginning of the far-field impact strongly the development portion of the jet. The far field / fully developed or self-similar region is located downstream of the transition zone. The characteristics of the flow field in this region are independent of the nature of boundary condition.

Another approach consists of dividing the development of the jet on two phases that are the zone of flow establishment (ZFE) and the zone of established flow (ZEF). According to Browne et al. (1984), the ZFE include the potential core and the region of transition to a self-similar region.

The self-similarity (Abdel-Rahman, 2010) was introduced to simply the behavior turbulence flows. Main parameters used for self-similarity of turbulent jet are the center velocity, which is the peak of the velocity profile (U_m), and the half width of the jet (b_0) which corresponds to the distance between half of the centerline velocity and the centerline velocity on the bell-shaped velocity profile. Empirical solution for the evolution of this quantities is found in $U_m/U_0=(3/5)/(x/b_0)^{1/2}$ with half width $b_0 = 0.11*x$, Rajaratnam (1976); with U_0 the jet velocity at the inlet.

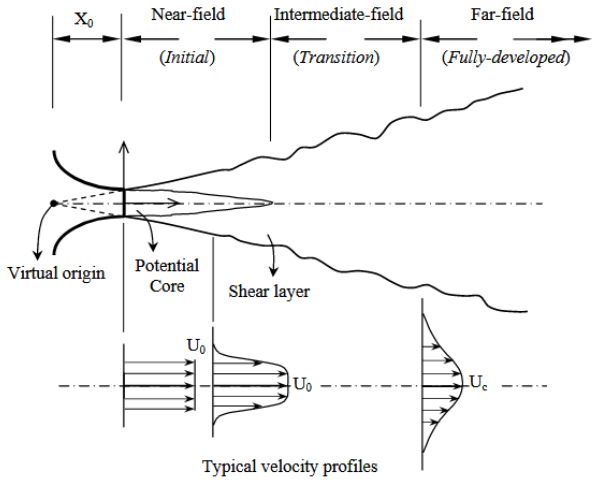

Figure D2: Schematic of the free turbulent jet evolution based on field transition. From Abdel-Rahman (2010)

Bounded jets can be classified into three main categories: wall jets, free surface jets and shallow water jets, which discharge near or at a boundary, respectively solid boundary, free surface, or both. Wall jets, defined by Launder and Rodi (1981), refer to a shear flow directed along a wall where the streamwise velocity over a certain region within the shear flow exceeds that in the external stream due to the momentum supplied linearly. Wall jets have been a subject of extensive research for several decades, with several reviews available on the topic, including those by Launder and Rodi (1981, 1983), Abrahamsson et al. (1997), and George et al. (1997). To measure the velocity profiles and turbulent characteristics of wall jets, several authors have employed advanced techniques such as LDV, ADV and PIV. Notable examples include Ead and Rajaratnam (2002), Pilechi et al. (2011), Eriksson (1998), Kaffel et al. (2015), and Guo et al. (2017). Similar to free jets, wall jets can be divided into three regions based on the velocity profile: the potential core region (PC), which has a uniform velocity profile; the characteristic decay region (CD), where the nozzle characteristics have a significant impact on the jet evolution, including the near-field and intermediate field and the radial decay region (RD), which is analogous to the far-field region for free jets. Padmanabham and Gowda (1991) described the velocity profiles in the PC and CD regions, as shown in *Figure* . An empirical solution for wall jets in the far-field region is also defined. $U_m/U_0=(3/5)/(x/b_0)^{1/2}$ with $b_0 = 0.068*x$.

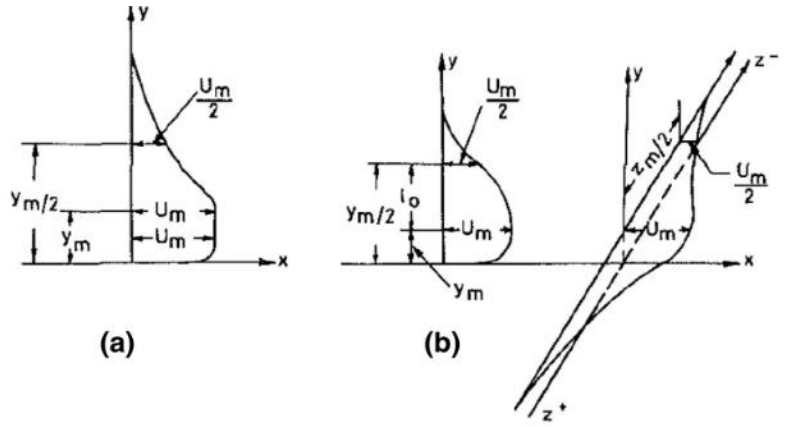

Figure D3: Velocity profiles in different regions of a wall jet: (a) the potential core, (b), Characteristic and radial decay. From Padmanabham and Gowda (1991)

The free surface jet has received relatively less attention compared to the wall and free jets, despite sharing some common characteristics with the wall jet. However, the nature of the boundary can create some fundamental differences between them. While the wall boundary requires zero velocity (no-slip boundary condition), the free surface allows non-zero velocity and imposes a kinematic boundary condition such that the normal velocity corresponds to the variation

of the free surface. Some researchers have investigated the impact of turbulent structures generated by the jet on the free surface. For instance, at high Froude numbers, Rajaratnam and Humphries (1984) observed a decrease in velocity near the surface due to wave generation. Walker et al. (1995) studied the effects of Froude and Reynolds numbers on the turbulence structure and interaction between the subsurface turbulence and free surface. They found a decrease in surface-normal turbulence intensities near the free surface and an increase in turbulence intensities. Tay et al. (2017) examined a submerged rectangular jet near the free surface using the PIV method to measure mean and turbulent characteristics in the free surface. The authors discovered that the interaction between the jet and the free surface had a greater impact on surface-normal velocity than mean streamwise velocity. They also presented a velocity profile schematic of the free surface jet, which revealed the presence of a recirculation region in the near-field area

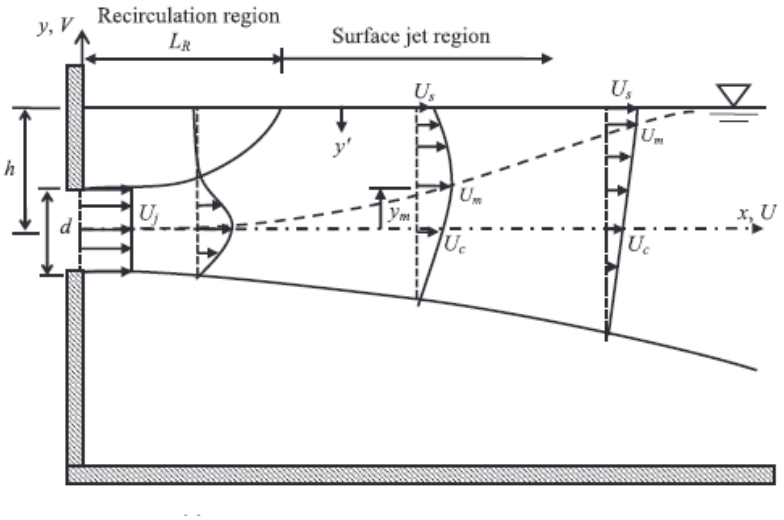

Figure D4: Schematic of flow field of free surface jet. From Tay et al. (2015)

Shallow water jet could be defined by jet bounded by wall in one side and free surface on the other. Less important literature could be found about this subject. The effect of a discharge of non-buoyant jet into shallow environment was studies by Rajaratnam (1976). LDV was used by Dracos et al. (1992) for studying the jet discharging on shallow water receiving environment with infinite lateral extent. Similarly to free and wall jet, three regions of jet evolution (near, intermediate and far) fields are found. Using PIV method, Shinneeb (2006) studied a shallow water round jet with a Reynolds number of 9000. Jet positions in the vertical were varied.

As presented previously, jet type could be defined as free or bounded jets. Most of previous studies are presented on open environment. Jet could also be an inlet boundary conditions of

confined environment such as cavity, reservoir, ponds, tanks or shallow reservoir… In this context, some laboratory experiments were interested on shallow reservoir with a jet at the inlet. Stovin and Saul (1994) performed a series of experiments on a rectangular reservoir whose inlet and outlet were circular pipes. Adamsson et al. (2005) performed an experimental study on a large basin (i.e., 13 m long and 9 m wide and 0.8 m high); the inlet was a circular jet with a diameter of 0.23 m and the outlet was a weir. Two larges symmetrical patterns were observed. Dufresne (2008) conducted 55 experiments in a rectangular reservoir with a circular pipe at the inlet and a frontal weir at the outlet. Author observed an asymmetrical and stationary flow for low water heights and a symmetrical and stationary flow for higher water heights. A pseudo periodic regime appeared between these two cases. In a broader context than shallow reservoirs, round axisymmetric turbulent jet is considered as a classical prototype of shear flow family (composed of wakes, mixing layers...). Immense studies and literature could be found about this subject. Generally, when the jet is a part of confined structure, previous studies showed more interest on the global flow patterns of those structure than the proper behavior of the jet.

Appendix E. Validation of ADVP probe (Chapter 4)

Is ADVP (Acoustic Doppler Velocity Profiler) a reliable instrument for our specific application?

Good quality of measurements is crucial for appropriate understanding of physics and right interpretation of experimental results. Studies using ADVP probe for turbulent jet applications are rare in literature. ADVP used the Doppler technic to measure the velocity. After few criticisms concerning its use found (Macvicar et al., 2014; Craig et al., 2011; Friedrich et al., 2014), Leng and Chanson (2017) compared steady and unsteady velocity profiling in bores and positive surges. For steady flows, authors found well data agreement between the ADVP and ADV in terms of instantaneous median velocity and velocity fluctuations. For positive surges, a good accuracy of longitudinal velocity recirculation and deceleration is found. Nevertheless, errors are found in terms of time average data and velocity fluctuations outside the boundary layer. Duma et al. (2014) compared a profile of mean streamwise velocity components and turbulent kinetic energy for two configurations in channel with quasi-uniform and smooth-to-rough transition. Only one velocity components were measured for UVP, turbulent kinetic energy was deduced from Nezu's coefficient (Nezu and Nakagawa, 1993). Good data agreement is found in upper layer and less well accuracy near the bottom. Another work in this topic, was done by Lacey at al. (2018); authors compared mean velocities and turbulent characteristics on an open channel hydraulic flume. They found a good agreement in terms of mean values of longitudinal and lateral velocities near the "sweet spot" and discrepancies in term of vertical velocities, TKE and one component of Reynolds stress tensor. One of the latest studies in terms of validating accuracy of ADVP consists of evaluating the assessment of ADVP from user perspective by Liu et al. (2022). Under the same hydraulic conditions, a sensitivity analysis was made on user parameters choice such as sampling rate, ping algorithm, range to first cell, transmit pulse size and cell size. Results highlighted the impact of probe configuration setting on results. For example, a deviation superior of 50% is found of mean flow velocity and difference up to 8 times could be found for shear stress calculation.

Comparison of adv and ADVP measurements

Comparison between ADV and ADVP results was made under two hydraulic conditions of rectangular reservoir for with a jet vertical position set at Z_{jet}/H= 0.75. For each hydraulic conditions, 22 points (ADV) / profiles (ADVP) were measured using each probe. A second validation step consists of evaluating the repeatability of results; two hydraulic conditions were tested. For each hydraulic condition, 66 points of measurements using ADVP are compared for a case one and case two. The vertical jet position is set to Z_{jet}/H= 0.50 For ADV/ADVP comparison

and repeatability of the results, first hydraulic condition was tested with R= 50000 and second one with R= 175000. Turbulent Kinetic energy, average and temporal standard deviation of longitudinal and transversal velocity are compared.

For validation of the experimental device, a Sontek/YSI 16-MHz MicroADV (Acoustic Doppler Velocimeter) were used, it consists also of acoustic doppler technology. The sampling volume is located 5 cm from the probe and the velocity range is programmable. Acquisition frequency was set to 50hz.

Results are showing a general good agreement between ADV/ADVP for mean longitudinal and transversal velocity for both tested hydraulic conditions in profile 1 and profile 2. Profile 1 is in the beginning of the intermediate-field zone of the jet. However, it is observed that standard deviation is larger for the ADVP cases comparing to ADV cases. This is naturally explained by the fact that the difference in frequencies of the two devices, 50hz for the traditional ADV and 100hz for the ADVP. This offers a larger sample size and number of points for the ADVP for the same duration of measurements. Results of the turbulent kinetic energy show a good agreement for the configurations with a R = 50000 for profile 1 and 2. For a higher Reynolds number 175000, comparison is showing accurate results except for points x = -0.045 m and the point x = 0.015 m located at the profile 1. Those points are situated in the main direction of the jet. At the end of the near field zone, the large turbulent structures take place before dissipating gradually which makes the turbulence very high and measurements at this location particularly sensitive. In addition, the difference could be partially attributes to the difference in standard deviation of velocity components because of different acquisition frequency.

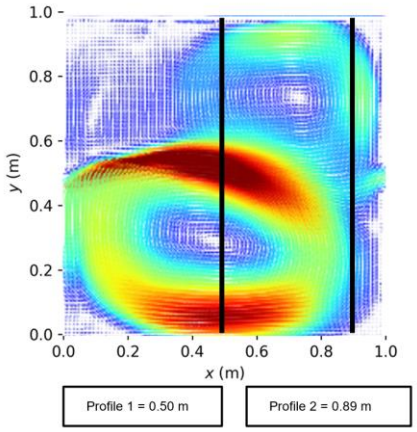

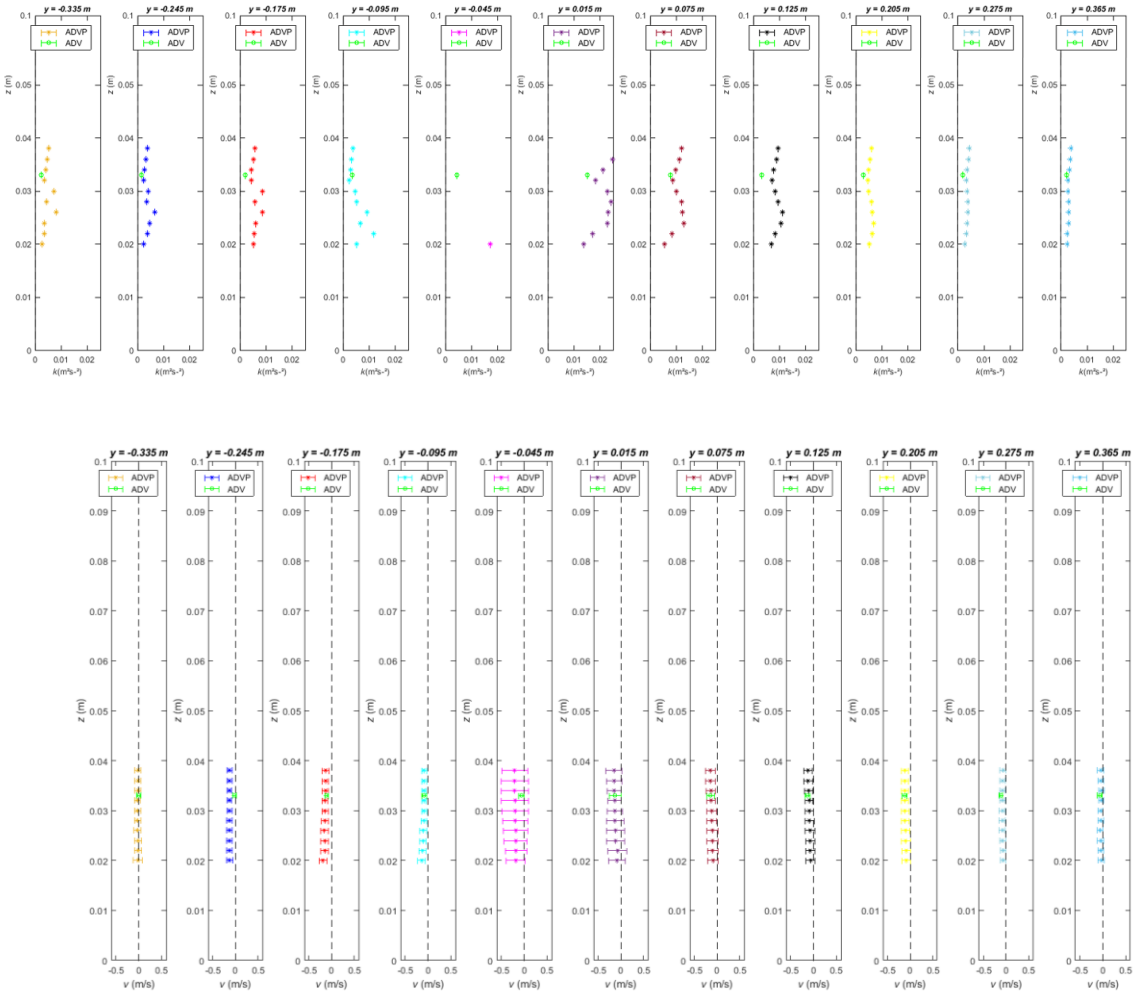

Figure E1: Horizontal and longitudinal velocity profiles with ADVP profilers and ADV (green) located at x =0.5 m for configuration with Q=0.00175 m³/s – H=0.10 m, Z_{jet}/H =0.75

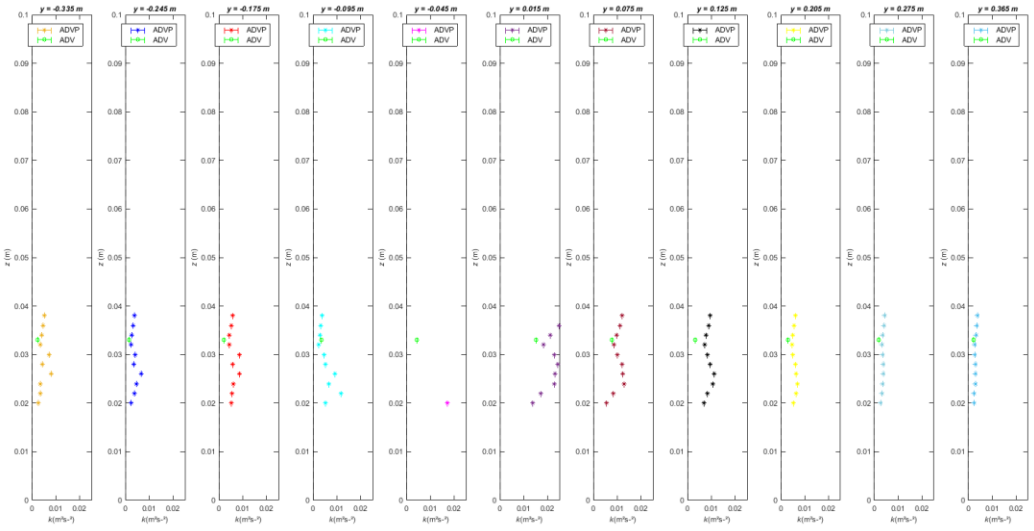

Figure E2: Turbulent kinetic energy velocity profiles with ADVP profilers and ADV (green) located at x =0.5 m for configuration with Q=0.00175 m³/s – H=0.10 m, Z_{jet}/H =0.75

Comparison ADVP/ADV – *Q*=0.0005 m³/s – *H*=0.10 m, Z_{jet}/H =0.75.

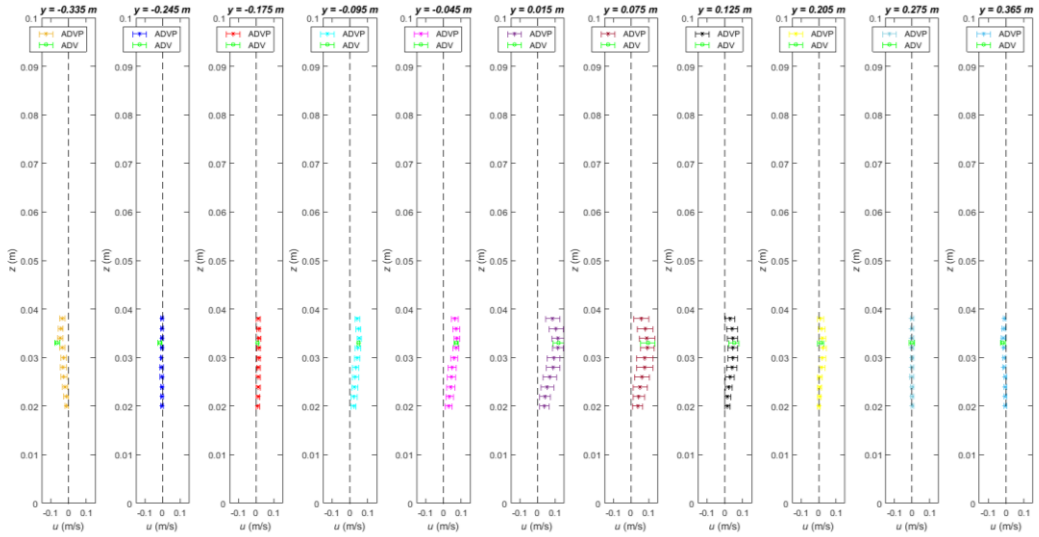

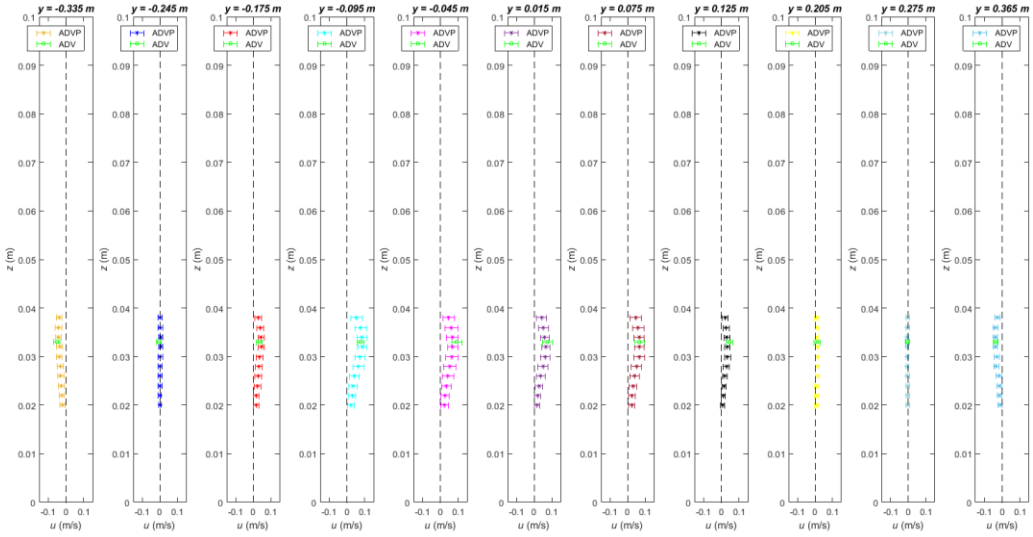
y = -0.335 m
y = -0.245 m
y = -0.175 m
y = -0.095 m
y = -0.045 m
y = 0.015 m
y = 0.075 m
y = 0.125 m
y = 0.205 m
y = 0.275 m
y = 0.365 m
ADVP
ADV
z (m)
u (m/s)

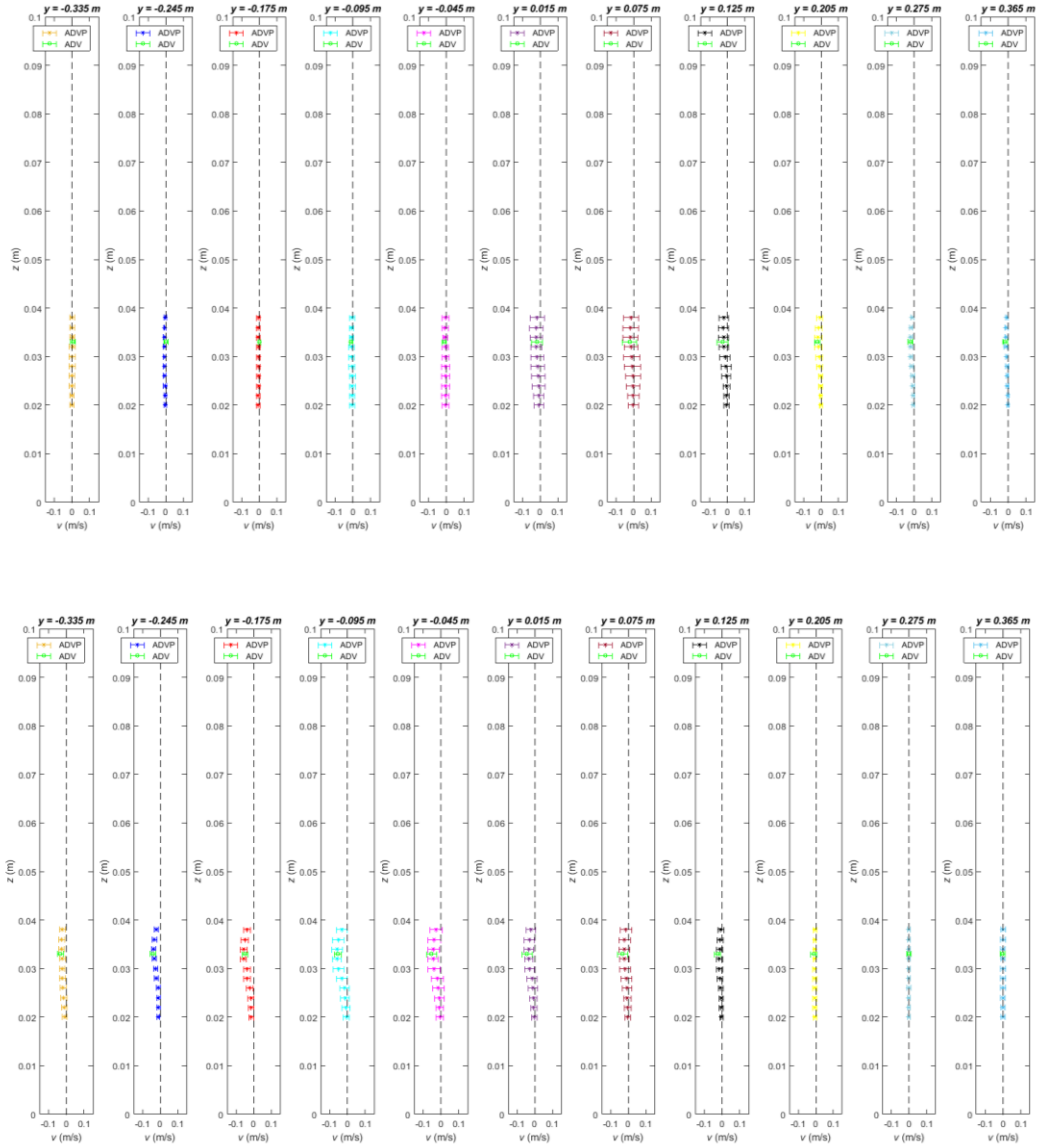

Figure E3: Horizontal and longitudinal velocity profiles with ADVP profilers and ADV (green) located at x =0.5 m for configuration with Q=0.0005m³/s – H=0.10 m, Z_{jet}/H =0.75

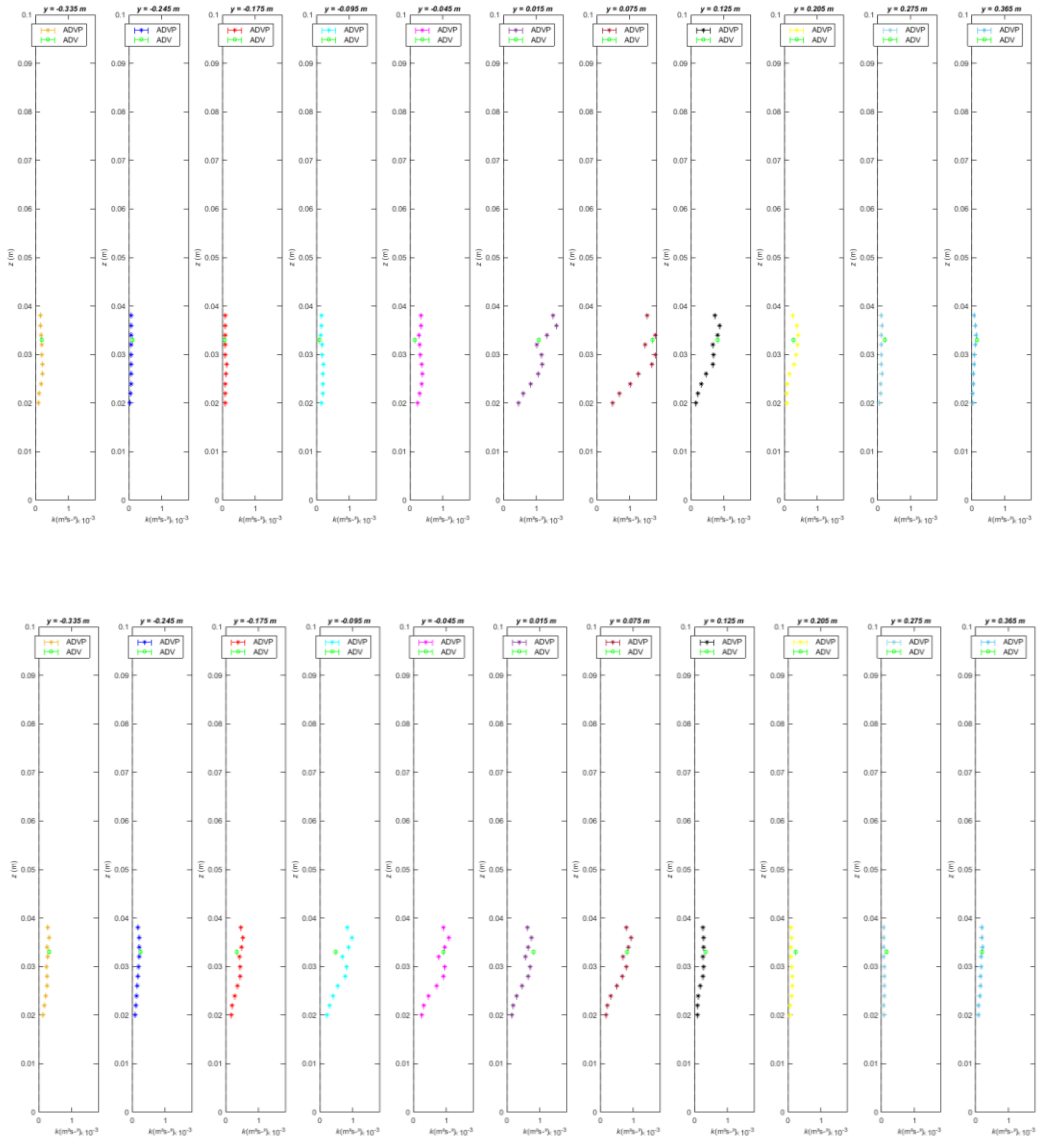

Figure E4: Turbulent kinetic energy velocity profiles with ADVP profilers and ADV (green) located at x =0.5 m for configuration with Q=0.0005 m³/s – H=0.10 m, Z_{jet}/H =0.75

Comparison ADVP/ADV – Q=0.00175 m^3/s – H=0.10 m, Z_{jet}/H =0.75.

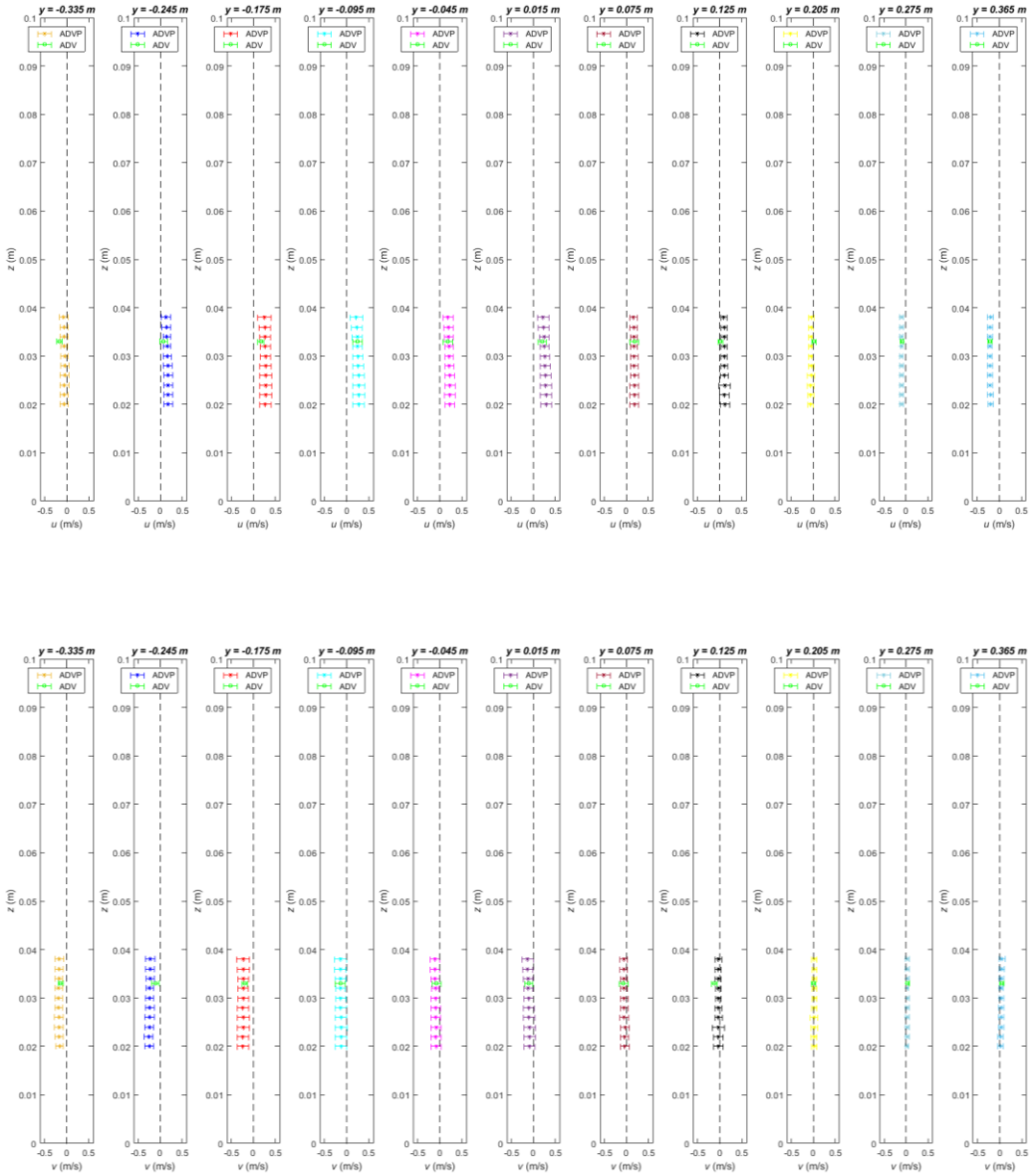

Figure E5: Horizontal and longitudinal velocity profiles with ADVP profilers and ADV (green) located at x =0.5 m for configuration with Q=0.00175 m^3/s – H=0.10 m, Z_{jet}/H =0.75.

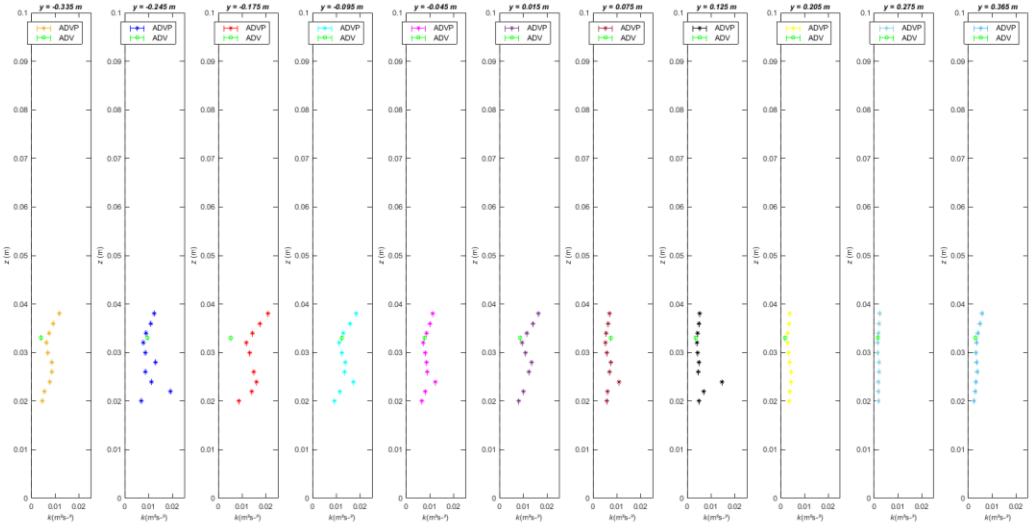

Figure E6: Turbulent kinetic energy velocity profiles with ADVP profilers and ADV (green) located at x =0.5 m for configuration with Q=0.00175 m^3/s – H=0.10 m, Z_{jet}/H =0.75.

REPEATABILITY OF MEASUREMENTS

After a first validation between the ADV and ADVP tools for two hydraulic conditions, the repeatability of the results is an important step that allows to have more confidence in the stationarity of the results and in the precision on ADVP probe. A very good agreement is found for mean and standard deviation of horizontal and longitudinal velocity components for profile 1 and profile 2 under the two hydraulic conditions. Figure shows a sample of those results. Concerning the TKE, good results are found for points profile 2 and more variability is found for profile 1 especially for points located at the jet direction. Same reasons highlighted previously about the turbulent aspect of the flow at this location could explain these differences. A “C” shape is found for TKE profiles. Similar shapes are found on Lacey et al., (2018) and Duma (2014) works. Those shapes make difficult to evaluate the exact intensity of TKE profiles. For the rest of the study, the measurements considered for the continuation will be extracted of the sweet spot of the ADVP. This point is located at 5 cm from the transmitter and show the higher Signal to Noise ratio (SNR) in the profile.

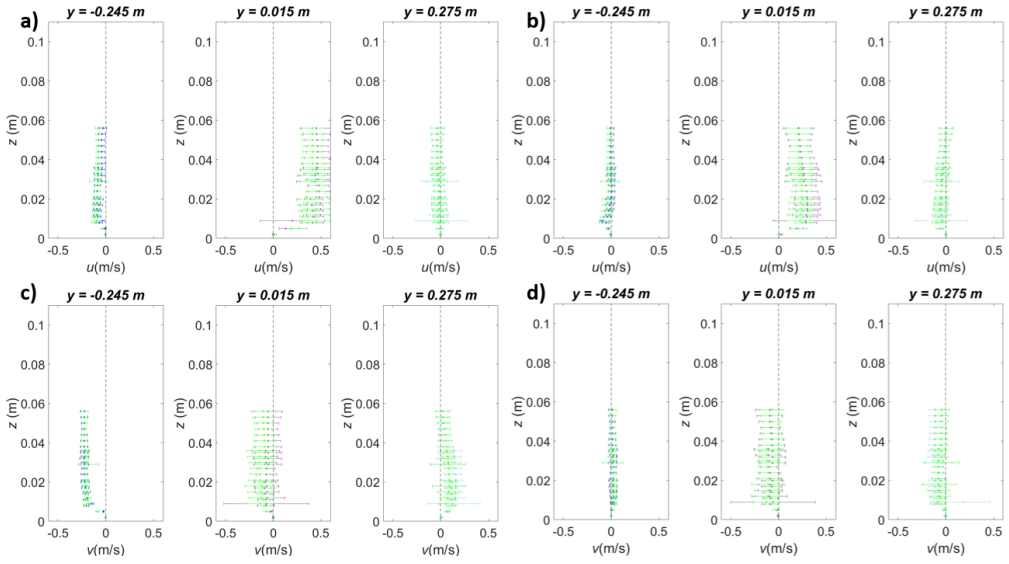

Figure E7: Horizontal and longitudinal velocity profiles velocity profiles with ADVP to evaluate the repeatability, profiles are located at x =0.5 m for configuration with Q=0.00175 m³/s – H=0.10 m, Z_{jet}/H =0.50.

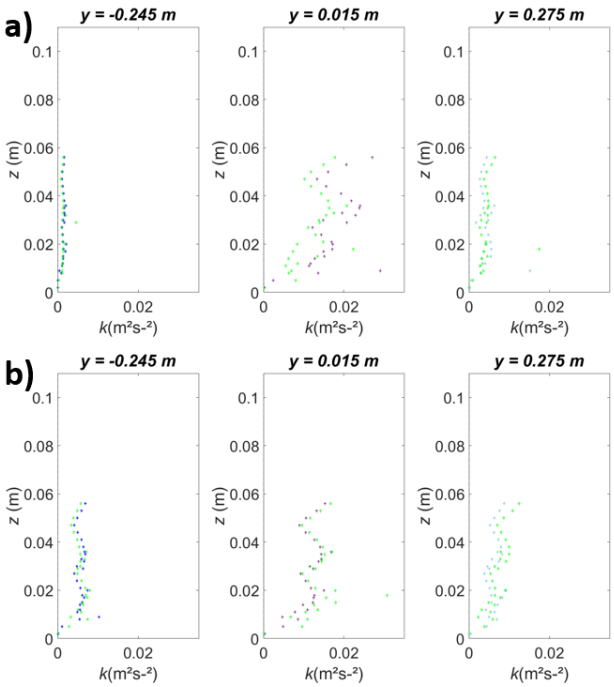

Figure E8: Turbulent kinetic energy profiles with ADVP to evaluate the repeatability, profiles are located at x =0.5 m for configuration with Q=0.00175 m³/s – H=0.10 m, Z_{jet}/H =0.50.

Repeatability results – Q=0.00175m^3/s – H=0.10 m, Z_{jet}/H =0.50.

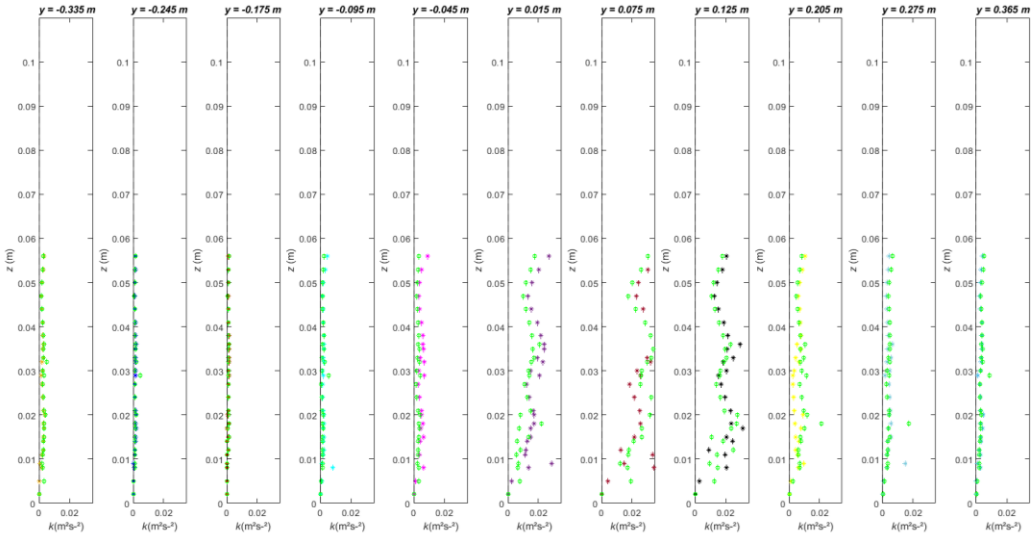

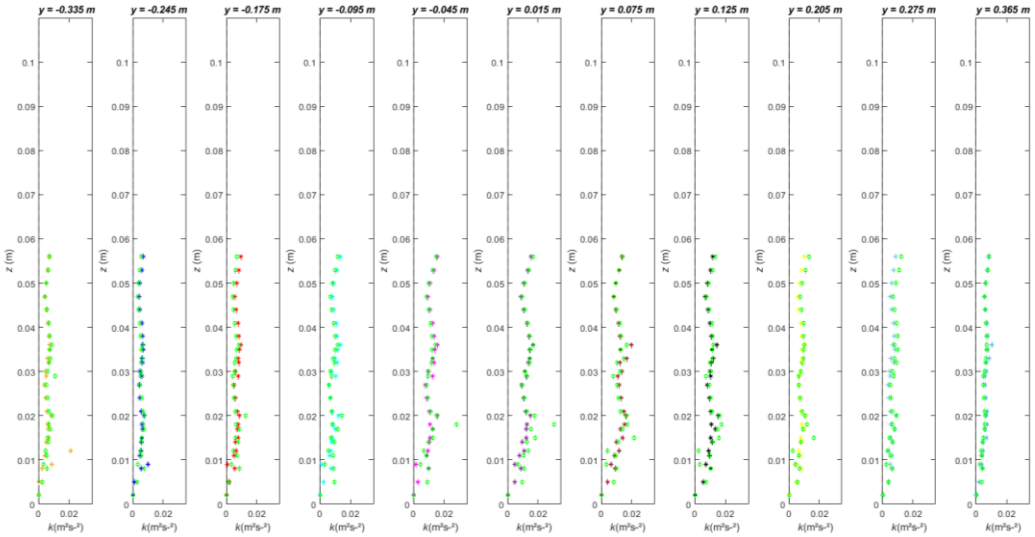

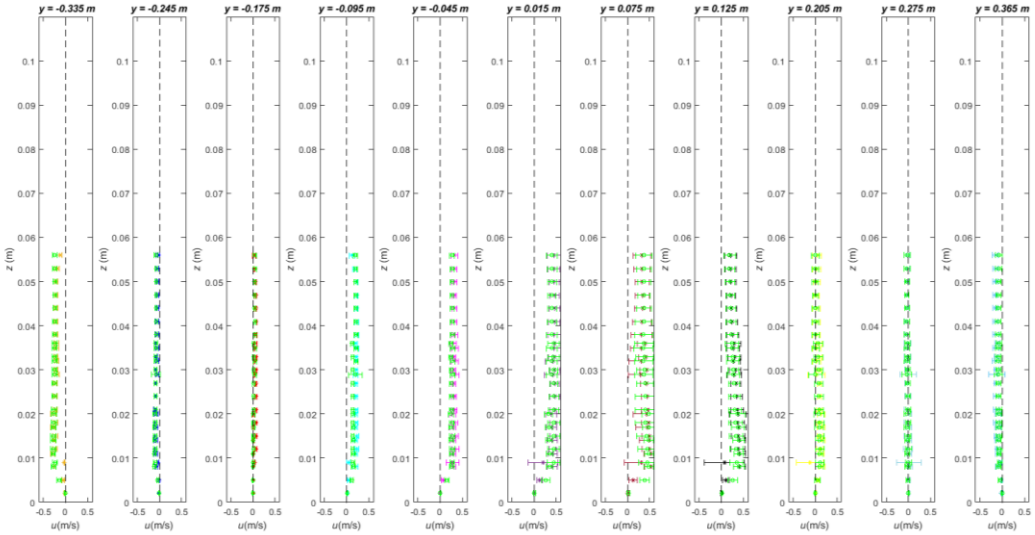
y = -0.335 m
y = -0.245 m
y = -0.175 m
y = -0.095 m
y = -0.045 m
y = 0.015 m
y = 0.075 m
y = 0.125 m
y = 0.205 m
y = 0.275 m
y = 0.365 m
z (m)
u(m/s)

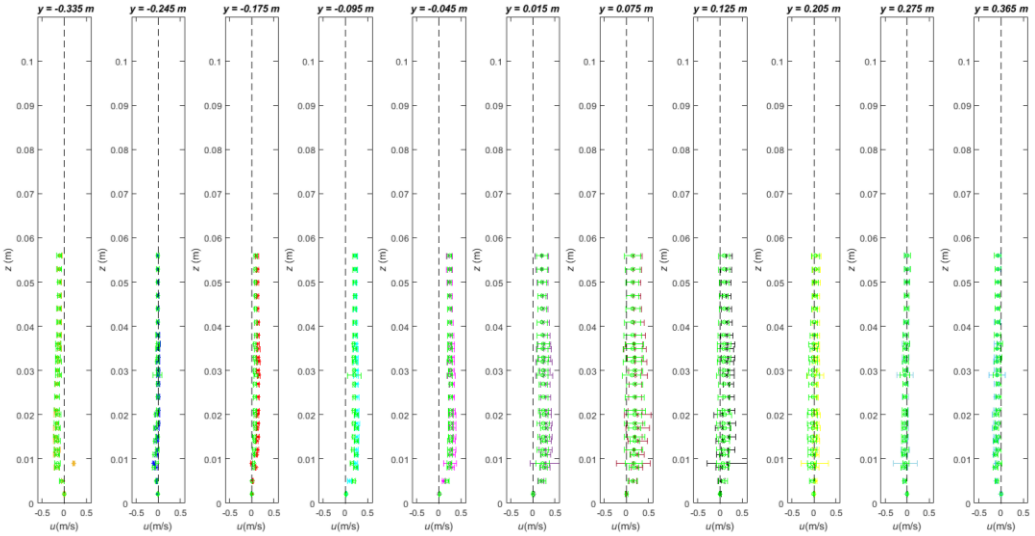
y = -0.335 m
y = -0.245 m
y = -0.175 m
y = -0.095 m
y = -0.045 m
y = 0.015 m
y = 0.075 m
y = 0.125 m
y = 0.205 m
y = 0.275 m
y = 0.365 m
z (m)
u(m/s)

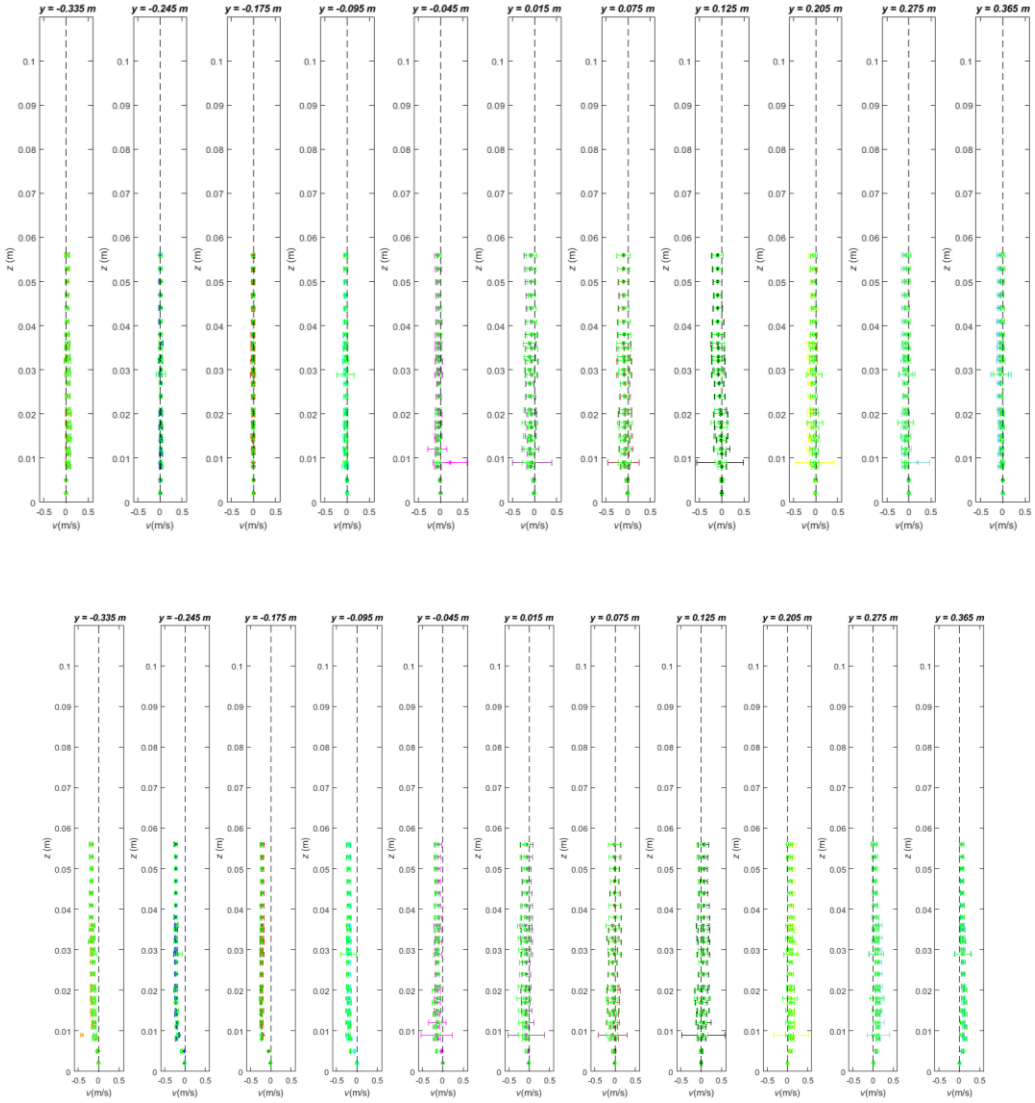

Figure E9: Horizontal and longitudinal velocity profiles velocity profiles with ADVP to evaluate the repeatability, profiles are located at x =0.5 m for configuration with Q=0.00175 m^3/s – H=0.10 m, Z_{jet}/H =0.50

Conclusions

The validation of the ADVP probe was performed by comparing it to the ADV under two different hydraulic conditions. The longitudinal and transverse velocity averages demonstrated satisfactory agreement, while the comparison of turbulent kinetic energy was less accurate. However, the repeatability of the results ensured the stationarity and accuracy of the data. Although the results were generally satisfactory for both hydraulic conditions, some discrepancies were observed in the points located in the main direction of the jet and in profile 1.

Appendix F. Effect on hydraulics conditions and jet position on mean velocities (Chapter 4)

What effects do reservoir length, jet position and hydraulic conditions have on longitudinal, transverse and vertical velocity profiles at different position in the vertical?

After comparing the longitudinal velocity profiles at the surface and along the vertical axis for each configuration, we examined the influence of jet position and hydraulic conditions on each measured velocity profile for the three velocity components: u, v, and w. To facilitate the comparison, the longitudinal velocities were standardized relative to a reference velocity U_{ref} = Q / (b_0 H). Configurations (12,13) correspond to Z_{jet}/H = 0.50 with two flow rates, Q = 0.00175 m^3/s and Q = 0.003 m^3/s, while configurations (14,15) also correspond to Z_{jet}/H = 0.50 with two flow rates, Q = 0.00175 m^3/s and Q = 0.003 m^3/s.

Longitudinal velocity

For the long basins and for measurements along the vertical axis, the normalized velocities exhibit similarity in terms of velocity shape and magnitude. However, it is worth noting that for measurements close to the bottom at z = 0.016 m, the intensities are higher for configurations 12 and 13 with a middle jet compared to configurations 18 and 19 with a near-surface jet. The results indicate that the jet position and hydraulic conditions have minimal impact on the behavior of longitudinal velocity intermediate field (x = 1.00 m) and far field (x = 1.70 m) from the jet.

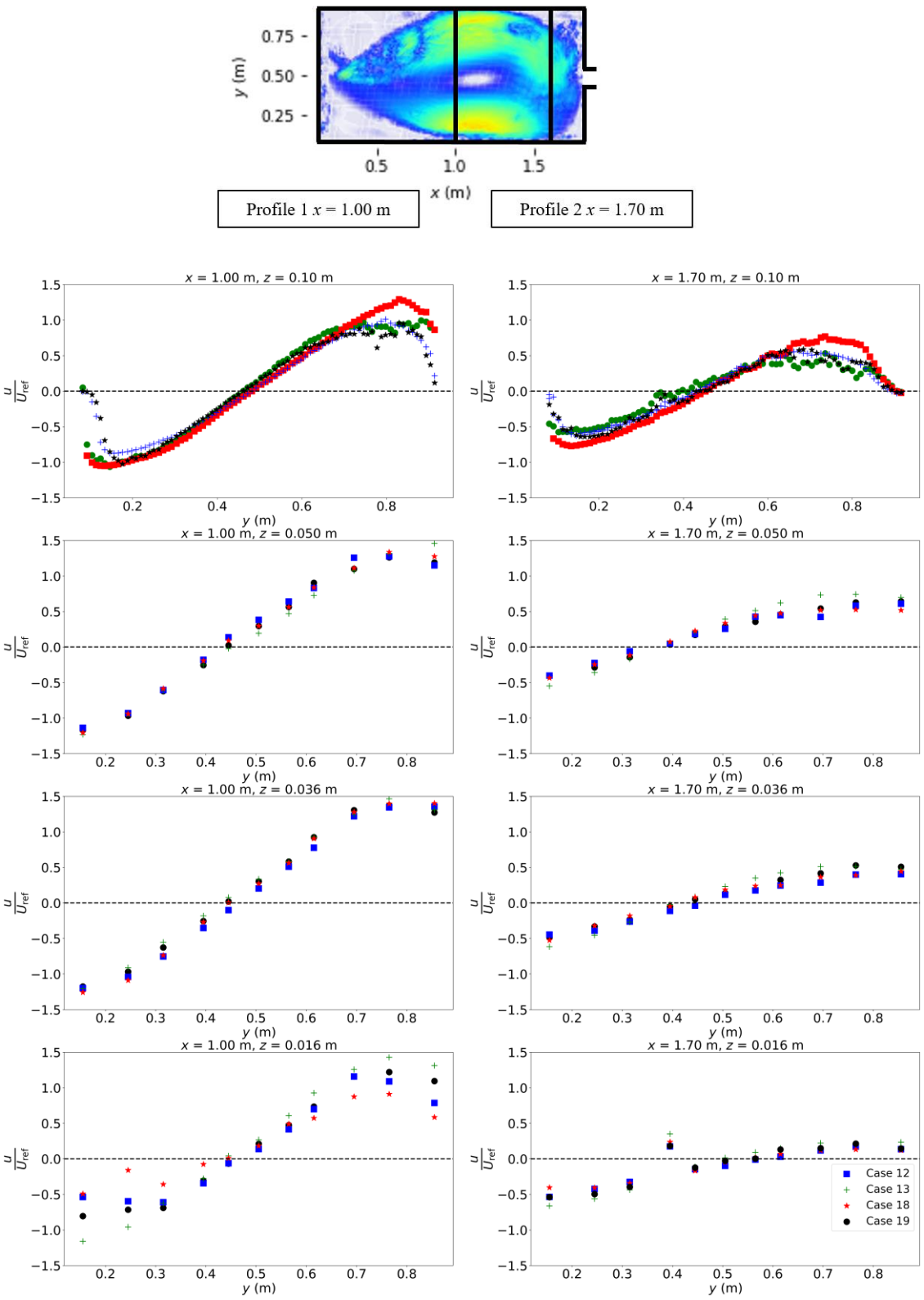

Figure F1: Comparison of longitudinal velocity at different location on the vertical for Case 12, case 13, case 18 and case 19.

Regarding the short basins, we observe the following surface measurements. Normalized velocities exhibit a similar shape and intensity regardless of hydraulic conditions. However, it is worth noting that for configurations with higher flow rates, there is an increased velocity intensity at the surface, particularly on Profile 1. As the flow rate is increased, the jet tends to direct itself towards the free surface.

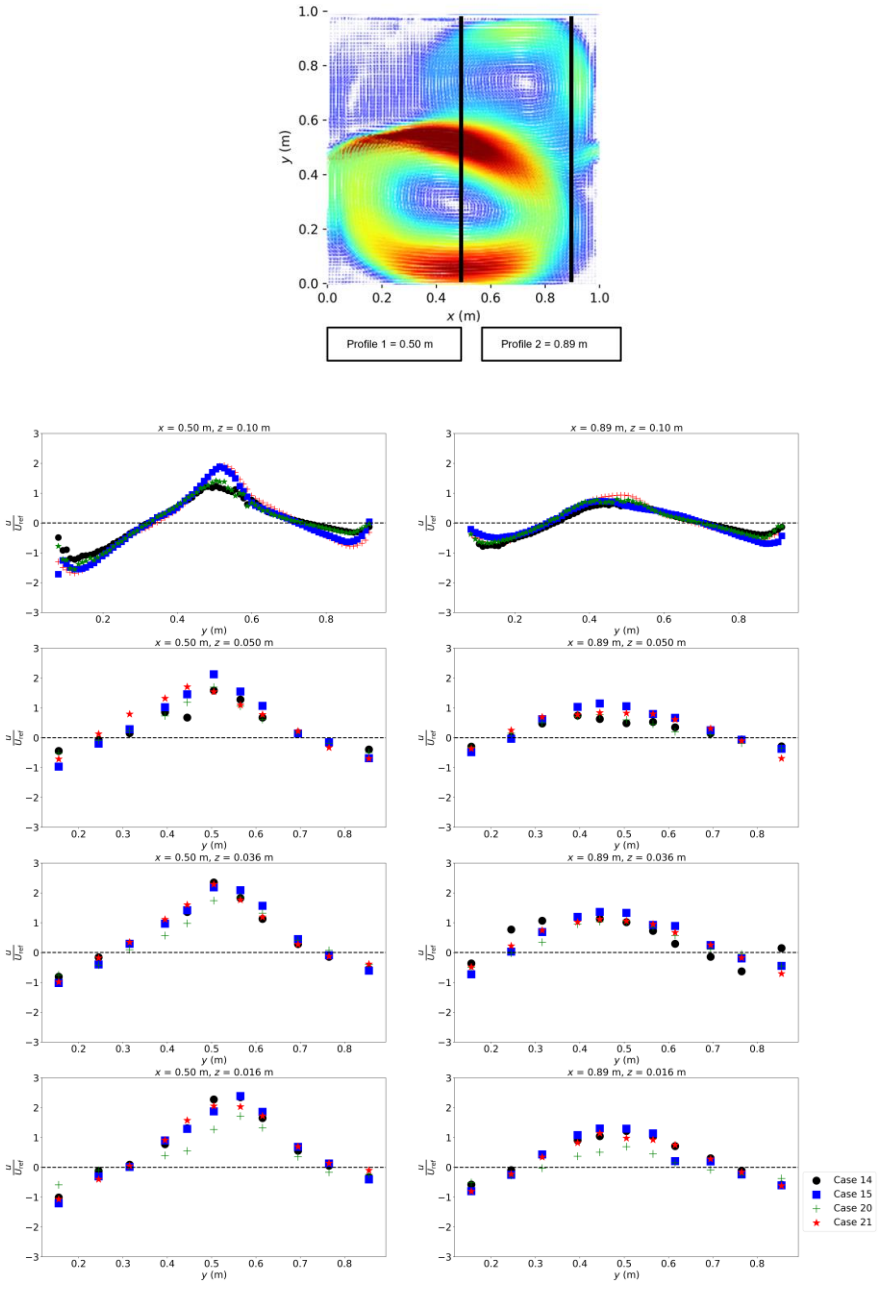

Figure F2: Comparison of longitudinal velocity at different location on the vertical for Case 14, case 15, case 20 and case 21

Transversal velocity

On a profile situated within an intermediate region, we observe variations among the different configurations at different positions. Specifically at a depth of z = 0.050 m, velocities in configuration 13 are nearly negligible, which explains why, in this particular setup, the longitudinal velocity becomes more prominent and prevails over the transverse velocities. At a depth of z = 0.036 m, the profiles display more uniform characteristics, except for the point located at 0.875 m, which corresponds to the primary jet direction. This point is slightly more influenced by transverse velocities in configurations at mid-depth. As we approach the bottom, we notice increasing heterogeneity among the various configurations, with the jet adjacent to the bottom consistently dominating over the near-surface jet. When transitioning to a more distant location at x = 1.70 m, we observe that the transverse velocities become negatives across the entire profile and their maximum amplitudes nearly double between x = 1.00 m and x = 1.70 m, in contrast to the longitudinal velocities.

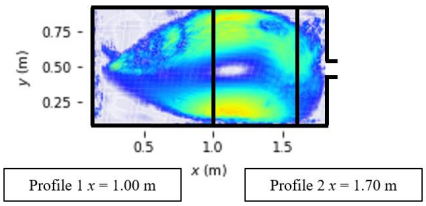

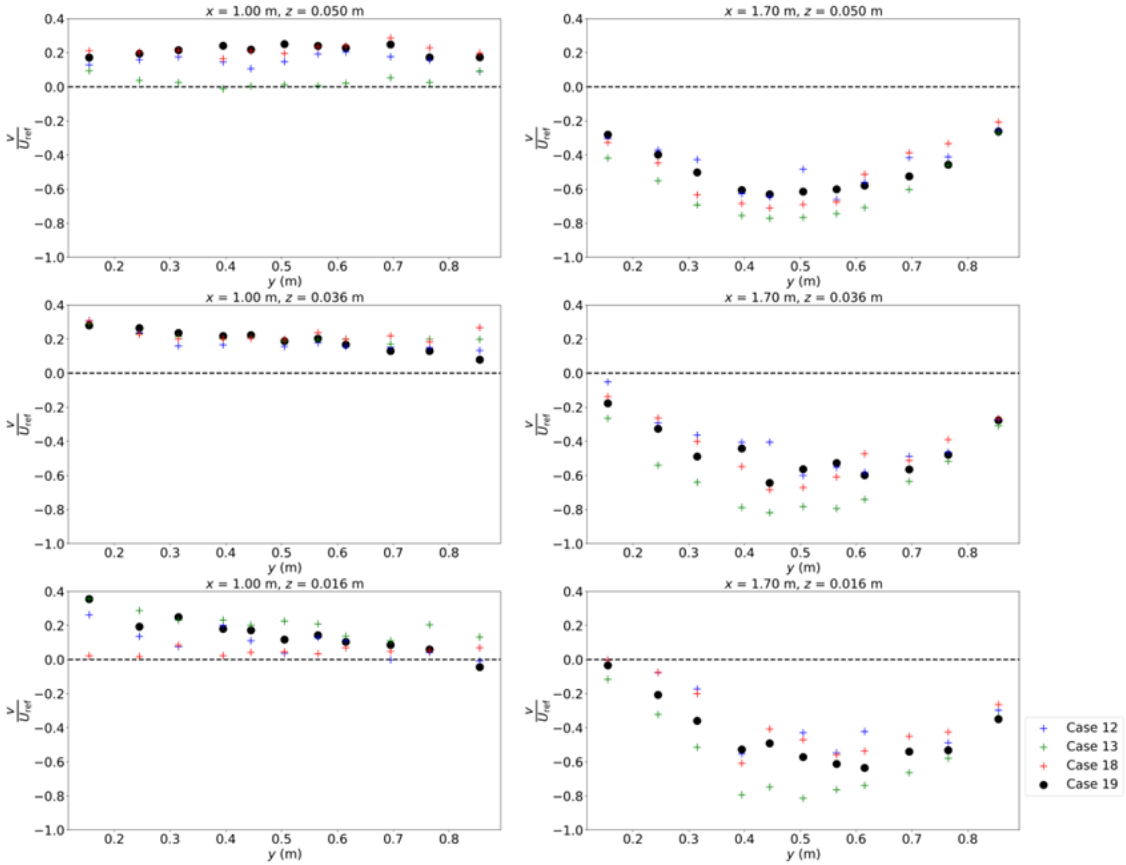

Figure F3: Comparison of transversal velocity at different location on the vertical for Case 12, case 13, case 18 and case 19.

In the case of the short basins, we observe that as the flow rate increases, on Profile 1, it becomes apparent that the profiles of the four configurations exhibit similar shapes at the three vertical positions. As we approach the bottom, we notice that a value at a point that was negative at z = 0.050 m and z = 0.036 m becomes positive. When considering the velocity intensities, we observe that at z = 0.050 m, the velocities at low flow rates for a Z_{jet}/H = 0.50 configuration are higher than those for Z_{jet}/H = 0.75 and the opposite occurs when the flow rate is increased.

On Profile 2, the shape and distribution of velocities across this profile are similar for all four configurations. However, notable differences are observed in terms of normalized transverse velocity intensities. Unlike Profile 1, the Z_{jet}/H = 0.50 jet exhibits higher intensities at a height of z = 0.050 m. As we move closer to the bottom, the velocity profiles become more uniform.

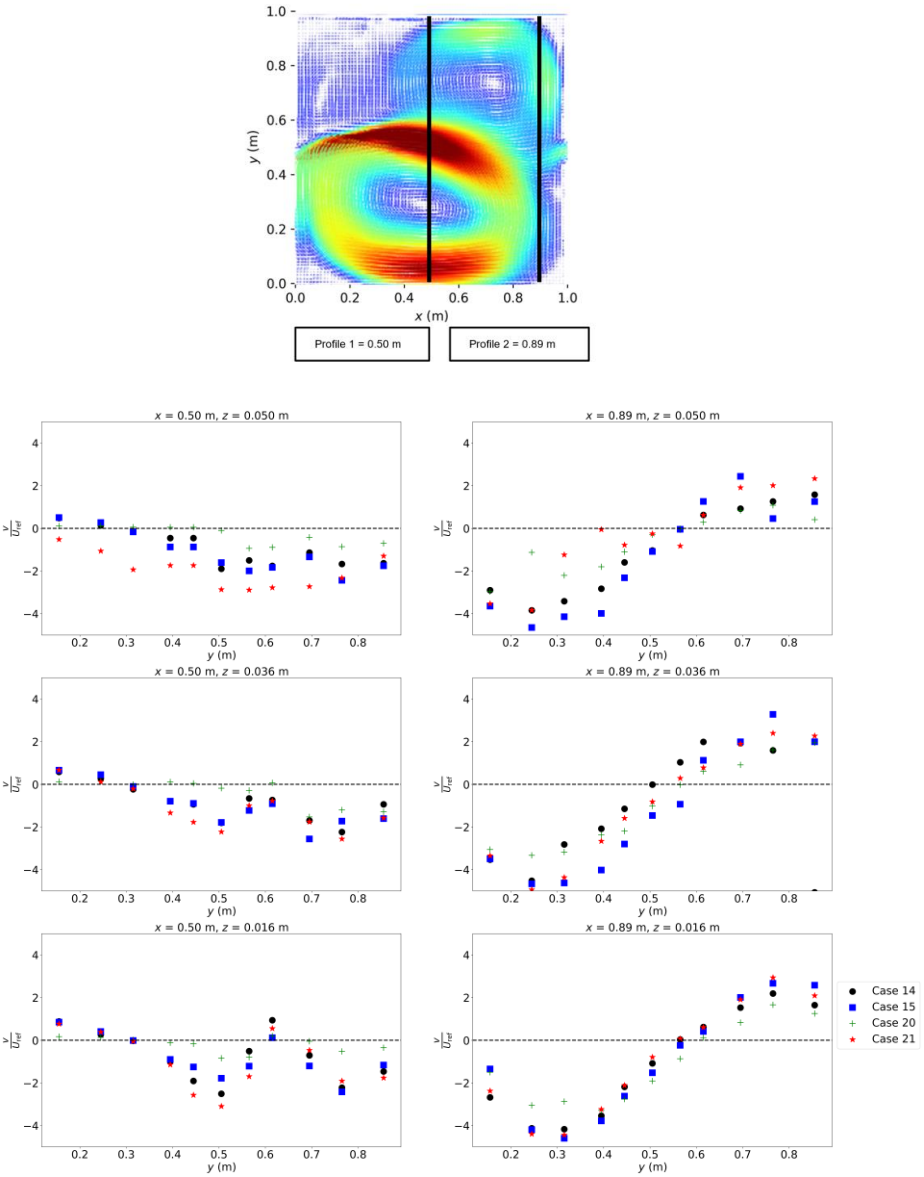

Figure F4: Comparison of transversal velocity at different location on the vertical for Case 14, case 15, case 20 and case 21

Vertical velocity

In the case of the long basins, when comparing the three vertical positions on Profile 1, it is evident that the four configurations share similar velocity profile shapes, except for a point located at x = 0.0855 m.

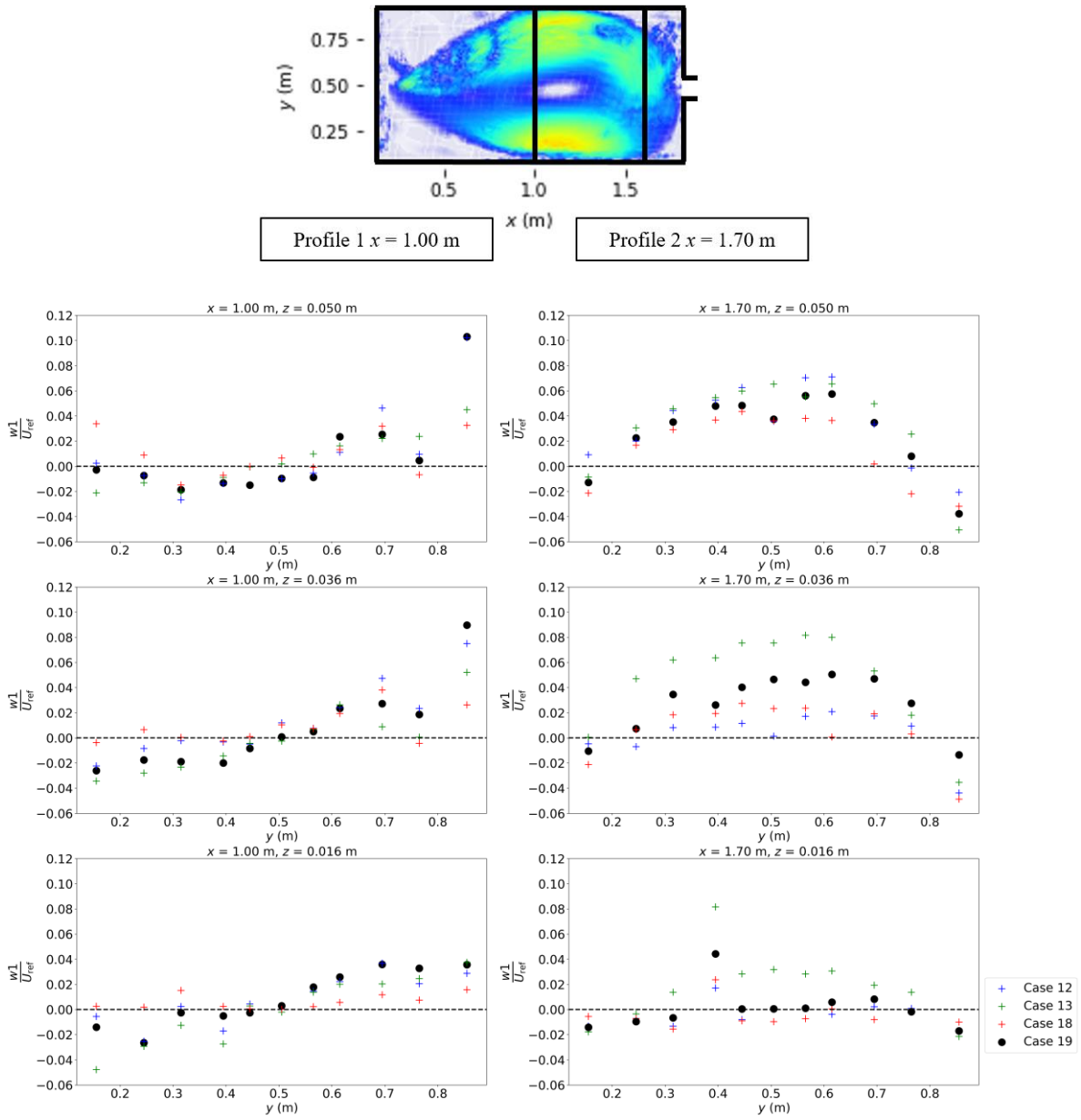

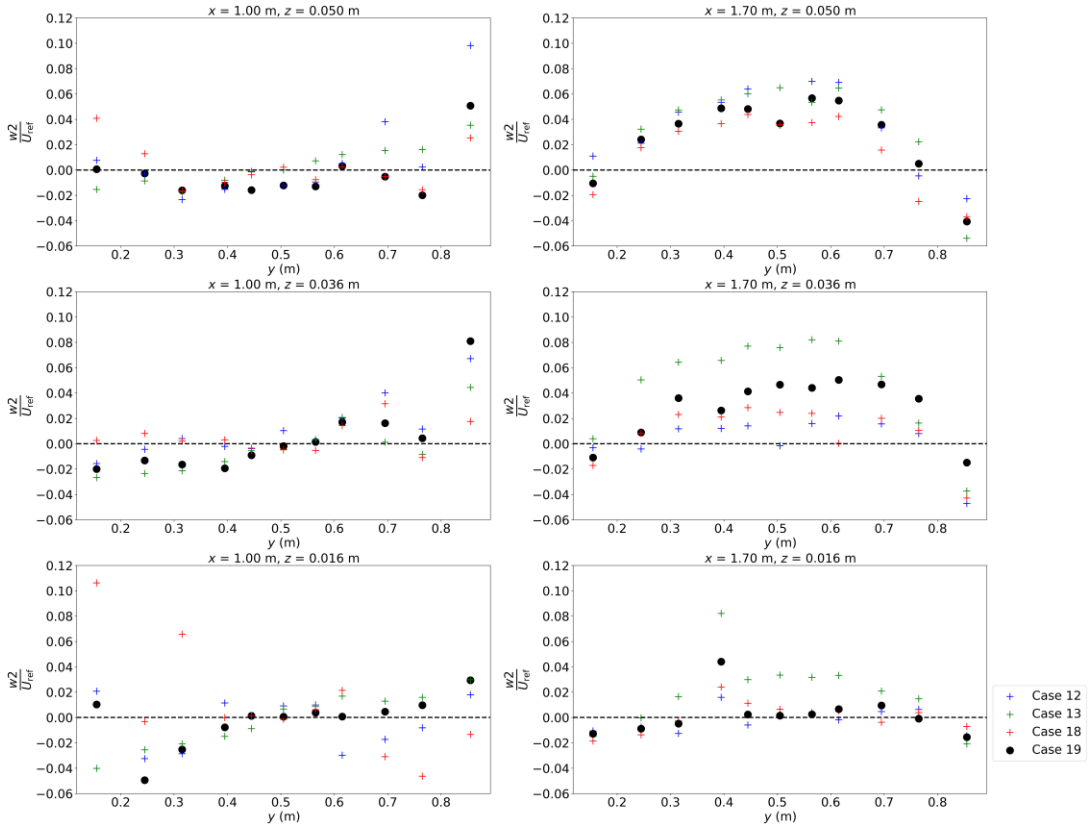

Figure F5: Comparison of vertical velocity (W1 and W2) at different location on the vertical for Case 12, case 13, case 18 and case 19

For the short basins, both Profile 1 and Profile 2 exhibit similar shapes across the different vertical positions for all four configurations. However, there is a noticeable difference in terms of intensity, especially for the Z_{jet}/H = 0.75 configuration at high flow rates. This difference diminishes as we approach the bottom, unlike the longitudinal velocities.

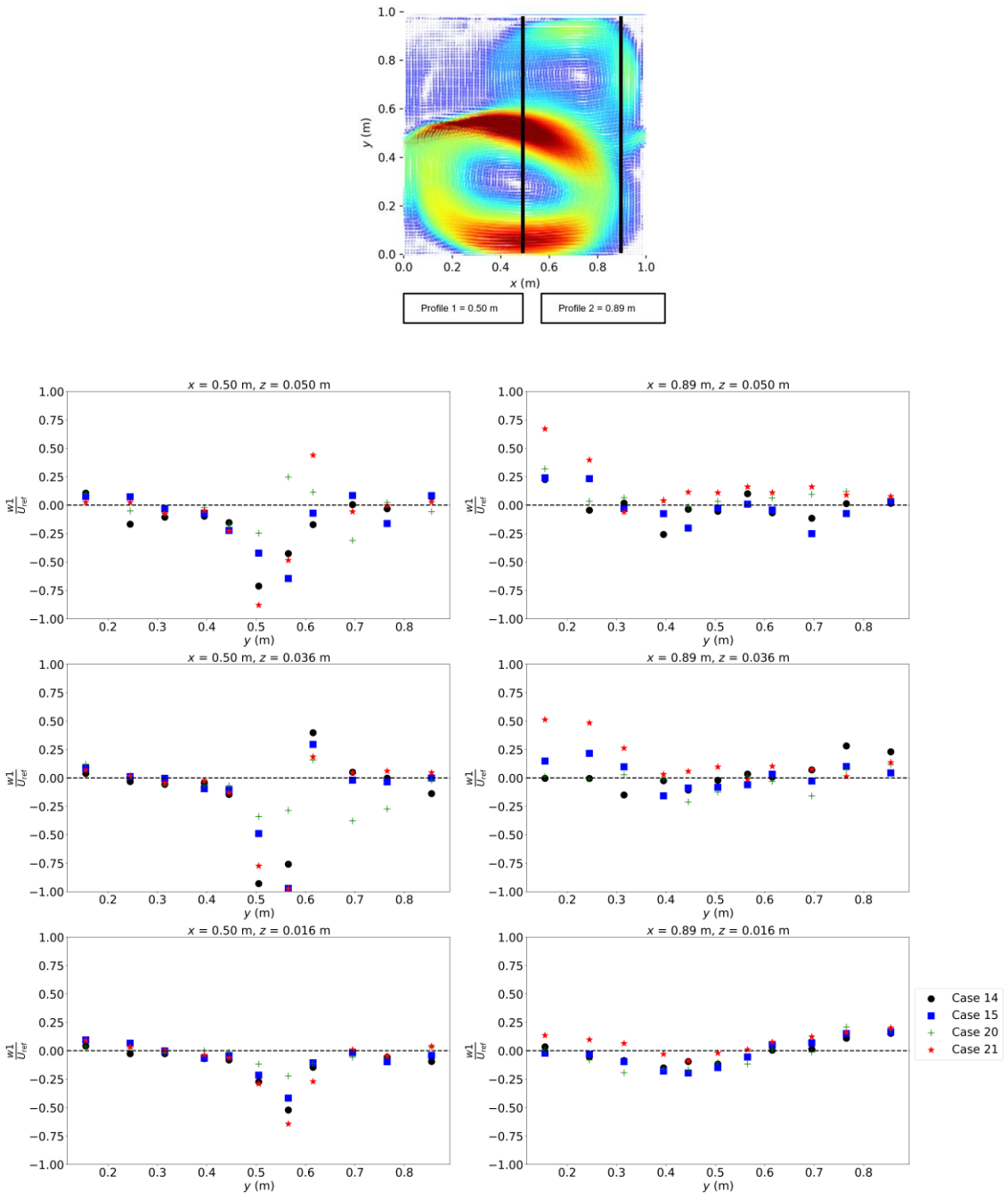

Figure F6: Comparison of vertical velocity at different location on the vertical for Case 14, case 15, case 20 and case 21

Appendix G. Reynold stress and Lumley triangle (Chapter 4)

What are the turbulence states observed within the reservoir?

Each component of the Reynolds shear tensor represents a different aspect of the turbulence in the flow. <*u*'*u*'>, <*v*'*v*'>and <*w*'*w*'> represent the normal stresses in the flow, which are related to the pressure fluctuations. <*u*'*v*'>, <*u*'*w*'>, and <*v*'*w*'>, represent the shear stresses in the flow, which are related to the vorticity and rotation of the fluid. We observe that the components in the diagonal of the Reynolds tensor matrix are dominant. The vorticity and rotation of the fluid are therefore negligible. For profile 1, the component according to *u* is the most dominant especially in the points located in the main direction of the jet. For profile 2, the longitudinal component has the same order of magnitude as the total kinetic energy. For the longitudinal, transerval and vertical components, the position of the velocity peak shifts slightly from profile 1 to profile 2.

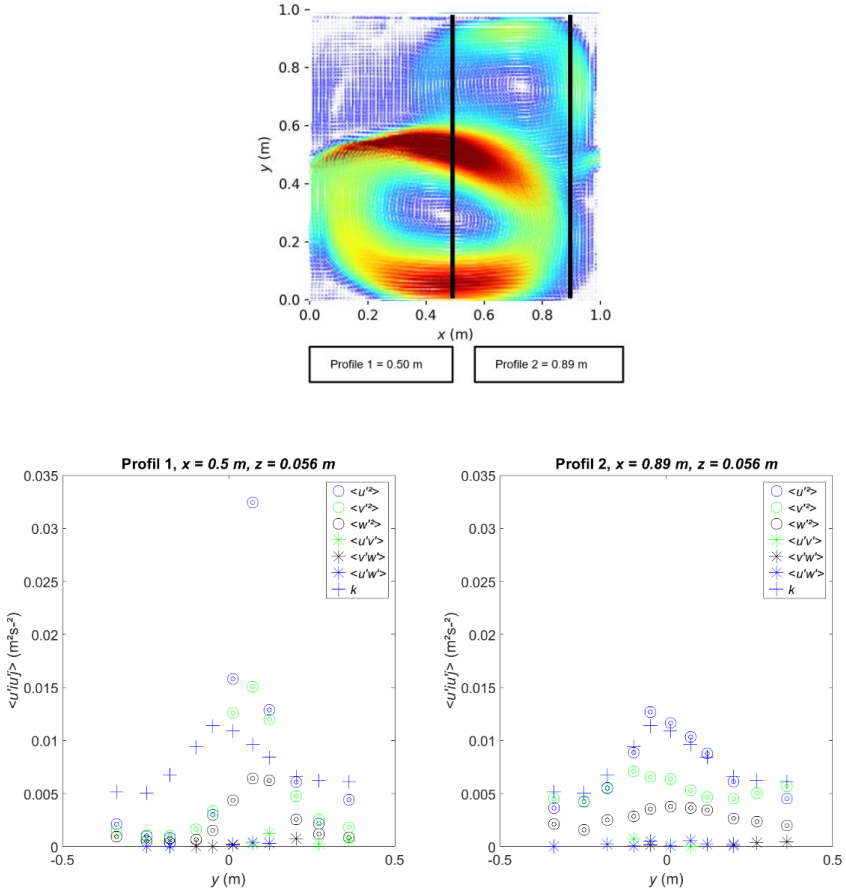

Figure G1: Comparison of Reynolds stress components and turbulent kinetic energy for reference case.

Lumley turbulence triangle is a useful tool for visualisation of turbulence anisotropy and to identify different states of turbulence from reference flows such as channel, mixing layer, turbulent jet... Any realizable state of tensors anisotropy must be contained in the triangle. Points outside correspond to non-realiable Reynolds stress with negative or complex eigenvalues. Using invariants of the anisotropic component of the Reynolds stress tensor a, second and third invariant, respectiveley $II = -a_{ij}a_{ji}/2$ and $III = a_{ij}a_{jk}a_{kj}/3$, are plotted in the cooordinate system $\eta = \xi$ where $\eta = (-III/3)^{1/2}$ *and* $\xi = (-II/3)^{1/3}$. Three borders cover the triangle consisting of three lines. One line builded from (-1/6, 1/6) coordinates corresponding to axysimetrical turbulence named Pancake-shaped turbulence/oblate spherioid. A second line builded from (1/3, 1/3) coordinates corresponding to axisymetrical turbulence named Cigar Shaped / Prolate shroid. A third border is represented by $\eta = (1/27 + 2\xi^3)^{1/2}$ which correspond to 2D turbulence or elliptical disc-shaped. Three turbulence states are found in the corner of the triangle, 2D axisymmetric turbulence (-1/6,1/6), one composant turbulence (1D) for point (1/3, 1/3) and 3D isotropic state corresponding to point (0,0). Lumley and Newman (1977), as well as Lumley (1978), outlined turbulence classification system based on the characteristics of the energy ellipsoid. In the context of homogeneous turbulence following an axisymmetric contraction, the energy ellipsoid assumes a pancake-like configuration due to the reduction of one component of turbulent kinetic energy relative to the other two. During an axisymmetric contraction, the turbulence eddies undergo stretching in the axial direction. Conversely, in the case of turbulence following an axisymmetric expansion, the energy ellipsoid takes on a cigar-like shape, primarily because one component of turbulent kinetic energy surpasses the other two. However, it is important to note that in this scenario, the turbulence eddies do not exhibit a distinct or preferred structure, nor do they align along a particular direction. This is attributed to the simultaneous compression in the axial direction and stretching in other directions, as illustrated by Rogers and Moin (1987).

For short reservoir, 66 measurement points were distributed in two positions x = 0.50 m and x = 0.89 m with three profiles (11 points per profile) at each position. For long reservoir 99 measurement points distributed in three positions x = 0.50 m, x = 1.00 m and x = 1.70 m with three profiles (11 points per profile) at each position. The measurement points are extracted from the sweet spot of the profile measured by the ADVP. The results for short and long basins are presented in the two figures below.

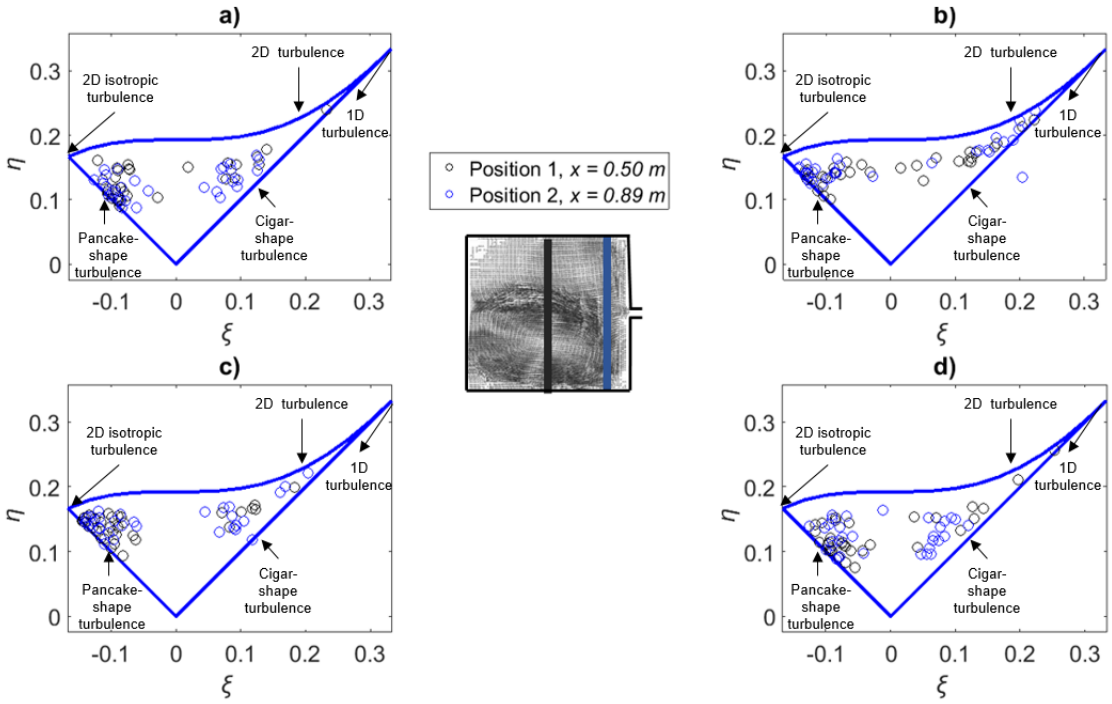

Figure G2: Lumley triangle in (ξ, η) system coordonate for short reservoir

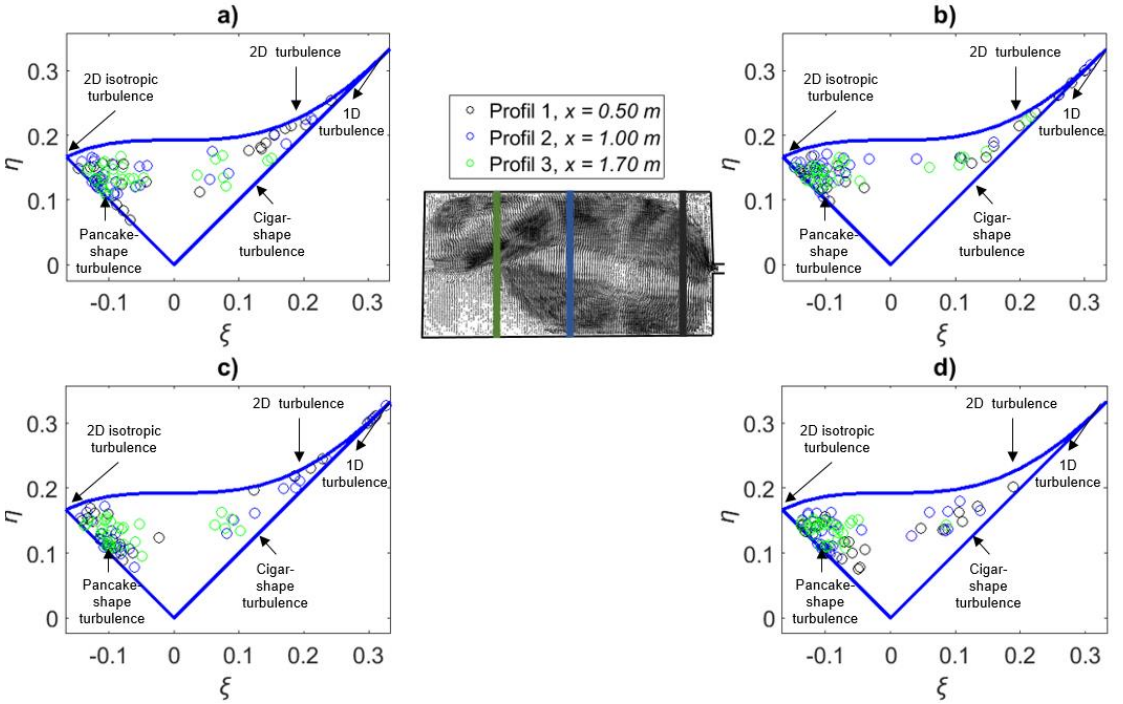

Figure G3: Lumley triangle in (ξ, η) system coordonate for long reservoir

The results show a global view on the anistropy trends in the whole reservoir. It is observed that all points are concentrated on the two parts corresponding to the axisymmetric turbulence of the reservoir. Points are divided between Cigar-shaped turbulence and Pancake-Shaped turbulence, with a slightly higher density on the part on the left side where $\eta = -\xi$. Points located on the right side and $\eta = \xi$ belong mainly to profile 2. We also notice that there is no transient state passing through the isotropic state.

The results are reassuring regarding the quality of measuremnts because all the points are included in the triangle except one outlier, and lines $\eta = -\xi$ and $\eta = \xi$ where points are globaly located, correspond respectively to states of mixing layer and turbulent channels/jets in litterature (Pope, 2000). On the other hand, we observe that the points have a slight tendency to approach an isotropic and anistropic 2D state. This could be explained by the shallow water character of the studied case. Analyzing turbulent regimes helps in selecting the appropriate turbulence model for numerical simulations. Results from Lumley triangle show that anisotropic turbulence models are more suitable for the tested configurations

Appendix H. Exploratory of Spectral analysis (FFT, PSD, Wavelet) (Chapter 4)

What signal processing tools are employed to detect the presence of coherent structures based on intrusive measurements?

The contribution of coherent structures to the total energy of the flow varies, depending on the case, from 10% (boundary layer, far field) to 25% (mixing layer, wake, near field jet). Moreover, from a dynamic point of view, the coherent structures play a very important role in the mixing processes. A control of turbulent flows could be done through the control of turbulent structures. Signal processing tools of turbulent signal allow to decrypt the content of temporal turbulent signal. An overview is given by Borgnat (2006). Different tools are available to extract self-similarity, coherent structures and bursting phenomena. Among these tools, we find the Fast Fourier Transform (FFT), the Power Spectral Density (PSD), the spectrogram (Gabor transform) and the continuous wavelet analysis which allow the evolution of the signal in a temporal and frequency graph. A general overview of Wavelet analysis and their application on turbulence is given by Farge (2022).

Fast Fourier Transform (FFT)

Essentially, the Fourier transformation consists of taking some signal either in space or in time and writing it in terms of the frequency components that add up to make this signal through decomposing it in terms of sinus and cosines which are forming an orthogonal basis for the space of represented functions. It is the analog of Fourier series for periodic functions. Discrete Fourier Transform (DST) is a way of taking of vectors of data, which allow having data defined at n points in some intervals instead of having analytical function. The FFT (Fast Fourier Transformation) algorithm is used to calculate in more efficient and time-consuming way the DST. The obtained signal closely resembles the signals depicted in Pope's book (2000) for a turbulent jet. FFT analysis reveals the existence of numerous frequencies, with a pronounced intensity peak at lower frequencies. It is worth noting that FFT analysis is typically more appropriate for entirely periodic signals. As illustrated in the following figure, turbulent signals lack periodicity.

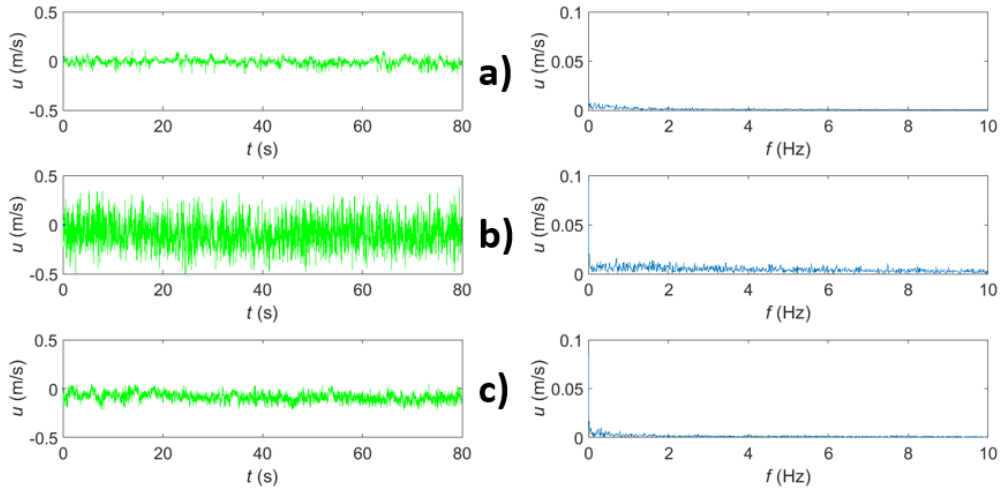

Figure H1: Temporal frequency domain for three points on configurations 12.

Power spectral density (PSD)

Power Spectral Density of a signal is the Fourier transform of the autocorrelation function of the square of the modulus of the Fourier transform, which represents the power distribution on the frequency axis. PSD shows the strong and weak frequencies variation, at which frequencies variations. In turbulence, the PSD describes how the energy is transferred from the large eddies to the smaller one according to Richardson Cascade. S is the power spectrum in units ofm^2/Hz.

$$S(f) = I\int_0^{\infty} x(t)e^{-i2\pi ft}dt\ I^2$$

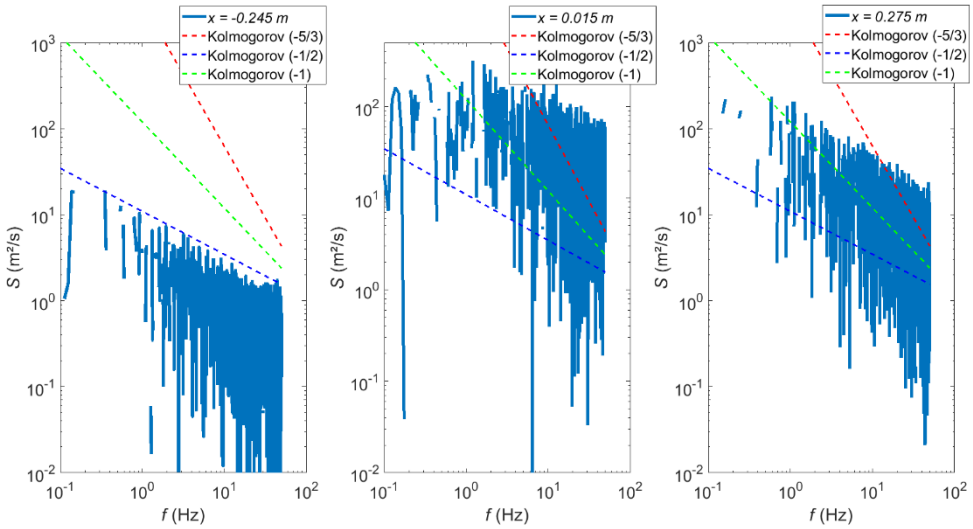

Figure H2: PSD for three points on configurations 12.

Wavelet analysis (Morelet)

Wavelet transform or multi-resolution analysis could be seen as supercharged Fourier transform,. This allows generalizing an idea of sines and cosines providing an orthogonal basis to other orthogonal functions that may provide better representation of certain type of function. It consists of a hierarchical grading of time and frequency information. The idea is that the lower frequencies change more slowly in time then a less temporal accuracy is needed. The temporal accuracy is getting more important for higher frequencies, but uncertainty will increase to determine what frequency is turning on and off in that range. It could be compared to a spectrogram tailored to spend much information in the region as necessary. As for Fourier transform, the time series is projected on an orthogonal basis consisting of hierarchy of orthogonal functions that are going to be smaller and smaller in time or in space. It starts with a mother wavelet $\Psi(t)$. From this wavelet, it is possible to derive all smaller wavelet.

$$\Psi_{a,b}= 1/a^{1/2}\ \Psi(\frac{t-b}{a})$$

$W_{\Psi}(f)(a,b) =<f(t), \Psi_{a,b}(t)>$ (inner product). b would shift the gaussian left or right in time, picking which window in time we are and would make the wavelet bigger or smaller. As an increase, we are going up the level and b is going to correspondingly slide the window across out time signal. Morlet wavelet is a complex function given by

$$\Psi(t)=\exp(2i\pi w_0\ t -t^2/2).$$

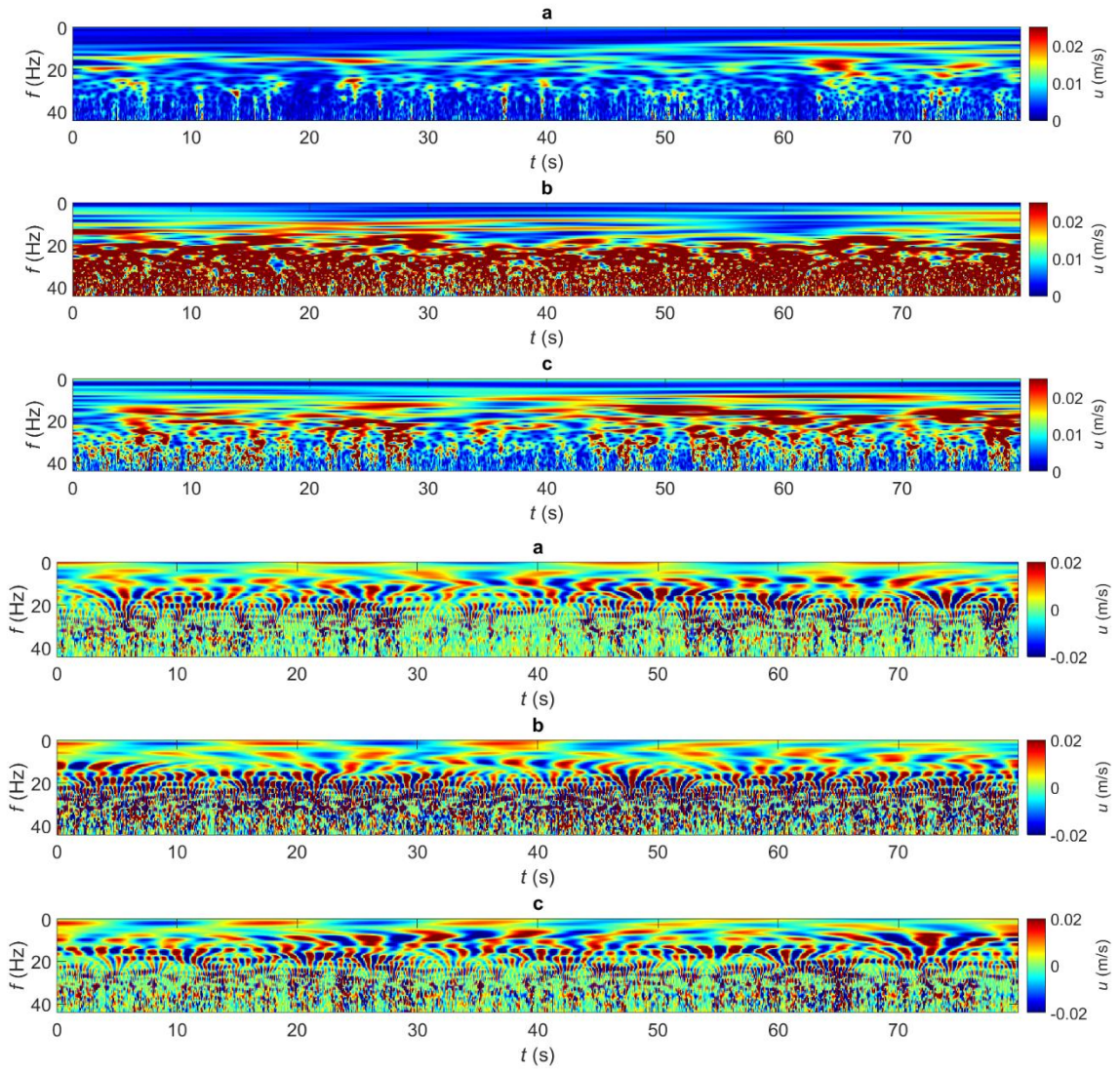

Figure H3: Wavelet analysis using Morlet function of three points on configurations 12.

Appendix I. Experience set-up for H = 0.20 m (Chapter 4)

A series of 20 (twenty) additional experiments were conducted with *clear water and* H = 0.20 m:

Table I1: Additional experiments with clear water and H = 0.20 m

Inlet	Test ID	L_1 (m)	ΔB (m)	SF	Q (m^3/s) (10^{-4})	Z_{jet}/H	Flow type
Channel	23	2.00	0.4525	8.84	10	0.50	A1
	24				35		A1
Jet	25	2.00		8.84	5	0.10	BF
	26				17.5		BF
	27				30		BF
	28	1.05		4.64	5	0.10	BF
	29				17.5		BF
	30				30		BF
	31	2.00		8.84	5	0.50	U
	32				17.5		U
	33				30		U
	34	1.05		4.64	5	0.50	A1*
	35				17.5		A1*
	36				30		A1*
	37	2.00		8.84	5	0.75	U
	38				17.5		U
	39				30		U
	40	1.05		4.64	5	0.75	A1*
	41				17.5		A1*
	42				30		S

Jet at *H* = 0.20 m, *Q* = *0.001 m³/s*

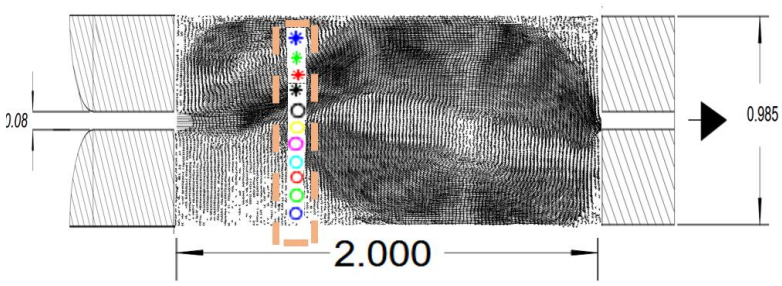

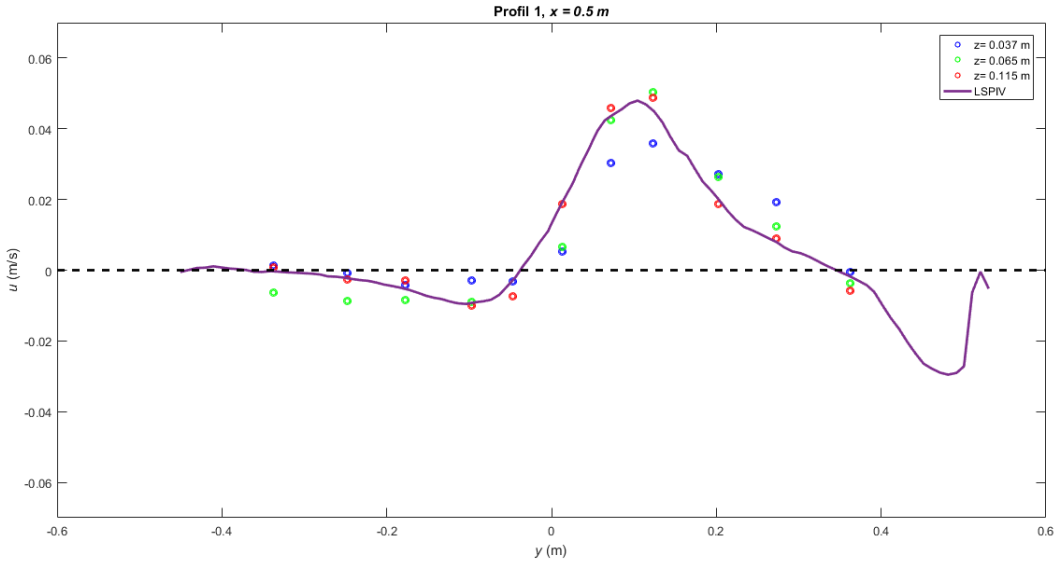

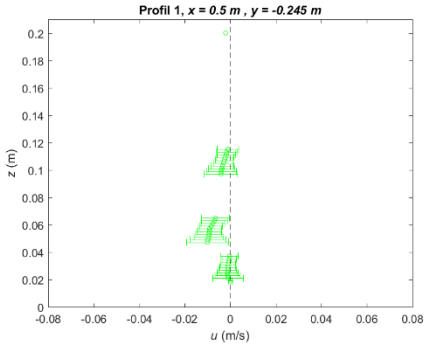

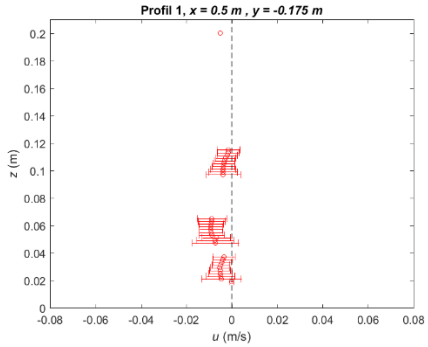

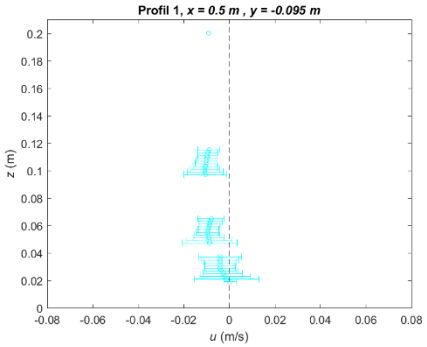

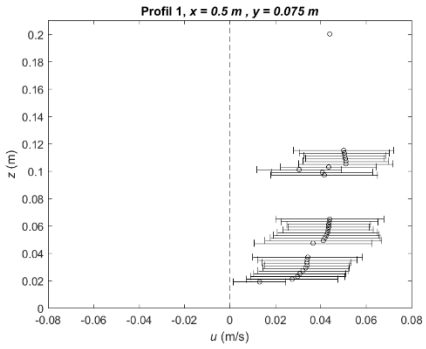

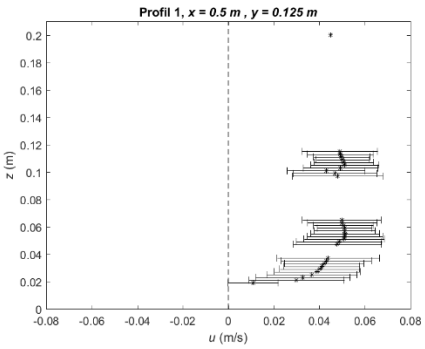

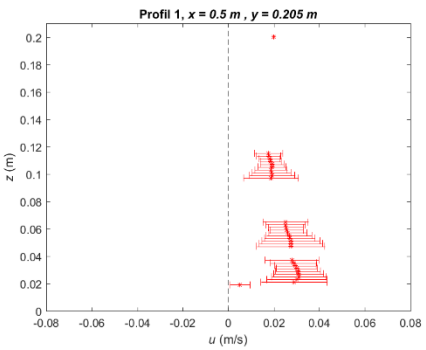

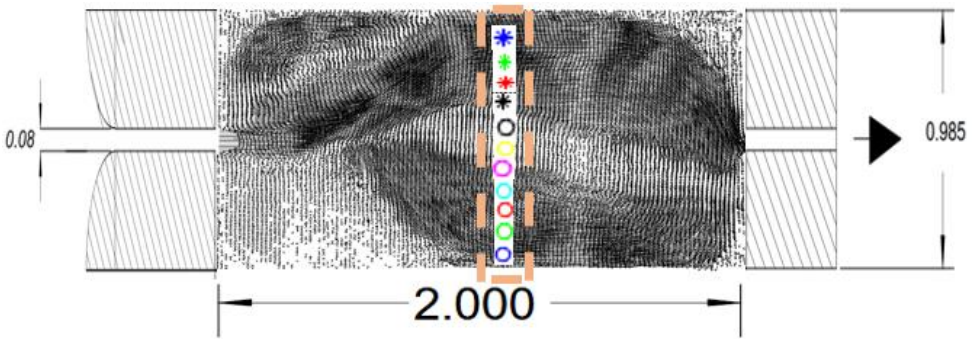
0.08
0.985
2.000

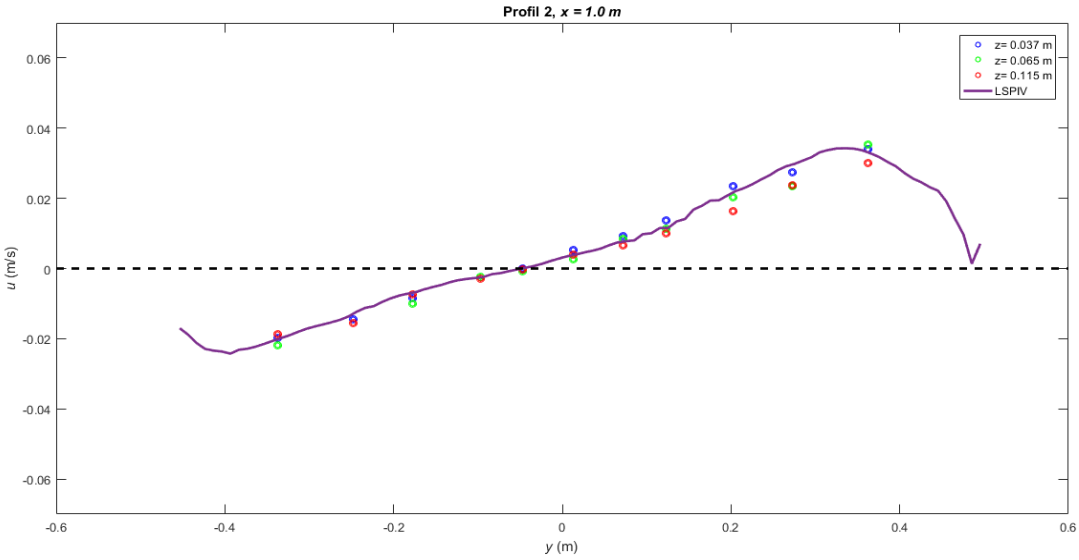
Profil 2, x = 1.0 m
z= 0.037 m
z= 0.065 m
z= 0.115 m
LSPIV
u (m/s)
y (m)

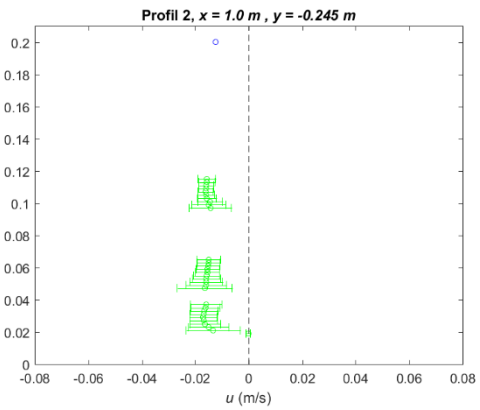
Profil 2, x = 1.0 m , y = -0.245 m
u (m/s)

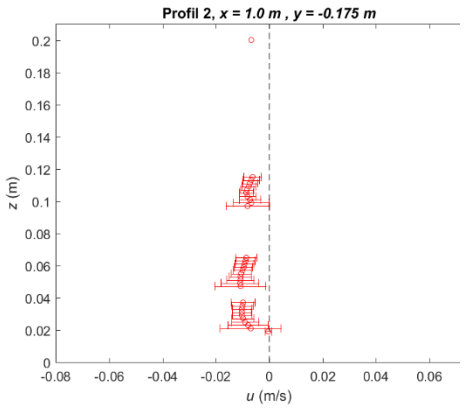
Profil 2, x = 1.0 m , y = -0.175 m
z (m)
u (m/s)

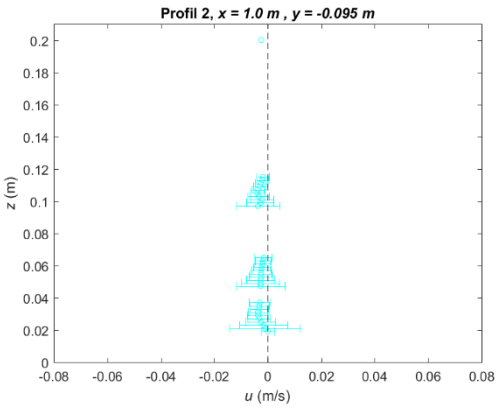
Profil 2, x = 1.0 m , y = -0.095 m
z (m)
u (m/s)

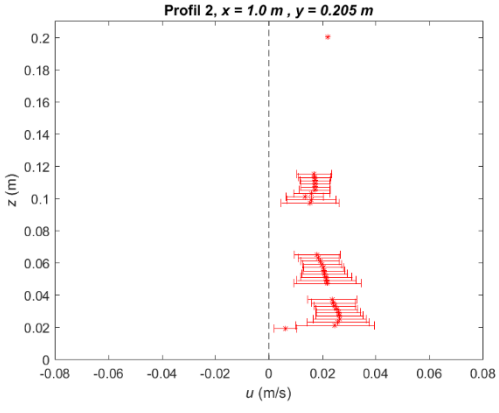
Profil 2, x = 1.0 m , y = 0.205 m
z (m)
u (m/s)

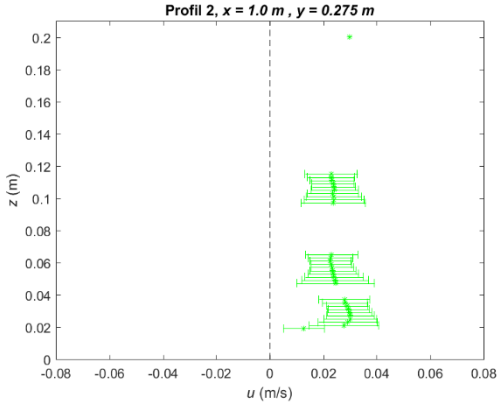
Profil 2, x = 1.0 m , y = 0.275 m
z (m)
u (m/s)

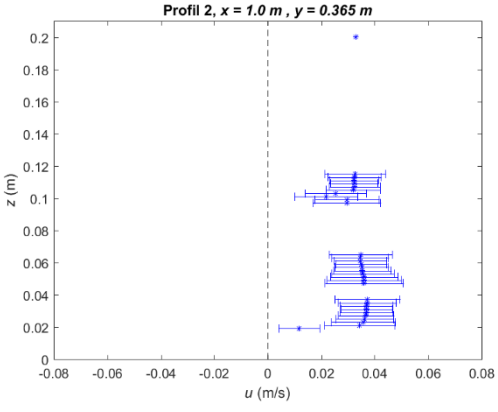
Profil 2, x = 1.0 m , y = 0.365 m
z (m)
u (m/s)

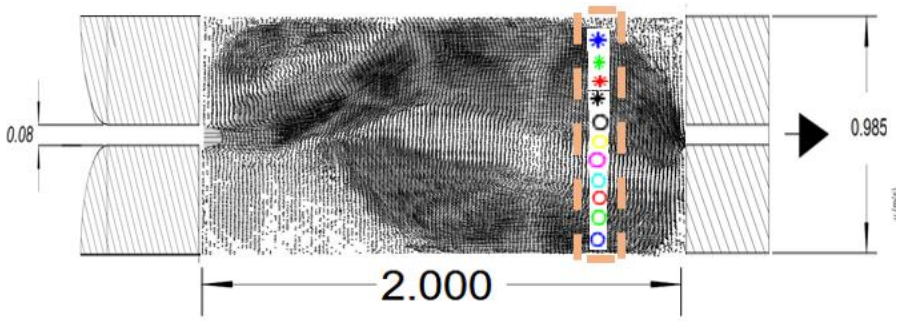

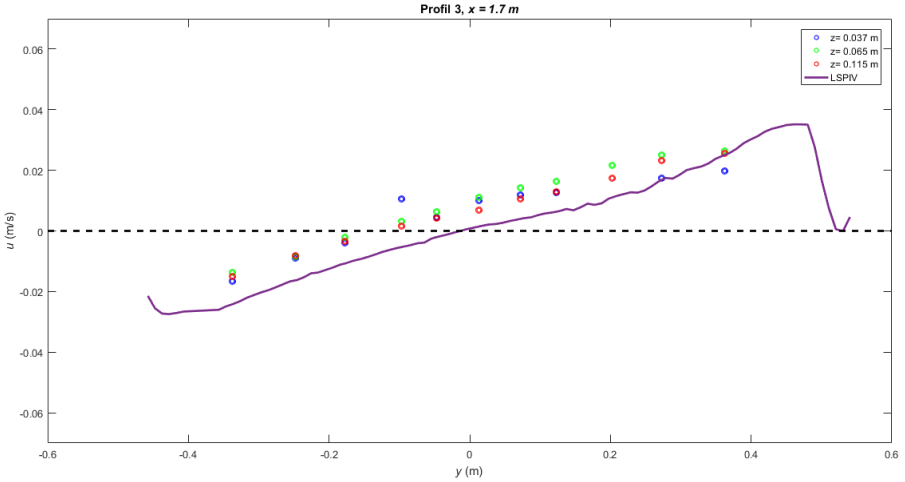

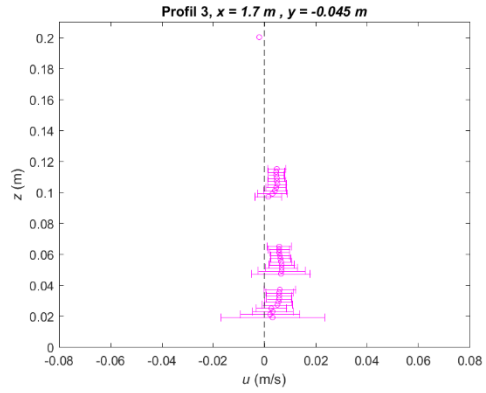

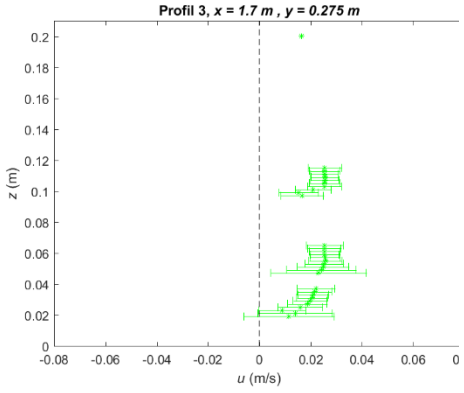

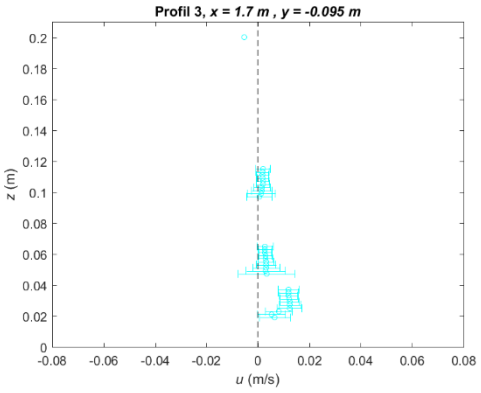

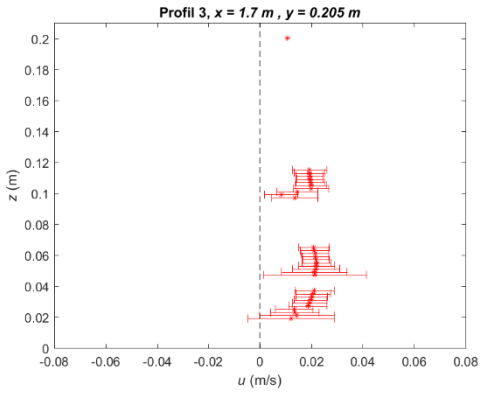

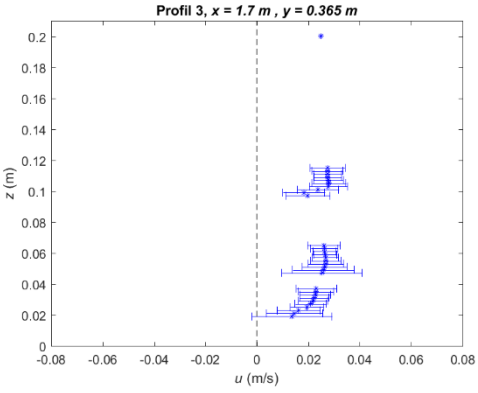

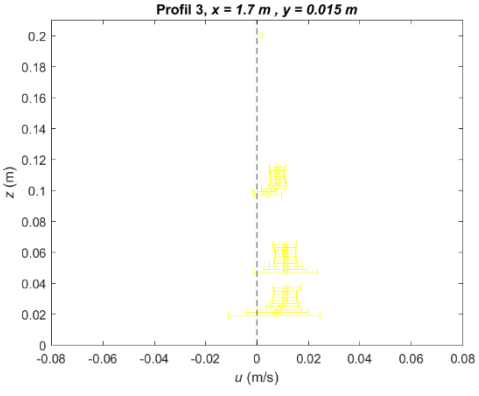

Figure I1: Reference case -Free surface channel Q=.0.001m³/s - H = 0.20 m

Jet at Z_{jet}/H = 0.10

For a jet positioned at the bottom, the flow pattern differs from that with H = 0.10 m, which exhibits a stable flow. In this jet position, observed in both short and long basins under various hydraulic conditions, we witness a jet that remains localized at the bottom with the presence of surface return currents emerging at the outlet channel. Similar results were studied by Stovin (1996). It is noted that for low flow rates, the intensity of return currents is negligible. The surface water plane with sawdust remains fixed, both in the long and short basins. In the case of the short basin, it is observed that the intensity of return currents is higher in the middle of the channel and more widely distributed around it.

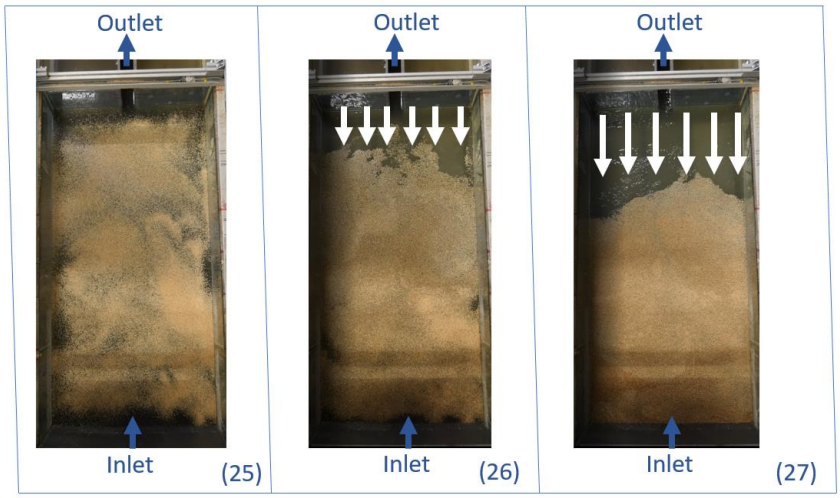

Figure I2: Flow patterns at the surface for short reservoir with Z_{jet}/H = 0.10 for three hydraulic conditions.

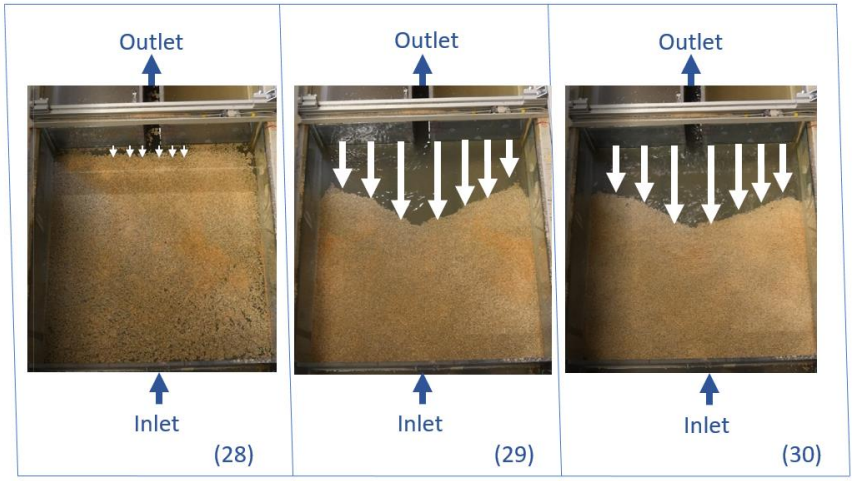

Figure I3: Flow patterns at the surface for long reservoir with Z_{jet}/H = 0.10 for three hydraulic conditions.

Jet at Z_{jet}/H = 0.50

For Z_{jet}/H = 0.50, we observe distinct behavior between long and short basins. In long basins, we observe a quasi-periodic switch of the jet from the left side to the right side, resulting in a non-stationary state. Similar findings have been reported in a rectangular cavity by various researchers and the mechanism behind this jet oscillation is associated with pressure effects (Mataoui et al., 2010). The systems have in common the presence of a delayed feedback loop, whether implicit or explicit, that initiates the oscillatory pattern (Rigolt 2015). The same author elaborated the three consecutive phases of the jet oscillation. These include the pressure-driven growth of the oscillation, amplitude limitation due to confinement and the delayed elimination of the pressure deficit in the recirculation zone through a feedback loop. In the case of short basins, we identify the flow typology as A1*.

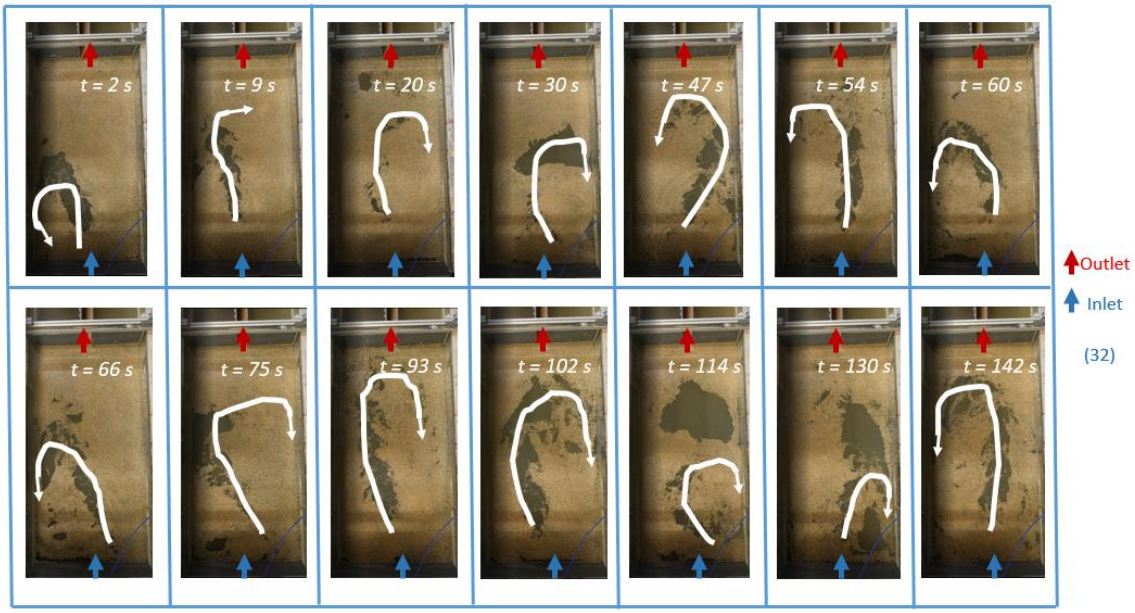

Figure I4: Evolution of unsteady flow patterns at the surface for long reservoir with Z_{jet}/H = 0.50 for middle hydraulic condition.

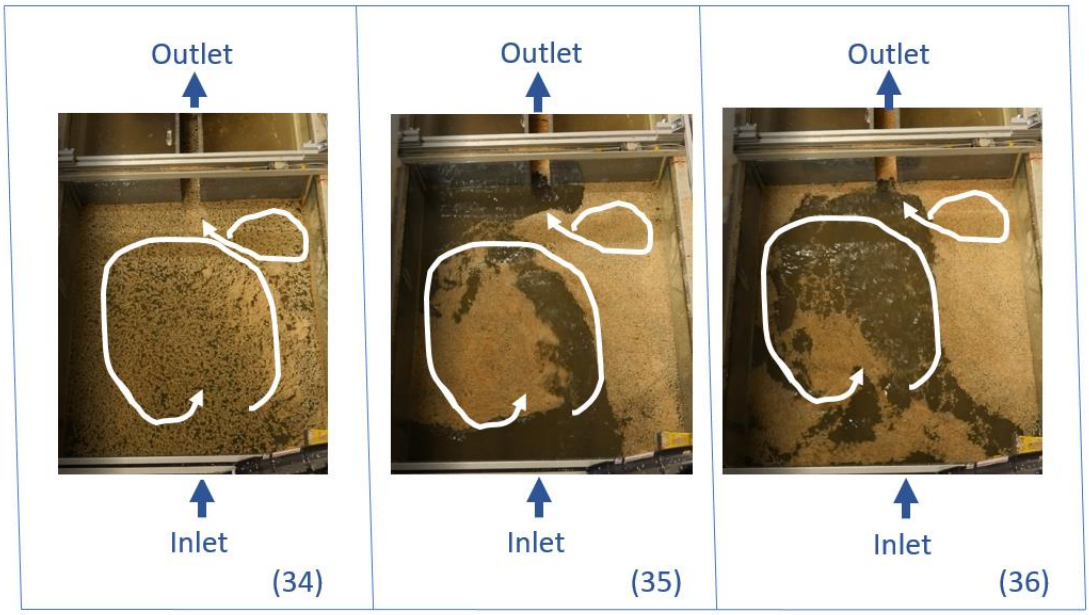

Figure I5: Flow patterns at the surface for long reservoir with Z_{jet}/H = 0.50 for three hydraulic conditions.

Jet at Z_{jet}/H = 0.75

Also, for Z_{jet}/H = 0.75, a distinct behavior between long and short basins is found. For long reservoir an oscillatory regime is found. For short reservoir, A1* regime is found for low and average flowrate and a symmetrical regime is found for high flowrate.

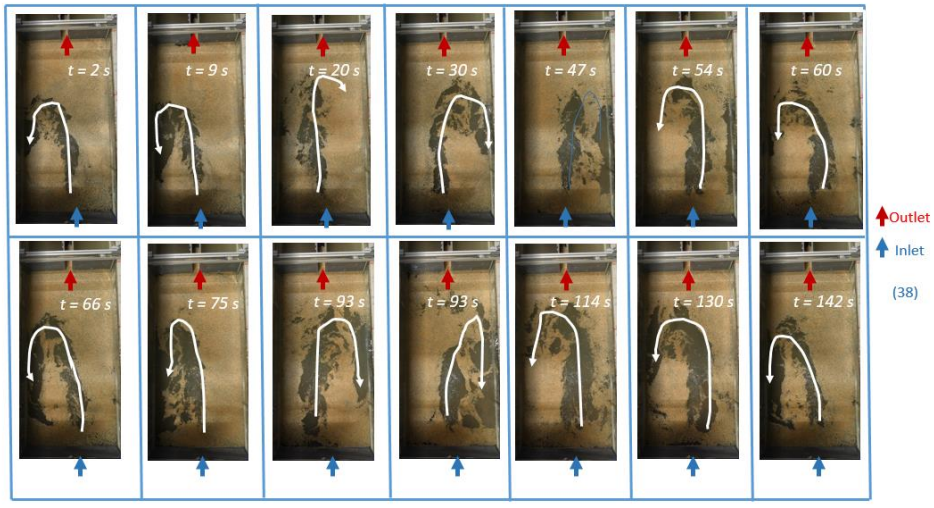

Figure I6: Evolution of unsteady flow patterns at the surface for long reservoir with Z_{jet}/H = 0.75 for middle hydraulic condition.

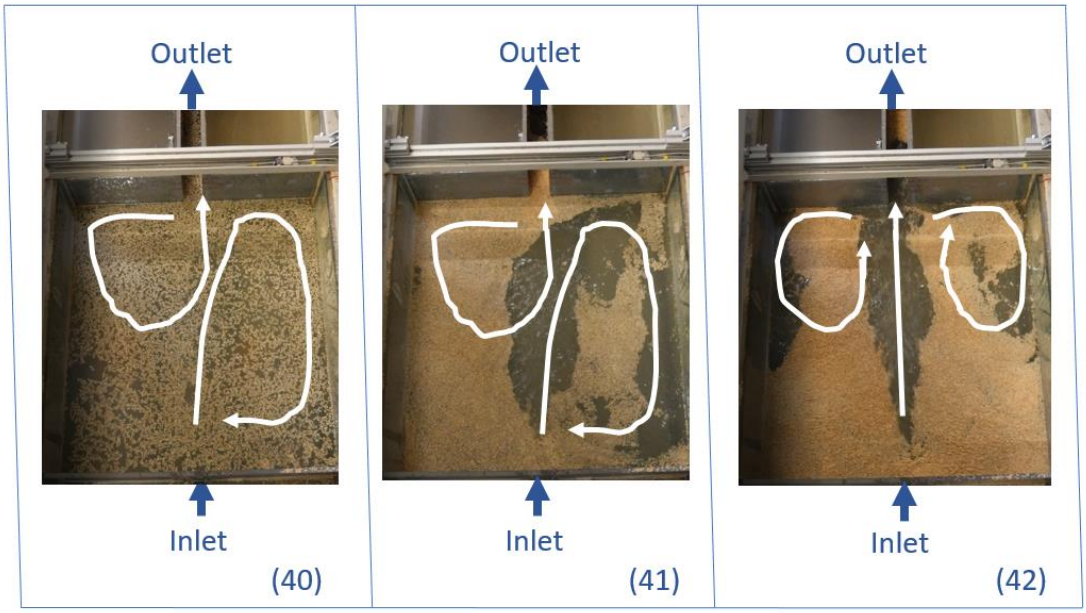

Figure I7: Flow patterns at the surface for long reservoir with $Z_{jet}/H = 0.75$ for three hydraulic

Appendix J. Additional numerical results with code_saturne (Chapter 7)

Tetrahedral meshing for short reservoir

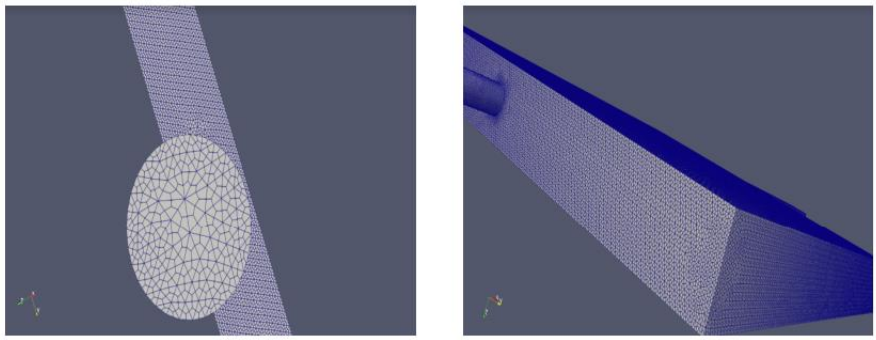

(a) Jet mesh (b) reservoir mesh

Figure J1: Tetrahedral meshing

The same simulation was carried out with the same setting as the tetrahedral case. The number of elements in the tetrahedral-to hexahedral mesh was closely matched to the tetrahedral mesh (1.22 million for hexahedral vs 1.35 million for tetrahedral).

Figure below presents a comparison between numerical and experimental results for both *u* and *v* velocity components along the reservoir width and for different *x* and *z* positions. A significant discrepancies are observed between numerical and experimental velocity values, it was concluded that the tetrahedral mesh is more faithful to reality, leading to the continuation of the study with the tetrahedral mesh.

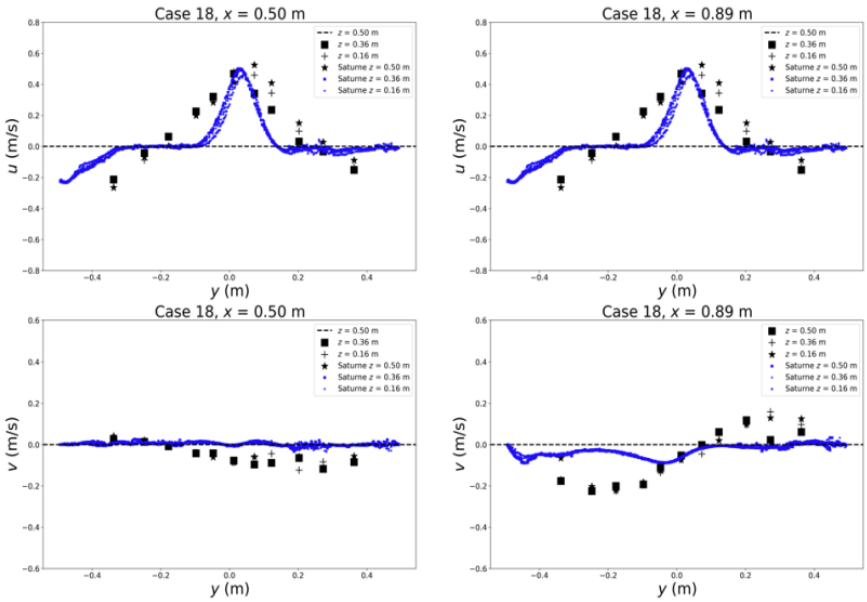

Figure J2: Comparison with longitudinal profiles for tetrahedral meshing

Refined mesh for long reservoir

An additional test was conducted using a different mesh and the K-omega SST model, resulting in an improved prediction of the attachment point. Figure below illustrates the evolution of the jet in this scenario. The refinement improves the results in terms of flow patterns prediction and comparison with velocity profiles at the vertical.

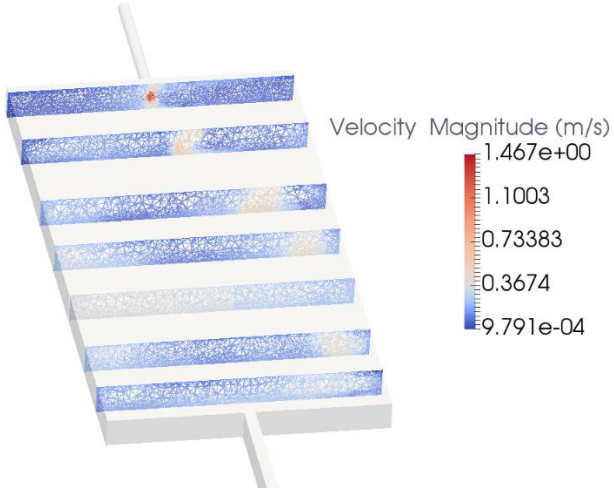

Figure J3: Flow patterns at different slice of a configuration 18.

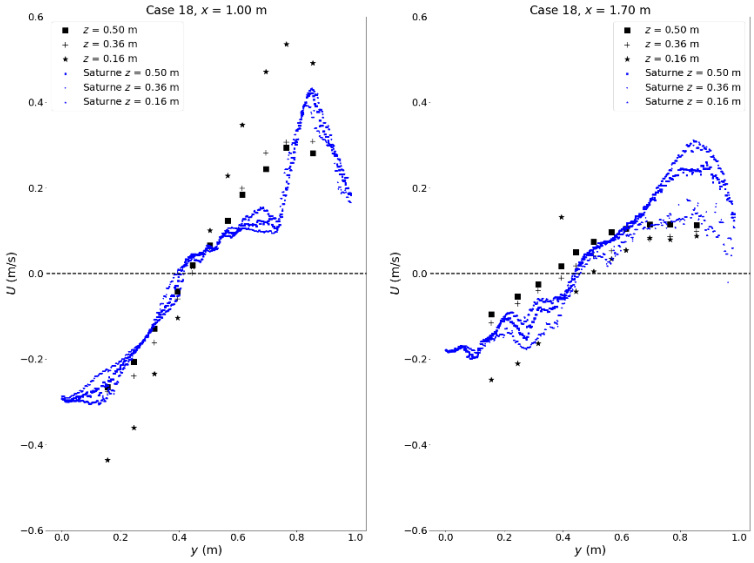

Figure J4: Comparison of numerical and experimental longitudinal velocity profiles.

Appendix K. Hydro-sedimentary simulations with TELEMAC-2D and GAIA for Camnasio et al. (2013) (Chapter 3)

Numerical hydro-sedimentary simulations were conducted to replicate the sediment deposits observed by Camnasio et al. (2013). After performing mesh sensitivity analysis, a mesh size of 0.0125 m was selected for the sedimentary component. Sensitivity analysis of numerical schemes indicated that the characteristics method yielded results closer to experimental measurements. Subsequently, a sensitivity analysis was carried out on the diffusion coefficient denoted as *K* and the different deposition laws, namely Formula 1 (Zyserman-Fredsoe), Formula 3 (Van Rijn), and Formula 4 (Soulsby & Van Rijn) of GAIA (see Gaia user manual). In this initial sensitivity analysis, we only considered suspension transport and excluded bedload transport. We observed that deposition zones were identified for all configurations, but the modeled thickness significantly exceeded the experimental measurements.

A more detailed analysis through automatic calibration is required to determine the influence of each parameter, allowing us to find the setup that best matches the measurements. Due to time constraints, it couldn't be accomplished within the scope of the thesis.

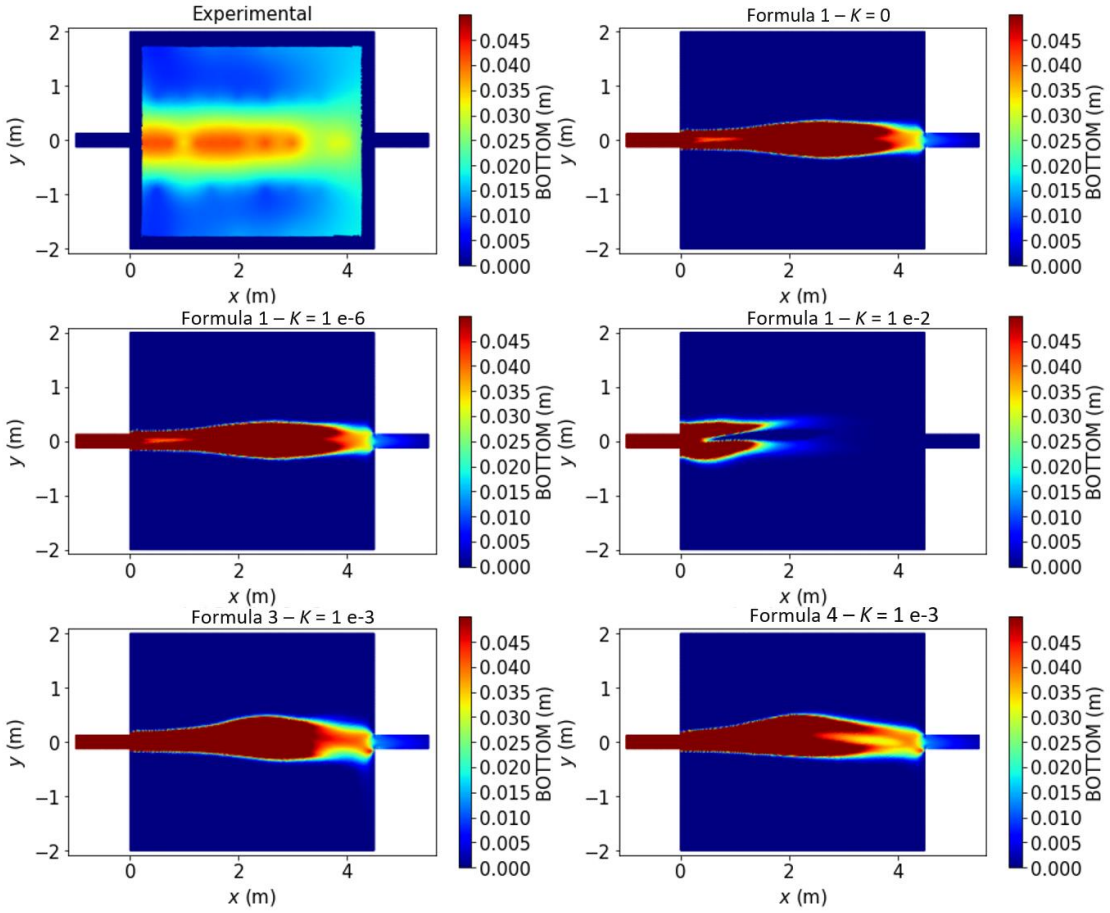

Figure K1: Sensitivity results for C-C configuration

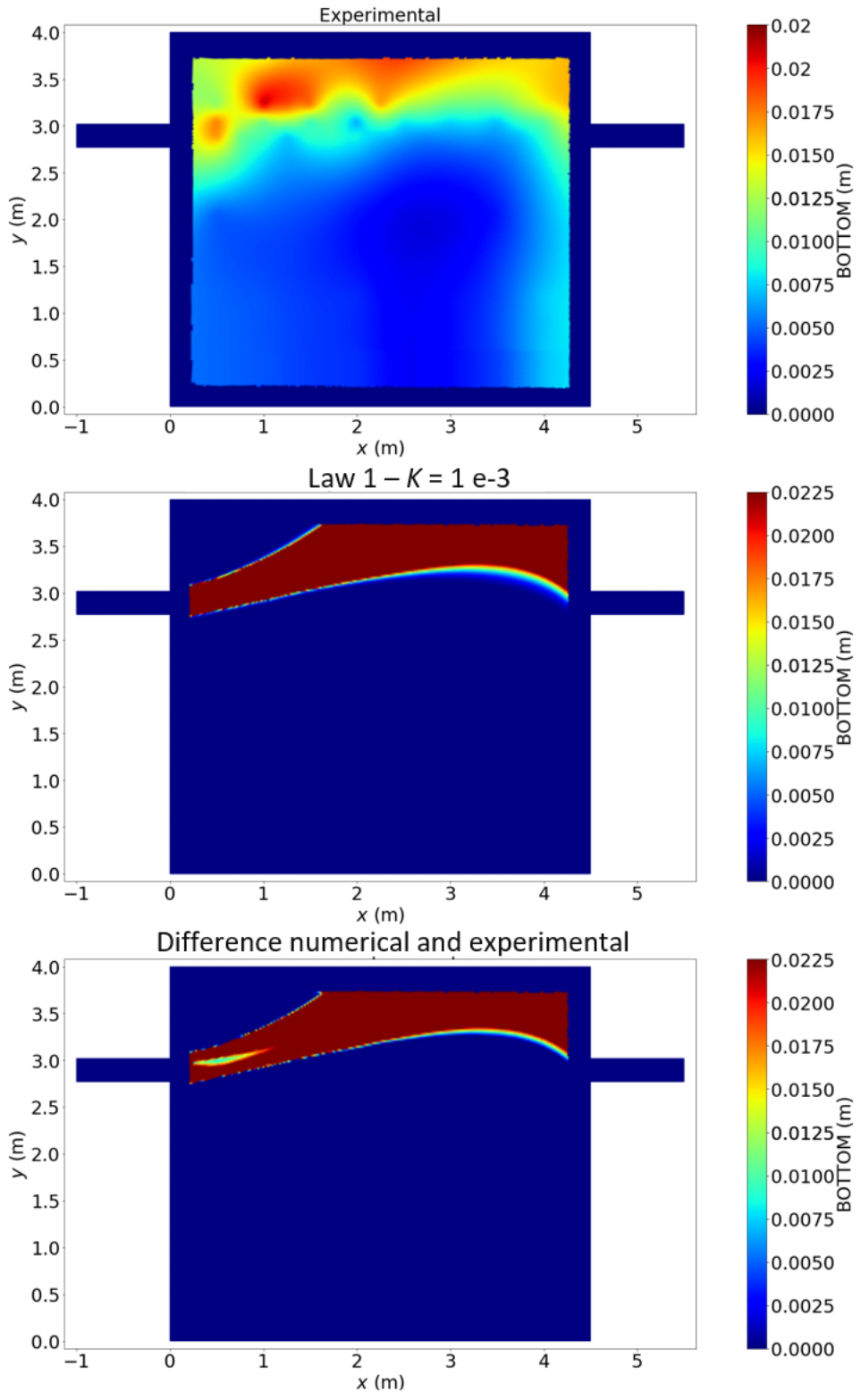

Figure K2: Sensitivity results for L-L configuration

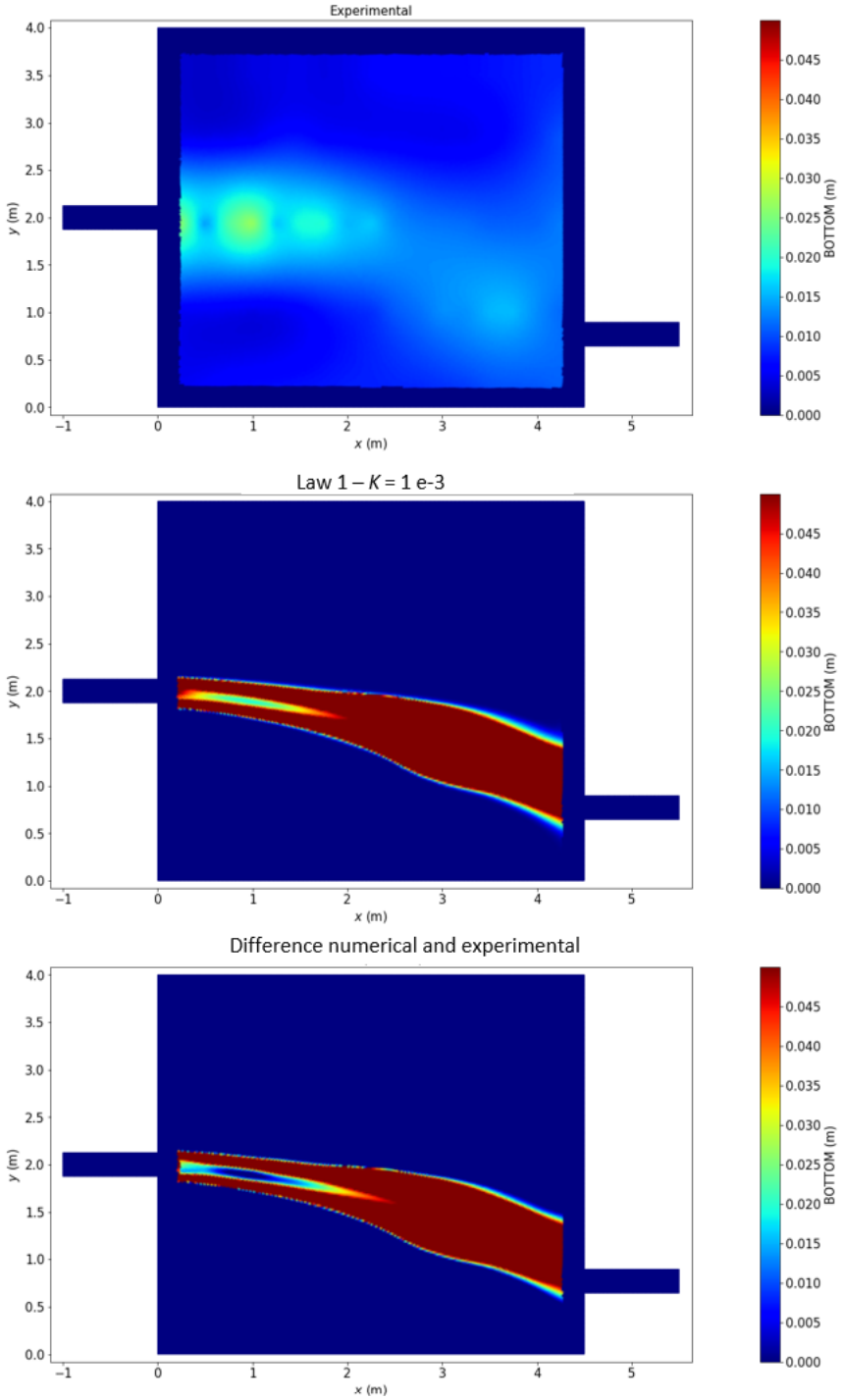

Figure K3: Sensitivity results for C-R configuration

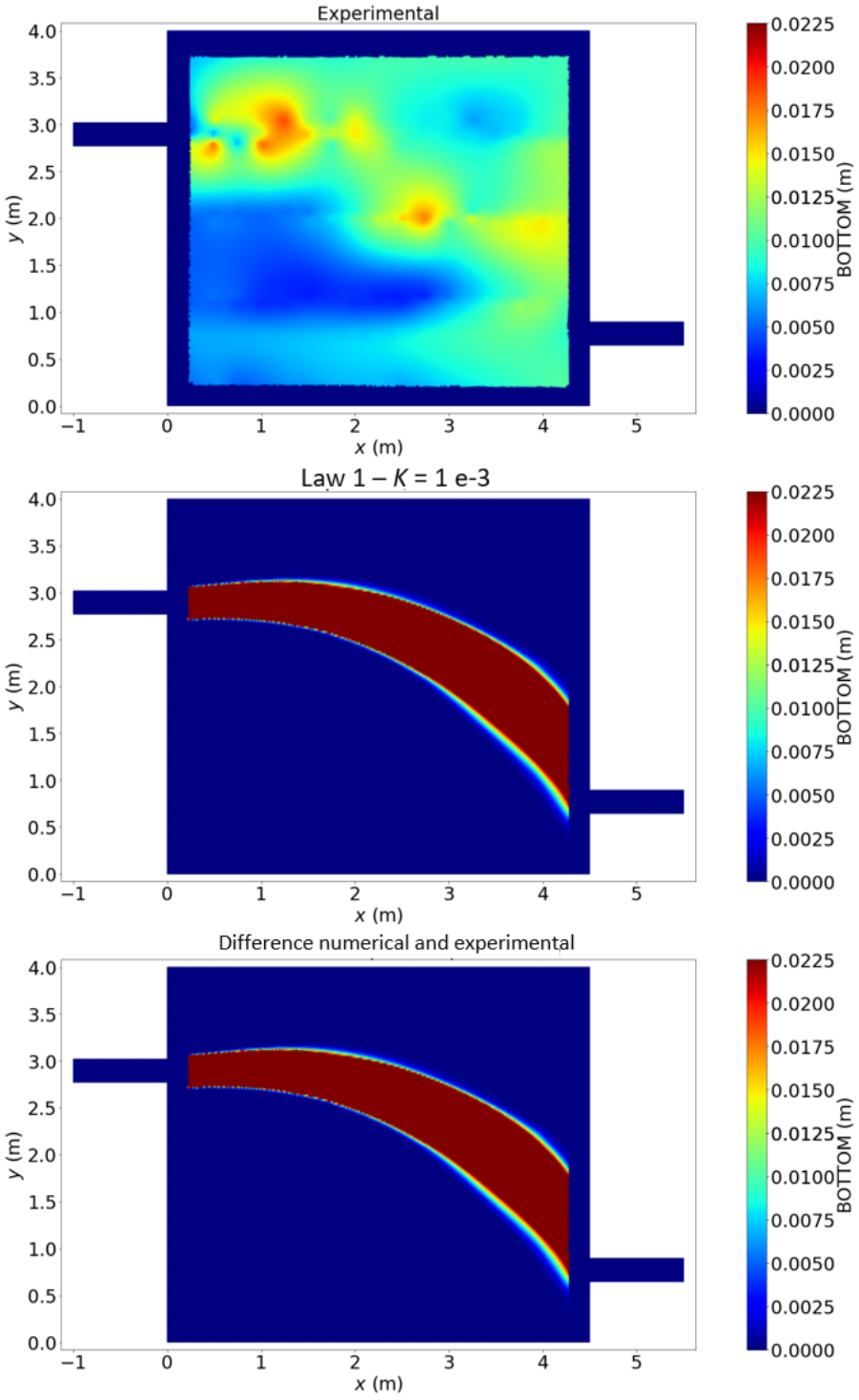

Figure K4: Sensitivity results for L-R configuration

Appendix L. Experimental set-up photos (Chapters 3, 4 and 5)

Configuration with channel at the inlet.

Configuration with pressurized jet.

Magneto flow meter (left) and Centrifugal pump(right).

Figure L1: Photos of experimental set-up.

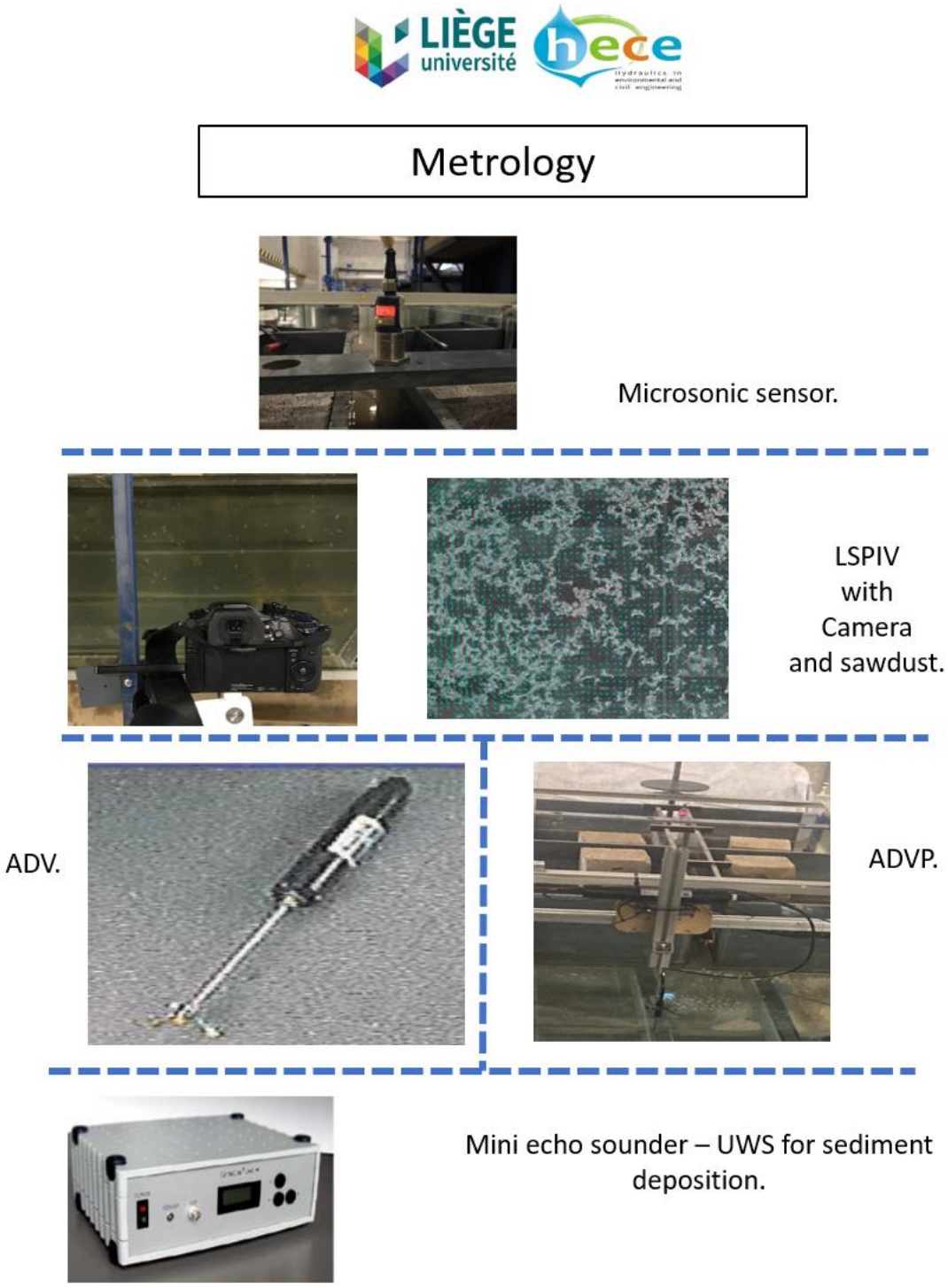

Figure L2: Photos of Metrology devices.

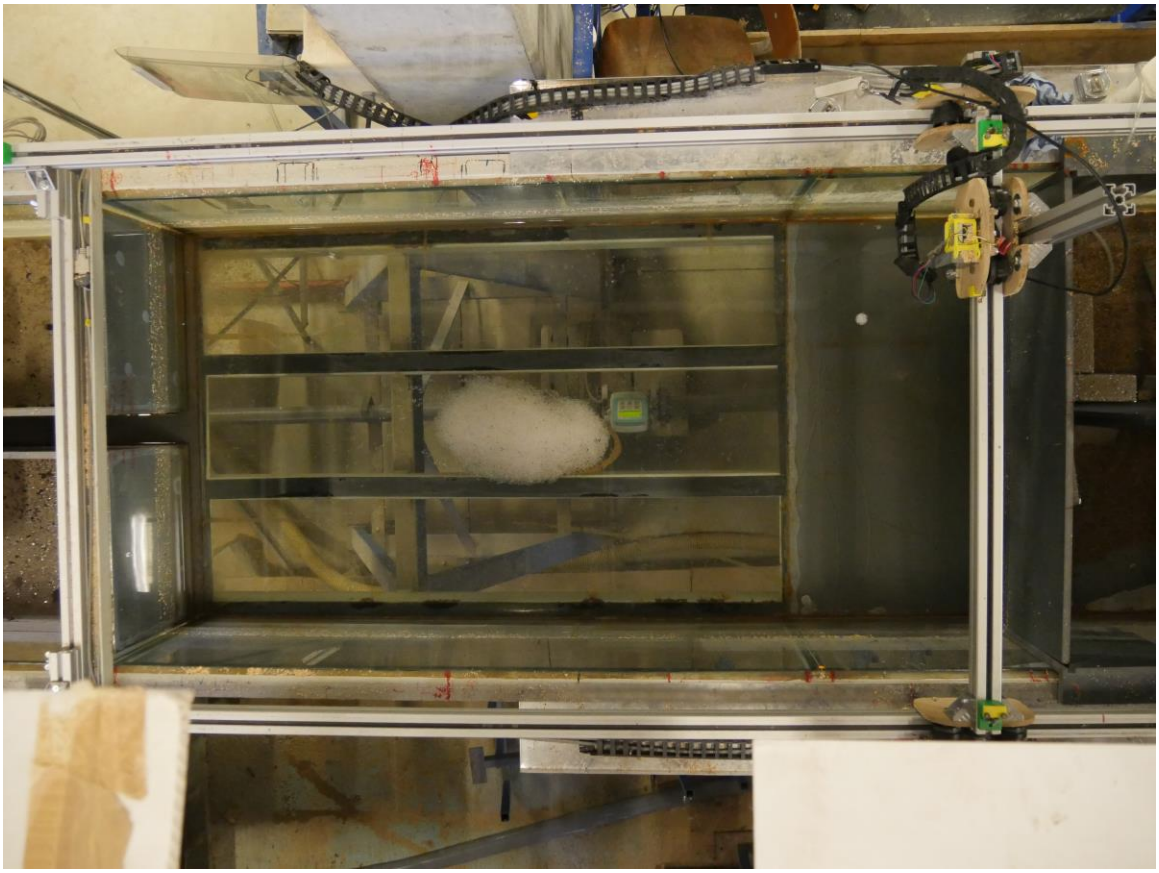

Figure L3: Photo of sediment deposits.

Appendix M. code_saturne, URANS and LES turbulence models (Chapter 2)

For turbulent flows, the strategy is to treat the velocity field **u** as stochastic when the flow transitions to a turbulent state. This stochastic velocity field is then decomposed into a mean field denoted by $\underline{\bar{u}}$ and a fluctuating field $\underline{u}'$:

$$\underline{u} = \underline{\bar{u}} + \underline{u}'$$

The Reynolds average operator $\overline{(\cdot)}$ is applied to Navier-Stokes Equation:

$$\frac{\partial \rho}{\partial t} + div(\rho \underline{\bar{u}}) = \Gamma,$$

$$\rho \frac{\partial \underline{\underline{u}}}{\partial t} + \underline{\underline{\nabla \bar{u}}} \cdot (\rho \underline{\bar{u}}) = -\underline{\nabla \bar{P}} + \underline{div}\left(\mu \left[\underline{\underline{\nabla \bar{u}}} + \underline{\underline{\nabla \bar{u}}}^T - \frac{2}{3} tr\left(\underline{\underline{\nabla \bar{u}}}\right) \underline{\underline{Id}}\right]\right) + \rho \underline{g} - \underline{div}\left(\rho \underline{\underline{R}}\right)$$
$$+ \underline{ST_u} - \rho \underline{\underline{K}} \underline{\bar{u}} + \Gamma\left(\underline{\bar{u}}^{in} - \underline{\bar{u}}\right)$$

Only the mean fields $\underline{\bar{u}}$ and $\overline{P}$ are computed. An additional term $\underline{\underline{R}}$ is present in the Reynolds Equations, where it is defined as the covariance tensor of the fluctuating velocity field. This tensor is referred to as the Reynolds stress tensor.

$$\underline{\underline{R}} \equiv \underline{u}' \otimes \underline{u}'$$

the latter necessitates a closure model, the selection of which is contingent upon the turbulence model being employed. There are two primary categories of such models:

- Eddy Viscosity Models EVM which assume that the Reynolds stress tensor is aligned with the strain rate tensor of the mean flow $\left(\underline{\underline{S}} \equiv \frac{1}{2}\left(\underline{\underline{\nabla u}} + \underline{\underline{\nabla u}}^T\right)\right)$:

$$\rho \underline{\underline{R}} = \frac{2}{3} \rho k \underline{\underline{1}} - 2\mu_T \underline{\underline{S}}^D$$

The turbulent kinetic energy k is expressed as:

$$k \equiv \frac{1}{2} tr\left(\underline{\underline{R}}\right)$$

- Equations for the variables k and ε (standard $k - \varepsilon$ model)

$$\rho \frac{\partial \mathrm{k}}{\partial \mathrm{t}} + \underline{\nabla \mathrm{k}} \cdot (\rho \underline{\mathrm{u}}) - \mathrm{div}\left[\left(\mu + \frac{\mu_\mathrm{t}}{\sigma_\mathrm{k}}\right) \underline{\nabla \mathrm{k}}\right] = \mathcal{P} + \mathcal{G} - \rho\varepsilon + \Gamma \mathrm{k}^{\mathrm{in}} + \mathrm{ST}_\mathrm{k}$$

$$\rho \frac{\partial \varepsilon}{\partial \mathrm{t}} + \underline{\nabla \varepsilon} \cdot (\rho \underline{\mathrm{u}}) - \mathrm{div}\left[\left(\mu + \frac{\mu_\mathrm{t}}{\sigma_{\bar{\varepsilon}}}\right) \underline{\nabla \varepsilon}\right] = \mathrm{C}_{\varepsilon_1} \frac{\varepsilon}{\mathrm{k}} \left[\mathcal{P} + \left(1 - \mathrm{C}_{\varepsilon_3}\right)\mathcal{G}\right] - \rho \mathrm{C}_{\varepsilon_2} \frac{\varepsilon^2}{\mathrm{k}} + \Gamma \varepsilon^{\mathrm{in}} + \mathrm{ST}_\varepsilon$$

Where $\mathcal{P}$ is the production term produced by mean shear:

$$\mathcal{P} = -\rho \underline{\underline{\mathrm{R}}} : \underline{\underline{\nabla \mathrm{u}}} = -\left[-2\mu_\mathrm{T} \underline{\underline{\mathrm{S}}}^\mathrm{D} + \frac{2}{3} \rho \mathrm{k} \underline{\underline{1}}\right] : \underline{\underline{\mathrm{S}}}$$

$$= 2\mu_T \underline{\underline{S}}^D : \underline{\underline{S}}^D - \frac{2}{3}\rho k \mathrm{tr}\left(\underline{\underline{\nabla u}}\right)$$

Where $\mathcal{P}$ is the production term created by gravity effects:

$$\mathcal{G} = \frac{1}{\rho}\frac{\mu_T}{\sigma_t}\underline{\nabla}\rho \cdot \underline{g}$$

μ_T is the dynamic turbulent viscosity and must be modelled. Note that the viscous part $\mu_T \underline{\underline{S}}^D$ of the Reynolds stresses is simply added to the viscous part of the stress tensor $\mu_l \underline{\underline{S}}^D$ so that the momentum equation for the mean velocity is similar to the one of a laminar flow with a variable viscosity $\mu = \mu_l + \mu_T$. FiveEVM are available in code_saturne: k - ε standard, k - ε with Linear Production(LP), k - $\underline{\omega}$ SST, Spalart Allmaras, and an Elliptic Blending model $\mathrm{BL} - \mathrm{v2/k}$
The dynamic turbulent viscosity can be written:

$$\mu_T = \rho C_\mu \frac{k^2}{\varepsilon}$$

ST_k and ST_ε are some eventual source terms that can be added. The constants of the model are $C_\mu = 0.09$, $C_{\varepsilon_1} = 1.44$, $C_{\varepsilon_2} = 1.92$, $\sigma_k = 1.0$, $\sigma_k = 1.3$, $C_{\varepsilon_3} = 0$ if $\mathcal{G} \geq 0$ (unstable stratification) and $C_{\varepsilon_3} = 1$ if $\mathcal{G} \leq 0$ (stable stratification).

- Spalart-Allmaras turbulence model involves a transport equation for a scalar parameter $\tilde{\nu}$, which is directly connected to the turbulent viscosity μ_T. A more recent advancement expanded this model to handle rough walls, primarily for investigating atmospheric flows. Additionally, this model found success in analyzing turbomachinery flows, leading to the development of various model variants in that context. The transport equation of $\tilde{\nu}$ reads:

$$\rho\frac{\partial \tilde{\nu}}{\partial t} + \underline{\nabla}\tilde{\nu} \cdot \left(\rho \underline{u}\right) = c_{b1}\rho\tilde{S}\tilde{\nu} - c_{w1}f_w\rho\left(\frac{\tilde{\nu}}{d}\right)^2 + \frac{1}{\sigma}\mathrm{div}\left((\mu + \rho\tilde{\nu})\underline{\nabla}\tilde{\nu}\right) + c_{b2}\rho\left|\underline{\nabla}\tilde{\nu}\right|^2\Big] + \Gamma\left(\widetilde{\nu^{in}} - \widetilde{\nu^{n}}\right) + ST^{imp}\tilde{\nu} + ST^{exp}$$

where $\widetilde{\nu^{in}}$ is the injection value of $\tilde{\nu}$ in case of any mass source term, and $ST_{\tilde{\nu}}^{imp}$ and $ST_{\tilde{\nu}}^{exp}$ are respectively the implicit and explicit additional user source terms.

- $\underline{k}$ - $\underline{\omega}$ Shear Stress Transport (SST) model solves transport equations for turbulent kinetic energy (k) and specific dissipation rate (ω) with two formulations. Near walls, it employs the w equation with wall damping for accurate predictions. In free-stream regions, the k-equation is used. This model offers versatility in predicting a wide range of flow behaviors.

- $BL-v2/k$ is an elliptic-blending derived $\overline{v^2}-f$ model. Designed for low Reynolds numbers, this model requires that the wall distance of the first off-wall cell center be approximately of the same order as unity when expressed in terms of viscous units.

Differential Reynolds Stress Models (DRSM) that solve a transport equation for the components of the Reynolds stress tensor $\underline{\underline{R}}$ throughout the simulation and are easily accessible for use in the momentum equation. The model equation is:

$$\frac{DR_{ij}}{Dt} = D_{ij} + P_{ij} + \Pi_{ij} + \Omega_{ij} - \varepsilon_{ij}$$

D_{ij} is the diffusion term, P_{ij} is the production term, ε_{ij} is the dissipation rate, Π_{ij} is the pressure-strain correlation term and Ω_{ij} is the rotational term.

Two $\overline{\overline{DRSM}}$ models are available in code_saturne:

- R_{ij}- ε SSG: Reynolds stresses tensor coefficients are calculated by solving transport equations for these variables, and an equation for energy dissipation rate ε. The focus lies in approximating pressure-strain correlations, with the chosen forms yielding satisfactory stress distribution near walls and in free shear flows.
- Elliptic Blending version EB-RSM: The model is constructed based on modifying the pressure–strain tensor's formulation, which initially considers variations near a wall. This formulation is adjusted to match the conventional expression valid far away from the wall, achieved through a blending function denoted as α. To determine this blending function, an elliptic equation is solved. This new approach retains the essential characteristics of Durbin's Reynolds-stress model. However, it diverges in that it replaces the requirement to solve six elliptic equations (one for each stress component) with just a single scalar elliptic equation. This model, known as the 'elliptic blending model,' offers substantial simplification while upholding the fundamental physical basis behind the concept of elliptic relaxation.
- Large Eddy Simulation LES consists in spatially filtering the $\underline{u}$ field using an operator denoted by $\widetilde{(\cdot)}$. Applying the latter filter to the Navier-Stokes Equations gives:

$$\frac{\partial \rho}{\partial t} + div\left(\rho \underline{\tilde{u}}\right) = \Gamma$$

$$\rho \frac{\partial \underline{\tilde{u}}}{\partial t} + \underline{\nabla \tilde{u}} \cdot \left(\rho \underline{\tilde{u}}\right) = -\underline{\nabla \tilde{P}} + \underline{div}\left(2\mu \underline{\tilde{S}^D}\right) + \rho \underline{\underline{g}} - \underline{div}\left(\rho \underline{u' \otimes u''}\right) + \underline{ST_{\underline{u}}} - \rho \underline{\underline{K}}\,\underline{\tilde{u}} + \Gamma\left(\underline{\tilde{u}}^{in} - \underline{\tilde{u}}\right)$$

where $\underline{u}'$are non-filtered fluctuations. An eddy viscosity hypothesis is made on the additional resulting tensor:

$$\rho\widetilde{\underline{u}'\otimes\underline{u}'} = \frac{2}{3}\rho k\underline{\underline{Id}} - 2\mu_T\underline{\underline{S}}^D$$

where the above turbulent viscosity μ_T now accounts only for sub-grid effects.

Finite volume approach

The passage explains how equations are integrated over mesh cells using the finite volume approach, focusing on integrating various terms like 0^{th}order, convection, diffusion, and gradients using a budget method. The co-located finite volume method's key feature is discussed: variables linked to the same point (cell center), emphasizing gradient calculations.

Suppose N_{cell} represents the cell count. For the discretized field Y, it possesses N_{cell}degrees of freedom labeled as Y_c where c ranges from 1 to N_{cell}, as explicitly defined by:

$$Y_c \equiv \frac{1}{|V_c|}\int_{V_c} Y \sim dV$$

Since the discretized field Y is assumed to exhibit linearity within each individual cell, the value of Y_c at the cell center $\underline{x}_c$ of V_c can serve as its identification:

$$Y_{\underline{x}_c} = Y_c$$

0^{th}-order terms: Subsequently, terms devoid of spatial derivatives, referred to as 0^{th} -order terms, are integrated to establish their averages across the cell. For instance, $\rho\underline{g}$transforms into $|V_c|\rho_c\underline{g}$, where signifies the volume of the cell V_c, and $\rho_c$represents the mean value of ρ over the control volume (cell) V_c.

Divergence operator-conservative gradient terms: The integration of divergence terms (also known as flux terms or conservative terms) is carried out employing the Green relation. This incorporation yields cell face values, allowing fluxes to emerge naturally. For example, an expression like $\underline{div}\left(Y\underline{\underline{1}}\right)$ is:

$$\int_{V_c}\underline{div}\left(Y\underline{\underline{1}}\right)dV = \sum_{f\in\mathcal{F}_c} Y_f\underline{S}_{c>\bar{c}}$$

In expression (I.4.3), face values of the field Y appear. They are defined as:

$$Y_f \equiv \frac{1}{|\underline{S}|_f}\int_f Y \sim dS$$

This ensures the precision of relationship (I.4.3). Since the field Y exhibits linearity across the face f, $Y_f$can be linked to the center$\underline{x}_f$ of the respective face:

$$Y_{\underline{x}_f} = Y_f$$

Convection operator-mass flux terms: We will now direct our attention to the convective term $\mathrm{div}(\mathrm{Y}\rho\underline{\mathrm{u}})$, and simultaneously address the unsteady term $\frac{\partial(\rho \mathrm{Y})}{\partial \mathrm{t}}$. In fact, when the field $Y$is carried by the convective field $\rho\underline{\mathrm{u}}$ the equilibrium of the quantity ρYwithin a cell c is expressed employing Leibniz's theorem as follows (*):

$$\frac{\mathrm{d}}{\mathrm{dt}}\left(\int_{\mathrm{V_c}} \rho \mathrm{Y} \sim \mathrm{dV}\right) = \int_{\mathrm{V_c}} \frac{\partial \rho \mathrm{Y}}{\partial \mathrm{t}} \sim \mathrm{dV} + \int_{\partial \mathrm{V_c}} \mathrm{Y}\, \underline{\rho \mathrm{u}} \cdot \mathrm{d}\underline{\mathrm{S}}$$

$$= \int_{\mathrm{V_c}} \frac{\partial \rho \mathrm{Y}}{\partial \mathrm{t}} \mathrm{div}(\mathrm{Y}\rho\underline{\mathrm{u}}) \mathrm{dV}$$

Furthermore, the unsteady and convection terms are commonly expressed in a non-conservative form within the framework of continuous formalism:

$$\frac{\partial(\rho \mathrm{Y})}{\partial \mathrm{t}} + \mathrm{div}(\mathrm{Y}\rho\underline{\mathrm{u}}) = \rho \frac{\partial \mathrm{Y}}{\partial \mathrm{t}} + \underline{\nabla}\mathrm{Y} \cdot (\rho\underline{\mathrm{u}}) + \Gamma \mathrm{Y}$$

It's important to recognize that for the previous equation to remain valid, the continuity equation needs to be satisfied. If the preservation of (*) is desired even in discrete volume scenarios, the definition of the convection term should take the form (**):

$$\int_{\mathrm{V_c}} \underline{\nabla}\mathrm{Y} \cdot (\rho\underline{\mathrm{u}}) \mathrm{dV} \equiv \int_{\mathrm{V_c}} \mathrm{div}(\mathrm{Y}\rho\underline{\mathrm{u}}) \mathrm{d}\,\mathrm{V} - \mathrm{Y_c} \int_{\mathrm{V_c}} \mathrm{div}(\rho\underline{\mathrm{u}}) \mathrm{d}\,\mathrm{V}$$

$$= \int_{\partial \mathrm{V_c}} \mathrm{Y}\, \rho\underline{\mathrm{u}} \cdot \mathrm{d}\underline{\mathrm{S}} - \mathrm{Y_c} \int_{\partial \mathrm{V_c}} \rho\underline{\mathrm{u}} \cdot \mathrm{d}\underline{\mathrm{S}}$$

$$= \sum_{\mathrm{f} \in \mathcal{F}_c} (\mathrm{Y_f} - \mathrm{Y_c}) (\rho\underline{\mathrm{u}})_{\mathrm{f}} \cdot \underline{\mathrm{S}}_{\mathrm{c}>\bar{\mathrm{c}}}$$

The second line is derived by applying Green's formula once again. In equation (**), it is necessary to express both the face value $Y_f$and the magnitude of the mass flux $(\rho\underline{\mathrm{u}})_{\mathrm{f}} \cdot \underline{\mathrm{S}}_{\mathrm{c}>\bar{\mathrm{c}}}$. Various available convective schemes (such as upwind, centered, SOLU, etc.) are used for this purpose. Let $\dot{m_{c>\bar{c}}}$ denote the outward mass flux from cell c through the face f.

$$\dot{\mathrm{m}_{\mathrm{c}>\bar{\mathrm{c}}}} \equiv (\rho\underline{\mathrm{u}})_{\mathrm{f}} \cdot \underline{\mathrm{S}}_{\mathrm{c}>\bar{\mathrm{c}}}$$

It's important to observe that this convective flux finds its natural definition at cell faces and is consequently stored in that location within the code. In the subsequent content, the convection term is denoted as:

$$\int_{\mathrm{V_c}} \underline{\nabla}\mathrm{Y} \cdot (\rho\underline{\mathrm{u}}) \mathrm{dV} = \sum_{\mathrm{f} \in \mathcal{F}_c} \mathrm{C}_{\mathrm{c}>\bar{\mathrm{c}}}(\dot{\mathrm{m}_{\mathrm{c}>\bar{\mathrm{c}}}}, \mathrm{Y})$$

where $C_{c>\bar{c}}(\dot{m_{c>\bar{c}}}, Y)$ is defined by:

$$\mathrm{C}_{\mathrm{c}>\bar{\mathrm{c}}}(\dot{\mathrm{m}}_{\mathrm{f}}, \mathrm{Y}) \equiv (\mathrm{Y_f} - \mathrm{Y_c}) \dot{\mathrm{m}_{\mathrm{c}>\bar{\mathrm{c}}}}$$

Laplacian operator-diffusive terms: the diffusive term $div(K\underline{\nabla}Y)$can be written as follow:

$$\int_{V_c} \mathrm{div}\left(K\underline{\nabla}Y\right)\mathrm{d}\,V \equiv \sum_{f\in\mathcal{F}_c} K_f\underline{\nabla}_f Y \cdot \underline{S}_{c>\bar{c}}$$

Here, K_f represents the face diffusivity, and $\underline{\nabla}_f Y$ signifies the face gradient. Subsequently, the diffusive term is labeled as:

$$\int_{V_c} \mathrm{div}\left(K\underline{\nabla}Y\right)\mathrm{d}\,V = \sum_{f\in\mathcal{F}_c} D_{c>\bar{c}}(K_f Y)$$

where the diffusive flux $D_{c>\bar{c}}\left(K_f Y\right)$ over the face f is defined by

$$D_{c>\bar{c}}(K_f, Y) \equiv K_f\underline{\nabla}_f Y \cdot \underline{S}_{c>\bar{c}} o$$

REFERENCES

Abbott, D., & Kline, S. (1962). Experimental investigation of subsonic turbulent flow over single and double backward-facing steps. Journal of Basic Engineering, 84, 317-325.

Abrahamsson, H. (1997). On turbulent wall jets. Ph.D. Thesis, Chalmers University of Technology, Gothenburg, Sweden.

Adel, Abdel-Rahman. (2010). A Review of Effects of Initial and Boundary Conditions on Turbulent Jets. WSEAS Transactions on Fluid Mechanics, 5, 257-275.

Adamsson, A., Bergdahl, L., & Lyngfelt, S. (2005). Measurement and three-dimensional simulation of flow in a rectangular detention tank. Urban Water Journal, 2(4), 277-287.

Aloui, F., & Souhar, M. (2000). Experimental study of turbulent asymmetric flow in a flat duct with symmetric sudden expansion. Journal of Fluids Engineering, 122, 174-177.

Battaglia, F., & Papadopoulos, G. (2006). Bifurcation Characteristics of Flows in Rectangular Sudden Expansion Channels. Journal of Fluids Engineering, 128(4), 671-679.

Bradshaw, P. (1971). An introduction to turbulence and its measurement. Pergamon Press.

Browne, L. W., Antonia, R. A., & Chambers, A. J. (1984). The interaction regions of a turbulent jet. Journal of Fluid Mechanics, 149, 355-373.

Borgnat, P. (2006). Signal processing methods related to models of turbulence. In Harmonic Analysis and Rational Approximation (Lecture Notes in Control and Information Sciences, Vol. 327, pp. 277-301). Springer.

Bourgoin, A., El kadi Abderrezzak, K., Benhamadouche, S. & Ata, R. (2021). An adoption of the Spalart-Allmaras turbulence model for two- and three-dimensional free surface environmental flows. Journal of Hydraulic Research, 59(2), pp. 314-328.

Camnasio, E., Orsi, E., & Schleiss, A. J. (2011). Experimental study of velocity fields in rectangular shallow reservoirs. Journal of Hydraulic Research, 49, 352-358.

Camnasio, E., Erpicum, S., Orsi, E., Pirotton, M., Schleiss, A. J., & Dewals, B. (2013). Coupling between flow and sediment deposition in rectangular shallow reservoirs. Journal of Hydraulic Research, 51(5), 535-547.

Camnasio, E., Erpicum, S., Archambeau, P., Pirotton, M., & Dewals, B. (2014). Prediction of mean and turbulent kinetic energy in rectangular shallow reservoirs. Engineering Applications of Computational Fluid Mechanics, 8(4), 586-597.

Cherdron, W., Durst, F., & Whitelaw, J. (1978). Asymmetric flows and instabilities in symmetric ducts with sudden expansions. Journal of Fluid Mechanics, 84, 13-31.

Choufi, L., Kettab, A., & Schleiss, A. J. (2014). Effect of bottom roughness of a shallow rectangular reservoir on the flow field. La Houille Blanche, 83-92.

Claude, N., Secher, M., Deng, J., Valette, E., & Duclercq, M. (2019). 2D and 3D numerical modeling of the flow and sediment transport in shallow reservoirs: application to a real case. XXVIth Telemac & Mascaret User Club.

code saturne 8.0 Theory Guide: https://www.code-saturne.org/documentation/8.0/theory.pdf

Craig, R. G. A., Loadman, C., Clement, B., Ruesello, B. J., & Siegel, E. (2011). Characterization and Testing of a new Bistatic Profiling Acoustic Doppler Velocimeter: The Vectrino-II. In Proc. IEEE/OES/CWTM 10th Working Conference on Current, Waves and Turbulence Measurement (CWTM), Monterey, Canada, 20-23 March (pp. 246-252).

Davies, J. T. (1966). Chemical Engineering Progress, 62(9), 89.

Dewals, B., Kantoush, S., Erpicum, S., Pirotton, M., & Schleiss, A. J. (2008). Experimental and numerical analysis of flow instabilities in rectangular shallow basins. Environmental Fluid Mechanics, 8, 31-54.

Dewals, B., Peltier, Y., Pirotton, M., Archambeau, P., & Erpicum, S. (2014). Bi-Stable Flow Fields and Two-Way Couplings between Flow and Sedimentation in Shallow Reservoirs. In 3rd IAHR Europe Congress, Book of Proceedings. Porto, Portugal.

Dracos, T., Giger, M., & Jirka, G. H. (1992). Plane turbulent jets in a bounded fluid layer. Journal of Fluid Mechanics, 241, 587-614.

Dufresne, M. (2008). La modélisation 3D du transport solide dans les bassins en assainissement: du pilote expérimental à l'ouvrage réel (3D modeling of solid transport in wastewater basins: from experimental pilot to real reservoir) [Doctoral dissertation, Université Louis Pasteur, Strasbourg, France].

Dufresne, M., Vazquez, J., Terfous, A., Ghenaim, A., & Poulet, J. B. (2009). CFD modeling of solid separation in three combined sewer overflow chambers. Journal of Environmental Engineering, 135, 776-787.

Dufresne, M., Dewals, B., Erpicum, S., Archambeau, P., & Pirotton, M. (2010a). Classification of flow patterns in rectangular shallow reservoirs. Journal of Hydraulic Research, 48(2), 197-204.

Dufresne, M., Dewals, B. J., Erpicum, S., Archambeau, P., & Pirotton, M. (2010b). Experimental investigation of flow pattern and sediment deposition in rectangular shallow reservoirs. International Journal of Sediment Research, 25(3), 258-270.

Dufresne, M., Dewals, B. J., Erpicum, S., Archambeau, P., & Pirotton, M. (2011). "Numerical Investigation of Flow Patterns in Rectangular Shallow Reservoirs." Engineering Applications of Computational Fluid Mechanics, 5(2), 247-258.

Dufresne, M., Dewals, B., Erpicum, S., Archambeau, P. & Pirotton, M. (2012). Flow patterns and sediment deposition in rectangular shallow reservoirs. Water and Environment Journal 26, 504-510.

Duma, D., Erpicum, S., Archambeau, P., Pirotton, M., & Dewals, B. (2014). Velocity and Turbulence Measurements for Assessing the Stability of Riverbeds: a Comparison between UVP and ADVP. In R. Lehfeldt & R. Kopmann (Eds.), ICHE 2014. Proceedings of the 11th International Conference on Hydroscience & Engineering, September 28 - October 2, 2014, Hamburg, Germany (pp. 539-544). Karlsruhe: Bundesanstalt für Wasserbau.

Durst, F., Melling, A., & Whitelaw, J. (1974). Low Reynolds number flow over a plane symmetrical sudden expansion. Journal of Fluid Mechanics, 64, 111.

Ead, S. A., & Rajaratnam, N. (2002). Plane turbulent wall jets in shallow tailwater. Journal of Engineering Mechanics, 128(2), 143-155.

El kadi Abderrezzak, K., Die Moran, A., Tassi, P., R. Ata, Herouvet, J. M. (2015). Modelling river bank erosion using a 2D depth-averaged numerical model of flow and non-cohesive, non-uniform sediment transport. Advances in Water Research, 93, 75-88.

Escudier, M.P., Oliveira, P.J., & Poole, R.J. (2002). Turbulent flow through a plane sudden expansion of modest aspect ratio. Physics of Fluids, 14, 3641-3654.

Eriksson, J. G., Karlsson, R. I., & Persson, J. (1998). An experimental study of a two-dimensional plane turbulent wall jet. Experiments in Fluids, 25, 50-60.

Esmaeili, T., Sumi, T., Kantoush, S., Haun, S., & Rüther, N. (2015). Three-dimensional numerical modeling of the flow field in shallow reservoirs. ICE-Water Management, 169, 229-244.

Farge, M. (2022). The evolution of turbulence theories and the need for continuous wavelets.

Fearn, R., Mullin, T., & Cliffe, K. (1990). Nonlinear flow phenomena in a symmetric sudden expansion. Journal of Fluid Mechanics, 211, 595-608.

Ferrara, V., Erpicum, S., Archambeau, P., Pirotton, M., & Dewals, B. (2018). Flow field in shallow reservoir with varying inlet and outlet position. Journal of Hydraulic Research, 56, 689-696.

Friedrich, H., Spiller, S. M., & Rüther, N. (2014). Near-bed flow over a fixed gravel bed. In Proc. 7th International Conference on Fluvial Hydraulics (River Flow), Lausanne, Switzerland, 3-5 Sept (pp. 279-285).

Telemac-Mascaret Modelling System (v8p4).GAIA User Manual.

George, W. K., Abrahamsson, H., Eriksson, J., Lofdahl, L., & Karlsson, R. (1997). A similarity theory for the plane turbulent wall jet. Submitted for publication. Also: Internal Report 97/7, Dept. of Thermo and Fluid Dynamics, Chalmers University of Technology, Gothenburg, Sweden.

Goring, D.G., & Nikora, V.I. (2002). Despiking Acoustic Doppler Velocimeter Data. Journal of Hydraulic Engineering, 128(1), 117-126.

Görtz, J., Aouad, M., Wieprecht, S., & Terheiden, K. (2022). Assessment of pumped hydropower energy storage potential along rivers and shorelines. Renewable and Sustainable Energy Reviews, Elsevier, vol. 165(C).

Guimet, V., & Laurence, D. (2002). A linearised turbulent production in the k-ε model for engineering applications. Engineering Turbulence Modelling and Experiments 5, 157–166. doi:10.1016/b978-008044114-6/50014-4.

Guo, T., Rau, M. J., Vlachos, P. P., & Garimella, S. V. (2017). Axisymmetric wall jet development in confined jet impingement. Physics of Fluids, 29.

Guzman, C.B., Cohen, S., Xavier, M., Swingle, T., Qiu, W., & Nepf, H. (2018). Island topographies to reduce short-circuiting in stormwater detention ponds and treatment wetlands. Ecological Engineering, 117, 182-193.

Hervouet, J.M. (2007). "Hydrodynamics of free-surface flows- Modelling with finite element method: John Wiley & Sons," 341p.

Hervouet, J.M., Sara, P, & Mario, Ricchiuto. (2017). Residual distribution advection schemes in Telemac. [Research Report] RR-9087, Inria Bordeaux Sud-Ouest., pp.70.

Hinze, J.O. (1975). Turbulence (2nd ed.). McGraw-Hill.

Hurther, D., & Lemmin, U. (2001). A Correction Method for Turbulence Measurements with a 3D Acoustic Doppler Velocity Profiler. Journal of Atmospheric and Oceanic Technology, 18, 446-458.

Hussain, A. K. M. F. (1983). Coherent structures – reality and myth. Physics of Fluids, 26(10), 2816-2825.

Isenmann, M. (2016). Approche euler – lagrange pour la modelisation du transport solide dans les ouvrages de decantation (Euler–Lagrange Approach for Solid Transport Modeling in Sedimentation Facilities). [Doctoral dissertation, Université Louis Pasteur, Strasbourg, France].

Izdori, F., Semiao, A. J. C., & Perona, P. (2019). The role of environmental variables in waste stabilization ponds' morphodynamics. Frontiers in Environmental Science, 7.

Kaffel, A., Moureh, J., Harion, J. L., & Russeil, S. (2015). Experimental investigation of a plane wall jet subjected to an external lateral flow. Experiments in Fluids, 56, 56-95.

Kalitzin, G., Medic, G., Iaccarino, G., & Durbin, P. (2005). Near-wall behavior of RANS turbulence models and implications for wall functions. Journal of Computational Physics, 204, 265-291.

Kalter, R., Tummers, M.J., Kenjereš, S., Righolt, B.W., & Kleijn, C.R. (2014). Effects of electromagnetic forcing on self-sustained jet oscillations. Physics of Fluids 26 (6),065101.

Kantoush, S.A. (2008). Experimental study on the influence of the geometry of shallow reservoirs on flow patterns and sedimentation by suspended sediments. PhD Thesis, EPFL, Lausanne, Switzerland.

Kantoush, S.A., De Cesare, G., Boillat, J.L., & Schleiss, A.J. (2008a). Flow field investigation in a rectangular shallow reservoir using UVP, LSPIV, and numerical modeling. Flow Measurement & Instrumentation, 19, 139-144.

Kantoush, S.A., Bollaert, E., & Schleiss, A.J. (2008b). Experimental and numerical modeling of sedimentation in a rectangular shallow basin. International Journal of Sediment Research, 23(3), 212-232.

Kantoush, S.A., & Schleiss, A.J. (2009). Channel formation in large shallow reservoirs with different geometries during flushing. Journal of Environmental Technology, 855-863.

Kantoush, S.A., Sumi, T., & Schleiss, A.J. (2010). Geometry effect on flow and sediment deposition pattern in shallow basins. Annual Journal of Hydraulic Engineering, JSCE, 54, 212-232.

Kantoush, S.A., & Schleiss, A.J. (2014). Influence of geometry shape factor on trapping and flushing efficiencies. Taylor & Francis Group.

Koskiaho, J. (2003). Flow velocity retardation and sediment retention in two constructed wetland-ponds. Ecological Engineering, 19, 325-337.

Kline S.J., Reynolds W.C., Schraub F.A., & Runstadler P.W. (1967). The structure of turbulent boundary layers. Journal of Fluid Mechanics, 30, 741.

Krone R.B. (1962). Flume studies of the transport of sediment in estuarial shoaling processes. Final report. Hydraulic Engineering and Sanitary Engineering Research Laboratory, University of California, Berkeley, Calif., USA

Lacey, J., Duguay, J., & MacVicar, B. (2018). Comparison of velocity and turbulence profiles obtained with a Vectrino Profiler and PIV. E3S Web Conf. 2018, 40, 05070.

Lakzian, E., Saghi, H., & Kooshki, O. (2020). Numerical simulation of sediment deposition and trapping efficiency estimation in settling basins, considering secondary flows. International Journal of Sediment Research, 35, 347-354.

Launder, B. E., & Rodi, W. (1981). The turbulent wall jet. Progress in Aerospace Sciences, 19, 81-128.

Launder, B. E., & Rodi, W. (1983). The turbulent wall jet - Measurements and modeling. Annual Review of Fluid Mechanics, 15, 429-459.

Leng, X., & Chanson, H. (2017). Unsteady velocity profiling in bores and positive surges. Flow Measurement and Instrumentation, 54, 136-145.

Liu, D., Al-Obaidi, K., & Valyrakis, M. (2022). The assessment of an Acoustic Doppler Velocimetry profiler from a user's perspective. Acta Geophysica.

Liu, X., Xue, H., Hua, Z., Yao, Q., & Hu, J. (2013). Inverse calculation model for optimal design of rectangular sedimentation tanks. Journal of Environmental Engineering (United States), 139, 455-459.

Lumley, J. L., & Newman, G. R. (1977). The return to isotropy of homogeneous turbulence. Journal of Fluid Mechanics, 82, 161.

Lumley, J. L. (1978). Computational modeling of turbulent flows. In Advances in Applied Mechanics, vol. 18, pp. 123-175. Academic.

Luyckx, G., Vaes, G., & Berlamont, J. (1999). Experimental investigation on the efficiency of a high side weir overflow. Water Science and Technology, 39 (2), 61-68.

Macvicar, S., Dilling, J., Lacey, K., & Hipel (2014). A Quality Analysis of the Vectrino II Instrument using a New Open-source MATLAB Toolbox and 2D ARMA Models to Detect and Replace Spikes. In Proceedings of the 7th International Conference on Fluvial Hydraulics (River Flow), Lausanne, Switzerland, 3-5 Sept.

Maurel, A., Ern, P., Zielinska, B., and Wesfreid, J.E. (1996). Experimental study of self-sustained oscillations in a confined jet. Physical Review, 54(4), 3643-3651.

Metflow, S.A (2002). UVP Monitor: Model UVP-DUO with software version 3. User's Guide. Lausanne, Switzerland.

Mouris, K., Beckers, F. and Haun, S. (2018). Three-dimensional numerical modeling of hydraulics and morphodynamics of the Schwarzenbach reservoir. E3S Web Conference, 40, 03005.

Miozzi, M., Lalli, F., & Romano, G. P. (2010) Experimental investigation of a free-surface turbulent jet with Coanda effect. Experiments in Fluids, 49, 341-353.

Miozzi, M., and Romano, G. P. (2020). Propagation of perturbations and meandering in a free surface shallow water jet. Experiments in Fluids, 61.

Mizushima, J., Okamoto, H., & Yamaguchi, H. (1996). Stability of flow in a channel with a suddenly expanded part. Physics of Fluids, 8, 2933-2942.

Mizushima, J., & Shiotani, Y. (2001). Transitions and instabilities of flow in a symmetric channel with a suddenly expanded and contracted part. Journal of Fluid Mechanics, 434, 355-369.

Nezu, I., & Nakagawa, H. (1993). Turbulence in Open Channel Flows. IAHR Monograph.

Padmanabham, G., & Lakshmana Gowda, B. H. (1991). Mean and turbulence characteristics of a class of three-dimensional wall jets. Part I: Mean flow characteristics. Journal of Fluid Engineering, 113, 620-628.

Partheniades. (1965). Erosion and deposition of cohesive soils. Journal of the Hydraulics Division, 91(1), 105-139.

Peltier, Y., Erpicum, S., Archambeau, P., Pirotton, M., & Dewals, B. (2014). Experimental investigation of meandering jets in shallow reservoirs. Environmental Fluid Mechanics, 14(3), 699-710.

Peng, Y.; Zhou, J.G.; Burrows, R. (2011). Modelling solute transport in shallow water with the Lattice Boltzmann method. Computer and Fluids 2011, 50, 181-188.

Persson, J. (2000). The hydraulic performance of ponds of various layouts. Urban Water, 2, 243-250.

Pilechi, A., Mohammadian, A., & Rennie, C. (2011). Experimental and numerical study of turbulent wall jets. In 20th Canadian Hydrotechnical Conference, Ottawa, Canada.

Quarini, G., Innes, H., Smith, M., & Wise, D. (1996). Hydrodynamic modelling of sedimentation tanks. Journal of Process Mechanical Engineering, 210(2),83-91.

Pope, S. (2000). Turbulent Flows. Cambridge: Cambridge University Press. doi:10.1017/CBO9780511840531.

Rajaratnam, N. (1976). Turbulent jets. Elsevier Scientific Publishing Company, Amsterdam, pp. 661-669, 671.

Rajaratnam, N., & Humphries, J. A. (1984). Turbulent non-buoyant surface jets. Journal of Hydraulic Research, 22(2), 103-115.

Restivo, A., & Whitelaw, J. H. (1978). Turbulence characteristics of the flow downstream of a symmetric, plane sudden expansion. Journal Fluids Engineering, 100, 308.

Righolt, B. W., Kenjeres, S., Kalter, R., Tummers, M. J., & Kleijn, C. R. (2015). Dynamics of an oscillating turbulent jet in a confined cavity. Physics of Fluids, 27(9).

Rogers, M. M., & Moin, P. (1987). The structure of the vorticity field in homogeneous turbulent flows. Journal of Fluid Mechanics, 176, 33-66.

Saul, A.J. & Ellis, D.R. (1992). Sediment deposition in storage tanks. Water Science and Technology, 25(8), 189-198.

Schleiss, A.J., Franca, M.J., Juez, C., & De Cesare, G. (2016). Reservoir Sedimentation. Journal of Hydraulic Research, 54, 595-614.

Secher, M., Hervouet, J.-M., Tassi, P., Valette, E., & Villaret, C. (2013). Numerical Modelling of Two-Dimensional Flow Patterns in Shallow Rectangular Basins. Advances in Hydroinformatics, 499–510.

Shinneeb, M. (2006). Confinement Effects in Shallow Water Jets. University of Saskatchewan, Saskatchewan, Canada.

Shoarinezhad, W., Wieprecht, S., Kantoush, S. A., & Haun, S. (2023). Applying optimization methods for automatic calibration of 3D morphodynamic numerical models of shallow reservoirs: comparison between lozenge- and hexagon-shaped reservoirs. Journal of Hydroinformatics, 25(1), 85-100.

SMESH Documentation: https://docs.salome-platform.org/latest/gui/SMESH/index.html.

Stamou, A.I. (2002). Verification and application of a mathematical model for the assessment of the effect of guiding walls on the hydraulic efficiency of chlorination tanks. Journal of Hydroinformatics, 4 (4), 245-254.

Stamou, A. (2008). Improving the hydraulic efficiency of water process tanks using CFD models. Chemical Engineering and Processing: Process Intensification, 47(8), 1179-1189.

Stovin, V.R., & Saul, A.J. (1994). Sedimentation in Storage Tank Structures. Water Science and Technology, 29, 363-37.

Stovin, Virginia Ruth (1996) The prediction of sediment deposition in storage chambers based on laboratory observations and numerical simulation. PhD thesis, University of Sheffield.

Tamayol, A., Firoozabadi, & B., Ashjari, M.A. (2010). "Hydrodynamics of Secondary Settling Tanks and Increasing Their Performance Using Baffles." Journal of Environmental Engineering, 136(1), 32-39.

Tarpagkou, R., and Pantokratoras, A. (2013). CFD methodology for sedimentation tanks: the effect of secondary phase on fluid phase using DPM coupled calculations, Applied Mathematical Modelling, 37, 3478–3494.

Tay, G. F., Mishra, A., Kuhn, D. A., & Tachie, M. F. (2017). Free surface effects on the statistical properties of a submerged rectangular jet. Physics of Fluids, 29, 025101.

Theodorsen, T. (1955). The structure of turbulence. In 50 Jahre Grenzschictforschung, edited by H. Gortler and W. Tollmein (Friedrich Vieweg & Sohn, Braunschweig, 1955).

Townsend, A. A. (1987). Organized eddy structures in turbulent flows. Physical-Chemical Hydrodynamics, 8(1), 23–30.

Tsavdaris, A., Mitchell, S., & Williams, J. B. (2015). Computational fluid dynamics modelling of different detention pond configurations in the interest of sustainable flow regimes and gravity sedimentation potential, Water and Environment Journal, 129-139.

Van Dyke M (1982). An album of fluid motion, The Parabolic Press, Stanford, California, USA.

Walker, D. T., Chen, C. Y., & Willmarth, W. W. (1995). Turbulent structure in free-surface jet flows. Journal of Fluid Mechanics, 291, 223-261.

Wallace, J.M. (1985). The vertical structure of bounded turbulent shear flow. Flow of real fluids. 235,253-268.

Westhoff, M.C., Erpicum, S., Archambeau, P., Pirotton, M., & Dewals, B. (2018). Maximum energy dissipation to explain velocity fields in shallow reservoirs. Journal of Hydraulic Research, 56, 221-230.

Wille, R, & Fernholz, H .(1965). Report on the first European mechanics colloquium on the Coanda effect. Journal of Fluid Mechanics, 23(4), 801-819.

Zahabi, H., Torabi, M., Alamatian, E., Bahiraei, M., & Goodarzi, M. (2018). Effects of geometry and hydraulic characteristics of shallow reservoirs on sediment entrapment. Water, 10(12), 1725.